XFEM for the Homogenization of Constitutive Properties and its Stabilization for the Computation of Interface Tractions

Ahmed Yacoub

A Thesis

in

the Department

of

Building, Civil and Environmental Engineering (BCEE)

Presented in Partial Fulfillment of the Requirements

For the Degree of Master of Applied Science (Civil Engineering) at

Concordia University

Montreal, Quebec, Canada

April 2025

CONCORDIA UNIVERSITY

School of Graduate Studies

This is to certify that the thesis is prepared

By: Ahmed Yacoub

Title: XFEM for the Homogenization of Constitutive Properties and its Stabilization for the Computation of Interface Tractions

and submitted in partial fulfillment of the requirements for the degree of

Master of Applied Science (Civil Engineering)

complies with the regulations of the University and meets the standards with respect to originality and quality.

Signed by the final Examining Committee:

_____ Chair

Dr. Ahmed Soliman

_____ Examiner

Dr. Ahmed Soliman

_____ Examiner

Dr. Biao Li

_____ Supervisor

Dr. Emre Erkmen

Approved by: _____

Dr. Po-Han Chen, Graduate Program Director

_____

Dr. Mourad Debbabi, Dean of Faculty

Abstract

XFEM for the Homogenization of Constitutive Properties and its Stabilization for the Computation of Interface Tractions

Ahmed Yacoub

A computational homogenization method for assessing the local stress distributions and effective mechanical characteristics of composite materials is presented in this work. Using the (XFEM) modeling capabilities, the effects of bonding assumptions on interface tractions, local stress fields, and homogenized constitutive properties are examined. The possibility of standard XFEM-based models to generate spurious oscillatory tractions at the bond interfaces is shown, with interface stiffness affecting the oscillations' magnitude. A stabilized XFEM framework is suggested as a solution to this problem in order to lessen the oscillatory behavior at matrix-inclusion interfaces. Comparisons with results from other modeling methodologies that are accessible in the literature provide a thorough validation of the developed stabilizing strategy. The suggested methodology's resilience and adaptability are further illustrated by its application to a number of Representative Volume Element (RVE) cases. The impacts of mesh refinement, interface stiffness, and RVE boundary conditions on the precision and effectiveness of the suggested method are investigated parametrically. The findings show that the stabilized XFEM may produce dependable traction results across bond interfaces and emphasize the significance of interface stiffness in the precise prediction of stress distributions. Additionally, it is demonstrated that the suggested approach offers reliable and effective results for a variety of composite microstructural configurations. By providing a reliable tool for the homogenization and analysis of composites with imperfect interfaces under various mechanical loading situations, this work advances XFEM-based computational approaches.

Acknowledgement

I wish to convey my deep gratitude to God Almighty for enabling this journey. Additionally, I extend my heartfelt thanks to my supervisor, Prof. Emre Erkmen, for welcoming me into his research group and for his immense support and patience throughout this process. His expert guidance was instrumental in the successful completion of my research project and in achieving my academic goals. I am profoundly appreciative of his unwavering support and encouragement.

I also wish to express my sincere appreciation to my family for their unwavering support throughout my master's degree and research endeavors. I am especially thankful to my mother and sister, whose encouragement, understanding, and steadfast belief in my abilities have provided me with the strength and motivation needed to persevere. Their love and dedication have been vital to my success.

Finally, I would like to acknowledge Prof. Emre Erkmen for his financial support, which played a critical role in the success of my research project, facilitated by his faculty research funding and research grant.

Table of Contents

List of Figures

List of Tables

Chapter 1

Introduction

1.1 Background and Motivation

1.1.1 Overview of Finite Element Methods (FEM)

The (FEM) is a widely used numerical technique in engineering and applied sciences for solving problems involving complex geometries, material properties, and boundary conditions. It is particularly valuable for structural analysis, where the aim is to understand how materials and structures respond to forces, stresses, and environmental conditions. FEM allows engineers and scientists to discretize a continuous domain into smaller, finite elements, making it easier to solve complex differential equations that describe the behaviour of the system. Each element is connected at discrete points called nodes, and the governing equations are solved over these elements, allowing for an estimation of the solution across the entire domain.

One significant benefit of the (FEM) is its adaptability in accommodating various geometrical configurations and boundary conditions, making it an indispensable tool in structural analysis. Traditional analytical methods often fall short when dealing with irregular shapes, non-homogeneous materials, or complex loadings, whereas FEM can efficiently model such conditions by dividing the structure into smaller, simpler parts. Applications of FEM are extensive and include analyzing stress and strain in mechanical components,

predicting deformation in civil engineering structures, and simulating thermal or fluid dynamics in various systems. Its ability to model the behaviour of both linear and non-linear systems adds to its versatility.

FEM's significance in structural analysis lies in its ability to provide accurate and reliable predictions for how structures will behave under various loading conditions. In mechanical engineering, for example, FEM is used to design machine parts, automotive components, and aerospace structures, ensuring that they meet safety and performance standards. In civil engineering, it is employed to analyze buildings, bridges, and dams, ensuring that these structures can withstand environmental forces like wind, earthquakes, and gravity. This precision not only enhances safety but also leads to cost-efficient designs by optimizing material usage and preventing over-engineering. By enabling the simulation of complex real-world problems, (FEM) enables engineers to evaluate multiple design alternatives prior to the construction of physical prototypes, thereby conserving both time and resources during the design phase. Moreover, FEM has been integrated with optimization techniques to create designs that meet specific performance criteria while minimizing weight, cost, or material usage. Its role in predicting failure modes, such as buckling or cracking, further ensures that structures are designed with an adequate margin of safety.

1.1.2 Limitations of Standard FEM

The (FEM) serves as an effective approach for addressing numerous engineering challenges; however, it encounters considerable difficulties when managing internal boundaries, fractures, and discontinuities. Standard FEM relies on a mesh that adapts to the specific geometry of the problem domain, including any internal features such as cracks or material interfaces. This mesh-dependent approach, which is contingent on the mesh, presents challenges when internal boundaries or discontinuities are misaligned with the mesh structure. The precision of the solution is influenced by the extent to which the mesh effectively represents these characteristics. Refined meshes can improve accuracy, but this often comes at a high computational cost, particularly in three-dimensional problems or when dealing with evolving discontinuities like propagating cracks.

One of the primary difficulties associated with the application of conventional Finite Element Method (FEM) for problems with cracks or discontinuities is the need to re-mesh the domain as these features evolve. Cracks, for example, create singularities within the

stress field, necessitating a refined mesh in that area to accurately model the stress concentration at the tip of the crack. As the crack expands, it is necessary to update the mesh in a dynamic manner, which can lead to significant computational overhead and complexity in implementation. Additionally, re-meshing can introduce errors, especially when interpolating the solution from the previous mesh to the updated version. These limitations make standard FEM unsuitable for problems involving moving or evolving discontinuities unless sophisticated re-meshing algorithms are employed.

Another issue is that standard FEM struggles with the representation of discontinuities in displacement fields, such as those caused by cracks. The approach generally presumes that the displacement field remains continuous at the boundaries of the elements, which is not the case in problems with cracks or sharp material interfaces. This assumption leads to poor accuracy and convergence when modelling phenomena like crack opening or sliding along a discontinuity. For instance, cracks necessitate that the displacement field exhibits discontinuity at the surfaces of the crack, but standard FEM cannot easily accommodate such behaviour without modifications to the mesh.

In addition, material interfaces or internal boundaries in multi-phase materials pose challenges for standard FEM. In problems involving composite materials or other heterogeneous media, the material properties change abruptly at interfaces. The conventional finite element method necessitates that the mesh aligns with these interfaces, which can be difficult in complex geometries or when dealing with micro-structural features. Misalignment between the mesh and the interfaces can lead to inaccurate stress and strain predictions at the boundaries, affecting the overall accuracy of the simulation. Moreover, capturing fine-scale features, such as inclusions or voids within a material, necessitates a highly refined mesh, which increases computational costs significantly.

These challenges underscore the limitations of standard FEM in addressing problems involving discontinuities and internal boundaries. Alternative approaches, such as the (XFEM), have been introduced to address these challenges by enabling the representation of discontinuities independently from the mesh structure. This significantly reduces the need for re-meshing and enhances the method's capability to model complex phenomena such as crack propagation, material phase transitions, and the behaviour of multi-phase materials.

1.1.3 Motivation for XFEM

The (XFEM) was developed to to overcome the constraints of conventional Finite Element Method (FEM), especially in managing discontinuities such as cracks, material interfaces, and various internal boundaries. In standard FEM, the mesh must conform to the geometry of the problem, meaning that any discontinuities need to align with the mesh elements. This creates significant challenges when modelling evolving or complex discontinuities, as it often necessitates re-meshing and increases computational effort. Additionally, standard FEM assumes continuity in the displacement field across element boundaries, which makes it difficult to model discontinuities accurately without modifying the mesh.

XFEM overcomes these limitations by decoupling the mesh from the location of discontinuities. This is accomplished by augmenting the solution space with extra degrees of freedom that are concentrated in the areas where discontinuities arise. The enrichment functions enable the displacement field to exhibit discontinuities within an element, eliminating the necessity for the mesh to align with these discontinuities. In the case of crack modelling, for example, XFEM introduces enrichment functions that represent the cracks' geometry and the associated discontinuous displacement field, allowing cracks to be modelled independently of the mesh. This significantly reduces the need for re-meshing and simplifies the handling of evolving cracks, making XFEM far more efficient for fracture mechanics problems.

One of the significant advancements in the (XFEM) is the incorporation of the Partition of Unity Method (PUM), which facilitates the enhancement of the finite element approximation space. Incorporating specialized functions that encapsulate the behaviour of discontinuities (such as the Heaviside function for cracks), XFEM can accurately represent complex phenomena like crack opening or material separation, without altering the underlying mesh. The enrichment process enables the (XFEM) to preserve the computational efficiency characteristic of the Finite Element Method (FEM), while simultaneously broadening its applicability to a diverse array of problems, including those involving non-aligned internal boundaries and interfaces.

XFEM's ability to decouple the mesh from the discontinuities also makes it highly effective in modelling problems involving multi-phase materials or composite structures. In conventional finite element methods (FEM), it is essential for the mesh to be sufficiently refined

to accurately represent the precise positions of material interfaces, which can be inefficient or computationally prohibitive in cases where the interfaces are complex or evolve. XFEM bypasses this issue by allowing material interfaces to be embedded within the elements, without requiring the mesh to conform to them. The implementation of this approach not only increases the precision of the solution but also boosts computational efficiency, allowing for the utilization of a standard mesh even when faced with intricate internal boundaries.

1.2 Detailed Description of XFEM

1.2.1 Partition of Unity Concept

The approaches grounded in the (PU) are essential for the progression of enrichment techniques within the context of the (XFEM), and they play a critical role in allowing XFEM to handle discontinuities and complex internal boundaries more efficiently. The approaches discussed are founded on the principle of enhancing the approximation space of conventional finite elements through the integration of supplementary functions. These functions are designed to effectively represent the local characteristics of the solution, all while avoiding any alterations to the fundamental finite element mesh. This enrichment process is what enables XFEM to accurately model phenomena such as cracks and material interfaces, even when these features do not align with the mesh.

The research conducted by Melenk and Babuška [32] established the theoretical underpinnings of the (PUFEM). In their foundational work, they proposed the concept of leveraging the (PU) property inherent in finite element shape functions to enhance the solution space by incorporating functions that capture the local characteristics of the problem. The (PU) property denotes the characteristic that the conventional finite element shape functions aggregate to one at every location within the domain, thereby establishing a foundation for the integration of supplementary information into the solution. By multiplying these shape functions with enrichment functions that capture local features, such as discontinuities or singularities, the overall approximation can be tailored to the specific characteristics of the problem.

In the framework of the (XFEM), the (PU) technique is especially advantageous as it facilitates the independent representation of discontinuities, such as cracks, regardless of

the underlying mesh configuration. In the field of fracture mechanics, the Heaviside step function is frequently employed as an enrichment function to effectively represent the discontinuous displacement field that occurs at a crack. The partition of unity framework ensures that this enrichment is applied only in regions where it is needed near the crack or discontinuity without affecting the rest of the domain. The localized enrichment significantly improves the solution's accuracy without requiring the mesh to align with the crack geometry, thus removing the necessity for costly re-meshing processes.

Furthermore, the partition of unity approach extends its applicability beyond the domain of fracture mechanics. The XFEM framework not only utilizes the Heaviside function but also integrates functions designed to represent singularities at the tips of cracks. These include asymptotic functions that characterize the stress distribution surrounding a crack tip. This capability is vital for accurately modeling the stress intensity factors, which are crucial for predicting crack propagation and potential failure. By enriching the solution space with these specialized functions, XFEM can handle problems that involve sharp gradients or singularities more effectively than standard FEM.

Furthermore, the partition of unity approach extends its applicability beyond the domain of fracture mechanics. In problems involving material interfaces or inclusions, enrichment functions that describe the behaviour of the interface can be introduced. For instance, in multi-phase materials, where different material properties exist on either side of an interface, XFEM can use enrichment functions to model the discontinuity in material behaviour. This approach eliminates the necessity for the mesh to determine the exact position of the interface, a task that would otherwise demand an exceedingly fine mesh to accurately represent the discontinuity.

1.2.2 Enrichment Functions in XFEM

Enrichment functions are essential in the (XFEM), especially for the precise representation of cracks and discontinuities. These functions allow XFEM to represent complex features within the problem domain, such as crack openings or material interfaces, without necessitating the alignment of the finite element mesh with these features. In conventional finite element methods, it is necessary to refine and modify the mesh to accurately represent the geometry of discontinuities, which can be computationally expensive and prone to inaccuracies, especially when dealing with evolving features like propagating cracks. Enrichment

functions address these issues by augmenting the finite element approximation space with additional terms that represent the local behaviour near the discontinuity, allowing XFEM to achieve higher accuracy without re-meshing.

In the context of crack modeling, enrichment functions are developed to address the discontinuous displacement observed at the crack faces as well as the stress singularity present at the crack tip. A frequently utilized enrichment function in the (XFEM) is the Heaviside step function, which effectively models the discontinuity in the displacement field that occurs at a crack. This function is utilized in a localized manner on the elements that are intersected by the crack, facilitating a discontinuous displacement field across the crack without necessitating that the mesh explicitly aligns with the geometry of the crack e.g., Moës et al. [38] and Belytschko et al. [5]. The Heaviside function is particularly useful in capturing the behaviour of open cracks, where the displacement on both sides of the crack face varies, and standard FEM would struggle to model this discontinuity without significant re-meshing.

The singular stress field near a crack tip is modeled using crack tip enrichment functions, alongside the Heaviside function. These functions are typically derived from the analytical solutions of stress intensity factors in the field of fracture mechanics, and they accurately depict the asymptotic characteristics of the stress field as it approaches the crack tip. The utilization of these enrichment functions presents a significant benefit, as they enable the (XFEM) to accurately represent stress concentrations without the necessity of refining the mesh in proximity to the crack tip. This requirement for mesh refinement is typically essential in traditional finite element methods (FEM) e.g., Belytschko and Black [4]. By enriching the solution space with these specialized functions, XFEM can achieve higher accuracy in predicting crack propagation and failure, even in cases where the crack path is complex or evolves. Additionally, comparable XFEM-based enrichment techniques for examining crack openings have been presented in the works of in Wells and Sluys [55], Moës and Belytschko [37] and Mergheim et al. [34].

An additional significant benefit of enrichment functions in the (XFEM) is their inherent flexibility. Depending on the characteristics of the discontinuity, a variety of enrichment functions can be utilized to accurately represent different phenomena. For example, in problems involving material interfaces or inclusions, enrichment functions that represent the difference in material properties across the interface can be introduced. This allows XFEM to model sharp changes in material behaviour without needing to align the mesh

with the interface e.g., Sukumar et al. [51]. In traditional FEM, accurately capturing such interfaces would require a highly refined mesh, which would significantly increase the computational cost. XFEM, through the use of enrichment functions, allows these features to be represented independently of the mesh, reducing computational demands while maintaining accuracy.

1.3 Challenges in XFEM

1.3.1 Locking and Spurious Oscillations

In the (XFEM), spurious oscillations and locking are significant challenges that arise when dealing with stiff interface conditions, where material properties exhibit sharp discontinuities across an interface, such as in cracks or material boundaries. These problems primarily arise from the interdependence of degrees of freedom at the interface, which can result in pathological behaviour in the numerical solution, especially when low-order finite elements are used. Understanding these problems is crucial for improving the accuracy and robustness of XFEM in simulations involving discontinuities.

Spurious oscillations typically manifest in the form of unrealistic fluctuations in the computed stress or displacement fields near an interface. These oscillations are especially prevalent in problems involving stiff interfaces, where the material on one side of the discontinuity is significantly stiffer than on the other. For example, in crack modeling, when the crack faces are modeled as stiff interfaces (such as in cases of cohesive zone models), the XFEM approach may struggle to accurately represent the gradual transition of stresses in the area surrounding the crack tip, leading to oscillatory behavior that compromises the physical interpretation of the issue. A similar issue is observed in composite materials with stiff inclusions embedded within a softer matrix, where the stress distribution near the inclusion interface can become oscillatory, leading to inaccuracies in predicting failure mechanisms.

First worth mentioning is the work of Simone [49], where for a discontinuity of arbitrary orientation with respect to the mesh, variations in the traction profile were observed. These oscillations in traction became stronger for higher values of the discontinuity stiffness and caused serious deterioration in the accuracy of the local solution around cracks.

This problem became particularly important when the XFEM was used as an interface or cohesive element. In fact, the following hypothesis has been put forward: pathological interrelation of the degrees of freedom in the same side of the fractured domain constitutes a main factor resulting in the spurious traction oscillations exhibited by the discontinuous elements using the partition-of-unity formulations. The authors in Latifaghili et al. [28] introduced an enrichment strategy based on the use of Laplace shape functions to alleviate the problem of oscillatory traction profiles arising from the standard XFEM method. The formulation of the proposed finite element and its implementation are independent of the type of parent element or geometry of the crack/interface thanks to the adaptability of polygonal interpolants. Issues at both the elemental and structural levels have been considered, including linear elastic models with very stiff interfaces and problems of nonlinear crack growth. Assessment of the robustness and accuracy of the formulation was done by examining force-displacement responses, traction profiles across discontinuities, stress contours, and jump openings.

1.3.2 Integration Schemes

The selection of integration schemes within the framework of the (XFEM) is pivotal in influencing the precision and computational efficiency of the numerical solution, especially in the presence of discontinuities like cracks or material interfaces. Traditional Gaussian quadrature, widely used in standard FEM, faces significant challenges in XFEM due to the presence of enrichment functions that introduce discontinuities and singularities into the finite element approximation. The intricacies involved necessitate the use of specialized integration methods to ensure the precision of the solution while also controlling computational expenses. In standard FEM, Gaussian quadrature performs well because the shape functions exhibit smoothness and continuity throughout the elements. In the context of the (XFEM), elements that are penetrated by a crack or discontinuity incorporate enrichment functions. These functions may include the Heaviside function, which accounts for displacement discontinuities, as well as asymptotic functions that address singularities at the tips of cracks. These functions introduce discontinuities within the elements, which significantly degrade the accuracy of standard Gaussian quadrature. This inaccuracy occurs because the quadrature points, which are uniformly distributed across the element, fail to capture the abrupt changes introduced by the enrichment functions. For instance, in crack

modelling, where the displacement field exhibits discontinuity at the location of the crack., standard integration schemes often yield oscillatory or inaccurate results for stress and displacement distributions.

To address these challenges, various integration schemes have been developed and refined. One widely adopted approach is sub-element integration, where the intersected elements are divided into smaller sub domains that align with the discontinuity. Within each sub domain, the enrichment functions become smooth and continuous, allowing Gaussian quadrature to accurately integrate the contributions. This approach improves accuracy by localizing the integration to regions with homogeneous behaviour. However, the computational expense may rise considerably as a result of the necessity for further subdivisions of sub-elements, especially in three-dimensional scenarios or when dealing with intricate crack geometries.

Another important method is integration with adaptive quadrature, where the number and placement of quadrature points are adaptively adjusted to capture the effects of the discontinuities. Adaptive schemes concentrate more quadrature points near regions with high gradients or abrupt changes, such as crack tips or material interfaces, while using fewer points in smooth regions. This strategy optimizes computational efficiency by focusing computational effort where it is most needed, ensuring high accuracy without excessive computational overhead. Adaptive integration is particularly effective in problems with evolving cracks, where the geometry of the discontinuity changes over time, and fixed integration schemes may fail to remain accurate.

The numerical integration of singular enrichment functions near crack tips poses an additional challenge. The enrichment functions used to capture crack-tip behaviour, such as those based on the asymptotic stress fields, exhibit singularities that cannot be effectively incorporated through conventional quadrature methods. To overcome this, specialized crack-tip quadrature rules have been developed. These rules place quadrature points in a manner that aligns with the behaviour of the singular enrichment functions, enabling accurate evaluation of stress intensity factors and various parameters associated with the crack tip. For example, the work by Moës et al. [38] demonstrated the importance of integrating crack-tip enrichment functions accurately to avoid errors in stress intensity factor predictions, which are critical in fracture mechanics.

Furthermore, the effects of different integration schemes on computational efficiency must be carefully balanced with their impact on accuracy. While sub-element and adaptive

quadrature techniques improve accuracy, the associated computational expense is elevated as a result of the greater quantity of quadrature points and operations required. In contrast, simplified or approximate integration schemes, such as lumped integration, reduce computational costs by using fewer quadrature points but may compromise accuracy, particularly in regions with steep gradients or discontinuities. The selection of the integration method is contingent upon the particular application and the balance between precision and computational efficiency.

For stiff interface problems, where locking and spurious oscillations are already significant concerns, improper integration schemes can exacerbate these issues. In these instances, it is crucial to accurately incorporate the enrichment functions to guarantee that the stiffness of the interface is appropriately depicted, avoiding the imposition of any artificial constraints. Studies such as Ahmed and Sluys [2] have shown that selecting appropriate integration schemes can help alleviate spurious oscillations and locking effects by improving the numerical accuracy of the enriched degrees of freedom.

1.3.3 Sub-Optimal Convergence

Sub-optimal convergence and oscillatory traction responses are well-documented challenges in the (XFEM) when dealing with stiff interface conditions. These issues arise due to the inherent difficulties in accurately representing the sharp discontinuities and complex mechanical behavior associated with stiff interfaces, such as those encountered in material interfaces, crack faces, or cohesive zones. In particular, when the utilization of low-order finite elements are used as the foundational basis functions, the degrees of freedom coupled across the stiff interface can result in pathological behavior, such as numerical oscillations in the traction profile or convergence rates that fail to meet theoretical expectations. These challenges have motivated the development of advanced stabilization techniques, with Lagrange multiplier-based strategies emerging as an effective approach to address these issues.

The problem of sub-optimal convergence in XFEM often occurs because traditional finite element formulations struggle to enforce the constraints imposed by stiff interfaces accurately. Ji and Dolbow [24] demonstrated that when the stiffness contrast between two regions is large, the standard XFEM formulation can exhibit convergence rates lower than expected, particularly for stress and traction fields. The enrichment functions used in XFEM, although designed to represent discontinuities, may not be sufficient to handle large stiff-

ness gradients without specialized techniques. This leads to inaccuracies in stress transfer across the interface, manifesting as errors in the numerical solution that persist even with mesh refinement. To address these challenges, Moës et al. [39] emphasizes the implementation of Dirichlet-type boundary conditions in the context of the X-FEM. X-FEM enables the representation of discontinuity surfaces or domain boundaries within meshes that may not strictly align with these surfaces. While the imposition of Neumann boundary conditions on boundaries intersecting element interiors is relatively straightforward and preserves the optimal convergence rate of the background mesh, significantly less attention has been given to Dirichlet boundary conditions, particularly in the limiting case of stiff boundary conditions. To address this gap, Moës et al. [39] introduces a novel strategy for imposing Dirichlet boundary conditions while maintaining the optimal convergence rate. The approach relies on the construction of an appropriate Lagrange multiplier space along the boundary. Furthermore, Béchet et al. [3] introduced a formulation that explicitly imposes interface conditions using Lagrange multipliers. By introducing supplementary degrees of freedom at the interface, Lagrange multipliers enforce continuity conditions or prescribed tractions more rigorously, ensuring that the mechanical behaviour at the interface is captured accurately. This approach successfully separates the finite element mesh from the position of the discontinuity, thereby addressing the constraints associated with low-order elements.

Recently, Erkmen and Dias-da Costa [12] investigated the performance of the XFEM in simulating stiff embedded interfaces and inclusions. It is well established in XFEM literature that ill-conditioned stiffness matrices and oscillatory behavior in the traction field at interfaces are significant challenges. The severity of these issues largely depends on the choice of basis functions and the orientation of the interface. Analysis of discontinuity jumps revealed that quadratic bubble residuals are a major contributor to the oscillatory behavior, and their effect is exacerbated in systems with highly stiff interfaces due to poor conditioning.

To address these challenges, the authors proposed a variationally consistent method that eliminates bubble residuals using an assumed strain approach. Additionally, Legendre polynomials and their orthogonality properties were employed to further improve the conditioning of the stiffness matrices. The reformulated method demonstrated robustness in enforcing Dirichlet-type boundary conditions on crack interfaces, including scenarios such as crack closure and initially rigid cohesive laws. Furthermore, the study examined the

impact of numerical oscillations on the prediction of effective composite properties using XFEM-based computational homogenization techniques.

1.4 XFEM in Multi-Phase Materials

1.4.1 Heterogeneous Materials

Multi-phase materials, including composites, concrete, and fiber-reinforced substances, are extensively utilized in engineering applications owing to their exceptional mechanical characteristics. These materials exhibit high strength-to-weight ratios, remarkable durability, and performance that can be specifically tailored to meet diverse requirements. These materials are characterized by their heterogeneous micro-structures, where multiple constituents such as fibers, aggregates, or inclusions are embedded within a matrix. For example, fiber-reinforced composites are composed of robust fibers embedded in a polymer matrix, providing anisotropic characteristics that can be adjusted to meet the requirements of particular load-bearing applications. Similarly, concrete comprises aggregates and cement paste, resulting in complex behaviour under loading, including crack initiation and propagation. While these materials provide significant advantages over traditional homogeneous materials, accurately modelling their behaviour presents substantial computational challenges because of their intricate internal structures and the relationships among various phases.

Homogenization has emerged as a necessary computational approach to overcome these challenges, particularly when simulating the response of large-scale structural components made of multi-phase materials. Directly resolving the fine-scale heterogeneities within these materials requires an extremely fine mesh, which results in prohibitive computational costs for large problems. For instance, explicitly modelling each fiber in a fiber-reinforced composite or each aggregate particle in concrete would lead to an impractically large number of degrees of freedom, even for modern high-performance computing resources. As a result, homogenization techniques are employed to smooth out the small-scale variations in the material structure by replacing the heterogeneous medium with an equivalent homogeneous material that exhibits averaged or effective properties.

In the homogenization process, a Representative Volume Element (RVE) is typically defined to capture the statistical behaviour of the material's micro-structure. The RVE is

a small, representative portion of the material that includes all relevant features of the heterogeneity, such as inclusions, fibers, or voids. By analysing the response of the RVE under various loading conditions, effective material properties such as stiffness, strength, and thermal conductivity can be determined and subsequently used in macroscopic structural models. This two-scale modelling approach significantly reduces computational costs while retaining sufficient accuracy to predict the material's overall behavior. Studies such as Holmes [23] and Qian et al. [47] have demonstrated the effectiveness of homogenization in multi-phase materials, showing that the approach provides reliable predictions for both elastic and inelastic responses.

For composite materials, homogenization techniques are particularly powerful when combined with numerical methods like the (XFEM). The (XFEM) has demonstrated significant benefits in addressing discontinuities caused by inclusions, cracks, or voids, as it does not necessitate the finite element mesh to align with these features. For example, Gal et al. [16], Bosco et al. [8], Svenning et al. [52], Patil et al. [45], Nguyen et al. [41], Erkmen and Dias-da Costa [12], Erkmen and Dias-da Costa [11] and Norouzi et al. [44] integrated XFEM into homogenization frameworks to analyse the mechanical properties of composites with complex micro-structures. By leveraging XFEM's ability to model arbitrary internal boundaries and discontinuities, the homogenization process can efficiently incorporate the effects of micro-structural features without resorting to computationally expensive mesh refinements.

1.5 Applications and Extensions of XFEM

1.5.1 Crack Modeling in Various Materials

The (XFEM) has found extensive applications in modelling cracks, fractures, and phase changes across various real-world materials and engineering disciplines. Its ability to handle discontinuities without requiring mesh alignment makes it an invaluable tool for predicting the mechanical behaviour of structures and materials under complex loading conditions.

In the field of fracture mechanics, the (XFEM) is extensively utilized to model the propagation of cracks in materials such as metals, concrete, and composite structures. For instance, in metal structures subjected to fatigue loading, cracks often initiate at stress

concentrations and propagate over time, eventually leading to catastrophic failure. Moës et al. [38] demonstrated that XFEM could accurately model crack growth without remeshing, enabling efficient simulation of fatigue-driven crack paths. Similarly, Belytschko and Black [4] applied discontinuous enrichment functions to represent crack openings in metallic components. This capability is critical for industries like aerospace and automotive, where fatigue life prediction is essential for ensuring structural integrity.

In the case of concrete, which is prone to crack formation due to its brittle nature, XFEM has proven particularly effective for analyzing fracture processes. Concrete constructions including dams, bridges, and edifices are subject to mechanical, thermal, or environmental loading, leading to crack initiation and propagation. Wells and Sluys [55] adopted XFEM to model cohesive cracks in concrete, capturing the traction-separation behaviour along crack surfaces. Their work allowed for more realistic simulation of crack openings and energy dissipation mechanisms in concrete structures.

1.5.2 Inclusion and Interface Problems

The (XFEM) excels in handling inclusions and interfaces within heterogeneous materials due to its ability to represent internal boundaries without requiring the mesh to conform to these interfaces. This ability holds particular importance in the modeling of heterogeneous materials, including composites, concrete, and multi-phase substances, where the internal architecture is defined by the presence of inclusions, voids, and interfaces. Traditional finite element methods (FEM) struggle with these complexities as they require a conforming mesh, leading to high computational costs and difficulties in mesh generation, especially when the interface geometry is intricate or evolves over time.

The (XFEM) tackles these issues by utilizing enrichment functions, which enable the finite element mesh to maintain its independence from the discontinuities present. For example, Sukumar et al. [51] demonstrated how XFEM could model inclusions and holes within a material matrix using level-set functions to define the interface geometry. By augmenting the approximation space with discontinuous functions, XFEM effectively models the material behavior in the vicinity of the inclusion or interface while preserving the integrity of the original mesh. This makes XFEM particularly efficient for introducing inclusions of arbitrary shapes into the computational domain, such as circular, elliptical, or irregular inclusions, which are common in fiber-reinforced composites and porous media.

In computational homogenization, the (XFEM) is essential for assessing the effective properties of heterogeneous materials. For instance, Gal et al. [16] and Bosco et al. [8] applied XFEM to analyze representative volume elements (RVEs) containing inclusions and interfaces, enabling the accurate prediction of macroscopic material behavior while accounting for microscopic heterogeneities. By keeping the mesh regular and unaltered, the (XFEM) facilitates the smooth integration of internal boundaries related to inclusions, thereby enhancing both computational efficiency and precision.

Furthermore, XFEM has been used to analyze stiff interfaces within multi-phase materials, where the material properties exhibit significant discontinuities across the boundaries. These stiff interfaces often arise in laminated composites, masonry, and other multi-constituent materials. Erkmen and Dias-da Costa [12] highlighted XFEM's ability to alleviate spurious oscillations and locking, which are common issues when modeling stiff interfaces with traditional FEM. By decoupling the mesh from the discontinuities, XFEM enables precise representation of the interface behavior, including the stress and strain distribution near the boundaries.

Overall, XFEM's ability to handle inclusions and interfaces within heterogeneous materials stems from its enriched approximation space, which captures the discontinuities without the need for a conforming mesh. This flexibility makes XFEM particularly suitable for modeling complex material behaviors in composites, porous media, and multi-phase systems, where internal boundaries are essential in influencing the mechanical behavior of materials.

1.6 Outlines

The subsequent sections of this thesis are organized as follows. This work presents a computational homogenization technique aimed at assessing the effective stiffness characteristics of composite materials, employing the (XFEM) to simulate two-dimensional representative volume elements (RVEs). Utilizing the features of XFEM, this approach considers the imperfect adhesion between inclusions and the surrounding matrix. To address potential oscillatory behavior at the matrix-inclusion interface under stiff interface conditions, a stabilization technique is proposed. The methodology is implemented within an in-house software framework to accommodate the stabilization procedure. Results obtained using

the proposed modeling technique are validated against benchmark data from the literature. Furthermore, parametric analyses are conducted to examine the effects of interface stiffness, mesh resolution, and the boundary conditions of the (RVE) on the calculated effective properties.

Chapter 2 provides a comprehensive overview of key aspects of homogenization in materials science, structured to guide the reader through foundational and advanced concepts. It begins by introducing the field equations and their weak forms, establishing the governing equations for stress and displacement fields in heterogeneous materials. Building on this framework, the discussion transitions to the principle of scale separation and first-order homogenization, detailing the derivation of homogenization equations and the role of asymptotic expansion in determining homogenized properties. The chapter further develops a variational setting for homogenization, emphasizing the weak form of equilibrium equations and the computation of the effective stress tensor within a variational framework. Lastly, it examines the representative volume element (RVE) boundary value problem, highlighting the selection of boundary conditions, their impact on effective material properties, and the application of finite element analysis to solve the RVE problem effectively.

Chapter 3 provides a comprehensive exploration of computational homogenization using the extended finite element method (XFEM), with a focus on implementing and analyzing Representative Volume Element (RVE) boundary conditions. It begins by detailing the numerical framework for RVE boundary conditions, employing vector-matrix notation to formulate stress, displacement, and related tensors. The interpolation of displacement and Lagrange multiplier fields leads to an algebraic representation of the RVE problem, with boundary decomposition enabling constraint application. The chapter progresses to uniform displacement gradient conditions, where macroscopic displacement gradients define boundary displacements without micro-scale fluctuations, simplifying algebraic formulations for nodal displacements and stress fields. It then examines uniform traction boundary conditions, allowing displacement fluctuations while ensuring stress uniformity, with derivations culminating in a matrix-based implementation. Periodic displacement conditions are addressed next, accommodating fine-scale displacement periodicity and anti-periodic traction, ensuring compatibility and equilibrium across boundaries through reduced degrees of freedom. The interpolation of displacement and Lagrange multiplier fields is subsequently discussed, emphasizing the accurate modeling of discontinuities and element-level efficiency. Finally, section 3.4 concludes with a detailed stabilization methodology to address traction

oscillations in XFEM. By decomposing the displacement jump function and incorporating a stabilization term using Legendre polynomials, the approach ensures numerical robustness without compromising accuracy. Implementation procedures, including stabilized shape functions and governing equations, integrate this stabilization framework seamlessly into XFEM, enhancing its applicability in computational homogenization.

Chapter 4 on case studies focuses on validating the XFEM-based computational homogenization procedure by comparing its results with established methods from literature. Overall, the validation results confirm the accuracy and reliability of the developed XFEM-based computational homogenization approach. The selection of the stabilization parameter χ in the Stabilized (S-XFEM) is important for controlling oscillations induced by quadratic bubble terms at the interface. While setting $\chi = 1$ has been effective in certain cases, a universally optimal value does not exist due to variations in material properties, geometry, and interface conditions. This chapter also introduces a novel criterion for selecting χ systematically and compares it with established methods from literature. The study demonstrates that the proposed methodology offers a robust and adaptable framework for determining χ, providing enhanced stabilization across a range of XFEM applications.

Chapter 5 on parametric studies investigates the influence of various parameters on the homogenized elastic properties of an RVE model. It begins with an analysis of the **Effect of Mesh Size**, where different mesh resolutions are compared in terms of their impact on stress calculations. Following this, the **Illustrating the Interface Bond Effect** section examines the role of boundary conditions and interface stiffness on stress distribution. Within this section, **Alternative RVE Boundary Conditions** are explored by analyzing the variation in average stresses under periodic, displacement, and traction boundary conditions, emphasizing the significance of interface stiffness. Additionally, the **Modeling of Fibres as Inclusions via the XFEM** subsection extends this investigation by comparing XFEM and FEM approaches in fiber-reinforced composites, highlighting how the imperfect bond assumption in XFEM leads to different stiffness contributions than the perfect bond assumption in FEM. Additionally, this chapter addresses the **Stabilization of the XFEM for Stiff Interface Bond**, demonstrating the implementation and effectiveness of the modified XFEM methodology through parametric studies on previously introduced cases. Lastly, this chapter introduces the criterion for selecting the optimal χ value, which is applied to four distinct cases representing different inclusion scenarios in a representative volume element (RVE). A range of material properties is examined to ensure a comprehensive analysis,

including the effects of stiff and imperfect bonds at the matrix-inclusion interface. The modulus of elasticity of both the matrix and inclusions varies across four studies to reflect different mechanical contrasts. For each study, tables summarize the material properties of the RVE components, followed by the optimal χ values obtained for various displacement gradients and interface stiffness conditions.

Lastly, conclusions are presented in chapter 6.

Chapter 2

Computational Homogenization

2.1 Introduction

Computational homogenization is a vital tool for understanding the behavior of heterogeneous materials, which have gained significant attention in engineering and materials science. These materials, known for their intricate microstructures, exhibit spatially varying properties at the microscopic level. Such variations pose considerable challenges in accurately predicting the macroscopic behavior of materials, which is essential for the design and assessment of engineering structures.

2.1.1 Motivation

The motivation for exploring computational homogenization stems from the pressing need to develop efficient and accurate predictive tools for heterogeneous materials. Traditional approaches often struggle to effectively capture the complex multiscale interactions at the microscopic level, which play an important role in defining the overall material response. This work aims to provide a deeper understanding and enhanced predictive capabilities for the mechanical behavior of heterogeneous materials through computational homogenization techniques.

2.1.2 Literature Review

The concept of homogenization has been extensively explored in the existing literature. Foundational contributions by Hashin and Shtrikman [19], Hill [21], and Eshelby [13] established the groundwork for understanding the effective properties of composite materials. For instance, Hashin and Shtrikman [19] introduced variational principles to derive rigorous bounds for the effective elastic moduli of composite materials, marking a significant advancement, particularly for multiphase composites. Similarly, Hill [21] extended self-consistent modeling, which assumes that each phase whether inclusions or matrix experiences an average field equivalent to the composite's effective field. This method remains widely used for estimating the effective moduli of materials with random microstructures.

In subsequent years, computational approaches such as the (FEM) have enabled numerical solutions to homogenization problems. More recent studies, including those by Kanit et al. [25] and Miehe and Koch [36], have advanced the field by addressing challenges related to the size and boundary conditions of the (RVE). Despite these advancements, a clear need persists for robust methodologies capable of accurately capturing the effects of microstructural variations on macroscopic properties.

2.1.3 Methodology

In this chapter, we present a detailed exploration of computational homogenization, beginning with the formulation of field equations and their weak forms. We assume a continuous stress field, while the displacement field is allowed to be discontinuous at interfaces. This approach captures the essential features of heterogeneous materials, where discontinuities arise naturally due to differences in material properties at the micro-scale. We introduce the displacement, stress, location, and material parameters in both vector and index notation, but primarily use index notation for tensor operations to facilitate the derivation of homogenization equations. Our methodology involves deriving the equilibrium equations governing the behaviour of the heterogeneous domain. We express the stress tensor in terms of the displacement gradient through the constitutive relation and establish the equilibrium conditions. By applying the Galerkin weak form, we obtain a set of integral equations that form the basis for the homogenization process. A key aspect of our approach is the separation of scales, which underpins the first-order homogenization method. We assume that the

heterogeneous medium exhibits rapidly oscillating properties, with heterogeneities much smaller than the overall size of the medium. This allows us to define an effective material property matrix that captures the averaged behaviour of the micro-structure. We introduce a scaling parameter, η, representing the ratio between the micro and macro-structure sizes. As η approaches zero, the homogenized property matrix becomes independent of location, enabling the formulation of a simplified, homogenized problem. The chapter further elaborates on the variational setting for homogenization and integrating the balance equations over a representative volume element (RVE). To solve the cell problem inherent in homogenization, we introduce a finite-sized RVE and explore different boundary value problems. We derive the relationship between local stress fields and average displacement gradients, which forms the basis for computing the effective property tensor.

2.1.4 Chapter Structure

This chapter is organized to offer a detailed overview of the essential aspects of homogenization in materials science. It begins with a discussion on **field equations and their weak forms**, providing the foundational framework by defining the governing equations for stress and displacement fields in heterogeneous materials. The focus then shifts to **separation of scales and first-order homogenization**, where the principle of scale separation is introduced, and first-order homogenization equations are derived. This section also explains the asymptotic expansion of the displacement field and its impact on the homogenized properties.

Subsequently, the chapter develops the **variational setting for homogenization**, presenting the variational framework necessary to address the computational homogenization problem. Emphasis is placed on deriving the weak form of equilibrium equations and computing the effective stress tensor. Finally, the chapter addresses the **RVE boundary value problem**, examining the role of the (RVE) in the homogenization process. This section explores the selection of appropriate boundary conditions, their influence on effective material properties, and the methodology for solving the RVE problem using finite element analysis.

2.1.5 Summary

By the end of this chapter, we will have established a comprehensive framework for computational homogenization, integrating theoretical formulations with practical numerical techniques. This framework not only enhances our understanding of heterogeneous materials but also provides a robust tool for predicting their macroscopic behaviour from microscopic details. The approaches and findings presented in this chapter play an important role in enhancing the design and evaluation of engineering materials, thereby facilitating advancements in material science and engineering applications.

2.2 Field equations and the weak form

In computational mechanics, particularly within finite element analysis (FEA), understanding the behavior of stress and displacement fields is essential for accurate selection of interpolation functions, modelling and simulation. The governing equations, or field equations, describe the physical behavior of these fields, and their reformulation into the weak form makes them suitable for numerical solutions.

In computational homogenization, the stress field is generally assumed to be continuous throughout the heterogeneous domain, meaning that the stress components do not exhibit abrupt jumps across material interfaces. However, after numerical discretization such as using the finite element method (FEM), the stress field may only be weakly continuous between elements. This means that while global equilibrium is maintained, small discontinuities may appear due to numerical approximations. These discontinuities can be mitigated by using advanced techniques such as enriched finite element formulations (e.g., XFEM) or by refining the mesh. On the other hand, the displacement field exhibits discontinuities across interfaces between different materials or along cracks and defects. This discontinuity occurs because different materials respond differently to applied loads, leading to mismatched displacements at material boundaries. For instance, at the interface between a stiff and a soft material, the displacement on one side may be significantly smaller than on the other, resulting in a discontinuous jump.

To describe these mechanical fields, both vector notation and index notation are introduced. Vector notation provides a compact representation of physical quantities. For

example, the displacement vector field in a two-dimensional (2D) system is expressed as

$$\mathbf{u} = u_i = \langle u_1 \quad u_2 \rangle^{\mathrm{T}} \tag{2.1}$$

where u_1 and u_2 represent the displacement components in the x_1 and x_2 directions, respectively. On the other hand, index notation is often preferred for rigorous derivations of homogenization equations. This notation explicitly expresses tensor components, simplifying the manipulation of terms involving differentiation and summation. In this context, the displacement components are denoted as u_i, with the subscript i taking values of 1 or 2 for 2D problems.

The stress tensor σ_{ij} in a heterogeneous domain represents the internal forces per unit area acting in the i-th direction on a plane perpendicular to the j-th direction. within the material. It is related to the displacement gradient through the constitutive relation, which describes how the material responds to deformation. This relation, given by

$$\boldsymbol{\sigma} = \sigma_{ij} = D_{ijkl} \frac{\partial u_k}{\partial x_l} \tag{2.2}$$

The equation expresses the stress σ_{ij} as a linear function of the displacement gradient $\frac{\partial u_k}{\partial x_l}$. The displacement gradient represents how the displacement field u_k changes with respect to spatial coordinates x_l, which is essential in characterizing strain in the material. The fourth-order stiffness tensor D_{ijkl} (also known as the elasticity tensor) relates stress to strain, encapsulating the mechanical properties of the material. It contains information about the material's stiffness and elasticity in different directions. Due to the heterogeneous nature of the domain, D_{ijkl} varies with position, meaning that the mechanical properties of the material can change across the domain. The domain consists of materials with different properties, leading to variations in the stiffness tensor. The stiffness components D_{ijkl} generally depend on the location vector $\mathbf{x}$, which is expressed as

$$\mathbf{x} = x_i = \langle x_1 \quad x_2 \rangle^{\mathrm{T}} \tag{2.3}$$

Here, the components x_1 and x_2 correspond to the position along the horizontal and verti-

cal axes, respectively. Together, these components uniquely specify a location within the domain, enabling precise identification of material properties, boundaries, and physical features. In a homogeneous material, D_{ijkl} would be constant throughout the domain, leading to a uniform stress-strain relationship, whereas in heterogeneous materials such as composites or materials with voids, D_{ijkl} varies spatially, leading to complex stress distributions.

In computational homogenization, analyzing a material's response in three dimensions (3D) requires handling a six-dimensional stress and strain tensor. However, to simplify the mathematical formulation and computational effort, this analysis is restricted to a two-dimensional (2D) model. This means that only the in-plane components of displacement, stress, and strain are considered. Since we are dealing with 2D modeling, the indices i, j, k, l in the stress-strain relationship range between 1 and 2 (i.e., corresponding to two spatial directions, typically x_1 and x_2) rather than spanning from 1 to 3 as in 3D problems. The stiffness tensor D_{ijkl} (also called the elasticity tensor) relates stress to strain and determines how a material deforms under loading. In a general 3D case, D_{ijkl} has 81 components ($3^4 = 81$), but due to various symmetry conditions, the number of independent components is significantly reduced. For a 2D linear elastic material, the symmetry conditions include minor symmetry and major symmetry. The stress tensor exhibits minor symmetry, meaning $\sigma_{ij} = \sigma_{ji}$, which arises from the balance of angular momentum in the absence of body moments. This symmetry implies that the stiffness tensor satisfies $D_{ijkl} = D_{ijlk}$. Additionally, the stiffness tensor satisfies major symmetry, meaning $D_{ijkl} = D_{klij}$, which follows from the symmetry of strain energy density in linear elasticity. In the 2D case, only components involving indices 1 and 2 are considered, and the shear stress components are symmetric, i.e., $\sigma_{12} = \sigma_{21}$. This further reduces the number of independent stiffness components, simplifying the analysis of the material's mechanical behavior.

Considering the above symmetries, the constitutive equation in 2D plane stress or plane strain conditions can be rewritten using Voigt notation, where the stress and strain tensors are converted into vector form. The components are arranged as

$$\boldsymbol{\sigma} = \begin{bmatrix} \sigma_{11} \\ \sigma_{22} \\ \sigma_{12} \end{bmatrix}, \quad \boldsymbol{\varepsilon} = \begin{bmatrix} \varepsilon_{11} \\ \varepsilon_{22} \\ 2\varepsilon_{12} \end{bmatrix} \tag{2.4}$$

Thus, the elasticity tensor D_{ijkl} is expressed as a 3×3 stiffness matrix $\mathbf{D}$

$$\mathbf{D} = \begin{bmatrix} D_{1111} & D_{1122} & D_{1112} \\ D_{1122} & D_{2222} & D_{2212} \\ D_{1112} & D_{2212} & D_{1212} \end{bmatrix} \tag{2.5}$$

Each entry in the stiffness matrix corresponds to a combination of stress-strain relationships. The six independent components of D_{ijkl} arise due to the above symmetries, which drastically reduce the number of independent parameters from 16 (in a general 2D tensor) to 6. The diagonal terms D_{1111} and D_{2222} represent the material's stiffness in the principal directions x_1 and x_2, respectively. The term D_{1122} describes the coupling effect between normal stresses σ_{11} and σ_{22}, illustrating how deformation in one direction influences the other. The off-diagonal terms D_{1112}, D_{2212}, and D_{1212} relate shear stress to normal strain and vice versa, capturing the interaction between different types of deformation. The symmetry conditions ensure that only six independent components remain, significantly simplifying the numerical implementation in computational homogenization. This matrix form is particularly useful in finite element analysis (FEA) and computational homogenization, as it provides a compact and efficient way to compute stress-strain relationships.

The equilibrium equations can be written as

$$\frac{\partial \sigma_{ij}}{\partial x_j} = p_i \quad \text{in} \quad \Omega \tag{2.6}$$

$$u_i = r_i \quad \text{in} \quad \Gamma_D \tag{2.7}$$

$$\sigma_{ji} n_i = -s_j \quad \text{in} \quad \Gamma_N \tag{2.8}$$

Here, Eq. (2.6) defines the balance of forces within a deformable material body, ensuring that it achieves static equilibrium under the influence of both internal and external forces. The left-hand side, $\frac{\partial \sigma_{ij}}{\partial x_j}$, represents the divergence of the stress tensor σ_{ij}. This term captures the spatial variation of stresses within the material, describing how these stresses change from one point to another in response to deformation. On the right-hand side, the term p_i denotes the external body force per unit volume acting on the material. Such forces can result from applied loads or other sources. The subscript i indicates the spatial direction in which the force is applied. To maintain equilibrium, these external forces must be coun-

terbalanced by the internal stresses within the material. This equilibrium condition applies within a specified domain Ω, which represents the material body being analyzed.

Eq. (2.7) defines a Dirichlet boundary condition, commonly designated as Γ_D. This condition specifies the displacement field u_i on a segment of the boundary Γ_D within the domain. It prescribes fixed values for the displacements u_i in one or more specified directions i, eliminating any degrees of freedom for the system to adjust autonomously in those directions. Instead, the displacement field is strictly constrained to align with the predetermined values r_i established by the boundary condition. This equation explicitly represents the prescribed displacements in the i-th direction. These fixed displacements are often derived from physical constraints or tailored design requirements. By enforcing these displacements on the boundary Γ_D, the system's behavior is directed and influenced in accordance with the intended deformation pattern.

Eq. (2.8) defines a Neumann boundary condition on Γ_N, specifying the traction vector (external forces) along a portion of the boundary. Here, σ_{ji} represents the stress tensor components, where j indicates the force direction and i corresponds to the normal to the surface. The unit normal vector's components, n_i, define the boundary orientation, with $\mathbf{n}$ pointing outward. The product $\sigma_{ji}n_i$ gives the j-th component of the traction vector, describing the stress acting along the boundary in the normal direction. This term reflects internal forces within the material. Meanwhile, s_j represents the externally applied surface traction in the j-th direction, indicating the force per unit area exerted on Γ_N. The negative sign in Eq. (2.8) indicates that the applied traction acts in the direction opposite to the outward normal stress vector, ensuring force equilibrium. External forces applied to the boundary act inward, while internal stress forces act outward. For equilibrium, the internal stress vector ($\sigma_{ji}n_i$) must balance the external applied traction ($-s_j$), ensuring their sum is zero. This is particularly evident in compressive loading, where the material's internal stress opposes the applied force, maintaining balance.

In boundary value problems, Dirichlet and Neumann conditions define how a physical system behaves at its boundaries. These two types of boundaries are distinct, non-overlapping and dividing the entire external boundary of the domain. Mathematically, this is expressed as $\partial\Omega = \Gamma$, where $\Gamma = \Gamma_D \cup \Gamma_N$ and $\Gamma_D \cap \Gamma_N = \varnothing$. Here, $\partial\Omega$ represents the outer boundary of the domain Ω, enclosing all points that define its limits. Dirichlet conditions are imposed on Γ_D, while Neumann conditions apply to Γ_N. The equation shows that the boundary is fully partitioned into these two regions, ensuring every point belongs to either

Γ_D or Γ_N, but not both. This strict separation prevents conflicts, guaranteeing well-defined boundary conditions.

The Galerkin weak form of the above governing equilibrium equations from Eqs. (2.6) to (2.8) can be expressed after introducing the variation of the displacement field δu_i and using integration by parts as shown in Appendix A.1.1 as

$$\int_\Omega \delta \frac{\partial u_i}{\partial x_j} \sigma_{ij} \, \mathrm{d}\Omega + \int_\Omega \delta u_i p_i \, \mathrm{d}\Omega + \int_{\Gamma_N} \delta u_i s_i \, \mathrm{d}\Gamma = 0 \tag{2.9}$$

where the admissible displacement field u_i is prescribed at the boundary Γ_D as in Eq. (2.7) and therefore, its variation vanishes, i.e., $\delta u_i = 0$ in Γ_D.

In the first term, $\delta \frac{\partial u_i}{\partial x_j}$ represents the virtual strain, where δu_i denotes a virtual displacement a small, arbitrary variation in the displacement field and $\frac{\partial u_i}{\partial x_j}$ corresponds to the strain tensor component. Here, σ_{ij} represents the stress tensor component, capturing the internal forces within the material. The integration $\mathrm{d}\Omega$ spans the entire domain Ω, representing the volume of the material under analysis. Physically, this term quantifies the work done by internal stresses as a result of virtual strains within the material, accounting for the internal distribution of forces responding to deformation.

In the second term, δu_i remains the virtual displacement field, while p_i denotes the body force per unit volume acting on the material. Similar to the first term, $\mathrm{d}\Omega$ involves integration over the entire domain Ω. This term represents the work done by external body forces on the material due to the virtual displacements, highlighting the interaction between applied forces and the material's deformation.

In the third term, δu_i is again the virtual displacement field, while s_i refers to the traction (force per unit area) specified along the Neumann boundary Γ_N. The integration $\mathrm{d}\Gamma$ is carried out over this boundary Γ_N. Physically, this term describes the work done by external surface tractions forces applied to the material's surface due to the virtual displacements.

Eq. (2.9) embodies the principle of virtual work, asserting that the total virtual work done by internal stresses and external forces (including both body forces and surface tractions) must equal zero for any arbitrary virtual displacement δu_i. This principle ensures that the weak form of the equilibrium equations is satisfied, providing a foundational expression of balance in the material system.

2.3 Separation of Scales and First Order Homogenization

A heterogeneous medium refers to a substance or material that exhibits variations in its properties across different regions or points within it. In simpler meaning, it's a substance that isn't uniform throughout, but rather consists of different components or regions with distinct characteristics. These differences may appear in a range of physical characteristics, including density, composition, or conductivity. For instance, a heterogeneous medium could be a composite material made up of different types of particles, each with its own unique properties. The key aspect of a heterogeneous medium is that it lacks uniformity, requiring a more refined approach to understanding its behaviour compared to homogeneous materials. This understanding is essential in fields such as materials science, geology, and fluid dynamics, where the properties of the medium significantly influence its overall behaviour and performance. Here, we adopt the assumption that the heterogeneous medium has rapidly oscillating properties and the sizes of the heterogeneities are small compared to the overall size of the medium. And, this assumption means that these properties change quickly over small distances. For example, in a composite material with alternating layers of different substances, the material properties might oscillate between those of each constituent material very frequently. Also, each individual region where the properties are different is much smaller than the overall dimensions of the material. For instance, if we consider a metal with embedded ceramic particles, the ceramic particles are much smaller than the metal piece itself. By assuming that the heterogeneities are small compared to the overall size of the medium, we can simplify the complex problem of varying properties into a more manageable form. Furthermore, this assumption is valid as long as the size of the heterogeneities is significantly smaller than the overall dimensions. This ensures that the oscillations do not dominate the behaviour of the medium on a macroscopic scale.

When dealing with such rapidly oscillating properties, it's often impractical to model each small-scale heterogeneity individually. Instead, a technique called homogenization is used. Homogenization is the mathematical technique used to transition from the micro-scale to the macro-scale. It involves averaging out the microscopic variations to obtain effective or homogenized properties that represent the material's behaviour on a larger scale. The objective here is to derive the macroscopic stiffness properties of a material from its known microscopic properties. This means deriving an average stiffness that captures the

combined effects of all the micro-scale components. In terms of micro-properties, we're referring to the properties of the material at a very fine scale, such as the properties of individual component in a composite material. These micro-properties of the material can exhibit considerable variation from one location to another, attributable to its heterogeneous characteristics. In terms of macro stiffness properties, these properties refer to the overall stiffness or mechanical behaviour of a material at a macroscopic level. Once we have computed these macroscopic stiffness properties using homogenization, the small-scale variations present in the micro-properties are no longer explicitly accounted for in the homogenized problem. The homogenized equilibrium equation is expressed as

$$\hat{D}_{ijkl}\frac{\partial^2 \bar{u}_i}{\partial x_j \partial x_k} = p_l \quad \text{in} \quad \Omega \tag{2.10}$$

This Eq. (2.10) represents the homogenized equilibrium in a heterogeneous medium. It expresses the balance of internal forces (represented by the effective stiffness tensor and the displacement field) with the external body forces. The left-hand side of the equation $\hat{D}_{ijkl}\frac{\partial^2 \bar{u}_i}{\partial x_j \partial x_k}$ represents the internal stress distribution within the material, where $\hat{D}_{ijkl}$ represents the effective stiffness tensor of the homogenized material. It is a fourth-order tensor derived from the homogenization process. The effective stiffness tensor characterizes the macroscopic elastic properties of the material. And, it expresses the average behaviour of the microscopic heterogeneities within the material. One significant feature of the effective material property matrix $\hat{D}_{ijkl}$ is that its components are independent of the location within the material. This means that, unlike the original heterogeneous micro-properties, the effective properties do not vary from point to point. Instead, they represent a uniform, averaged behaviour across the entire material domain. In Eq. (2.10), $\bar{u}_i$ represents the macroscopic displacement field, which describes the overall deformation of the material at a larger scale, ignoring the small-scale variations. The term $\frac{\partial^2 \bar{u}_i}{\partial x_j \partial x_k}$ represents the second partial derivatives of the displacement field with respect to the spatial coordinates x_j and x_k. This term corresponds to the strain components in the material. The right-hand side of the equation, p_l, represents the external body forces per unit volume acting within the material in the l-th direction. Body forces include gravitational forces or any distributed forces acting throughout the volume of the material. This equation indicates that the change in the internal stresses are in equilibrium with the applied body forces, ensuring the overall force balance in the material. Ω is the domain over which the equation is defined. It represents

the region of the material or structure being analysed. Furthermore, The Eq. (2.10) is derived through the process of homogenization, which averages the microscopic properties to obtain effective macroscopic properties. By using the effective stiffness tensor, the equation simplifies the analysis of heterogeneous materials by focusing on their averaged behaviour rather than detailed micro-structural variations.

In order to capture the small-scale influence on the effective property, a scaling parameter η is introduced. This scaling parameter η is a critical concept used to bridge the gap between the micro-structure and the macro-structure of a material. The parameter η represents the ratio between the characteristic size of the micro-structure (the small-scale features) and the characteristic size of the macro-structure (the large-scale domain). Mathematically, it is defined as $\eta = \frac{l_{\text{micro}}}{L_{\text{macro}}}$, where l_{micro} is the length scale of the micro-structural features, and L_{macro} is the length scale of the macroscopic domain. The introduction of η allows the model to incorporate the effects of small-scale heterogeneities on the overall material properties. This scaling parameter ensures that the variations in the micro-structure are appropriately reflected in the homogenized, or effective, properties of the material. The homogenized property matrix denoted as $\hat{D}_{ijkl}$ is defined analytically in the limit as the scaling parameter η approaches zero ($\eta \to 0$). When η approaches zero, it signifies that the micro-structural features become infinitesimally small compared to the macro-structure. This case is important in the homogenization process, where the goal is to average out the micro-structural variations to derive uniform macroscopic properties. As $\eta \to 0$, the detailed micro-structural variations are effectively smoothed out, leading to the definition of the homogenized property matrix $\hat{D}_{ijkl}$. This matrix expresses the averaged mechanical properties of the material, allowing it to be treated as homogeneous at the macroscopic scale. To more accurately describe this homogenization process, the size of the heterogeneity is introduced as a variable. This addition allows the homogeneous case to be described as a special instance within the context of heterogeneous materials. By adjusting the heterogeneity size, it is possible to shift from a detailed micro-structural analysis to a simplified, homogeneous description, making $\hat{D}_{ijkl}$ relevant across different scales. In practical terms, introducing the size of heterogeneity as a variable provides a flexible modelling approach. It enables the consideration of micro-structural influences when necessary while also allowing for the treatment of materials as homogeneous when appropriate. This dual capability is particularly valuable in engineering applications, where different levels of detail might be required for different analyses see Figure 2.1.

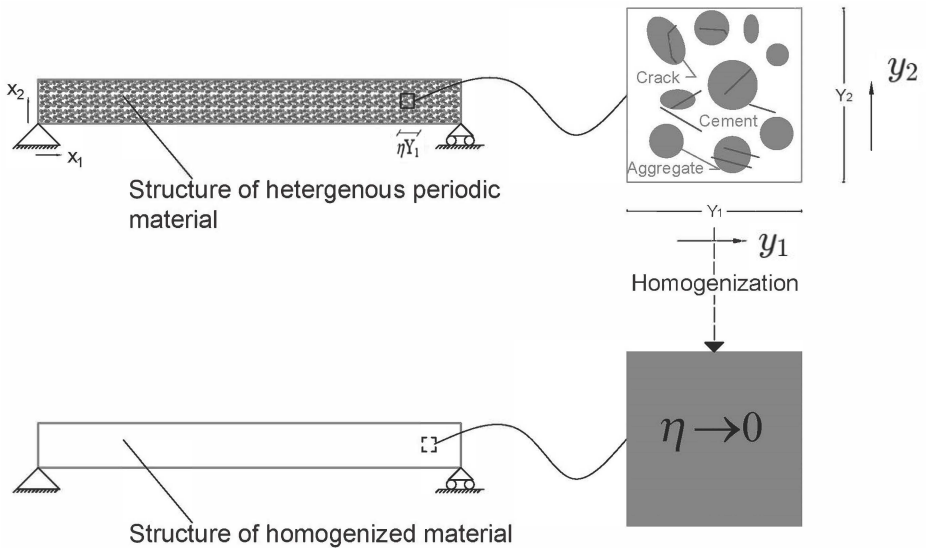

Figure 2.1: Homogenized material as a special case when inclusions are infinitesimally small, i.e.,$\eta \to 0$

The solution $\bar{u}_i$ in Eq. (2.10) is referred to the first approximate solution. It represents an initial approximation of the displacement field that satisfies the equilibrium conditions within the material domain Ω. While this solution may not perfectly capture every detail of the material behaviour, it serves as a starting point for further analysis and refinement. The main idea is to simplify the solution of a complex, heterogeneous problem by utilizing the solution of a simpler, homogeneous problem. This approach originates from the understanding that solving complex problems directly can be computationally intensive or analytically challenging. By approximating the solution using a simpler problem, such as the homogeneous problem, we can organize the analysis while still capturing essential aspects of the material behaviour. Therefore, The complete displacement field u_i is represented in the form of asymptotic expansion as

$$u_i(x_i, y_i) = \bar{u}_i(x_i, y_i) + \eta\bar{\bar{u}}_i(x_i, y_i) + \eta^2\bar{\bar{\bar{u}}}_i(x_i, y_i) + \dots \tag{2.11}$$

The Eq. (2.11) represents the complete displacement field u_i as an asymptotic expansion in terms of a small parameter η. This asymptotic expansion is a mathematical technique used to approximate a function or solution by expressing it as a series of terms, where each successive term provides a more accurate approximation. This expansion offers a systematic approach to approximating the complete displacement field of heterogeneous materials.

By building upon a simpler homogenized solution and iteratively adding corrections proportional to powers of η. Where, $u_i(x_i, y_i)$ represents the complete displacement field, which is a function of the spatial coordinates x_i and y_i. It characterizes the deformation of the material at every point in space. In $\bar{u}_i(x_i, y_i)$, $\bar{u}_i$ denotes the solution of a simpler homogenized problem, where the material is treated as homogeneous. This solution serves as the initial approximation to the displacement field, capturing the average behaviour of the material. In $\eta\bar{\bar{u}}_i(x_i, y_i)$, the $\eta\bar{\bar{u}}_i$ introduces the first-order correction to the homogenized solution. It represents the influence of micro-structural variations and heterogeneities on the displacement field. The parameter η scales the magnitude of this correction, with smaller values indicating finer micro-structural features. And, $\eta^2\bar{\bar{\bar{u}}}_i(x_i, y_i)$ further refines the approximation by incorporating second-order corrections to the displacement field. It captures additional details of the material's micro-structure, contributing to a more accurate representation of the deformation behaviour. Moreover, the ellipsis $(\ldots)$ indicates that the expansion continues indefinitely, with higher-order terms providing increasingly refined corrections to the displacement field. In practical scenarios, the series usually converges by limiting it to a certain number of terms, where additional contributions become negligible.

The concept of oscillatory behaviour which happens in heterogeneous materials arises from their basic complexity, where changes in micro-structure result in spatially dependent fluctuations in mechanical properties. These fluctuations appear as small-scale oscillations in the material's response, showcasing the complex interaction between various system scales. These oscillations are most noticeable in areas where the material shows substantial heterogeneity, causing localized deviations from the typical behaviour. According to the asymptotic expansion, such oscillatory behaviour is captured by higher-order contributions beyond the homogenized solution $\bar{u}_i$. These contributions, represented by terms like $\bar{\bar{u}}_i$, $\bar{\bar{\bar{u}}}_i$, and so on, account for increasingly detailed micro-structural effects that influence the overall deformation field. While the homogenized solution provides a rough approximation of the material response, the higher-order terms refine this approximation by incorporating corrections that capture the small-scale oscillations present in the system. Each successive term in the expansion contributes to the characterization of these oscillations, revealing their spatial distribution and magnitude across the material domain. By iteratively adding higher-order terms, we can gain insight into the fine-scale variations that underlie the macroscopic behaviour of the material. These contributions clarify the localized effects of heterogeneity, highlighting regions where deviations from homogenized behaviour are most pronounced.

Furthermore, the differing orders of η in Equation (2.11) create a hierarchy among the effects of each term in the series.

The scaling parameter η, as we discussed before, represents the ratio between the size of the micro-structure and the macro-structure in a heterogeneous material. As η varies, the position vector x_i might change its reference, making it difficult to maintain a consistent description of material points. This dependency on η complicates the construction of solutions that are valid across different scales. To address the challenge of constructing globally valid solutions that remain consistent as the scaling parameter η changes, it is essential to ensure that the position vector x_i is independent of η. This is achieved by incorporating two distinct spatial scales into the analysis. These scales are the slow scale and the fast scale. This dual-scale approach allows for a more precise representation of the material's behaviour at both the macro and micro levels. The position vector x_i is designated as the slow scale, or macro-scale coordinate. This scale measures variations within the global region of interest, capturing the overall, large-scale behaviour of the material. By defining x_i as the slow scale, it effectively averages out the fine-scale fluctuations caused by the material's heterogeneities. As a result, x_i remains consistent and always refers to the same material point, regardless of variations in the scaling parameter η. The fast scale, on the other hand, measures small-scale variations within one period cell of the micro-structure, capturing the fine-scale details and oscillations due to heterogeneity. This scale is represented in Eq. (2.11) by y_i. The fast coordinate y_i is defined as $y_i = x_i/\eta$ to capture the variations within the micro-structure or heterogeneities that are small compared to the overall size of the medium. In a heterogeneous medium, properties such as material stiffness may vary rapidly at a small scale. By introducing $y_i = x_i/\eta$, we separate the problem into a macro-scale (slow scale) described by x_i and a micro-scale (fast scale) described by y_i. This allows us to handle variations at different scales independently. And, the parameter η is small, representing the ratio between the size of the micro-structure and the macro-structure. When η is small, the fast coordinate y_i can vary significantly even when x_i varies slightly. This helps in capturing the rapid oscillations in the micro-structure. Also, the fast coordinate y_i enables us to analyse the periodicity and detailed behaviour within a single representative volume element (RVE) of the micro-structure. This is essential for determining the effective properties of the heterogeneous material. Furthermore, defining $y_i = x_i/\eta$ simplifies the mathematical treatment of the problem. It allows the use of asymptotic expansion techniques to systematically derive the effective (homogenized) properties

by considering terms of different orders of η. Overall, this definition helps to decouple the small-scale oscillations from the overall behaviour of the structure, making it easier to derive homogenized equations that describe the macroscopic properties of the heterogeneous material.

In a standard single-scale analysis, the derivative with respect to the coordinate x_i is straightforward $\frac{\partial}{\partial x_i}$. This operator captures how a quantity changes with respect to the position x_i on the macro-scale. When incorporating the micro-scale coordinate y_i, we need to account for variations on both scales. The micro-scale coordinate y_i is defined as $y_i = \frac{x_i}{\eta}$. Here, η is a small parameter representing the ratio between the micro-scale and the macro-scale. When $\eta \to 0$, it implies that the micro-scale length is becoming much smaller compared to the macro-scale length. In other words, the micro-structural features are very small relative to the overall size of the material. In multi-scale analysis, as η becomes smaller, the value of y_i increases for a given x_i. This means that for any fixed point in the macro-scale (given x_i), the corresponding micro-scale variations captured by y_i span a larger range. To account for both the macro-scale and micro-scale variations, we use the chain rule for differentiation. This rule allows us to express the derivative with respect to x_i as a combination of derivatives with respect to both x_i and y_i. Applying the chain rule as Holmes [23], the derivative with respect to x_i transforms as follows

$$\frac{\partial}{\partial x_i} \to \frac{\partial}{\partial x_i} + \frac{\partial y_i}{\partial x_i}\frac{\partial}{\partial y_i} \tag{2.12}$$

Since $y_i = x_i/\eta$, the derivative $\frac{\partial y_i}{\partial x_i}$ simplifies to $\frac{\partial y_i}{\partial x_i} = \frac{1}{\eta}$. Substituting $\frac{\partial y_i}{\partial x_i}$ into the chain rule expression Eq. (2.12) , we obtain the combined derivative operator

$$\frac{\partial}{\partial x_i} \to \frac{\partial}{\partial x_i} + \frac{1}{\eta}\frac{\partial}{\partial y_i} \tag{2.13}$$

This transformed derivative operator means that when we differentiate a function with respect to x_i, we must consider both the macro-scale derivative $\frac{\partial}{\partial x_i}$ and the micro-scale derivative $\frac{1}{\eta}\frac{\partial}{\partial y_i}$. Here, $\frac{\partial}{\partial x_i}$ captures the slow, global variations in the function with respect to the macro-scale coordinate. $\frac{1}{\eta}\frac{\partial}{\partial y_i}$ captures the fast, local variations in the function with respect to the micro-scale coordinate, scaled by $1/\eta$ to represent more details at the micro-scale. In the combined derivative operator Eq. (2.13), the term $\frac{1}{\eta}\frac{\partial}{\partial y_i}$ becomes more significant

as η decreases. Since $\frac{1}{\eta}$ is a large factor when η is small, the contribution of the micro-scale derivative $\frac{\partial}{\partial y_i}$ is amplified. Because $\frac{1}{\eta}$ is large, any small variations in the micro-scale coordinate y_i will be magnified when η is small. This means that the finer details of the micro-structure have a more pronounced impact on the overall behaviour of the material as η approaches zero. Essentially, the micro-scale variations are more noticeable and influential in the analysis. Furthermore, imagine looking at a detailed pattern on a fabric through a magnifying glass. As you zoom in (analogous to decreasing η), the complex details of the pattern become more visible and pronounced. Similarly, as η approaches zero in multi-scale analysis, the fine-scale features of the material (micro-scale variations) become more significant in the overall description of the material behaviour.

Many materials, especially composites and heterogeneous materials, show micro-structural features that influence their mechanical behaviour. So, we need to extend our analysis domain to include the micro-scale domain, and that helps us capture the effects of these micro-structural features on the material's overall behaviour. The extended domain facilitates a multi-scale analysis, where both macroscopic and microscopic effects are considered simultaneously. Also, the extended domain supports the use of asymptotic expansions, where the displacement field u_i is expanded in terms of contributions from different scales. Furthermore, many micro-structural features show periodic behaviour, such as the repeating pattern of inclusions in a composite material. This extended domain captures this periodicity, allowing for the analysis of how variations within one period cell affect the overall material behaviour. This extended domain is expressed by

$$\Omega^{\eta} = \Omega \times \eta \mathrm{Y} \tag{2.14}$$

where, the macroscopic domain, denoted by Ω, represents the entire region of interest at the macro-scale where the physical problem (such as stress or displacement in a material) is defined. This is the larger scale at which we observe the overall behaviour of the material or structure. At this level, the material properties might appear homogeneous or smoothly varying without considering the finer details of the micro-structure. And, the microscopic cell domain, denoted by Y, represents a single repeating unit of the micro-structure. This cell captures the detailed, periodic variations in material properties at the micro-scale. For instance, if the material has a composite structure with repeating patterns, Y would include

one instance of that pattern. This cell is much smaller compared to the overall size of Ω and is assumed to repeat periodically throughout the entire material. And, the parameter η is a small, dimensionless quantity representing the ratio between the size of the micro-structure and the macro-structure. Essentially, η scales the micro-structure so that it fits within the context of the macro-scale analysis. When we multiply the micro-scale domain Y by η, we obtain $\eta\mathrm{Y}$, which represents the micro-scale domain scaled down relative to the macro-scale. And, the combined analysis domain, Ω^η, is defined as the Cartesian product of the macroscopic domain Ω and the scaled microscopic domain $\eta\mathrm{Y}$. This extended domain means we are considering both the macro-scale and micro-scale effects simultaneously. Imagine a large structure like a beam (Ω). Inside this beam, there are tiny repeating cells (fibers, grains, etc.) represented by Y. To analyse how these tiny cells affect the whole beam, we scale down these cells by η and then consider the beam as a combination of the large structure and the scaled-down cells. This combined view is the extended analysis domain Ω^η. Furthermore, by including $\eta\mathrm{Y}$ in the domain definition, we incorporate the detailed micro-structural variations within the macro-scale analysis. This allows us to account for the influence of the fine-scale details on the overall behaviour of the material. The micro-scale domain Y is periodic, meaning it repeats itself throughout the material. By extending the analysis domain to include $\eta\mathrm{Y}$, we ensure that these periodic micro-structural patterns are considered in the analysis. The use of the small parameter η helps to separate the scales mathematically. The macro-scale variations are described by the coordinates in Ω, while the micro-scale variations are described by the coordinates in Y. This separation is crucial for applying multi-scale analysis techniques, such as homogenization. The extended domain facilitates the homogenization process, where we aim to derive effective macroscopic properties by averaging the microscopic properties. By analysing the periodic cell Y and scaling it with η, we can determine how the micro-scale features influence the macro-scale properties. From a mathematical perspective, defining the domain as $\Omega^\eta = \Omega \times \eta\mathrm{Y}$ simplifies the formulation of the problem. It allows us to systematically apply partial derivatives and other operations that take into account both macro and micro-scale effects.

Eq. (2.6) describes the equilibrium of stresses within the domain Ω. However, in the context of homogenization, where we extend the analysis to include both macroscopic and microscopic scales, this equation needs to be modified to accommodate the scaled micro-structural domain. As we explained before, to make the position vector x_i independent of the scaling parameter η and ensure that it refers to the same material point regardless of

changes in η, we introduce another coordinate vector $y_i = x_i/\eta$. The purpose of introducing y_i is to incorporate a fast coordinate system that measures variations within one period cell of the micro-structure. As a consequence of introducing the scaled coordinate y_i, derivative operations must be adjusted accordingly to maintain consistency. The partial derivative with respect to x_j $\left(\frac{\partial}{\partial x_j}\right)$ is transformed into a sum of two terms. These terms are the original derivative and an additional term involving the scaled coordinate y_j. This transformation is denoted as $\frac{\partial}{\partial x_j} \rightarrow \frac{\partial}{\partial x_j} + \frac{1}{\eta}\frac{\partial}{\partial y_j}$. Applying the transformation to the original equilibrium equation (2.6), we obtain the following modified equation

$$\frac{\partial \sigma_{ij}}{\partial x_j} + \frac{1}{\eta}\frac{\partial \sigma_{ij}}{\partial y_j} = p_i \tag{2.15}$$

This modified equation (2.15) accounts for the scaled micro-structural domain by including the additional derivative term with respect to y_j. The additional term involving $\frac{\partial}{\partial y_j}$ captures the variations in stresses within the micro-structure's period cell. Then, the asymptotic expansion of the stress tensor can be written as

$$\sigma_{ij} = \tilde{\sigma}_{ij} + \eta\tilde{\tilde{\sigma}}_{ij} + \eta^2\tilde{\tilde{\tilde{\sigma}}}_{ij} + \dots \tag{2.16}$$

where, the term $\tilde{\sigma}_{ij}$ represents the leading contribution to the stress tensor, corresponding to the macroscopic stress field. It characterizes the material's overall response at the largest scale, encompassing effects from external loads, boundary conditions, and bulk properties. This term provides a broad description of how the material behaves under macroscopic loading. The first-order microscopic correction, $\eta\tilde{\tilde{\sigma}}_{ij}$, accounts for the influence of micro-structural variations on the stress distribution. It captures deviations from the macroscopic behavior due to local heterogeneities, interface interactions, and small-scale structural features. Higher-order corrections, such as $\eta^2\tilde{\tilde{\tilde{\sigma}}}_{ij}$ and subsequent terms, refine the stress representation by incorporating finer-scale effects. These terms become increasingly relevant when micro-structural influences are more pronounced, providing a more detailed characterization of the material's response. By including these higher-order contributions, the expansion accounts for additional complexities and interactions that modify the overall stress distribution beyond the macroscopic approximation. By substituting Eq. (2.11) into Eq. (2.2) and using the derivative transform in Eq. (2.13) as shown in Appendix A.2.1, we get

$$\check{\sigma}_{ij} = D_{ijkl} \frac{\partial \bar{u}_k}{\partial y_l} \tag{2.17}$$

$$\tilde{\sigma}_{ij} = D_{ijkl} \left(\frac{\partial \bar{u}_k}{\partial x_l} + \frac{\partial \bar{\bar{u}}_k}{\partial y_l} \right) = \bar{\sigma}_{ij} + \bar{\bar{\sigma}}_{ij} \tag{2.18}$$

$$\tilde{\bar{\sigma}}_{ij} = D_{ijkl} \left(\frac{\partial \bar{\bar{u}}_k}{\partial x_l} + \frac{\partial \bar{\bar{\bar{u}}}_k}{\partial y_l} \right) \tag{2.19}$$

In Eq. (2.17), $\check{\sigma}_{ij}$ represents the stress contribution arising exclusively from micro-scale fluctuations. The material stiffness tensor D_{ijkl} governs the relationship between stress and strain through the constitutive equation. The term $\frac{\partial \bar{u}_k}{\partial y_l}$ denotes the gradient of the macroscopic displacement field $\bar{u}_k$ with respect to the micro-scale coordinate y_l, describing how displacement changes within the fine-scale structure. Physically, this equation expresses the micro-scale stress $\check{\sigma}_{ij}$ as a function of the macroscopic displacement gradient at the micro-scale. It highlights how local stress variations arise from deformation at small scales. Moreover, the equation implies that the micro-scale stress is directly linked to the macroscopic displacement gradient within the micro-scale coordinate system, reflecting the fine-scale material response.

In Eq. (2.18), $\tilde{\sigma}_{ij}$ represents the leading-order term in the asymptotic expansion of the stress tensor, incorporating both macro and micro scale effects. The material stiffness tensor D_{ijkl} defines the stress-strain relationship. The term $\frac{\partial \bar{u}_k}{\partial x_l}$ represents the macroscopic displacement gradient with respect to the macro-scale coordinate x_l, describing large-scale deformation. Meanwhile, $\frac{\partial \bar{\bar{u}}_k}{\partial y_l}$ corresponds to the gradient of the first-order micro-scale displacement correction $\bar{\bar{u}}_k$ in terms of the micro-scale coordinate y_l, capturing fine-scale variations. The macro-scale stress component is given by $\bar{\sigma}_{ij} = D_{ijkl} \frac{\partial \bar{u}_k}{\partial x_l}$, while the micro-scale stress correction is $\bar{\bar{\sigma}}_{ij} = D_{ijkl} \frac{\partial \bar{\bar{u}}_k}{\partial y_l}$. Physically, this equation expresses the total stress $\tilde{\sigma}_{ij}$ as the sum of these two contributions, reflecting both large-scale behavior and micro-scale refinements. By incorporating first-order micro-scale corrections, it provides a more detailed representation of the overall stress distribution, demonstrating how both scales influence the material response.

In Eq. (2.19), $\tilde{\bar{\sigma}}_{ij}$ represents the first-order correction in the asymptotic expansion of the stress tensor, accounting for higher-order effects. The material stiffness tensor D_{ijkl}

governs the stress-strain relationship. The term $\frac{\partial \bar{\bar{u}}_k}{\partial x_l}$ denotes the gradient of the first-order micro-scale displacement correction $\bar{\bar{u}}_k$ with respect to the macro-scale coordinate x_l, while $\frac{\partial \bar{\bar{\bar{u}}}_k}{\partial y_l}$ represents the gradient of the second-order micro-scale displacement correction $\bar{\bar{\bar{u}}}_k$ relative to the micro-scale coordinate y_l. Physically, this equation defines the first-order stress component $\tilde{\bar{\sigma}}_{ij}$, incorporating contributions from both macroscopic and higher-order micro-scale displacement gradients. It refines the stress representation by capturing finer details of the material response due to more complex micro-structural variations.

Together, Eqs. (2.17), (2.18), and (2.19) illustrate the hierarchical nature of the stress tensor in a heterogeneous material. This multi-scale expansion systematically incorporates different levels of micro-scale corrections, enhancing the accuracy of stress predictions under various loading conditions. Each term in the series refines the model, offering a comprehensive framework for understanding the interplay between macroscopic behavior and microscopic interactions.

The stress σ_{ij} is expanded as a series in Eq. (2.16). Here, $\tilde{\sigma}_{ij}$ represents the leading-order stress (zero order in η), while $\eta\tilde{\bar{\sigma}}_{ij}$ and $\eta^2\tilde{\bar{\bar{\sigma}}}_{ij}$ correspond to the first and second order corrections, respectively, with higher-order terms following the same pattern. Notably, the expansion does not include a term of the form $\eta^{-1}\check{\sigma}_{ij}$, which is important to the analysis. From multiscale theory, $\check{\sigma}_{ij} = D_{ijkl}\frac{\partial \bar{u}_k}{\partial y_l}$. If this term were present in the series, the stress expression would take the form

$$\sigma_{ij} = \eta^{-1}\check{\sigma}_{ij} + \tilde{\sigma}_{ij} + \eta\tilde{\bar{\sigma}}_{ij} + \eta^2\tilde{\bar{\bar{\sigma}}}_{ij} + \dots \tag{2.20}$$

As η approaches zero, the η^{-1} term would become unbounded, leading to a singular stress field. However, in multiscale analysis, σ_{ij} is assumed to be periodic in the microscopic coordinates y, meaning it must remain finite. The presence of $\eta^{-1}\check{\sigma}_{ij}$ would contradict this requirement, implying an unphysical, infinitely large stress component. To ensure that σ_{ij} remains bounded and periodic, $\eta^{-1}\check{\sigma}_{ij}$ must vanish, leading to the condition

$$\check{\sigma}_{ij} = D_{ijkl}\frac{\partial \bar{u}_k}{\partial y_l} = 0 \tag{2.21}$$

This ensures that the stress expansion remains physically meaningful and consistent with the assumptions of homogenization theory.

Equation (2.21) states that the product of the material stiffness tensor D_{ijkl} and the

partial derivative of $\bar{u}_k$ with respect to the fast coordinate y_l must be zero. There are limited ways to satisfy this condition. One possibility is $D_{ijkl} = 0$, which would imply that the material has no stiffness, which is a physically unrealistic scenario for most materials. The other possibility is $\frac{\partial \bar{u}_k}{\partial y_l} = 0$, meaning the displacement field $\bar{u}_k$ remains constant with respect to y_l. Since the material stiffness tensor is generally non-zero, the only viable conclusion is that $\bar{u}_k$ does not vary with y_l, making it a function of only the macroscopic coordinate x_i, i.e., $\bar{u}_i = \bar{u}_i(x_i)$. This result confirms that $\bar{u}_i$ represents the macroscopic displacement field, averaging out micro-scale fluctuations. Its independence from y_i indicates that it captures only the overall deformation of the structure, omitting the fine-scale variations introduced by the material's microstructure.

The stress tensor expansion in terms of the small parameter η is given by Eq. (2.16). To simplify the analysis, we retain only the first non-zero term, $\tilde{\sigma}_{ij}$, while disregarding higher-order contributions. This reduces the stress expression to

$$\sigma_{ij} = \tilde{\sigma}_{ij} \tag{2.22}$$

As a result, terms such as $\eta\tilde{\tilde{\sigma}}_{ij}$ are omitted. Similarly, the displacement field u_i is expressed as an asymptotic expansion in Eq. (2.11). In this simplified approach, we keep only terms up to the first order, leading to

$$u_i = \bar{u}_i + \eta\bar{\bar{u}}_i \tag{2.23}$$

These approximations Eqs. (2.22) and (2.23) focuses on the dominant macroscopic behavior while ignoring higher-order finer-scale corrections except for the first order.

In Eq. (2.23), $\bar{u}_i$ represents the macroscopic displacement field, while $\eta\bar{\bar{u}}_i$ accounts for the first-order correction due to micro-scale variations. Additionally, the correction term $\bar{\bar{u}}_i$ is assumed to be periodic in the fast coordinates y_i, meaning it repeats within each unit cell Y. Mathematically, this periodicity is expressed as

$$\bar{\bar{u}}_i(x_i, y_i) = \bar{\bar{u}}_i(x_i, y_i + Y_i) \tag{2.24}$$

where, $\bar{\bar{u}}_i$ represents the first-order correction in the displacement field, accounting for microstructural influences that are not captured by the macroscopic displacement $\bar{u}_i$. In computational homogenization, this term reflects fine-scale variations due to material het-

erogeneities. The coordinates (x_i, y_i) specify where $\bar{\bar{u}}_i$ is evaluated. The macro-scale coordinates x_i describe the global position within the material, varying over the large-scale domain, while the fast coordinates $y_i = x_i/\eta$ capture fine-scale variations within a single period of the microstructure, changing more rapidly than x_i. The expression $\bar{\bar{u}}_i(x_i, y_i + Y_i)$ represents the displacement correction at a shifted micro-scale coordinate $y_i + Y_i$, where Y_i denotes the periodicity of the microstructure. This periodicity ensures that microstructural variations repeat at regular intervals, maintaining consistency in the material's heterogeneous structure. Eq. (2.24) reflects this periodic behavior, which is characteristic of materials such as composites or those with regularly spaced inclusions. For a given macro-scale position x_i, the micro-scale displacement correction $\bar{\bar{u}}_i$ remains consistent across repeated microstructural patterns, ensuring uniformity in the material response.

By substituting Eq. (2.18) into Eq. (2.15) and grouping the terms according to their order, i.e., $O(1)$ and $O(1/\eta)$ as shown in Appendix A.2.2, we get

$$\frac{\partial \sigma_{ij}}{\partial y_j} = 0 \quad \text{in} \quad \mathrm{Y} \tag{2.25}$$

$$\frac{\partial \sigma_{ij}}{\partial x_j} = p_i \quad \text{in} \quad \Omega \tag{2.26}$$

Equation (2.25) describes the equilibrium condition at the micro-scale. The stress tensor σ_{ij} represents internal forces per unit area within the material, with indices i and j indicating directions in a Cartesian coordinate system. The operator $\frac{\partial}{\partial y_j}$ denotes differentiation with respect to the fast coordinate y_j, capturing micro-scale variations. The domain Y corresponds to a single periodic cell in the micro-structure. This equation states that σ_{ij} is divergence-free within each periodic cell, meaning there are no net internal forces acting within an individual micro-structural unit. This ensures local equilibrium, maintaining the periodicity and structural consistency of the material.

Equation (2.26) expresses the equilibrium condition at the macro-scale. Here, σ_{ij} denotes the macroscopic stress tensor, which characterizes internal forces per unit area. The term $\frac{\partial}{\partial x_j}$ represents the partial derivative with respect to the slow coordinate x_j, capturing macro-scale variations. The quantity p_i corresponds to the body force per unit volume in the i-th direction, encompassing effects such as gravity or other external influences. The domain Ω refers to the entire material body at this scale. This equation asserts that the di-

vergence of σ_{ij} must match the applied body force p_i, ensuring force equilibrium within the material, a fundamental concept in continuum mechanics.

2.4 Variational Setting for Homogenization

The weak form of the equilibrium equation can be expressed by integrating the balance in Eq. (2.26) over a domain of one cell, using the variation of the first approximate displacement field $\delta\bar{u}_i$ and using integration by parts as shown in Appendix A.3.1 as

$$\int_\Omega \delta\frac{\partial\bar{u}_i}{\partial x_j}\hat{\sigma}_{ij}\,\mathrm{d}\Omega + \int_\Omega \delta\bar{u}_i p_i\,\mathrm{d}\Omega + \int_{\Gamma_N} \delta\bar{u}_i s_i\,\mathrm{d}\Gamma = 0 \tag{2.27}$$

In the first term, $\int_\Omega \delta\frac{\partial\bar{u}_i}{\partial x_j}\hat{\sigma}_{ij}\,\mathrm{d}\Omega$, the integral is taken over the domain Ω. Here, δ denotes a variation (or virtual displacement) of the displacement field, while $\frac{\partial\bar{u}_i}{\partial x_j}$ represents the strain tensor as the gradient of the displacement field $\bar{u}_i$. The term $\hat{\sigma}_{ij}$ corresponds to the homogenized stress field, and the overall expression represents the internal forces in the material. Integrating the product of the strain variation and effective stress over the domain provides a measure of the internal work done by these stresses.

In the second term, $\int_\Omega \delta\bar{u}_i p_i\,\mathrm{d}\Omega$, the integral again spans Ω, where $\delta\bar{u}_i$ is the variation of the displacement field, and p_i denotes the body force per unit volume. This term accounts for the work done by body forces, obtained by integrating their product with the displacement variation over the domain.

The third term, $\int_{\Gamma_N} \delta\bar{u}_i s_i\,\mathrm{d}\Gamma$, involves integration over the Neumann boundary Γ_N. Here, $\delta\bar{u}_i$ represents the variation of displacement at the boundary, and s_i is the specified traction (force per unit area) applied on Γ_N. This term quantifies the work done by surface tractions, integrating their interaction with the displacement variation along the boundary.

Equation (2.27) expresses the weak form of the equilibrium equation in a homogenized framework, ensuring that the sum of internal, body, and boundary forces equals zero for equilibrium. In computational homogenization, this formulation guarantees that the averaged material behavior satisfies equilibrium conditions. Additionally, in deriving Eq. (2.27), it is assumed that the source terms p_i (body forces) and s_i (surface tractions) are independent of the fast coordinate y_i. This assumption simplifies the problem by ensuring that these forces remain uniform across the microstructure, eliminating microscopic variations.

The homogenized or effective stress tensor $\hat{\sigma}_{ij}$ in Eq. (2.27) is obtained by averaging the stress tensor over a representative volume element (RVE), denoted here as one cell, Y

$$\hat{\sigma}_{ij} = |\mathrm{Y}|^{-1} \int_{\mathrm{Y}} \sigma_{ij} \, \mathrm{dY} \tag{2.28}$$

This averaging process is essential for several reasons. First, homogenization enables the derivation of macroscopic properties that characterize the overall behavior of a heterogeneous material. By averaging the stress tensor over a cell, a single effective value is obtained, making it applicable in large-scale equations. Additionally, using an effective stress tensor simplifies both analysis and computation, allowing standard continuum mechanics approaches to be applied without needing to resolve microscopic variations explicitly. Then, Eq. (2.28) can be further expanded using the fact that the stress tensor σ_{ij} can be decomposed into terms involving $\bar{\sigma}_{ij}$ and $\bar{\bar{\sigma}}_{ij}$ based on Eqs. (2.22) and (2.18)

$$\hat{\sigma}_{ij} = |\mathrm{Y}|^{-1} \int_{\mathrm{Y}} \sigma_{ij} \, \mathrm{dY} = |\mathrm{Y}|^{-1} \int_{\mathrm{Y}} (\bar{\sigma}_{ij} + \bar{\bar{\sigma}}_{ij}) \, \mathrm{dY} \tag{2.29}$$

where, the homogenized or effective stress tensor $\hat{\sigma}_{ij}$ represents the average stress state within the RVE, providing a macroscopic perspective on the stress distribution. The volume of the cell, $|\mathrm{Y}|$, is given by the integral $|\mathrm{Y}| = \int_{\mathrm{Y}} \mathrm{dY}$. The term $\int_{\mathrm{Y}} \sigma_{ij} \, \mathrm{dY}$ represents the total stress accumulated over the cell volume by integrating the local stress tensor σ_{ij} across Y. To obtain the effective stress, this total stress must be divided by the cell volume, which is achieved using the reciprocal $|\mathrm{Y}|^{-1}$, ensuring that $\hat{\sigma}_{ij}$ retains the correct stress units. The local stress tensor σ_{ij} consists of two components: $\bar{\sigma}_{ij}$, which varies at the macroscopic level, and $\bar{\bar{\sigma}}_{ij}$, which fluctuates at the microscopic scale within the cell. In the integral $\int_{\mathrm{Y}} \bar{\sigma}_{ij} \, \mathrm{dY}$, the macroscopic stress $\bar{\sigma}_{ij}$ is either constant or slowly varying, meaning its integral provides the dominant macroscopic contribution. Meanwhile, $\int_{\mathrm{Y}} \bar{\bar{\sigma}}_{ij} \, \mathrm{dY}$ accounts for microscopic fluctuations, averaging them over the cell volume. Ultimately, Eq. (2.29) ensures that the effective stress tensor captures the combined influence of both macroscopic and microscopic stress variations within the RVE, linking the small-scale material behavior to the overall macroscopic response.

For the solution of the global equilibrium problem in Eq. (2.27), the whole stress tensor

σ_{ij} needs to be expressed in terms of the average displacement gradient $\partial\bar{u}_i/\partial x_j$. For that purpose, Eq. (2.25) is used in the weak form by multiplying with the virtual displacement fluctuations $\delta\bar{\bar{u}}_i$ and integrating over a domain of one cell Y. After integration by parts with respect to fast coordinate y_i as shown in Appendix A.3.2, we get

$$\int_Y \delta\frac{\partial\bar{\bar{u}}_i}{\partial y_j}\,\sigma_{ij}\,\mathrm{dY} - \int_\Psi \delta\bar{\bar{u}}_i\sigma_{ij}n_j\,\mathrm{d\Psi} = 0 \tag{2.30}$$

Note that Eq. (2.25) describes the microscale equilibrium equation for a heterogeneous material, assuming the absence of body forces. It asserts that the divergence of the stress field must vanish at the microscale, ensuring local equilibrium. However, this equation alone does not establish the link between microscopic and macroscopic behavior. To bridge this gap, Eq. (2.30) is derived by integrating the microscale equilibrium equation over the periodic cell volume Y and applying the divergence theorem. Yet, at this stage, it remains incomplete as it does not explicitly incorporate scale separation. This principle, fundamental to computational homogenization, assumes that the macroscopic length scale L is much larger than the microscopic length scale ℓ, i.e., $\frac{\ell}{L} \ll 1$. Such an assumption allows the separation of microscale fluctuations from macroscopic behavior, leading to the decomposition of the total displacement field and the formulation of Eq. (2.23). To fully define the homogenized problem and ensure proper decoupling, suitable boundary conditions must be applied to the representative volume element (RVE). These conditions ultimately lead to Eq. (2.38), which provides a rigorous framework integrating both microscopic and macroscopic scales.

Eq. (2.30) represents the weak form of equilibrium within the periodic cell Y, ensuring balance between internal stresses and boundary interactions. The first term, $\int_Y \ldots \mathrm{dY}$, denotes integration over the periodic cell. The expression $\delta\frac{\partial\bar{\bar{u}}_i}{\partial y_j}$ corresponds to the variation of the displacement fluctuation gradient with respect to the fast coordinate y_j, describing how virtual displacement changes within the cell. The stress tensor σ_{ij} represents internal stresses arising from deformation. This term captures the internal work done by the stress σ_{ij} against the virtual strain variation, reflecting the interactions within the cell that contribute to equilibrium. The second term, $\int_\Psi \ldots \mathrm{d\Psi}$, integrates over the cell boundary Ψ. Here, $\delta\bar{\bar{u}}_i$ represents the virtual displacement fluctuation at the boundary, while σ_{ij} remains the stress tensor, now evaluated at the boundary of the cell Ψ. The unit normal vector component n_j specifies the outward direction at each boundary point. This term accounts for

boundary work done by the stress through the virtual displacement, capturing interactions between adjacent cells. Together, these terms ensure equilibrium in a weak sense, meaning the internal and boundary forces remain balanced under virtual displacements $\delta\bar{\bar{u}}_i$. This formulation is essential in homogenization, providing a foundation for deriving effective material properties by averaging over the periodic cell.

By enabling the separation of local (microscopic) and global (macroscopic) analyses, it plays an important role in homogenization, where macroscopic properties are extracted from the material's microstructure. Solving this problem establishes a relationship between the average displacement field gradients and the microscopic stress distribution. Once the microscopic solution is obtained, the resulting stress tensor σ_{ij} is averaged over the cell Y to compute the effective stress tensor $\hat{\sigma}_{ij}$ in Eq. (2.29). This homogenized stress tensor is then incorporated into the macroscopic equilibrium equation, Eq. (2.27), to characterize the material's response on a larger scale. Ultimately, this framework ensures that the macroscopic description accurately captures the influence of the heterogeneous microstructure, providing a reliable and efficient approach for analyzing complex materials.

2.5 RVE boundary value problem

To solve the cell problem in Eq. (2.30), a finite-size Representative Volume Element (RVE) is introduced. The RVE is the smallest portion of a material's microstructure that can reliably predict macroscopic mechanical behavior, particularly stiffness. It must be large enough to capture key microstructural features while remaining computationally efficient. For instance, in a fiber-reinforced composite, the RVE includes a representative number of fibers and surrounding matrix to account for their distribution and interactions. If the volume is too small, it may not capture the essential microstructural characteristics, leading to inaccurate macroscopic property estimations. The parameter η represents the ratio of the microscopic (RVE) to macroscopic length scale. When $\eta \neq 0$, the RVE is of finite size rather than infinitesimally small. Homogenization techniques are used to average microscale properties (e.g., stiffness, strength) to derive effective macroscopic properties. However, due to the finite RVE size, these properties are only approximate. A smaller RVE captures finer microstructural details, improving accuracy, but if too small, it may fail to reflect the material's true macroscopic behavior. Accurate boundary conditions are essential

to ensure the RVE represents the surrounding material correctly. However, exact boundary conditions are typically unknown, so approximations such as periodic, uniform traction, or uniform gradient conditions are commonly applied to improve accuracy.

Periodic boundary conditions assume that the material's microstructure repeats in a regular pattern, meaning opposite faces of the Representative Volume Element (RVE) maintain continuity in both displacement and stress fields. This ensures that the RVE behaves as if it were part of an infinite periodic array of identical units. In this framework, displacement remains continuous across opposite boundaries, and traction vectors are equal in magnitude but opposite in direction. For example, in a composite material with periodically arranged fibers, an RVE subjected to macroscopic deformation must exhibit displacement on one boundary that corresponds to the displacement on the opposite boundary, adjusted for the macroscopic strain. Likewise, forces acting on one face must be balanced by those on the opposing face. Applying periodic conditions enables the RVE to represent a larger material system while reducing boundary effects, leading to more accurate homogenized properties. However, this approach relies on the assumption of periodicity, which may not be valid for all materials, potentially limiting its applicability.

Uniform traction boundary conditions impose a constant stress or traction on the boundary of the RVE. This means that the surface forces (tractions) acting on the boundary of the RVE are uniform, representing a uniform stress state. For example, for an RVE under uniform compressive stress, the same compressive force is applied at every point on the boundary. This type of boundary condition is suitable in representing cases with uniform external loading. In addition, it may not capture the effects of inhomogeneous internal stress distributions and can lead to non-representative local stress fields if the microstructure is highly heterogeneous.

Uniform gradient boundary conditions impose a linear displacement or strain field across the RVE. This means that the displacements on the boundary of the RVE are prescribed such that they represent a uniform strain state. For example, for an RVE subjected to a uniform tensile strain, the displacement on the boundary increases linearly with the distance from the fixed end. This type of boundary condition is useful when the macroscopic strain field is uniform, such as in simple tension or compression tests. In addition, it's simple to implement and effective for homogeneous materials or when the macroscopic strain field is known. Furthermore, it may not accurately represent local stress concentrations or complex loading cases.

Each type of boundary conditions (uniform gradient, uniform traction, and periodic) serves different cases and assumptions about the material behaviour and loading conditions. By choosing the appropriate boundary condition, one can better approximate the macroscopic properties of materials from their microstructural characteristics under different loading cases, aiding in the study of material properties and behaviour under various stress and strain conditions.

In homogenization using a Representative Volume Element (RVE), the finite size of the RVE introduces challenges that affect the accuracy of the computed effective properties. One key issue is the micro-scale effect, which results from small-scale variations in stress, strain, or displacement fields, particularly at the RVE boundaries. These fluctuations arise due to material heterogeneity and discontinuities in microstructural features, such as inclusions or voids. Because homogenization assumes scale separation, meaning the microstructural details are much smaller than the macro-scale features, these micro-fluctuations may not be fully captured, leading to approximations in the homogenized properties. When the RVE boundaries do not align perfectly with microstructural features, discontinuities in mechanical fields can occur, affecting the predicted material behavior. The choice of boundary conditions (e.g., uniform strain, uniform traction, or periodic) directly influences the magnitude and pattern of these fluctuations. For instance, periodic boundary conditions enforce continuity across opposite faces, but micro-scale variations may still persist at the boundaries. The effective modulus, which characterizes the stiffness of the equivalent homogeneous material, is particularly sensitive to these micro-scale effects. Stress concentrations or redistributions at the boundaries can lead to an overestimation or underestimation of stiffness. Similarly, the effective stress field, which represents the averaged stress distribution, can exhibit non-uniform characteristics due to local stress variations, thereby influencing the overall load-bearing capacity and deformation behavior of the material. Since a finite RVE size means that true scale separation is not achieved, homogenized properties remain approximations rather than exact representations. The influence of boundary conditions must be carefully considered, especially in applications requiring high precision. Different boundary conditions impose distinct constraints on the stress and displacement fields, leading to variations in calculated effective properties. To quantify these effects, simulations with different boundary conditions should be conducted to assess their impact on the effective modulus and stress distribution. A more detailed discussion of the influence of boundary conditions on RVE solutions can be found in Kanit et al. [25], while the imple-

mentation of the chosen boundary conditions is covered in the next chapter 3.

In homogenization and composite material analysis, the Representative Volume Element (RVE) and its associated volume and boundary surface are essential concepts. The RVE volume, V_{RVE}, is a finite segment of the material's microstructure chosen for analysis. It must be large enough to statistically capture the material's macroscopic properties, such as stiffness, while remaining within the microscopic scale. The selection of V_{RVE} is important, as it needs to encompass key microstructural features like inclusions, voids, or fibers to ensure accurate predictions of effective properties. The boundary surface of the RVE, S_{RVE}, encloses V_{RVE} and plays an important role in defining boundary conditions during analysis. These conditions dictate how the microstructure interacts with its surroundings, influencing internal stress and strain distributions. At a smaller scale, the microscopic volume Y represents a fundamental repeating unit of the microstructure, serving as an idealized, infinitesimally small unit cell. The mathematical limit $\lim_{|V_{RVE}|\to 0} V_{RVE} = \mathrm{Y}$ indicates that as the RVE volume decreases to an infinitesimal size, it converges to the unit cell Y, which underpins the homogenization process. Similarly, Ψ denotes the boundary surface of the microscopic unit cell Y. The expression $\lim_{|Y_{RVE}|\to 0} S_{RVE} = \Psi$ signifies that as the RVE boundary surface shrinks, it approaches the boundary of the unit cell. This relationship highlights the increasing importance of micro-scale boundary conditions, which influence the accuracy of homogenized material properties. These limits have significant implications for homogenization. As V_{RVE} and S_{RVE} approach microscopic scales, the homogenized properties derived from the RVE analysis more accurately represent the material's behavior. Additionally, boundary conditions at the microscopic level become increasingly influential, emphasizing the need for careful selection to ensure precise homogenization results.

In first-order homogenization, the objective is to establish a connection between the macro-scale material response and its micro-scale structure through an RVE. A key element of this approach is specifying the displacement field at the RVE boundary. This field accounts for both the macroscopic average behavior and microscopic variations arising from material heterogeneity. The displacement at the RVE boundary, represented as $\psi_i \in S_{RVE}$, is expressed by

$$u_i(\psi_i) = \bar{u_i}(\bar{y_i}) + (\psi_j - \bar{y_j})g_{ij} + {u_i}' \tag{2.31}$$

where, ψ_i denotes a point on the boundary surface of the Representative Volume Element

(RVE), with the subscript i indicating a specific coordinate direction (e.g., y_i, where $i = 1, 2$ in two-dimensional space). The boundary surface of the RVE, S_{RVE}, consists of all points forming the outer edge of the RVE volume. When expressed as $\psi_i \in S_{RVE}$, it signifies that ψ_i lies on the RVE boundary rather than inside its volume, marking the interface between the RVE and its surroundings.

In the first term of Eq. (2.31), the macroscopic displacement field, $\bar{u_i}$, represents the solution to the homogenized equilibrium equation Eq. (2.27). This field describes the overall displacement at a larger scale, averaging out microstructural variations. The term $\bar{y_i}$ corresponds to the center of the RVE and is mathematically determined as the average position of all points within the volume

$$\bar{y_i} = |V_{RVE}|^{-1} \int_{V_{RVE}} y_i \, \mathrm{dY} \tag{2.32}$$

where, $\bar{y_i}$ represents the coordinate of the RVE center in the i-th direction, and $|V_{RVE}|$ denotes the total volume of the RVE. The integral $\int_{V_{RVE}} y_i \, \mathrm{dY}$ sums the y_i coordinates over all infinitesimal volume elements dY, providing the total "weight" of the coordinates. Dividing by the RVE volume yields the mean coordinate value in the i-th direction. The term $\bar{u_i}(\bar{y_i})$ represents the macroscopic displacement at the RVE center, obtained from the displacement field $\bar{u_i}$. In Eq. (2.31), this serves as the reference displacement at the RVE boundary.

In the second term of Eq. (2.31), ψ_j denotes the j-th coordinate of a boundary point on S_{RVE}, where displacement is evaluated. The term $\bar{y_j}$ represents the centroid of the RVE along the j-th direction and is determined as Eq. (2.32). This difference, $(\psi_j - \bar{y_j})$, quantifies the spatial offset from the RVE center to the boundary point, indicating both magnitude and direction. The displacement gradient field, g_{ij}, is given by $g_{ij} = \partial \bar{u_i} / \partial x_j$, representing the rate of change of the macroscopic displacement $\bar{u_i}$ with respect to coordinate x_j. This term captures the material's overall deformation at a larger scale. The product $(\psi_j - \bar{y_j}) g_{ij}$ accounts for the displacement contribution at ψ_i resulting from the macroscopic strain field.

In the third term of Eq. (2.31), u_i' represents micro-scale displacement fluctuations at the RVE boundary. These fluctuations arise from the fine-scale microstructural features, such as inclusions or voids, which are not fully captured by the macroscopic displacement field. The form of u_i' depends on the applied boundary conditions, such as uniform displacement gradient, uniform traction, or periodic conditions, ensuring consistency at the

microstructural level. In homogenization, u_i' is expressed as

$$\lim_{|V_{RVE}|\to 0} u_i'(\mathbf{\Psi}) \;=\; \eta \bar{\bar{u}}_i(\mathbf{\Psi}) \tag{2.33}$$

where, $\lim_{|V_{RVE}|\to 0}$ signifies the limit where the RVE volume approaches zero, meaning the RVE becomes an infinitesimally small representative sample of the material. The term $u_i'(\mathbf{\Psi})$ captures local deviations from the macroscopic displacement due to microstructural heterogeneities, which are generally unknown. The expression $\eta\bar{\bar{u}}_i(\mathbf{\Psi})$ introduces a first-order correction to the displacement field at the RVE boundary, reflecting the influence of microstructural variations. The scaling parameter η determines the magnitude of this correction, with smaller values corresponding to finer microstructural details. Physically, Eq. (2.33) describes how microstructural effects contribute to the displacement field at the RVE boundary. As the RVE size diminishes, $u_i'(\mathbf{\Psi})$ is scaled by η and the microscopic displacement field $\bar{\bar{u}}_i(\mathbf{\Psi})$. The presence of η indicates that while these fluctuations are small compared to the macroscopic displacement field, they remain significant in capturing the material's overall response.

When analyzing the local stress field within a Representative Volume Element (RVE), certain simplifications can be introduced to streamline the formulation without compromising generality. These involve selecting appropriate reference points and assumptions for the displacement field. The notation $\bar{y}_i$ represents the RVE centroid, determined by Eq. (2.32). By setting $\bar{y}_i = 0$, the coordinate system is shifted so that the origin aligns with the RVE center. This transformation facilitates the analysis by expressing the position of any point within the RVE relative to its center. Consequently, the displacement at any point ψ_i in the RVE can be formulated as Eq. (2.31). When $\bar{y}_i = 0$, the expression simplifies to

$$u_i(\psi_i) = \bar{u}_i(\bar{y}_i) + \psi_j g_{ij} + u_i' \tag{2.34}$$

The term $\bar{u}_i(\bar{y}_i)$ represents the macroscopic average displacement at the RVE centroid. Setting $\bar{u}_i(\bar{y}_i) = 0$ implies that the displacement field within the RVE is defined such that the average displacement over the RVE is zero. Under this assumption, the displacement field simplifies to

$$u_i(\psi_i) = \psi_j g_{ij} + u_i' \tag{2.35}$$

In Eq. (2.35), the term $\psi_j g_{ij}$ corresponds to the displacement induced by macroscopic strain, depending solely on the position vector ψ_j relative to the origin. The gradient tensor g_{ij} remains unchanged, describing the macroscopic deformation. Meanwhile, u_i' continues to capture the microstructural fluctuations, representing local deviations from the macroscopic displacement field. Shifting the coordinate system by setting $\bar{y}_i = 0$ eliminates the need to consider offsets, streamlining the formulation. Likewise, assuming $\bar{u}_i(\bar{y}_i) = 0$ allows the focus to remain on relative displacements, which are central to characterizing the material's response. These assumptions do not compromise generality, as the absolute displacement field can always be reconstructed by reintroducing the average displacement. Since the local stress field within the RVE primarily depends on displacement gradients rather than absolute values, these simplifications facilitate the analysis while preserving all essential mechanical information.

In homogenization, the displacement gradient g_{ij} plays a fundamental role in RVE deformation. It characterizes the macroscopic strain or deformation gradient, capturing large-scale material deformation caused by external forces while remaining independent of microstructural specifics. Since homogenization seeks to connect micro-scale behavior to macro-scale properties, g_{ij} serves as the most relevant deformation measure. In first-order homogenization, g_{ij} is imposed as a boundary condition on the RVE, ensuring that displacement at the boundary varies linearly with position. This directly governs RVE deformation, making it the primary driving term. Furthermore, incorporating g_{ij} allows for a linear approximation of the displacement field, a common strategy in first-order homogenization that simplifies analysis and aids in determining effective material properties.

Since RVE deformation is governed by the displacement gradient, this leads to an integral equation linking surface integrals over the RVE boundary to volume integrals within the RVE. In first-order homogenization, the displacement field u_i at any boundary point is described by Eq. (2.31). To simplify the formulation, we assume $\bar{u}_i(\bar{y}_i) = 0$ and $\bar{y}_i = 0$, reducing the displacement field to Eq. (2.35). To establish the connection between macroscopic and microscopic quantities, we multiply u_i by n_j and integrate over the boundary surface, yielding

$$\int_{S_{RVE}} u_i n_j \, \mathrm{d}\Psi \tag{2.36}$$

where, $u_i n_j$ represents the displacement component in the direction of the normal vector n_j, which is critical for understanding how displacement interacts with the RVE boundary. Since n_j defines the outward normal direction, this projection extracts the normal displacement contribution. In homogenization, boundary displacement behavior plays a key role in determining effective material properties. By integrating the normal displacement over the boundary, we gain insights into the influence of microscopic deformations on macroscopic responses. Applying the divergence theorem enables the conversion of a vector field's flux through a surface into a volume integral of its divergence. This transformation allows strain (or displacement gradient) volume integrals to be rewritten as surface integrals involving displacement and normal vectors, directly linking microscopic behavior to macroscopic deformation.

By substituting the simplified displacement field Eq. (2.35) into this integral (2.36), and considering that the forcing term for the deformation of the RVE is the displacement gradient as shown in Appendix A.4.1, we obtains

$$\frac{1}{2} \int_{S_{RVE}} (u_i n_j + u_j n_i) \, \mathrm{d}\Psi = g_{ij} \int_{V_{RVE}} \mathrm{dY} \tag{2.37}$$

In the left-hand side of Eq. (2.37), the factor $\frac{1}{2}$ ensures symmetric treatment of the displacement and normal vector interactions, avoiding double-counting of $u_i n_j$ and $u_j n_i$. The integral $\int_{S_{RVE}}$ represents an evaluation over the RVE boundary surface S_{RVE}, where u_i and u_j are the displacement components in the i-th and j-th directions, respectively, while n_i and n_j denote the corresponding unit normal components. The term $(u_i n_j + u_j n_i)$ accounts for both normal and tangential displacement contributions, ensuring a comprehensive characterization of the boundary's response. The infinitesimal surface element $\mathrm{d}\Psi$ represents a differential area on S_{RVE}. Physically, this expression describes the average deformation at the boundary, capturing its interaction with the imposed displacement field.

On the right-hand side of Eq. (2.37), g_{ij} represents the macroscopic displacement gradient component, defined as $g_{ij} = \partial \bar{u}_i / \partial x_j$, which quantifies the variation of the macroscopic displacement $\bar{u}_i$ along the j-th direction. The integral $\int_{V_{RVE}} \mathrm{dY}$ spans the volume V_{RVE}, effectively computing its total size. Physically, this term represents the product of the RVE's

volume and the macroscopic displacement gradient, encapsulating the large-scale deformation.

Eq. (2.37) establishes an important link between microscopic boundary displacements and macroscopic deformation. The left-hand side, involving boundary displacements interacting with normal vectors, is equated to the right-hand side, which expresses the macroscopic strain scaled by the RVE volume. This relationship ensures that the average microscopic boundary deformation aligns with the imposed macroscopic strain, reinforcing its significance in homogenization for deriving effective material properties.

Following Miehe and Koch [36], the Lagrange multiplier technique can be used to enforce the displacement gradient in the Representative Volume Element (RVE) problem. This approach guarantees that the displacement field within the RVE aligns with the prescribed macroscopic displacement gradient, ensuring coherence between microstructural and macrostructural analyses. Within the framework of variational principles and weak formulations, it imposes constraints with mathematical rigor. Specifically, it ensures that the microscopic displacement field u_i at the RVE boundary remains consistent with the macroscopic displacement gradient g_{ij}. So, the final weak form of local equilibrium of the RVE after imposing the constraint as shown in Appendix A.4.2

$$\int_{V_{RVE}} \delta \frac{\partial \bar{\bar{u}}_i}{\partial y_j} \sigma_{ij} \mathrm{dY} + \int_{S_{RVE}} \delta \bar{\bar{u}}_i \lambda_i \mathrm{d}\Psi + \int_{S_{RVE}} \delta \lambda_i \left(u_i - \psi_j g_{ij} \right) \mathrm{d}\Psi = 0 \tag{2.38}$$

In the first term of Eq. (2.38), $\int_{V_{RVE}} \ldots \mathrm{dY}$ denotes the integral over the volume of the Representative Volume Element (RVE), denoted by V_{RVE}. $\delta \frac{\partial \bar{\bar{u}}_i}{\partial y_j}$ is the virtual variation of the gradient of the displacement fluctuation $\bar{\bar{u}}_i$ with respect to the fast coordinate y_j. The displacement fluctuation $\bar{\bar{u}}_i$ represents the microstructural displacement field. σ_{ij} represents the microscopic stress field, which arises from the local equilibrium conditions within the RVE. Physically, this term characterizes the virtual work done by the microscopic stress field σ_{ij} against the virtual variation of the displacement gradient. It signifies the internal energy contribution due to stress-strain interactions within the microstructure of the RVE.

In the second term of Eq. (2.38), $\int_{S_{RVE}} \ldots \mathrm{d}\Psi$ denotes the integral over the boundary surface of the RVE, denoted by S_{RVE}. $\delta \bar{\bar{u}}_i$ is the virtual displacement fluctuation at the boundary of the RVE. λ_i is the Lagrange multiplier vector, which is introduced to enforce the constraint that the boundary displacement within the RVE should match the specified displacement gradient field. Physically, λ_i can be interpreted as the traction (force per unit

area) on the boundary of the RVE. This term accounts for the work done by the virtual displacement fluctuations against the Lagrange multipliers on the boundary of the RVE.

In the third term of Eq. (2.38), $\int_{S_{RVE}} \dots \mathrm{d}\Psi$ this again denotes the integral over the boundary surface of the RVE. $\delta\lambda_i$ is the virtual variation of the Lagrange multiplier vector λ_i. $(u_i - \psi_j g_{ij})$ represents the difference between the actual displacement u_i at the boundary and the displacement imposed by the specified gradient field g_{ij}. Here, ψ_j is the coordinate on the boundary surface, and $\psi_j g_{ij}$ is the displacement imposed by the gradient. This term enforces the constraint that the actual displacement at the boundary should match the displacement dictated by the specified gradient field, by ensuring the virtual variations of λ_i act appropriately.

In Eq. (2.38), $\int_{V_{RVE}} \mathrm{dY} = \int_{S_{RVE}} \psi_j n_j \mathrm{d}\Psi$ is applied. The volume integral $\int_{V_{RVE}} \mathrm{dY}$ computes the total volume of the RVE, where dY represents the differential volume element. Similarly, the surface integral $\int_{S_{RVE}} \psi_j n_j \mathrm{d}\Psi$ extends over the boundary of the RVE, with $\mathrm{d}\Psi$ denoting the differential surface element. Here, ψ_j represents the position vector components, while n_j corresponds to the outward unit normal vector component at the surface S_{RVE}. This equation is derived from the Divergence Theorem (or Gauss's Theorem), which establishes a connection between volume and surface integrals. In this case, it indicates that integrating the position vector projected into the normal direction over the surface of the RVE yields the same result as the volume integral over the entire RVE.

In Eq. (2.38), the term $\lambda_i = \sigma_{ij} n_j$ defines the boundary traction, where n_j is the outward unit normal to the RVE boundary S_{RVE}, and σ_{ij} represents the stress tensor components. The stress tensor governs the distribution of internal forces within the material, and multiplying it by the normal vector yields the traction λ_i, which ensures consistency between the displacement field inside the RVE and the applied macroscopic displacement gradient g_{ij}.

The traction λ_i at each boundary point consists of two key components. The normal traction corresponds to the force acting perpendicular to the boundary surface, given by $\sigma_{ij} n_j$ for $i = j$. This represents normal stresses $(\sigma_{xx}, \sigma_{yy}, \sigma_{zz})$ that induce pressure or tension along the normal direction. For example, if the boundary normal is along the x-axis (n_x), the normal traction in that direction is $\sigma_{xx} n_x$. The shear traction accounts for forces acting tangentially to the boundary, given by $\sigma_{ij} n_j$ for $i \neq j$. Shear stresses $(\sigma_{xy}, \sigma_{xz}, \sigma_{yz})$ contribute to this component, which governs shear deformation. For instance, if the normal vector is along the y-axis (n_y), the shear traction in the x-direction is $\sigma_{xy} n_y$, representing the tangential force per unit area. By decomposing λ_i into normal and shear components,

the total boundary traction at $\mathbf{\Psi} \in S_{RVE}$ is fully characterized. This ensures that the microscopic stress distribution within the RVE remains consistent with the imposed macroscopic strain conditions.

Solving Eq. (2.38) yields the microscopic stress field σ_{ij} in response to the imposed average displacement gradient g_{ij} on the RVE. This solution captures both the macroscopic behavior and the localized variations within the RVE. The link between the macroscopic stress field $\hat{\sigma}_{ij}$ and its microscopic counterpart σ_{ij} is expressed in Eq. (2.29). Here, $\hat{\sigma}_{ij}$ represents the homogenized stress tensor, obtained by averaging σ_{ij} over the RVE volume $|\mathrm{Y}|$, effectively filtering out microscale fluctuations and providing a macroscopic stress description. Then, by using Eq. (2.29), we derive the relationship

$$\hat{\sigma}_{ij} = \hat{D}_{ijkl}\, g_{kl} \tag{2.39}$$

Eq. (2.39) establishes the macroscopic stress field in terms of the effective material properties and the macroscopic strain (displacement gradient). The homogenized stress tensor $\hat{\sigma}_{ij}$ represents the average internal force distribution over the RVE, accounting for microstructural heterogeneities while describing the material's overall response. The effective stiffness tensor $\hat{D}_{ijkl}$ characterizes the macroscopic elastic properties derived from the microscale structure. It defines the relationship between macroscopic stress and strain, encapsulating the averaged material behavior. The displacement gradient tensor $g_{kl} = \frac{\partial u_k}{\partial x_l}$ quantifies spatial variations in the macroscopic displacement field, serving as a fundamental measure of deformation.

In two-scale analysis, $\hat{D}_{ijkl}$ plays an important role in linking microscale behavior to macroscopic properties. Derived from the RVE, it enables homogenization by incorporating microscale characteristics into macroscale models. The relation (2.39) serves as the foundation for solving macroscopic problems in complex materials, integrating microscale effects into large-scale simulations. When applied in formulations like the variational or Galerkin approach Eq. (2.27), $\hat{D}_{ijkl}$ ensures that the material response is accurately captured under various loading conditions. The global equilibrium equation in Eq. (2.27) accounts for macroscopic fields while incorporating microscale influences through $\hat{D}_{ijkl}$, facilitating a comprehensive two-scale analysis and ensuring that the model realistically represents the material's overall behavior.

To determine a material's effective macroscopic properties using a two-scale analysis,

the local RVE (Representative Volume Element) problem must be solved under appropriate boundary conditions. These conditions such as uniform gradient, uniform traction, or periodic boundary conditions must be carefully selected to accurately reflect the macroscale deformation. They are imposed on the RVE boundaries to generate a specific deformation pattern. Once these boundary conditions are applied, the local stress field σ_{ij} within the RVE is obtained by solving the equilibrium equations. The effective stress tensor $\hat{\sigma}_{ij}$ is then computed by averaging σ_{ij} over the RVE volume, as described in Eq. (2.29). To determine the components of the effective stiffness matrix $\hat{D}_{ijkl}$, the relationship between the macroscopic stress tensor $\hat{\sigma}_{ij}$ and the displacement gradient g_{kl} must be established, following Eq. (2.39). This equation states that the effective stress tensor is linearly related to the displacement gradient via the effective stiffness tensor $\hat{D}_{ijkl}$. In a 2D case, three independent displacement gradient cases are required to fully characterize $\hat{D}_{ijkl}$. These typically include pure shear and uniaxial tension/compression in different directions, ensuring that all possible deformations are accounted for. By solving the RVE problem for each displacement gradient, the corresponding stress responses $\hat{\sigma}_{ij}$ are obtained. The stiffness matrix components are then determined by solving a system of linear equations derived from these cases, as illustrated in Figure 2.2.

For practical computations, especially in 2D, we represent the tensors in matrix form. Then, as we discussed before, we apply three independent displacement gradients to the RVE to obtain the corresponding effective stress components. Case 1 where $g_{11} = 1$, $g_{22} = 0$, and $g_{12} = 0$. Case 2 where $g_{11} = 0$, $g_{22} = 1$, and $g_{12} = 0$. Case 3 where $g_{11} = 0$, $g_{22} = 0$, and $g_{12} = 1$. For each case, we solve the RVE problem to obtain the effective stress components $\hat{\sigma}_{ij}$. These are denoted as $\hat{\sigma}^1_{ij}$, $\hat{\sigma}^2_{ij}$, and $\hat{\sigma}^3_{ij}$ for the three respective cases. Then, we arrange the obtained stress components into a matrix form, aligning them with the applied displacement gradients. And, this gives us the following

$$\begin{bmatrix} \hat{\sigma}^1_{11} & \hat{\sigma}^2_{11} & \hat{\sigma}^3{}_{11} \\ \widehat{\sigma}^1_{22} & \widehat{\sigma}^2_{22} & \widehat{\sigma}^3_{22} \\ \widehat{\sigma}^1_{12} & \widehat{\sigma}^2_{12} & \widehat{\sigma}^3_{12} \end{bmatrix} = \begin{bmatrix} \widehat{D}_{1111} & \widehat{D}_{1122} & \widehat{D}_{1112} \\ \widehat{D}_{1122} & \widehat{D}_{2222} & \widehat{D}_{2212} \\ \widehat{D}_{1112} & \widehat{D}_{2212} & \widehat{D}_{1212} \end{bmatrix} \begin{bmatrix} 1 & 0 & 0 \\ 0 & 1 & 0 \\ 0 & 0 & 1 \end{bmatrix} \tag{2.40}$$

The components of the effective stiffness matrix $\hat{D}_{ijkl}$ are determined by solving a system of linear equations, where each column of the stress matrix corresponds to a specific

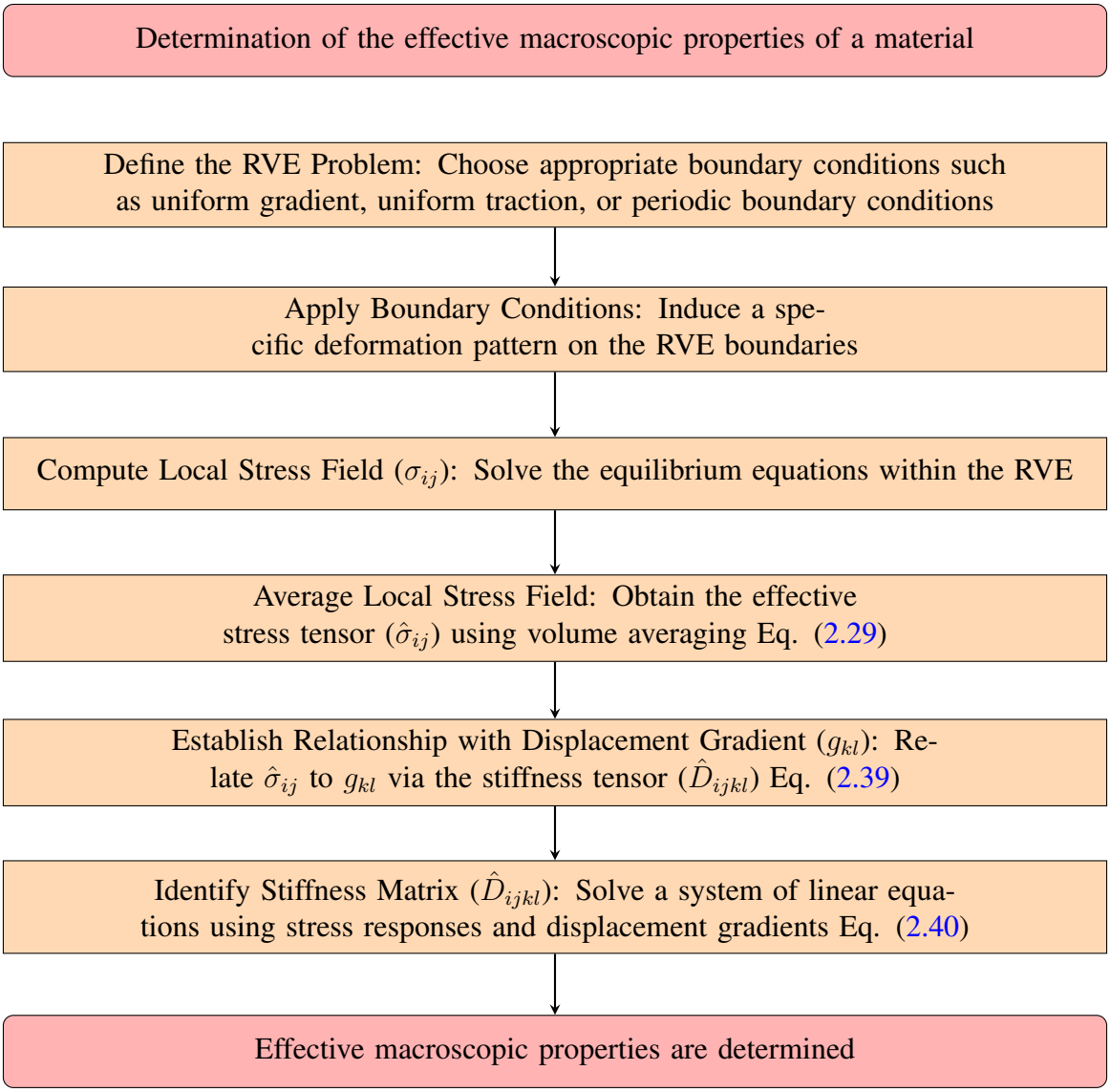

Figure 2.2: Two-Scale Analysis for Effective Macroscopic Properties

displacement gradient case. This approach allows for isolating and solving for individual components of $\hat{D}_{ijkl}$.

In the first case, setting $g_{11} = 1$, $g_{22} = 0$, and $g_{12} = 0$ prescribes a uniaxial strain in the x_1 direction. The condition $g_{11} = 1$ implies that displacement in x_1, denoted as u_1, varies linearly with x_1, representing uniform stretching or compression along this axis. Meanwhile, $g_{22} = 0$ ensures no deformation in the x_2 direction, and $g_{12} = 0$ eliminates shear deformation between x_1 and x_2. This setup isolates the effect of uniaxial strain in x_1 on the macroscopic stress component $\hat{\sigma}_{11}$, allowing the contribution of the microstructure to be assessed.

For the second case, the displacement gradient is set to $g_{11} = 0$, $g_{22} = 1$, and $g_{12} = 0$, inducing uniaxial strain in the x_2 direction. Here, $g_{22} = 1$ causes u_2 to vary linearly with x_2, resulting in uniform stretching or compression along this axis. The constraints $g_{11} = 0$ and $g_{12} = 0$ prevent deformation in x_1 and eliminate shear effects. This configuration isolates the influence of uniaxial strain in x_2 on the macroscopic stress component $\hat{\sigma}_{22}$.

The third case applies $g_{11} = 0$, $g_{22} = 0$, and $g_{12} = 1$, inducing pure shear deformation in the x_1-x_2 plane. The condition $g_{12} = 1$ means that u_1 varies linearly with x_2, introducing shear without normal stretching or compression. The constraints $g_{11} = 0$ and $g_{22} = 0$ ensure that no normal strain occurs in either direction. This setup isolates the effect of shear strain on the macroscopic shear stress component $\hat{\sigma}_{12}$.

By solving the RVE problem under these three independent displacement gradients, the corresponding macroscopic stress responses are obtained. These responses are then used to determine the stiffness matrix components, capturing the influence of the material's microstructure on its effective macroscopic properties.

In Eq. (2.40), these notations $\hat{\sigma}^1_{11}$, $\hat{\sigma}^1_{22}$, and $\hat{\sigma}^1_{12}$ represent specific components of the effective stress tensor $\hat{\sigma}_{ij}$ under the first displacement gradient condition. $\hat{\sigma}^1_{11}$ denotes the component of the effective stress tensor $\hat{\sigma}_{11}$ in Case 1. Physically, $\hat{\sigma}^1_{11}$ is the effective normal stress in the x_1 direction due to a uniaxial strain applied in the x_1 direction. This is a measure of how the material responds to stretching along the x_1 axis. And, $\hat{\sigma}^1_{22}$ represents the component of the effective stress tensor $\hat{\sigma}_{22}$ under the same case. Physically, $\hat{\sigma}^1_{22}$ is the effective normal stress in the x_2 direction when a uniaxial strain is applied in the x_1 direction. This term arises due to the Poisson effect, where deformation in the x_1 direction induces a stress response in the x_2 direction. And, $\hat{\sigma}^1_{12}$ denotes the component of the effective stress tensor $\hat{\sigma}_{12}$ under the same case. Physically, $\hat{\sigma}^1_{12}$ is the effective shear stress in the x_1-x_2 plane due to a uniaxial strain in the x_1 direction. This term reflects any shear stress response generated by the applied normal strain. Furthermore, these effective stress components are essential for determining the effective stiffness matrix $\hat{D}_{ijkl}$. $\hat{\sigma}^1_{11}$ contributes to $\hat{D}_{1111}$, relating normal stress in the x_1 direction to strain in the x_1 direction. And, $\hat{\sigma}^1_{22}$ contributes to $\hat{D}_{1122}$, relating normal stress in the x_2 direction to strain in the x_1 direction (Poisson's ratio effect). And, $\hat{\sigma}^1_{12}$ contributes to $\hat{D}_{1112}$, relating shear stress to normal strain, indicating any coupling between shear and normal responses.

In Eq. (2.40), these notations $\hat{\sigma}^2_{11}$, $\hat{\sigma}^2_{22}$, and $\hat{\sigma}^2_{12}$ represent specific components of the effective stress tensor $\hat{\sigma}_{ij}$ under the second displacement gradient condition. $\hat{\sigma}^2_{11}$ denotes

the component of the effective stress tensor $\hat{\sigma}_{11}$ in Case 2. Physically, $\hat{\sigma}^2_{11}$ is the effective normal stress in the x_1 direction due to a uniaxial strain applied in the x_2 direction. This term reflects the stress response in the x_1 direction resulting from deformation along the x_2 axis, which is often due to Poisson's effect. And, $\hat{\sigma}^2_{22}$ represents the component of the effective stress tensor $\hat{\sigma}_{22}$ under the same case. Physically, $\hat{\sigma}^2_{22}$ is the effective normal stress in the x_2 direction when a uniaxial strain is applied in the x_2 direction. This component directly measures how the material stretches along the x_2 axis under a corresponding strain. And, $\hat{\sigma}^2_{12}$ denotes the component of the effective stress tensor $\hat{\sigma}_{12}$ under the same case. Physically, $\hat{\sigma}^2_{12}$ is the effective shear stress in the x_1-x_2 plane due to a uniaxial strain in the x_2 direction. This term captures any shear stress response generated by the applied normal strain. Furthermore, These effective stress components are essential for determining the effective stiffness matrix $\hat{D}_{ijkl}$. $\hat{\sigma}^2_{11}$ contributes to $\hat{D}_{1122}$, relating normal stress in the x_1 direction to strain in the x_2 direction (Poisson's ratio effect). And, $\hat{\sigma}^2_{22}$ contributes to $\hat{D}_{2222}$, relating normal stress in the x_2 direction to strain in the x_2 direction. And, $\hat{\sigma}^2_{12}$ contributes to $\hat{D}_{2212}$, relating shear stress to normal strain in the x_2 direction, indicating any coupling between shear and normal responses.

In Eq. (2.40), these notations $\hat{\sigma}^3_{11}$, $\hat{\sigma}^3_{22}$, and $\hat{\sigma}^3_{12}$ represent specific components of the effective stress tensor $\hat{\sigma}_{ij}$ under the third displacement gradient condition. $\hat{\sigma}^3_{11}$ denotes the component of the effective stress tensor $\hat{\sigma}_{11}$ in case 3. Physically, $\hat{\sigma}^3_{11}$ is the effective normal stress in the x_1 direction due to a pure shear strain applied in the x_1-x_2 plane. This term reflects the stress response in the x_1 direction resulting from a shear deformation. And, $\hat{\sigma}^3_{22}$ represents the component of the effective stress tensor $\hat{\sigma}_{22}$ under the same case. Physically, $\hat{\sigma}^3_{22}$ is the effective normal stress in the x_2 direction when a pure shear strain is applied in the x_1-x_2 plane. This component measures the stress response in the x_2 direction due to shear deformation. And, $\hat{\sigma}^3_{12}$ denotes the component of the effective stress tensor $\hat{\sigma}_{12}$ under the same case. Physically, $\hat{\sigma}^3_{12}$ is the effective shear stress in the x_1-x_2 plane due to a pure shear strain. This term directly measures the shear stress response in the material. Furthermore, these effective stress components are essential for determining the effective stiffness matrix $\hat{D}_{ijkl}$. $\hat{\sigma}^3_{11}$ contributes to $\hat{D}_{1112}$, relating normal stress in the x_1 direction to shear strain. And, $\hat{\sigma}^3_{22}$ contributes to $\hat{D}_{2212}$, relating normal stress in the x_2 direction to shear strain. And, $\hat{\sigma}^3_{12}$ contributes to $\hat{D}_{1212}$, relating shear stress to shear strain in the x_1-x_2 plane.

2.6 Closing Remarks

The presented homogenization framework offers a robust methodology for analyzing heterogeneous materials by bridging the scales between microstructural properties and macroscopic behavior. The field equations and their weak form establish the foundation for this approach, emphasizing the necessity of continuity in stress fields and accommodating discontinuities in displacement fields at interfaces. By employing index notation and tensor representation, the constitutive relations and equilibrium equations are formulated to reflect the intrinsic complexities of heterogeneous media. The introduction of separation of scales and the adoption of a first-order homogenization approach enable the effective reduction of complex microstructural variations into simplified macroscopic properties, encapsulated within the homogenized stiffness matrix. This systematic decomposition not only facilitates the derivation of macro-scale equations but also retains the influence of microstructural details through periodic functions and scaling parameters, thereby ensuring a physically consistent and mathematically rigorous transition between scales.

The variational formulation of the homogenization process provides a clear pathway for integrating the governing equations. By replacing the heterogeneous domain with an equivalent homogeneous material, the framework allows for efficient computation while preserving the fidelity of the original problem. The application of this homogenization approach has significant implications for engineering and material science, enabling the design and optimization of advanced materials with tailored properties. Future research can extend this methodology to incorporate non-linear behaviors, multi-physics coupling, and three-dimensional domains, broadening its applicability and enhancing its potential to solve complex material modeling challenges.

Chapter 3

Computational Homogenization With XFEM

3.1 Introduction

Computational homogenization offers a robust framework for connecting microscale material behavior with macroscale response through Representative Volume Elements (RVEs). By leveraging the extended Finite Element Method (XFEM), the computational approach efficiently handles the challenges posed by heterogeneities, cracks, and discontinuities within the microstructure. This chapter focuses on the implementation of RVE boundary conditions in the XFEM framework, highlighting the mathematical formulation, numerical discretization, and the treatment of various boundary constraints such as uniform displacement, uniform traction, and periodic conditions. These techniques provide a systematic means to compute effective material properties and stress fields, enabling accurate modeling of complex materials in multiscale simulations.

The (XFEM) has become a widely adopted approach for modeling discontinuities, such as cracks or material interfaces, within finite element frameworks. However, when interfaces are modeled using standard XFEM formulations, excessive traction oscillations may arise, particularly under stiff interface assumptions. These oscillations can be attributed to

the presence of quadratic bubble terms in the displacement jump functions at the interface.

3.1.1 Motivation

The motivation for implementing computational homogenization with the Extended Finite Element Method (XFEM) arises from the need to accurately analyze heterogeneous materials at multiple scales. In many practical engineering applications, materials exhibit complex microstructures that significantly influence their macroscopic behavior. Computational homogenization provides a rigorous framework to bridge the micro and macro scales, ensuring that the overall response of a material is determined by its local properties. XFEM enhances this approach by enabling the efficient representation of discontinuities and heterogeneities without requiring conformal mesh refinement. This methodology allows for modeling representative volume elements (RVEs) with intricate microstructural features while maintaining computational efficiency and accuracy.

XFEM is a powerful numerical technique that accurately models discontinuities, such as cracks and material interfaces, without requiring the mesh to conform to their geometry. However, when modeling interfaces under stiff interface conditions, the standard XFEM formulation can lead to excessive traction oscillations. These oscillations arise due to the quadratic bubble terms inherent in the displacement jump functions, which, while capturing the interface behavior, can degrade the numerical stability and accuracy of the solution. To mitigate these oscillations, it is necessary to stabilize the displacement jump representation. A viable approach involves decomposing the discontinuity jump into two components: an element-wise constant term and a quadratic bubble component. By addressing the contribution of these bubble terms, numerical instabilities can be suppressed while retaining the accuracy of the interface solution. The stabilization approach further ensures numerical robustness by eliminating traction oscillations while preserving the accuracy of XFEM solutions.

3.1.2 Literature Review

The accurate modeling of discontinuities, such as cracks and material interfaces, has been a longstanding challenge in computational mechanics. Traditional finite element methods (FEM) require a mesh that conforms to discontinuities, often resulting in computational in-

efficiency and reduced flexibility in handling evolving geometries. To address these limitations, the extended Finite Element Method (XFEM) was developed, leveraging enrichment functions to represent discontinuities independently of the mesh. This approach enables XFEM to efficiently model crack propagation and material heterogeneity without the need for remeshing, as demonstrated in the foundational works of Moës et al. [38], Belytschko and Black [4] and Belytschko et al. [5]. Similar XFEM based enrichment strategies for the analysis of crack openings have been introduced in Wells and Sluys [55], Moës and Belytschko [37] and Mergheim et al. [34]. In the context of heterogeneous materials, the application of XFEM has been further extended to representative volume element (RVE) analyses. These studies aim to bridge microstructural behaviors and macroscopic responses, providing a framework for multiscale modeling. Pioneering efforts such as Michel et al. [35], Hashin and Shtrikman [19] and Hashin and Wendt [20] have demonstrated XFEM's capability to handle complex material interfaces, particularly in cases involving inclusions, voids, or crack networks. Such advancements have underscored XFEM's potential to deliver accurate stress and strain fields, even under nonuniform deformation states.

Over the years, various studies have explored the challenges associated with traction oscillations in the Extended Finite Element Method (XFEM), particularly under stiff interface conditions. It has been observed that the presence of quadratic bubble terms in the displacement jump functions contributes significantly to these oscillations, leading to numerical instabilities in the solution. Erkmen and Dias-da Costa [12] highlighted that while these bubble terms are necessary to capture the quadratic nature of the displacement field across the interface, they can also degrade the conditioning of the system matrix. The study emphasized that a stabilization technique is essential to control these instabilities and improve the robustness of XFEM for stiff interfaces.

To address this problem, Ventura and Tesei [54] introduced the concept of stabilization using fictitious spring-like parameters, which act as a control mechanism to suppress the oscillations. Ventura and Tesei [54] demonstrated that a sufficiently large stabilization parameter could effectively eliminate ill-conditioning while maintaining the accuracy of the XFEM solution. Importantly, this stabilization approach ensures that the oscillations are controlled without altering the fundamental interface behavior. Subsequent studies have further refined this approach by incorporating orthogonality conditions into the stabilization terms, ensuring that the additional stabilization does not interfere with the physical behavior being modeled.

Another critical advancement in stabilization techniques involves the use of Legendre polynomials to construct stabilization terms that satisfy orthogonality conditions. These polynomials provide a mathematically rigorous basis for eliminating the problematic quadratic bubble contributions without introducing artificial effects. The use of Legendre polynomials ensures that the stabilization terms remain consistent with the higher-order nature of the XFEM formulation, as demonstrated in several recent studies. This approach has been shown to provide a balance between stability and accuracy, making it a preferred choice for addressing oscillations in XFEM solutions.

Overall, the existing literature underscores the need for robust stabilization techniques to address traction oscillations in XFEM. By leveraging orthogonality conditions and stabilization parameters, researchers have developed effective strategies to improve the numerical stability and conditioning of XFEM formulations. This section 3.4 builds upon these foundational studies to present a comprehensive stabilization approach using Legendre polynomial-based terms, ensuring both accuracy and stability in interface modeling.

3.1.3 Methodology

In this chapter, we develop and implement a computational homogenization framework integrated with the Extended Finite Element Method (XFEM) to analyze the behavior of heterogeneous materials with discontinuities. The primary focus is on modeling representative volume elements (RVEs) to bridge the micro and macro scales effectively. The chapter begins with a detailed formulation of the boundary conditions necessary for homogenization, including uniform displacement, uniform traction, and periodic conditions, which are essential for achieving accurate macroscopic responses. XFEM is employed to efficiently represent discontinuities within the microstructure, such as cracks or material interfaces, without requiring conformal mesh refinement. The proposed methodology ensures computational efficiency while capturing the microstructural effects that influence the macroscopic behavior of materials.

The methodology adopted involves the numerical implementation of boundary conditions using XFEM-based formulations, followed by the solution of the governing equations at the microscale. We systematically address the challenges of non-matching interfaces, and ensure compatibility with the homogenization framework. The chapter also includes the derivation of effective macroscopic properties from the microstructural analysis. The

accuracy and robustness of the proposed approach are validated through numerical examples that demonstrate the capability of the XFEM-based homogenization technique to model heterogeneous materials with complex microstructures. This methodology provides a powerful tool for multiscale analysis, offering insights into the behavior of materials with discontinuities and heterogeneities.

In this section 3.4, we address the challenge of traction oscillations in the (XFEM) caused by the quadratic bubble terms in the displacement jump functions. Our goal is to develop a robust stabilization methodology that effectively suppresses these oscillations while maintaining the accuracy and consistency of the XFEM formulation. Building upon the decomposition approach proposed in the literature, the displacement jump is expressed as a combination of an element-wise constant term and a quadratic bubble component. This decomposition enables us to isolate the problematic bubble terms, which are known to contribute to ill-conditioning, and apply a stabilization mechanism to alleviate their effects.

Our stabilization strategy involves introducing a fictitious spring-like parameter, denoted as χ, into the formulation. This parameter scales an additional stabilization term constructed using Legendre polynomials, which inherently satisfy the orthogonality condition required for stabilization. The orthogonality condition ensures that the added stabilization term does not interfere with the physical behavior of the discontinuity interface. Specifically, we replace the original bubble component $\bar{\Theta}\boldsymbol{\beta}$ with a stabilized form, $\chi\hat{\boldsymbol{\Theta}}\boldsymbol{\beta}$, where $\bar{\Theta}$ is defined using Legendre polynomials up to a certain order. By adopting this approach, we provide a mathematically consistent framework that suppresses traction oscillations without introducing numerical artifacts.

To implement this methodology, we derive the stabilized shape functions for the interface in terms of both element geometry and interface coordinates. The stabilization term $\bar{\Theta}$ is explicitly constructed using Legendre polynomials of increasing order, starting with linear contributions and extending to higher-order terms as needed. This allows us to systematically control the stabilization effect based on the specific interface geometry and stiffness conditions.

In summary, this section 3.4 presents a systematic stabilization methodology that leverages the decomposition of the displacement jump and incorporates orthogonality-preserving stabilization terms constructed from Legendre polynomials. By integrating this approach into the XFEM formulation, we ensure numerical stability, suppress traction oscillations, and maintain solution accuracy, particularly for stiff interface problems. The following

subsections will provide the detailed mathematical derivation, implementation procedure, and verification of the proposed stabilization technique.

3.1.4 Chapter Structure

This chapter is organized to offer a detailed overview of the computational homogenization using XFEM. It begins with **Implementation of RVE Boundary Conditions**. This section introduces the numerical framework for implementing boundary conditions in Representative Volume Elements (RVEs) using the extended finite element method (XFEM). It begins by adopting vector-matrix notations for the stress, displacement, and related tensors. The displacement field and the Lagrange multiplier field are interpolated using approximation functions, leading to a mathematical formulation that describes the RVE problem in algebraic form. The boundary of the RVE is decomposed into specific regions, enabling the pairing of boundary points for the imposition of constraints. Detailed derivations explain how stress and displacement relations are handled at internal and boundary nodes, setting the stage for applying specific boundary conditions. Then, it moves to **Uniform Displacement Gradient RVE Boundary Conditions**. This section focuses on the assumption of a uniform displacement gradient along the boundaries. It explains how macroscopic displacement gradients determine the boundary node displacements, with no micro-scale fluctuations. By leveraging these assumptions, the RVE boundary is linearly mapped, and nodal displacements are explicitly derived. The formulation simplifies the algebraic representation of the RVE problem, facilitating the computation of nodal displacements and stress fields under these condition. Then, it moves to **Uniform Traction RVE Boundary Conditions**. Here, the discussion shifts to the case of uniform traction at the boundaries, where micro-fluctuations in displacement are allowed but stress uniformity is maintained. The Lagrange multiplier vector is reformulated to enforce uniform stress across the boundary. This section details the construction of the governing equations using matrix interpolations, ensuring consistency in stress distribution while handling nodal displacements through coupled equations. The derivations culminate in a matrix form that allows efficient numerical implementation of uniform traction constraints. Then, it moves to **Periodic Displacement RVE Boundary Conditions**. This section addresses the periodic boundary conditions for RVEs, accommodating fine-scale displacement fluctuations. It assumes that the displacement field is periodic across opposite boundaries, while traction remains

anti-periodic. These constraints are expressed algebraically, introducing reduced degrees of freedom for boundary stress. The final derivation provides a systematic method for enforcing periodic displacement and anti-periodic traction through interpolated boundary node relationships. This ensures compatibility and equilibrium across the boundary, critical for capturing the periodicity of microstructures in homogenization. Then, it moves to **Interpolation of Displacement and Lagrange Multiplier**. This part of the chapter discusses the interpolation of the displacement and Lagrange multiplier fields, which is crucial for solving the RVE problem efficiently using XFEM. The displacement field is expressed as a sum of continuous and discontinuous components, with the discontinuous component corresponding to the jump in displacement at the interface. This formulation allows for accurate modeling of the displacement field, especially in regions where there are significant changes in the material properties. The interpolation method is applied at the element level, ensuring that the solution is both accurate and computationally efficient.

Then, this chapter ended by **Stabilization of the XFEM**, which is structured to systematically present the stabilization methodology for addressing traction oscillations in the Extended Finite Element Method (XFEM). We begin by providing a detailed explanation of the mathematical formulation behind the stabilization process. Specifically, we decompose the displacement jump function into an element-wise constant term and a quadratic bubble component, identifying the contribution of the bubble terms as the primary source of oscillations. This decomposition lays the foundation for introducing the stabilization mechanism that ensures numerical robustness without compromising the accuracy of the solution. Next, we derive the stabilized form of the displacement jump by incorporating an additional stabilization term scaled by a parameter χ. The stabilization term, constructed using Legendre polynomials, satisfies an orthogonality condition that guarantees the stabilization effect does not introduce spurious numerical effects. At the end of section 3.4, we outline the implementation procedure for integrating the stabilization approach into the XFEM framework. This includes the construction of stabilized shape functions at the interface, the evaluation of key terms in the governing equations, and the incorporation of the stabilization matrix into the numerical formulation.

3.1.5 Summary

At the end of this chapter, we obtain a robust computational framework for multiscale analysis of heterogeneous materials with discontinuities, leveraging the Extended Finite Element Method (XFEM). The implementation of appropriate boundary conditions, including periodic, uniform displacement, and uniform traction conditions, ensures accurate homogenization of the microstructural response. The developed methodology successfully bridges the micro and macro scales by capturing the influence of microstructural features, such as cracks and material interfaces, on the overall macroscopic behavior. This framework provides a reliable tool for analyzing materials with heterogeneities, offering insights into their mechanical response and guiding future developments in multiscale modeling techniques. Also, we proceed logically from the mathematical formulation and derivation of the stabilization terms to their implementation. Each component builds upon the previous one, providing a clear and coherent presentation of the stabilization methodology. By the end of this chapter, the reader will have a comprehensive understanding of the proposed approach, its theoretical foundations, and its practical effectiveness in alleviating traction oscillations in XFEM.

3.2 Implementation of the RVE Boundary Conditions

For the derivations regarding the numerical implementation, in this section we switch to vector-matrix notations. Now, the goal is to derive equations suitable for numerical implementation. And, switching to vector-matrix notation simplifies the handling and computation of tensors, which are complex objects in their full form. Accordingly, stress and property tensors can be written in Voigt form. Voigt form, also known as Voigt notation, is a method of representing higher-order tensors, such as stress and strain tensors in a compact vector form. This simplification is particularly useful in numerical methods like finite element analysis, where operations on vectors and matrices are computationally more efficient than operations on higher-order tensors. Then, we will use the notations $\mathbf{u}$, $\boldsymbol{\sigma}$, g and $\mathbf{D}$, for the displacement vector, stress, displacement gradient and property tensors, respectively. Here, the displacement at each node of the mesh is represented as a vector. And, $\mathbf{u}$ represents the displacement vector containing all displacement components for the entire

system. And, the stress tensor σ_{ij} which is a second-order tensor, can be written in Voigt form as a vector for 2D and 3D stress states. For example, in continuum mechanics, a stress tensor σ_{ij} in 3D has 9 components ($i, j = 1, 2, 3$) and can be written as the following

$$\sigma_{ij} = \begin{bmatrix} \sigma_{11} & \sigma_{12} & \sigma_{13} \\ \sigma_{21} & \sigma_{22} & \sigma_{23} \\ \sigma_{31} & \sigma_{32} & \sigma_{33} \end{bmatrix} \tag{3.1}$$

Stress tensors are symmetric, meaning $\sigma_{ij} = \sigma_{ji}$. Due to this symmetry, the number of independent components reduces from 9 to 6 in 3D. And, Voigt notation reduces the components of the symmetric tensor into a vector format. For a 3D stress tensor, the 6 independent components are arranged as follows

$$\boldsymbol{\sigma} = \begin{pmatrix} \sigma_{11} \\ \sigma_{22} \\ \sigma_{33} \\ \sigma_{12} \\ \sigma_{13} \\ \sigma_{23} \end{pmatrix} \tag{3.2}$$

In 2D, the stress tensor σ_{ij} has 4 components ($i, j = 1, 2$) and can be written as the following

$$\sigma_{ij} = \begin{bmatrix} \sigma_{11} & \sigma_{12} \\ \sigma_{21} & \sigma_{22} \end{bmatrix} \tag{3.3}$$

Instead of storing the four tensor components, we store only three independent components in a vector form (Voigt notation) as the following

$$\boldsymbol{\sigma} = \begin{pmatrix} \sigma_{11} \\ \sigma_{22} \\ \sigma_{12} \end{pmatrix} \tag{3.4}$$

The displacement gradient tensor g_{ij}, which represents the spatial variation of displacement components, is also converted to Voigt form. It is a second-order tensor given by

$$g_{ij} = \frac{\partial u_i}{\partial x_j} \tag{3.5}$$

where, u_i are the displacement components. $u_1 = u$ is displacement in the x-direction. $u_2 = v$ is displacement in the y-direction. $u_3 = w$ is displacement in the z-direction. And, x_j are the spatial coordinates as $x_1 = x$, $x_2 = y$ and $x_3 = z$. In 3D, this displacement gradient tensor (which is not symmetric) can be represented as the following

$$g_{ij} = \begin{bmatrix} \frac{\partial u_1}{\partial x_1} & \frac{\partial u_1}{\partial x_2} & \frac{\partial u_1}{\partial x_3} \\ \frac{\partial u_2}{\partial x_1} & \frac{\partial u_2}{\partial x_2} & \frac{\partial u_2}{\partial x_3} \\ \frac{\partial u_3}{\partial x_1} & \frac{\partial u_3}{\partial x_2} & \frac{\partial u_3}{\partial x_3} \end{bmatrix} \tag{3.6}$$

Substituting the displacement components u, v, w, we get

$$g_{ij} = \begin{bmatrix} \frac{\partial u}{\partial x} & \frac{\partial u}{\partial y} & \frac{\partial u}{\partial z} \\ \frac{\partial v}{\partial x} & \frac{\partial v}{\partial y} & \frac{\partial v}{\partial z} \\ \frac{\partial w}{\partial x} & \frac{\partial w}{\partial y} & \frac{\partial w}{\partial z} \end{bmatrix} \tag{3.7}$$

This tensor describes how displacement varies within a 3D continuum and is fundamental in deformation analysis, particularly for computing strain and rotation components. In 3D Voigt notation, the displacement gradient tensor g_{ij} is represented as a 9-component vector. This is different from stress and strain Voigt notation, where symmetry reduces the number of components. Since the displacement gradient tensor is not symmetric, it must be stored

as a 9-component vector as the following

$$\mathbf{g} = \begin{pmatrix} g_{11} \\ g_{22} \\ g_{33} \\ g_{12} \\ g_{13} \\ g_{21} \\ g_{23} \\ g_{31} \\ g_{32} \end{pmatrix} = \begin{pmatrix} \frac{\partial u}{\partial x} \\ \frac{\partial v}{\partial y} \\ \frac{\partial w}{\partial z} \\ \frac{\partial u}{\partial y} \\ \frac{\partial u}{\partial z} \\ \frac{\partial v}{\partial x} \\ \frac{\partial v}{\partial z} \\ \frac{\partial w}{\partial x} \\ \frac{\partial w}{\partial y} \end{pmatrix} \tag{3.8}$$

In 2D, the displacement gradient tensor g_{ij} (which is not symmetric) can be represented as the following

$$g_{ij} = \begin{bmatrix} \frac{\partial u_1}{\partial x_1} & \frac{\partial u_1}{\partial x_2} \\ \frac{\partial u_2}{\partial x_1} & \frac{\partial u_2}{\partial x_2} \end{bmatrix} = \begin{bmatrix} \frac{\partial u}{\partial x} & \frac{\partial u}{\partial y} \\ \frac{\partial v}{\partial x} & \frac{\partial v}{\partial y} \end{bmatrix} \tag{3.9}$$

In 2D Voigt notation, the displacement gradient tensor g_{ij} is represented as a 3-component vector as the following

$$\mathbf{g} = \begin{pmatrix} g_{11} \\ g_{22} \\ g_{12} \end{pmatrix} = \begin{pmatrix} \frac{\partial u}{\partial x} \\ \frac{\partial v}{\partial y} \\ \frac{\partial u}{\partial y} + \frac{\partial v}{\partial x} \end{pmatrix} \tag{3.10}$$

And, this simplifies the representation of the deformation state. To develop the numerical solution procedure, we start by selecting appropriate forms for the displacement field $\mathbf{u}$ and the Lagrange multiplier field $\boldsymbol{\lambda}$. The purpose of this selection is to approximate these fields using interpolation functions, which facilitate the discretization and solution of the governing equations. In terms of displacement field $\mathbf{u}$, we express the displacement field $\mathbf{u}$ in terms of interpolation functions. Now, the displacement field is selected in the following form

$$\mathbf{u} = \mathbf{A}\mathbf{a} \tag{3.11}$$

In Eq. (3.11), $\mathbf{A}$ is a vector of selected approximation functions. These functions are chosen based on the problem domain and are used to interpolate the displacement field. Common

choices for $\mathbf{A}$ include polynomial functions, trigonometric functions, or finite element shape functions. $\mathbf{a}$ is a vector of unknown parameters (also known as nodal values) that need to be determined. After discretization, it represents the discretized degrees of freedom for the displacement field. Each component of $\mathbf{a}$ corresponds to a specific node in the discretized domain.

In terms of Lagrange Multiplier field $\boldsymbol{\lambda}$, similarly, we express the Lagrange multiplier field $\boldsymbol{\lambda}$ in terms of interpolation functions as the following

$$\boldsymbol{\lambda} = \mathbf{G}\mathbf{h} \tag{3.12}$$

In Eq. (3.12), $\mathbf{G}$ is a vector of selected approximation functions for the Lagrange multiplier field. The choice of functions in $\mathbf{G}$ depends on the specific constraints and problem domain. These functions ensure that the constraints are properly applied throughout the domain. Furthermore, $\mathbf{h}$ is a vector of unknown parameters related to the Lagrange multipliers. Similar to $\mathbf{a}$, these parameters are determined through the discretization process and represent the discretized values of the Lagrange multipliers. Each component of $\mathbf{h}$ corresponds to a specific node where the constraints are applied. By choosing the displacement field $\mathbf{u}$ and the Lagrange multiplier field $\boldsymbol{\lambda}$ in the forms $\mathbf{u} = \mathbf{A}\mathbf{a}$ and $\boldsymbol{\lambda} = \mathbf{G}\mathbf{h}$, we convert the continuous problem into a discrete one. This allows us to use numerical methods to solve for the unknown parameters $\mathbf{a}$ and $\mathbf{h}$. The vectors $\mathbf{A}$ and $\mathbf{G}$ contain the interpolation functions that approximate the fields, while $\mathbf{a}$ and $\mathbf{h}$ are the unknown coefficients determined through the discretization and solution process. This approach is fundamental in finite element analysis and other numerical methods used to solve partial differential equations in engineering and physics.

By substituting Eqs. (3.11) and (3.12) into Eq. (2.38), we obtains the algebraic form of the RVE problem as shown in Appendix B.1.1, we get

$$\begin{bmatrix} \mathbf{K} & \mathbf{S}^{\mathrm{T}} \\ \mathbf{S} & 0 \end{bmatrix} \begin{Bmatrix} \mathbf{a} \\ \mathbf{h} \end{Bmatrix} = \begin{Bmatrix} \mathbf{0} \\ \boldsymbol{\Theta}\mathbf{g} \end{Bmatrix} \tag{3.13}$$

where $\mathbf{K}$, $\mathbf{S}$ and $\boldsymbol{\Theta}$ can be identified as

$$\mathbf{K} = \int_{V_{RVE}} \left(\frac{\partial \mathbf{A}}{\partial \mathbf{y}} \right)^{\mathrm{T}} \mathbf{D} \frac{\partial \mathbf{A}}{\partial \mathbf{y}} \, \mathrm{dY} \tag{3.14}$$

$$\mathbf{S} = \int_{S_{RVE}} \mathbf{G}^{\mathrm{T}} \mathbf{A} \, \mathrm{d}\Psi \tag{3.15}$$

$$\mathbf{\Theta} = \int_{S_{RVE}} \mathbf{G}^{\mathrm{T}} \mathbf{\Psi}^{\mathrm{T}} \, \mathrm{d}\Psi \tag{3.16}$$

The algebraic system in Eq. (3.13) represents a constrained system governing the behavior of the (RVE) under imposed macroscopic deformation. It consists of the stiffness equation (first row) and the constraint equation (second row). Each term in the system represents a specific physical aspect of the problem. The stiffness matrix $\mathbf{K}$ comes from the weak form of the equilibrium equations and represents the internal stiffness of the RVE. It is obtained from the integration of the material's constitutive relation and displacement field derivatives. Physically, it captures how the microstructure resists deformation in response to applied forces. The coupling matrix $\mathbf{S}$ couples the displacement degrees of freedom $\mathbf{a}$ with the Lagrange multipliers $\mathbf{h}$. It ensures that the displacement field inside the RVE satisfies the boundary constraints imposed by the macroscopic deformation. This matrix appears because the RVE needs to be compatible with macroscopic boundary conditions. Regarding the Lagrange multiplier terms $\mathbf{S}^{\mathrm{T}}$ and $\mathbf{h}$, $\mathbf{S}^{\mathrm{T}}\mathbf{h}$ represents the reaction forces that arise from enforcing the macroscopic boundary constraints. And, the Lagrange multipliers $\mathbf{h}$ are physically interpreted as traction forces needed to enforce periodic boundary conditions on the RVE. Regarding the term $\mathbf{\Theta g}$, this term introduces the macroscopic deformation constraint. $\mathbf{g}$ represents the prescribed macroscopic strain or displacement gradient applied to the RVE. $\mathbf{\Theta}$ ensures that this macroscopic deformation is correctly applied over the RVE boundary.

Rewriting the system in equation form, first equation (force balance in the RVE) as

$$\mathbf{Ka} + \mathbf{S}^{\mathrm{T}}\mathbf{h} = 0 \tag{3.17}$$

This represents the equilibrium equation of the RVE. The internal forces (from the stiffness matrix $\mathbf{K}$) must balance the reaction forces imposed by the boundary constraints. In essence, the displacement field $\mathbf{a}$ inside the RVE is determined by the applied forces. The

second equation(macroscopic constraint enforcement) is given as

$$\mathbf{Sa} = \mathbf{\Theta g} \tag{3.18}$$

This enforces the macroscopic boundary conditions. It ensures that the microscopic displacement field $\mathbf{a}$ aligns with the macroscopic deformation described by $\mathbf{g}$. This equation enforces periodicity or other homogenization conditions. In the overall physical meaning, this system Eq. (3.13) describes how the microstructure of the RVE deforms under macroscopic strain. This system describes how the microstructure of the RVE deforms under macroscopic strain. It ensures that the microscopic equilibrium conditions are satisfied (first equation) while also enforcing the required macroscopic deformation (second equation). The presence of $\mathbf{S}$ and $\mathbf{S}^{\mathrm{T}}$ ensures that the RVE behavior is consistent with the applied boundary conditions. Furthermore, this system can be solved numerically to obtain the microstructural response and compute homogenized stress-strain relations. The solution $\mathbf{a}$ provides the micro-deformation field, while the reaction forces $\mathbf{h}$ give information about interfacial forces (tractions).

The expressions for $\mathbf{K}$, $\mathbf{S}$, and $\mathbf{\Theta}$ in Eq. (3.13) are central to the finite element method and provide insight into the physical behavior of the system. The stiffness matrix $\mathbf{K}$, as defined in Eq. (3.14), plays a fundamental role in the homogenization of the RVE. It serves as a link between microscopic and macroscopic mechanical behavior. Specifically, $\mathbf{K}$ characterizes the stiffness of the RVE by describing how the microstructure resists deformation under applied forces. Fundamentally, it quantifies the storage of strain energy within the material at the microscopic scale. The shape function gradient $\frac{\partial \mathbf{A}}{\partial \mathbf{y}}$ is associated with the matrix of shape functions, $\mathbf{A}$, which interpolates the displacement field within the RVE. The term $\frac{\partial \mathbf{A}}{\partial \mathbf{y}}$ represents the strain-displacement relationship, converting nodal displacements into strain. It defines how the displacement field varies across the volume element. The constitutive matrix $\mathbf{D}$, also referred to as the material property matrix, encapsulates the material's elastic properties, specifically the elastic stiffness tensor. It establishes the relationship between stress and strain through Hooke's law, $\boldsymbol{\sigma} = \mathbf{D}\boldsymbol{\varepsilon}$, where $\boldsymbol{\sigma}$ and $\boldsymbol{\varepsilon}$ denote the stress and strain tensors, respectively. This matrix governs the mechanical behavior of the material, including isotropic elasticity. Integration is carried out over the volume of the RVE, denoted as V_{RVE}, ensuring that the stiffness matrix $\mathbf{K}$ accounts for the entire microstructure rather than

a single point. This integral incorporates the contributions of all material points within the RVE. Finally, the transpose operation in $\left(\frac{\partial \mathbf{A}}{\partial \mathbf{y}}\right)^{\mathrm{T}}$ ensures dimensional consistency in matrix multiplication, preserving the mathematical validity of the formulation.

The coupling matrix $\mathbf{S}$, as defined in Eq. (3.15), plays an important role in enforcing constraints in the homogenization of the RVE. Specifically, $\mathbf{S}$ serves as a coupling matrix that links the nodal displacement field within the RVE to the Lagrange multiplier field, which enforces specific constraints. This matrix arises from the weak formulation of the boundary conditions and appears in the variational formulation of the RVE problem. Physically, it ensures the consistent application of boundary constraints when solving the system of equations. The transformation matrix of Lagrange multipliers, $\mathbf{G}^{\mathrm{T}}$, is associated with the Lagrange multiplier field $\boldsymbol{\lambda}$, which enforces displacement constraints on the boundary S_{RVE}. The presence of $\mathbf{G}^{\mathrm{T}}$ in the formulation stems from the variational principle, ensuring the correct transformation between the Lagrange multipliers and the displacement field. Physically, $\mathbf{G}$ distributes the effect of constraint forces across the RVE boundary. The shape function matrix $\mathbf{A}$ represents the shape functions that interpolate the displacement field within the RVE. It establishes the connection between nodal displacements and the overall displacement field inside the RVE. Physically, it ensures the smooth interpolation of displacement constraints along the RVE boundary. The integration in Eq. (3.15) is performed over the boundary surface S_{RVE}, ensuring that constraint contributions are applied exclusively at the boundary rather than throughout the entire volume. Overall, this integral equation enforces boundary constraints such as periodicity or other prescribed conditions while preventing the introduction of spurious deformation modes. Additionally, it functions as a constraint enforcement matrix, ensuring that boundary conditions are correctly implemented. Ultimately, the coupling matrix $\mathbf{S}$ is essential for accurately enforcing constraints and ensuring that the RVE solution properly represents the material's effective response.

The constraint projection matrix $\boldsymbol{\Theta}$, as defined in Eq. (3.16), appears in the final algebraic system Eq. (3.13), where it plays an important role in consistently enforcing boundary conditions. Specifically, $\boldsymbol{\Theta}$ serves as a constraint-related matrix that links the Lagrange multipliers used for boundary constraints with the macroscopic deformation gradient applied to the RVE. Physically, it ensures that the applied macroscopic boundary conditions are accurately projected onto the Lagrange multiplier field, facilitating the correct enforcement of various types of boundary constraints. The transformation matrix of Lagrange multipliers,

$\mathbf{G}^{\mathrm{T}}$, is associated with the Lagrange multiplier field $\boldsymbol{\lambda}$, which enforces constraints on the boundary S_{RVE}. The appearance of $\mathbf{G}^{\mathrm{T}}$ in the formulation arises from the variational principle, ensuring the proper transformation between the Lagrange multipliers and the nodal displacement field. Physically, $\mathbf{G}$ distributes the effect of constraint forces across the RVE boundary. The matrix $\boldsymbol{\Psi}^{\mathrm{T}}$ is a coordinate-dependent matrix associated with all nodal points on the boundary of the microstructure. It depends on the reference coordinates of each node on the RVE boundary and is defined in Eq. (B.30). Physically, $\boldsymbol{\Psi}$ transforms the macroscopic deformation gradient into a form compatible with the constraints enforced by the Lagrange multipliers. This transformation is reflected in the term $\boldsymbol{\Theta}\mathbf{g}$, which appears on the right-hand side of the final algebraic form of the RVE in Eq. (3.13). This relationship highlights the role of $\boldsymbol{\Theta}$ in linking macroscopic boundary conditions to constraint enforcement within the system. The integration in Eq. (3.16) is performed over the boundary surface S_{RVE}, ensuring that constraint contributions are applied exclusively at the boundary rather than throughout the entire volume. Physically, this integral accumulates the effects of the constraint projection across all boundary nodes. Overall, Eq. (3.16) ensures that the macroscopic deformation gradient is properly linked to the constraints enforced by the Lagrange multipliers, effectively bridging macroscopic deformation and local constraints. Since $\boldsymbol{\Psi}$ encodes the reference coordinates of nodes on S_{RVE}, the matrix $\boldsymbol{\Theta}$ facilitates the transformation of macroscopic strain conditions into boundary constraints at the microscopic level.

In Eq. (3.13), the stress field within the heterogeneous RVE domain is derived from the constitutive relationship (2.2) between stress and strain. In solid mechanics, the stress tensor $\boldsymbol{\sigma}$ (expressed in Voigt notation) is related to the strain tensor $\boldsymbol{\varepsilon}$ via the material stiffness tensor $\mathbf{D}$ as

$$\boldsymbol{\sigma} = \mathbf{D}\boldsymbol{\varepsilon} \tag{3.19}$$

where, $\mathbf{D}$ represents the material stiffness matrix, incorporating properties such as Young's modulus and Poisson's ratio. The strain tensor is defined as the spatial gradient of the displacement field $\mathbf{u}$ as

$$\boldsymbol{\varepsilon} = \frac{\partial \mathbf{u}}{\partial \mathbf{y}} \tag{3.20}$$

where $\mathbf{y}$ denotes the spatial coordinates in the RVE. Differentiating the displacement ap-

proximation Eq. (3.11), yields the strain-displacement relationship as

$$\frac{\partial \mathbf{u}}{\partial \mathbf{y}} = \frac{\partial \mathbf{A}}{\partial \mathbf{y}} \mathbf{a} \tag{3.21}$$

Substituting this into Eq. (3.19) provides the stress field in terms of the displacement approximation as

$$\boldsymbol{\sigma} = \mathbf{D} \frac{\partial \mathbf{A}}{\partial \mathbf{y}} \mathbf{a} \tag{3.22}$$

This formulation demonstrates how the stress at any point in the RVE depends on the displacement gradient, shaped by the approximation functions, and the material's constitutive response. The stiffness matrix $\mathbf{D}$ governs the transition from strain to stress, emphasizing the role of material properties in local deformation resistance.

To solve the RVE problem by using the general algebraic form in Eq. (3.13), we need to impose certain constraints on the boundary conditions. This can be done by manipulating the Lagrange multiplier field $\boldsymbol{\lambda}$ and/or the displacement field $\mathbf{u}$ at the boundary S_{RVE}. In terms of constraining the Lagrange Multiplier Field $\boldsymbol{\lambda}$, the Lagrange multiplier field $\boldsymbol{\lambda}$ physically represents the tractions or stresses at the boundary of the RVE. By imposing constraints on $\boldsymbol{\lambda}$, we are essentially prescribing the boundary stress conditions. Mathematically, imposing constraints on $\boldsymbol{\lambda}$ can be done by setting certain values or expressions for $\mathbf{h}$ in the matrix equation. For example, if we know the stress at the boundary, we can directly input these values. In terms of constraining the Displacement Field $\mathbf{u}$, the displacement field $\mathbf{u}$ physically describes how each point within the RVE moves. Constraining $\mathbf{u}$ means prescribing how the boundary of the RVE deforms. Mathematically, imposing constraints on $\mathbf{u}$ involves setting specific values or conditions for the displacement vector $\mathbf{a}$. For example, we might fix the displacement at certain boundary points to zero (Dirichlet boundary condition) or allow for a specific displacement gradient. In terms of combining constraints of both Lagrange multiplier field $\boldsymbol{\lambda}$ and the displacement field $\mathbf{u}$, a combination of displacement and traction (stress) boundary conditions is used to accurately represent the physical scenario. This approach allows us to capture both the deformation and the stress distribution within the RVE. Mathematically, the general matrix equation Eq. (3.13) facilitates the incorporation of both types of constraints.

The interior points of the RVE are located at $\mathbf{y} \in \bar{V}_{RVE} \setminus S_{RVE}$, i.e., $\left\{\mathbf{y} : \mathbf{y} \in \bar{V}_{RVE}\right.$

and $\mathbf{y} \notin S_{RVE}\}$, where $\bar{V}_{RVE}$ is the closure of the RVE domain, and $\mathbf{y}$ represents a position vector within the RVE. Also, V_{RVE} denotes the volume of the RVE. And, $\bar{V}_{RVE}$ represents the closure of the RVE volume, which includes both the interior and the boundary. In addition, S_{RVE} represents the surface or boundary of the RVE. Here, the interior points of the RVE are the points that lie strictly within the boundaries of the RVE, excluding the boundary itself. These are the points where the material behaviour is observed without direct boundary influences. The closure of the RVE domain, $\bar{V}_{RVE}$, includes all the points inside the RVE volume as well as the points on its boundary. In mathematical terms, closure means the set itself plus its boundary. Also, the boundary S_{RVE} is the surface that encloses the volume of the RVE. It is where external conditions, such as tractions or displacements, are applied in boundary value problems. And, the notation $\bar{V}_{RVE} \setminus S_{RVE}$ represents the set difference. It means taking the closure of the RVE domain and removing the boundary points S_{RVE}. Therefore, $\mathbf{y} \in \bar{V}_{RVE} \setminus S_{RVE}$ implies that the point $\mathbf{y}$ is within the RVE but not on its boundary. And, these are the true interior points of the RVE. So, in mathematical meaning, $\{\mathbf{y} : \mathbf{y} \in \bar{V}_{RVE}$ and $\mathbf{y} \notin S_{RVE}\}$ means we are considering all points $\mathbf{y}$ that belong to the closure of the RVE domain $\bar{V}_{RVE}$ but explicitly excluding those that are part of the boundary S_{RVE}. Also, by focusing on the interior points, we are interested in analysing the material properties and behaviours that are not directly affected by the boundary conditions. This allows us to understand the properties of the material within the RVE, such as stress and strain distributions, without the complications introduced by boundary effects.

On the other hand, for the purpose of imposing constraints, the boundary is decomposed into two parts, i.e., $S_{RVE} = S^{+}_{RVE} \cup S^{-}_{RVE}$ with outward normal $\mathbf{n}^{+} = -\mathbf{n}^{-}$ at associated points $\mathbf{\Psi}^{+} \in S^{+}_{RVE}$ and $\mathbf{\Psi}^{-} \in S^{-}_{RVE}$, respectively see Figure 3.1a. This decomposition helps in defining and applying specific boundary conditions or constraints separately on different portions of the boundary. The notation $S_{RVE} = S^{+}_{RVE} \cup S^{-}_{RVE}$ means that the entire boundary S_{RVE} is the union of the two parts S^{+}_{RVE} and S^{-}_{RVE}. Every point on the boundary belongs to either S^{+}_{RVE} or S^{-}_{RVE}. And, $\mathbf{n}^{+}$ is the outward normal vector at points on S^{+}_{RVE}. Also, $\mathbf{n}^{-}$ is the outward normal vector at points on S^{-}_{RVE}. The relationship $\mathbf{n}^{+} = -\mathbf{n}^{-}$ indicates that the normal vectors are oppositely directed at corresponding points on the two parts of the boundary. In addition, $\mathbf{\Psi}^{+}$ refers to points on the boundary part S^{+}_{RVE}. $\mathbf{\Psi}^{-}$ refers to points on the boundary part S^{-}_{RVE}. These points are associated in the sense that they may represent corresponding locations on the opposite sides of the RVE boundary, facilitating the definition of boundary conditions. Furthermore, the decomposition of the

boundary allows for more precise control and application of boundary conditions. This can be particularly useful in numerical simulations and finite element methods where different constraints might need to be applied on different parts of the boundary. For instance, one part of the boundary might be subject to prescribed displacements while the other part might be subject to prescribed tractions or forces.

In computational mechanics, ensuring that boundary conditions are properly handled is important for accurate simulation of material behavior. This is particularly important in the context of Representative Volume Elements (RVEs) used to model heterogeneous materials. As depicted in Figure 3.1b, a systematic approach is employed where each point on the boundary of the RVE is paired with a corresponding point, or image, on the opposite boundary. This method is executed in a standard and regular manner, following established conventions such as those detailed by e.g. Larsson et al. [27]. For a point $\mathbf{\Psi}^+$ located on the right boundary S^+_{RVE} of the RVE, its corresponding image point $\mathbf{\Psi}^-$ is found on the left boundary S^-_{RVE}. The critical aspect of this pairing is that both $\mathbf{\Psi}^+$ and $\mathbf{\Psi}^-$ share the same vertical coordinate, y_2. This means that if $\mathbf{\Psi}^+$ is at a particular height on the right boundary, $\mathbf{\Psi}^-$ will be at the same height on the left boundary. This ensures a vertical alignment and continuity across the RVE's width. Similarly, for a point $\mathbf{\Psi}^+$ on the top boundary S^+_{RVE}, the corresponding image point $\mathbf{\Psi}^-$ is located on the bottom boundary S^-_{RVE}. In this case, both points share the same horizontal coordinate, y_1. Thus, if $\mathbf{\Psi}^+$ is at a specific horizontal position on the top boundary, $\mathbf{\Psi}^-$ will be at the same position on the bottom boundary, maintaining horizontal alignment and continuity across the RVE's height. An important aspect of this boundary pairing is the handling of corner points. Each corner point on the RVE, which lies at the intersection of two boundaries, has two images. For example, a corner point on the top-right boundary will have an image on the top-left boundary and another on the bottom-right boundary. This dual pairing is necessary because corner points need to maintain continuity in both the horizontal and vertical directions. Furthermore, pairing points on opposite boundaries ensures that the displacement and stress fields are continuous across the boundaries. This set-up copies the infinite repetition of the RVE in a real material, which is essential for accurate homogenization and effective property estimation. In numerical simulations, this pairing allows for the application of constraints that enforce the periodicity of the solution. Also, it ensures that deformation or stress at one boundary is appropriately mirrored at the opposite boundary, maintaining the overall consistency of the model.

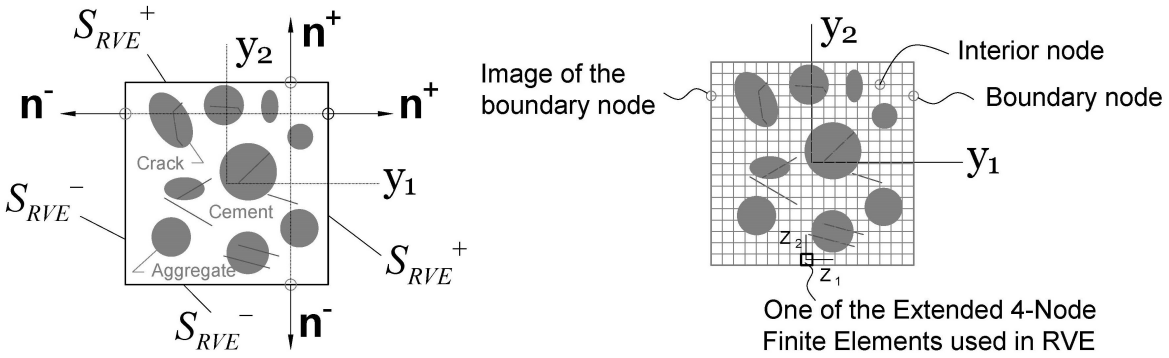

(a) Schematic picture

(b) Mesh for the numerical solution

Figure 3.1: RVE

In the algebraic formulation of the RVE problem, the Eq. (3.13) contains two key matrices. The stiffness matrix $\mathbf{K}$ which represents the relationship between the displacement degrees of freedom and the internal forces within the RVE. The constraint (coupling) matrix $\mathbf{S}$ which represents how the Lagrange multipliers (enforcing boundary conditions) interact with the displacement field. The displacement vector $\mathbf{a}$ contains the unknown nodal displacements at all nodes in the RVE domain. And, the RVE domain contains two types of nodes. Internal nodes (I) which are are located inside the RVE domain, meaning they are not on the boundary. And, boundary nodes (B) which are lie on the boundary S_{RVE}, where constraints (such as periodicity or Lagrange multipliers) are applied. Since the displacements are unknown at both types of nodes, we partition the nodal displacement vector $\mathbf{a}$ into

$$\mathbf{a} = \begin{Bmatrix} \mathbf{a}_I \\ \mathbf{a}_B \end{Bmatrix} \tag{3.23}$$

This equation represents the global nodal displacement vector $\mathbf{a}$, which contains the displacements of all nodes in the computational domain. It is partitioned into two components based on the location of the nodes. Regarding the internal displacement vector $\mathbf{a}_I$, $\mathbf{a}_I$ contains the displacement values of the internal nodes inside the RVE. These displacements are unknowns that must be solved as part of the finite element system. Regarding the boundary displacement vector $\mathbf{a}_B$, $\mathbf{a}_B$ contains the displacement values of the boundary nodes of the RVE. These displacements are either prescribed by boundary conditions or interact with internal nodes and constraint equations. Boundary nodes can be subject to periodic constraints or any other types in computational homogenization, Lagrange multipliers enforcing boundary conditions and applied macroscopic deformation through constraints. In

overall, this partitioning of $\mathbf{a}$ separates the displacement degrees of freedom into internal and boundary components. This is important because it allows for enforcing boundary conditions separately. It also helps in reducing computational complexity by solving for internal displacements while treating boundary conditions appropriately. It is essential for implementing constraint-based methods (like Lagrange multipliers) to enforce periodicity or other conditions in computational homogenization.

The stiffness matrix $\mathbf{K}$ originally governs the relationship between all nodal displacements and internal forces. However, because nodes are now classified as either internal or boundary nodes, the matrix is rewritten in a partitioned form as

$$\mathbf{K} = \begin{bmatrix} \mathbf{K}_{II} & \mathbf{K}_{IB} \\ \mathbf{K}_{IB}^{\mathrm{T}} & \mathbf{K}_{BB} \end{bmatrix} \tag{3.24}$$

In Eq. (3.24), the internal stiffness matrix $\mathbf{K}_{II}$ represents the stiffness contributions from interactions between internal nodes only. It determines how displacements at internal nodes influence the forces at other internal nodes. Also, It governs the response of the RVE's internal region without direct interaction with the boundary. The coupling stiffness matrix $\mathbf{K}_{IB}$ represents the stiffness contributions due to interactions between internal nodes and boundary nodes. It defines how boundary node displacements affect internal node forces. It also couples internal and boundary node displacements, making it crucial for ensuring consistency across the domain. The transpose of the coupling stiffness matrix $\mathbf{K}_{IB}^{\mathrm{T}}$ represents the stiffness contributions due to interactions between boundary nodes and internal nodes. It defines how internal node displacements affect forces at boundary nodes. It is the transpose of $\mathbf{K}_{IB}$, ensuring symmetry in the stiffness formulation. The boundary stiffness matrix $\mathbf{K}_{BB}$ represents the stiffness contributions from interactions between boundary nodes only. It governs how boundary displacements interact with each other. This sub-matrix is essential for implementing boundary conditions and constraints, such as periodic boundary conditions or imposed displacements. In overall, this partitioning of $\mathbf{K}$ that separates the stiffness contributions of internal and boundary nodes is so important for computational homogenization and finite element modeling. This partitioning helps in solving the system by focusing on internal nodes separately while enforcing boundary conditions. The structure allows for applying constraints (such as periodicity or Lagrange multipliers) at the bound-

ary while solving for the internal displacement field. It reflects how different parts of the RVE interact and how internal points deform under forces and how the boundary influences this behavior. Finally, this matrix structure (3.24) enables a systematic approach to solving the finite element equilibrium equations for the RVE while correctly handling boundary conditions.

Similarly, the constraint matrix $\mathbf{S}$, which enforces the boundary conditions in the computational homogenization framework. It arises in the algebraic form of the RVE problem and is related to the Lagrange multiplier method for imposing displacement constraints. The matrix is partitioned into two components based on the distinction between internal nodes and boundary nodes as

$$\mathbf{S} = \begin{bmatrix} \mathbf{S}_I & \mathbf{S}_B \end{bmatrix} \tag{3.25}$$

In Eq. (3.25), the constraint contribution for internal nodes $\mathbf{S}_I$ represents the influence of internal node displacements on the constraints imposed by the Lagrange multipliers. Since the constraints are only applied at the boundary, $\mathbf{S}_I = 0$ because the function $\mathbf{G}$, which defines the constraints, is zero inside the domain (i.e., at internal nodes). This means internal nodes are not directly involved in enforcing boundary conditions, which simplifies the formulation. The constraint contribution for boundary nodes $\mathbf{S}_B$ represents the influence of boundary node displacements on the imposed constraints. It defines how displacements at the boundary nodes interact with the Lagrange multiplier terms to enforce the desired constraints. This matrix ensures that boundary nodes satisfy the imposed periodicity or other constraint conditions in the RVE problem. In overall, the matrix $\mathbf{S}$ defines how the displacement field interacts with the Lagrange multiplier field $\boldsymbol{\lambda}$, which is used to enforce specific boundary conditions. And, the matrix $\mathbf{S}$ plays an important role in coupling the displacement field with boundary constraints, ensuring that the RVE behaves consistently under homogenization conditions.

By substituting the partitioned form of $\mathbf{K}$ and $\mathbf{a}$ into the equilibrium equation, we obtain

$$\mathbf{K}\mathbf{a} = \begin{bmatrix} \mathbf{K}_{II} & \mathbf{K}_{IB} \\ \mathbf{K}_{IB}^T & \mathbf{K}_{BB} \end{bmatrix} \begin{Bmatrix} \mathbf{a}_I \\ \mathbf{a}_B \end{Bmatrix} \tag{3.26}$$

This equation describes the system of equilibrium equations governing the response of the RVE under deformation. When multiplying $\mathbf{K}$ with $\mathbf{a}$, the result represents the nodal force

balance in the system. After performing the matrix-vector multiplication, the equation expands as

$$\begin{Bmatrix} \mathbf{K}_{II}\mathbf{a}_I + \mathbf{K}_{IB}\mathbf{a}_B \\ \mathbf{K}_{IB}^T\mathbf{a}_I + \mathbf{K}_{BB}\mathbf{a}_B \end{Bmatrix} \tag{3.27}$$

Each row represents the equilibrium equations for a subset of nodes. Regarding the first row (Internal node equilibrium) which is defined as

$$\mathbf{K}_{II}\mathbf{a}_I + \mathbf{K}_{IB}\mathbf{a}_B \tag{3.28}$$

This equation governs the internal nodes of the RVE. $\mathbf{K}_{II}\mathbf{a}_I$ represents the contribution to internal forces from internal displacements. $\mathbf{K}_{IB}\mathbf{a}_B$ represents the influence of boundary node displacements on internal node forces. The sum must balance to satisfy equilibrium. Regarding the second row (Boundary node equilibrium) which is defined as

$$\mathbf{K}_{IB}^T\mathbf{a}_I + \mathbf{K}_{BB}\mathbf{a}_B \tag{3.29}$$

This equation governs the boundary nodes of the RVE. $\mathbf{K}_{IB}^T\mathbf{a}_I$ represents the influence of internal node displacements on boundary node forces. $\mathbf{K}_{BB}\mathbf{a}_B$ represents the contribution to boundary forces from boundary displacements. The sum must satisfy equilibrium at the boundary nodes. In overall, Eq. (3.26) enforces mechanical equilibrium in the discretized system. The internal equilibrium equation ensures that forces within the interior of the RVE are balanced based on interactions with neighboring nodes. The boundary equilibrium equation accounts for how boundary displacements and constraints affect the system.

By substituting the partitioned form of $\mathbf{S}$ and $\mathbf{a}$ into the equilibrium equation, we obtain

$$\mathbf{S}\mathbf{a} = \begin{bmatrix} \mathbf{S}_I & \mathbf{S}_B \end{bmatrix} \begin{Bmatrix} \mathbf{a}_I \\ \mathbf{a}_B \end{Bmatrix} \tag{3.30}$$

This represents the constraints imposed by the Lagrange multiplier method in the RVE problem, ensuring that certain boundary conditions are satisfied. By Expanding the multi-

plication of Eq. (3.30), we get

$$\mathbf{S}_I\mathbf{a}_I + \mathbf{S}_B\mathbf{a}_B \tag{3.31}$$

Here, each term represents a different contribution. This term $\mathbf{S}_I\mathbf{a}_I$ describes how the internal displacements ($\mathbf{a}_I$) contribute to the constraint equations. Since the constraint conditions are only enforced on the boundary, and the matrix $\mathbf{S}$ is defined via a boundary integral, $\mathbf{S}_I = 0$ for internal nodes. This means internal displacements do not directly contribute to the constraints. This term $\mathbf{S}_B\mathbf{a}_B$ accounts for the influence of the boundary displacements ($\mathbf{a}_B$) on the constraint conditions. It ensures that the imposed boundary conditions (e.g., periodicity, displacement continuity, or traction constraints) are satisfied at the boundary. In overall, Eq. (3.30) enforces boundary constraints using the Lagrange multiplier approach. It ensures that boundary displacements satisfy the imposed conditions, such as periodicity or any other types in computational homogenization or continuity conditions in multi-scale modeling. Also, this equation plays an important role in maintaining kinematic compatibility at the boundary, ensuring that the microscopic RVE behavior aligns with the macroscopic boundary conditions.

Figure 3.1b, shows the boundary nodes and the interior nodes separately in order to explain the implementation of the boundary constraint conditions explicitly. The matrix $\mathbf{S}$ is specifically defined through a boundary integral, meaning that it is calculated based on the interactions and conditions at the boundary of the Representative Volume Element (RVE), denoted as S_{RVE}. This boundary integral approach implies that $\mathbf{S}$ captures contributions exclusively from the boundary nodes and not from the interior of the RVE. When we construct the matrix $\mathbf{S}$, we integrate over the boundary surface, focusing on how the boundary nodes interact with the Lagrange multipliers and the displacement field at the boundary. Given this procedure, the sub matrix $\mathbf{S}_I$, which would represent the influence of the Lagrange multipliers on the interior nodes, naturally vanishes. This vanishing occurs because the interior nodes, those located within the volume $\bar{V}_{RVE}$ but not on the boundary S_{RVE}, do not contribute to the boundary integral. In simpler terms, since $\mathbf{S}$ is defined only through interactions at the boundary, there is no contribution from nodes that are purely inside the volume, hence $\mathbf{S}_I$ becomes a zero matrix. Further reinforcing this concept is the role of the approximation functions for the Lagrange multipliers, denoted as $\mathbf{G}$. These functions are chosen to be non-zero only at the boundary nodes where constraints are applied. At any interior point $\mathbf{y} \in \bar{V}_{RVE} \setminus S_{RVE}$, the function $\mathbf{G}$ is zero. This design ensures that the Lagrange

multipliers do not influence the interior nodes, aligning with the boundary-focused nature of $\mathbf{S}$. Consequently, because $\mathbf{G}$ is zero for all interior nodes, the matrix $\mathbf{S}_I$ has no non-zero entries, thus confirming that it vanishes.

The system now explicitly handles the coupling between interior and boundary nodes while enforcing the constraints imposed by the Lagrange multipliers. By partitioning these matrices and vectors, the problem can be solved more efficiently, ensuring that boundary conditions are properly imposed and that the resulting system of equations is well-posed for numerical solution. This systematic approach ensures accurate representation and enforcement of mechanical equilibrium and boundary constraints in the finite element model of the RVE.

3.2.1 Uniform displacement gradient RVE boundary conditions

We begin with the assumption that the displacement gradient, denoted as g_{ij}, is uniform at the boundaries of the RVE. This implies that the displacement variation at the boundaries is consistent and linear. Consequently, we assume the absence of small-scale fluctuations in displacement at the boundary. Mathematically, this condition is expressed as $\mathbf{u}'(\mathbf{\Psi}) = \mathbf{0}$, where $\mathbf{u}'$ represents micro-scale fluctuations in displacement. The total displacement field $u_i(\psi_i)$ at any boundary point ψ_i is expressed in tensor notation in Eq. (2.31). When adopting Voigt notation, Eq. (2.31) takes the form

$$\mathbf{u}(\mathbf{\Psi}) = \bar{\mathbf{u}}(\bar{\mathbf{y}}) + (\mathbf{\Psi} - \bar{\mathbf{y}})^{\mathrm{T}}\mathbf{g} + \mathbf{u}'(\mathbf{\Psi}) \tag{3.32}$$

To maintain proper matrix multiplication in Voigt notation, the transpose $(\mathbf{\Psi}-\bar{\mathbf{y}})^{\mathrm{T}}$ is applied when multiplied by $\mathbf{g}$. Under the assumption of no micro-scale fluctuations ($\mathbf{u}'(\mathbf{\Psi}) = \mathbf{0}$), Eq. (3.32) simplifies to

$$\mathbf{u}(\mathbf{\Psi}) = \bar{\mathbf{u}}(\bar{\mathbf{y}}) + (\mathbf{\Psi} - \bar{\mathbf{y}})^{\mathrm{T}}\mathbf{g} \tag{3.33}$$

Here, $\bar{\mathbf{u}}(\bar{\mathbf{y}})$ represents the macroscopic or average displacement at the reference point $\bar{\mathbf{y}}$, while $(\mathbf{\Psi} - \bar{\mathbf{y}})^{\mathrm{T}}\mathbf{g}$ captures the contribution of the displacement gradient. For mathematical convenience, we choose the reference point as the origin, setting $\bar{\mathbf{y}} = \mathbf{0}$. Similarly, we assume that the macroscopic displacement at this reference point is zero, i.e., $\bar{\mathbf{u}}(\bar{\mathbf{y}}) = \mathbf{0}$. With these simplifications, the displacement at any boundary point $\mathbf{\Psi}$ depends solely on the

displacement gradient g, leading to

$$\mathbf{u}(\mathbf{\Psi}) = \mathbf{\Psi}^{\mathrm{T}}\mathbf{g} \tag{3.34}$$

This linear relationship indicates that the displacement at the boundary points is directly proportional to their spatial coordinates, scaled by the displacement gradient. Since the displacement at the boundary is determined entirely by the macroscopic displacement gradient, the boundary deformations remain linear. Consequently, each boundary point's displacement is a linear function of its position, resulting in a predictable and well-structured deformation pattern for the RVE boundary. Given this simplified displacement expression, the nodal displacements at the RVE boundary can be determined as

$$\mathbf{\Lambda}_B = \mathbf{\Psi}^{\mathrm{T}}\mathbf{g} \tag{3.35}$$

This equation provides a means to compute the boundary nodal displacements $\mathbf{\Lambda}_B$ by combining the geometric representation of the boundary surface ($\mathbf{\Psi}$) with the macroscopic displacement gradient (g). In Eq. (3.35), $\mathbf{\Lambda}_B$ denotes the vector of nodal displacements at the boundary nodes of the RVE, where the subscript B specifically refers to boundary nodes. These displacements describe the deformation of the RVE boundary under the applied macroscopic strain. $\mathbf{\Psi}$ represents the spatial coordinates of points defining the boundary surface geometry. $\mathbf{\Psi}^{\mathrm{T}}$, the transpose of $\mathbf{\Psi}$, reorganizes these boundary points into a format suitable for multiplication with g. g is the macroscopic displacement gradient tensor, which governs the overall deformation of the RVE and describes how the macroscopic strain influences the displacement field. This formulation ensures that the displacement values at the boundary nodes ($\mathbf{\Lambda}_B$) are consistently derived from the macroscopic deformation field (g) while accurately capturing the geometry of the RVE boundary. By aligning the nodal displacements with the imposed boundary conditions, this approach maintains the integrity of the numerical model and facilitates an accurate prediction of the RVE's mechanical response. Furthermore, the selected vector of approximation function for the displacement field $\mathbf{A}$ is assumed to have interpolatory property, i.e., $\mathbf{a}_{Bk} = \langle \mathbf{\Lambda}_{Bk} \rangle^{\mathrm{T}} = \langle \mathbf{u}_{B1}(\mathbf{\Psi}_k) \quad \mathbf{u}_{B2}(\mathbf{\Psi}_k) \rangle$, where $\mathbf{\Psi}_k$ is the coordinates of the k^{th} node on the boundary, i.e., $\mathbf{\Psi}_k \in S_{RVE}$, i.e $k = 1, 2, \ldots m$, $\mathbf{u}_{B1}$ and $\mathbf{u}_{B2}$ are the displacement components at the bound-

ary in horizontal and vertical directions, and $\mathbf{a}_B = \left\langle \begin{array}{ccccccc} \mathbf{a}_{B1} & \mathbf{a}_{B2} & \cdots & \mathbf{a}_{Bk} & \cdots & \mathbf{a}_{Bm} \end{array} \right\rangle^{\mathrm{T}}$, in which m is the number of boundary nodes.

By substituting Eq. (3.35), Eq. (3.24), and Eq. (3.25) into Eq. (3.13), we obtain the solution of the RVE problem as as shown in Appendix B.1.2

$$\begin{bmatrix} \mathbf{K}_{II} & \mathbf{S}_I^{\mathrm{T}} \\ \mathbf{S}_I & 0 \end{bmatrix} \begin{Bmatrix} \mathbf{a}_I \\ \mathbf{h} \end{Bmatrix} = \begin{Bmatrix} -\mathbf{K}_{IB}\boldsymbol{\Psi}^{\mathrm{T}}\mathbf{g} \\ \left(\boldsymbol{\Theta} - \mathbf{S}_B\boldsymbol{\Psi}^{\mathrm{T}}\right)\mathbf{g} \end{Bmatrix} \tag{3.36}$$

By expanding this matrix multiplication (3.36), we get

$$\mathbf{K}_{II}\mathbf{a}_I + \mathbf{S}_I^{\mathrm{T}}\mathbf{h} = -\mathbf{K}_{IB}\boldsymbol{\Psi}^{\mathrm{T}}\mathbf{g} \tag{3.37}$$

$$\mathbf{S}_I\mathbf{a}_I = \left(\boldsymbol{\Theta} - \mathbf{S}_B\boldsymbol{\Psi}^{\mathrm{T}}\right)\mathbf{g} \tag{3.38}$$

Given that $\mathbf{S}_I = 0$, $\mathbf{S}_I^{\mathrm{T}} = 0$ as well. Therefore, we can simplify Eq. (3.37) to

$$\mathbf{K}_{II}\mathbf{a}_I = -\mathbf{K}_{IB}\boldsymbol{\Psi}^{\mathrm{T}}\mathbf{g} \tag{3.39}$$

Also, Eq. (3.38) is simplified to

$$0 = \left(\boldsymbol{\Theta} - \mathbf{S}_B\boldsymbol{\Psi}^{\mathrm{T}}\right)\mathbf{g} \tag{3.40}$$

Then, this implies that

$$\boldsymbol{\Theta}\mathbf{g} = \mathbf{S}_B\boldsymbol{\Psi}^{\mathrm{T}}\mathbf{g} \tag{3.41}$$

Then, solving for $\mathbf{a}_I$ in the simplified equation (3.39), this gives

$$\mathbf{a}_I = -\mathbf{K}_{II}^{-1}\mathbf{K}_{IB}\boldsymbol{\Psi}^{\mathrm{T}}\mathbf{g} \tag{3.42}$$

This is the solution for the internal nodal displacements, $\mathbf{a}_I$, in terms of the stiffness matrices and the macroscopic displacement gradient.

The algebraic form of the RVE problem in Eq. (3.36) represents the finite element dis-

cretization of the RVE equilibrium equations, incorporating uniform displacement gradient boundary conditions through the Lagrange multiplier method. It ensures internal equilibrium within the RVE while enforcing the homogenization constraints on the boundary displacements. The Lagrange multipliers ($\mathbf{h}$) enforce these boundary conditions, ensuring that the imposed macroscopic deformation is satisfied. Furthermore, the system consists of two coupled equations. Equilibrium equation (3.37) for internal nodes ($\mathbf{a}_I$) enforces the balance of internal forces considering the boundary influences. Constraint equation (3.38) for boundary conditions ensures that the imposed macroscopic displacement gradient is correctly applied to the RVE boundary. The right-hand side of Eq. (3.36) expresses the external effects from macroscopic loading, which drive the RVE deformation. Overall, this formulation enables solving for the microscopic displacement field ($\mathbf{a}_I$) while ensuring proper enforcement of macroscopic kinematics via Lagrange multipliers.

3.2.2 Uniform traction RVE boundary conditions

Under the assumption of uniform stress, we aim to apply the same stress across all points on the boundary of the RVE. This uniform stress assumption implies that the stress components do not vary from point to point along the boundary. However, when considering the displacements corresponding to these stresses, we encounter a challenge. The displacement at each boundary point is not just a simple macroscopic displacement but includes micro-scale variations, represented as $\mathbf{u}'(\mathbf{\Psi})$. These micro-fluctuations arise from the material's local heterogeneities and mean that the displacement at any specific point on the boundary cannot be directly set to a precise value without considering these variations. Since $\mathbf{u}'(\mathbf{\Psi})$ is generally not zero, the displacements at the boundary nodes include both the average displacement due to the uniform stress and these additional micro-fluctuations. As a result, directly prescribing exact displacement values for each boundary node is not feasible because it would ignore the micro-fluctuations present within the material. Instead, boundary conditions must be handled in a way that accommodates these variations while maintaining the overall uniform stress condition.

To ensure uniform boundary stress within the RVE, boundary displacements must be carefully managed. Due to the presence of micro-fluctuations in the displacement field, directly prescribing point-wise boundary displacements can introduce stress variations, conflicting with the objective of maintaining uniform stress. To address this issue, the vector $\mathbf{h}$,

which contains the unknowns associated with the Lagrange multipliers used to enforce the boundary conditions, is expressed in a specific interpolated form as

$$\mathbf{h} = \mathbf{H}^{\mathrm{T}}\mathbf{r}, \tag{3.43}$$

where

$$\mathbf{r} = \left\langle \begin{array}{cc} r_1 & r_2 \end{array} \right\rangle^{\mathrm{T}} \tag{3.44}$$

and

$$\mathbf{H} = \begin{bmatrix} 1 & 0 & 1 & 0 & \cdots & -1 & 0 & -1 & 0 \\ 0 & 1 & 0 & 1 & \cdots & 0 & -1 & 0 & -1 \end{bmatrix} \tag{3.45}$$

Eq. (3.43) expresses the vector $\mathbf{h}$ in terms of a transformation matrix $\mathbf{H}^{\mathrm{T}}$ and a vector $\mathbf{r}$. The role of this equation is to enforce a uniform traction boundary condition by ensuring that the boundary stress remains uniform. Physically, $\mathbf{h}$ is a vector of nodal displacement constraints (Lagrange multipliers) applied to the boundary nodes. It represents the correction terms needed to maintain a uniform stress condition at the boundary. The size of $\mathbf{h}$ is equal to the number of boundary degrees of freedom. Each entry in $\mathbf{h}$ corresponds to a constraint imposed at a specific boundary node. In simpler terms, $\mathbf{h}$ adjusts the nodal displacements such that the boundary stress remains uniform. In Eq. (3.44), $\mathbf{r}$ is a vector of unknown parameters that define the uniform traction condition. It contains two components, r_1 and r_2, which are the only independent unknowns needed to describe the uniform traction state. Physically, these unknowns represent the generalized forces (Lagrange multipliers) needed to balance the applied uniform traction at the boundary. Instead of prescribing nodal displacements explicitly, we solve for $\mathbf{r}$, which allows the traction to remain uniform across all boundary nodes. In Eq. (3.45), $\mathbf{H}$ is a projection (interpolation) matrix that maps the two independent unknowns r_1, r_2 to all boundary nodes. Regarding the structure of $\mathbf{H}$, the first row contains only $1, 0, -1, 0$ patterns, meaning that each pair of boundary nodes is coupled in the x - direction. The second row contains only $0, 1, 0, -1$ patterns, ensuring the same coupling in the y - direction. The way the matrix is built ensures that nodes are images of each other (on opposite sides). Also, the interpolation enforces that the total traction is evenly distributed across the boundary. In overall, equation (3.43) ensures that the boundary displacements adjust in a way that maintains uniform stress conditions. In-

stead of prescribing nodal displacements directly, the two unknowns r_1, r_2 govern the entire boundary behavior. The interpolation matrix $\mathbf{H}$ ensures that corresponding boundary nodes are properly coupled.

By substituting Eq. (3.43) into Eq. (3.13) and using Eqs. (3.24) and (3.25), we obtain the solution of the RVE problem as as shown in Appendix B.1.3

$$\begin{bmatrix} \mathbf{K}_{II} & \mathbf{K}_{IB} & \mathbf{0} \\ \mathbf{K}_{IB}{}^{\mathrm{T}} & \mathbf{K}_{BB} & \mathbf{S}_B{}^{\mathrm{T}}\mathbf{H}^{\mathrm{T}} \\ \mathbf{0} & \mathbf{H}\mathbf{S}_B & \mathbf{0} \end{bmatrix} \begin{Bmatrix} \mathbf{a}_I \\ \mathbf{a}_B \\ \mathbf{r} \end{Bmatrix} = \begin{Bmatrix} \mathbf{0} \\ \mathbf{0} \\ \mathbf{H}\boldsymbol{\Theta}\mathbf{g} \end{Bmatrix} \tag{3.46}$$

In the context of the equations and the uniform traction boundary condition discussed, $\mathbf{h}$ is the vector of Lagrange multipliers associated with the enforcement of boundary conditions. It ensures that these conditions are uniformly applied across the boundary nodes. Similarly, $\mathbf{a}_B$ represents the displacement vector for the boundary nodes, containing the displacement values for each node on the boundary of the RVE. Both $\mathbf{h}$ and $\mathbf{a}_B$ are specifically defined at the boundary nodes, which form a subset of the total nodes in the system and play an important role in defining the boundary conditions. When imposing the uniform traction boundary condition, all boundary nodes must satisfy the same stress constraints. Consequently, the number of Lagrange multipliers in $\mathbf{h}$ must correspond to the number of boundary displacement components in $\mathbf{a}_B$. The matrix $\mathbf{H}$ is introduced to couple the boundary nodes, ensuring that each pair of nodes, which are images of each other at the boundary, are treated collectively. This structure necessitates that the application of boundary conditions via $\mathbf{h}$ spans all boundary nodes, leading to $\mathbf{h}$ having the same number of elements as $\mathbf{a}_B$. From a physical perspective, each degree of freedom at the boundary, represented by $\mathbf{a}_B$, requires a corresponding Lagrange multiplier to impose the boundary condition effectively. Therefore, to maintain consistency in the enforcement of boundary conditions, the vectors $\mathbf{h}$ and $\mathbf{a}_B$ must have the same dimensions.

The algebraic form of the RVE problem in Eq. (3.46) represents the discrete system of equations governing the equilibrium of an RVE under uniform traction boundary conditions. Physically, the equation captures the mechanical response of the RVE, ensuring that both internal equilibrium and boundary traction constraints are satisfied. The first two rows enforce the mechanical equilibrium of internal ($\mathbf{a}_I$) and boundary ($\mathbf{a}_B$) displacement degrees of freedom. The third row enforces the uniform traction boundary condition, ensuring that

the boundary displacements satisfy a prescribed macroscopic stress state. Mathematically, the stiffness sub-matrices ($\mathbf{K}_{II}, \mathbf{K}_{IB}, \mathbf{K}_{BB}$) represent the mechanical interactions between internal and boundary nodes. The constraint terms ($\mathbf{S}_B, \mathbf{H}$) enforce the prescribed boundary conditions. The vector $\mathbf{r}$ introduces a reduced set of unknowns, simplifying the imposition of uniform traction conditions. In overall, this formulation (3.46) ensures a well-posed algebraic system where the unknown displacement field ($\mathbf{a}_I, \mathbf{a}_B$) and Lagrange multiplier-like term ($\mathbf{r}$) collectively satisfy the governing equations of the homogenized problem.

3.2.3 Periodic displacement RVE boundary conditions

In the context of periodic displacement RVE boundary conditions, the fine scale fluctuations of the displacement field at the boundary do not vanish, meaning that $\mathbf{u}'(\mathbf{\Psi}) \neq 0$. This indicates that the microstructural variations in displacement are significant and must be accounted for in the model. Despite these fluctuations, it is assumed that due to the periodic nature of the RVE, the displacement fluctuations at a point on one boundary are identical to the fluctuations at the corresponding point on the opposite boundary. Specifically, for a point $\mathbf{\Psi}^+ \in S^+_{RVE}$ on one boundary, the displacement fluctuation $\mathbf{u}'(\mathbf{\Psi}^+)$ is the same as the displacement fluctuation $\mathbf{u}'(\mathbf{\Psi}^-)$ at the corresponding point $\mathbf{\Psi}^- \in S^-_{RVE}$ on the opposite boundary. This periodic boundary condition implies that the microstructural displacement fluctuations repeat in a regular pattern across the boundaries of the RVE. This is essential for accurately modelling materials with periodic microstructures, ensuring that the finite RVE behaves as part of an infinite periodic material. The periodic displacement conditions maintain continuity and consistency in the displacement field across the boundaries, facilitating the correct simulation of the material's response to external loads and other conditions.

To impose periodic boundary conditions for the displacement field, we start by considering the fine-scale displacement fluctuations at corresponding points on opposite boundaries of the RVE. The condition $\mathbf{u}'(\mathbf{\Psi}^+) - \mathbf{u}'(\mathbf{\Psi}^-) = 0$ states that these fine-scale displacement fluctuations must be identical at paired points on the boundaries S^+_{RVE} and S^-_{RVE}. And, this leads us to the constraint for periodicity. The displacement field $\mathbf{u}(\mathbf{\Psi})$ at any point $\mathbf{\Psi}$ at the RVE boundary can be decomposed into three components as Eq. (3.32), where $\bar{\mathbf{u}}(\bar{\mathbf{y}})$ is the macroscopic displacement or average displacement at the reference point $\bar{\mathbf{y}}$. And, $(\mathbf{\Psi} - \bar{\mathbf{y}})^{\mathrm{T}}\mathbf{g}$ is the contribution due to the macroscopic displacement gradient $\mathbf{g}$. Also, $\mathbf{u}'(\mathbf{\Psi})$ is the fine-scale fluctuation of the displacement field. Under periodic boundary conditions,

the fine-scale fluctuations at paired points on the boundary should be identical as

$$\mathbf{u}'(\boldsymbol{\Psi}^{+}) = \mathbf{u}'(\boldsymbol{\Psi}^{-}) \tag{3.47}$$

And, this implies that

$$\mathbf{u}'\left(\boldsymbol{\Psi}^{+}\right) - \mathbf{u}'\left(\boldsymbol{\Psi}^{-}\right) = 0 \tag{3.48}$$

Then, we consider the displacement field at two paired points $\boldsymbol{\Psi}_k^{+}$ and $\boldsymbol{\Psi}_k^{-}$ on the opposite boundaries of the RVE as

$$\mathbf{u}\left(\boldsymbol{\Psi}_k^{+}\right) = \bar{\mathbf{u}}\left(\bar{\mathbf{y}}\right) + \left(\boldsymbol{\Psi}_k^{+} - \bar{\mathbf{y}}\right)^{\mathrm{T}}\mathbf{g} + \mathbf{u}'\left(\boldsymbol{\Psi}_k^{+}\right) \tag{3.49}$$

$$\mathbf{u}\left(\boldsymbol{\Psi}_k^{-}\right) = \bar{\mathbf{u}}\left(\bar{\mathbf{y}}\right) + \left(\boldsymbol{\Psi}_k^{-} - \bar{\mathbf{y}}\right)^{\mathrm{T}}\mathbf{g} + \mathbf{u}'\left(\boldsymbol{\Psi}_k^{-}\right) \tag{3.50}$$

Then, by subtracting the displacement at $\boldsymbol{\Psi}_k^{-}$ from that at $\boldsymbol{\Psi}_k^{+}$

$$\mathbf{u}\left(\boldsymbol{\Psi}_k^{+}\right) - \mathbf{u}\left(\boldsymbol{\Psi}_k^{-}\right) = \left[\bar{\mathbf{u}}\left(\bar{\mathbf{y}}\right) + \left(\boldsymbol{\Psi}_k^{+} - \bar{\mathbf{y}}\right)^{\mathrm{T}}\mathbf{g} + \mathbf{u}'\left(\boldsymbol{\Psi}_k^{+}\right)\right] - \left[\bar{\mathbf{u}}\left(\bar{\mathbf{y}}\right) + \left(\boldsymbol{\Psi}_k^{-} - \bar{\mathbf{y}}\right)^{\mathrm{T}}\mathbf{g} + \mathbf{u}'\left(\boldsymbol{\Psi}_k^{-}\right)\right] \tag{3.51}$$

Since the macroscopic displacement $\bar{\mathbf{u}}(\bar{\mathbf{y}})$ is the same for both points, it cancels out. Also, by periodicity, $\mathbf{u}'\left(\boldsymbol{\Psi}_k^{+}\right) = \mathbf{u}'\left(\boldsymbol{\Psi}_k^{-}\right)$, we get

$$\mathbf{u}\left(\boldsymbol{\Psi}_k^{+}\right) - \mathbf{u}\left(\boldsymbol{\Psi}_k^{-}\right) = \left[\left(\boldsymbol{\Psi}_k^{+} - \bar{\mathbf{y}}\right)^{\mathrm{T}}\mathbf{g} - \left(\boldsymbol{\Psi}_k^{-} - \bar{\mathbf{y}}\right)^{\mathrm{T}}\mathbf{g}\right] \tag{3.52}$$

Then, the constraint for the periodicity condition can be introduced in the form of

$$\mathbf{u}\left(\boldsymbol{\Psi}_k^{+}\right) - \mathbf{u}\left(\boldsymbol{\Psi}_k^{-}\right) = \left(\boldsymbol{\Psi}_k^{+} - \boldsymbol{\Psi}_k^{-}\right)^{\mathrm{T}}\mathbf{g} \tag{3.53}$$

In Eq. (3.53), the term $\mathbf{u}\left(\boldsymbol{\Psi}_k^{+}\right)$ represents the displacement vector at the boundary point $\boldsymbol{\Psi}_k^{+}$, which corresponds to a specific point k on one side of the RVE boundary, denoted as S_{RVE}^{+}. Similarly, $\mathbf{u}\left(\boldsymbol{\Psi}_k^{-}\right)$ represents the displacement vector at the corresponding boundary point $\boldsymbol{\Psi}_k^{-}$, located on the opposite side of the RVE boundary, S_{RVE}^{-}. The difference

between these displacement vectors, $\mathbf{u}\left(\mathbf{\Psi}_k^+\right) - \mathbf{u}\left(\mathbf{\Psi}_k^-\right)$, quantifies the relative displacement between the paired boundary points $\mathbf{\Psi}_k^+$ and $\mathbf{\Psi}_k^-$. For a perfectly periodic structure, this displacement difference should arise solely from the macroscopic deformation of the material. Additionally, the term $\left(\mathbf{\Psi}_k^+ - \mathbf{\Psi}_k^-\right)^{\mathrm{T}}$ represents the transpose of the matrix difference between the coordinates of the paired boundary points. This matrix characterizes the spatial separation between the two corresponding points on opposite boundaries of the RVE. The macroscopic displacement gradient tensor, $\mathbf{g}$, describes the overall deformation applied to the RVE and determines how the macroscopic displacement field varies spatially across the domain. Overall, Eq. (3.53) ensures that the displacement field across the RVE boundary remains consistent with periodic boundary conditions. It guarantees that any displacement difference between paired boundary points arises solely from the imposed macroscopic deformation, thereby preserving the periodicity of the displacement field.

The concept of anti-periodic boundary traction is fundamental to understanding material behavior under periodic boundary conditions. In this framework, the boundary tractions (forces per unit area) at paired points on opposite sides of the boundary exhibit an anti-symmetric relationship. Specifically, the traction vectors acting on corresponding nodes across the boundary are equal in magnitude but opposite in direction. Mathematically, this anti-periodicity condition is expressed as

$$\boldsymbol{\lambda}^+ = -\boldsymbol{\lambda}^- \tag{3.54}$$

where $\boldsymbol{\lambda}^+$ and $\boldsymbol{\lambda}^-$ represent the traction vectors at boundary nodes $\mathbf{\Psi}^+ \in S_{RVE}^+$ and $\mathbf{\Psi}^- \in S_{RVE}^-$, respectively. The boundary traction $\boldsymbol{\lambda}$ corresponds to the forces per unit area acting on the surface nodes of the RVE, arising due to external loads or internal stresses. The nodes $\mathbf{\Psi}^+$ and $\mathbf{\Psi}^-$ are paired such that each point on one side of the boundary has a corresponding counterpart on the opposite side. From a physical perspective, this condition ensures force balance at the RVE boundary, maintaining mechanical equilibrium. For instance, if a node on one side of the boundary experiences a traction force in a given direction, the corresponding node on the opposite side experiences an equal force in the opposite direction. This anti-periodicity is important for preserving the periodic nature of the RVE, ensuring that internal stresses and deformations accurately reflect the material's microstructural response under applied loads. By enforcing anti-periodic boundary traction, the model effec-

tively captures the transmission of forces across the RVE boundaries in a manner consistent with the periodicity of the material.

By using anti-periodicity of the traction Eq. (3.54), the stress can be represented in a way that respects this anti-periodic condition at the boundary nodes. Instead of treating the traction at each boundary node separately, we can reduce the number of unknowns by recognizing that each pair of opposite nodes contributes only one independent degree of freedom. To achieve this, we introduce the vector $\mathbf{w}$, which represents the reduced degrees of freedom for the boundary stress. The relationship between the original boundary stress vector $\mathbf{h}$ and the reduced vector $\mathbf{w}$ is given by

$$\mathbf{h} = \mathbf{P}^{\mathrm{T}}\mathbf{w}, \tag{3.55}$$

where

$$\mathbf{P} = \begin{bmatrix} 1 & 0 & \cdots & 0 & \cdots & -1 & 0 & 0 & \cdots & 0 \\ 0 & 1 & \cdots & 0 & \cdots & 0 & -1 & 0 & \cdots & 0 \\ \vdots & \vdots & \ddots & \ddots & \vdots & \vdots & \vdots & \ddots & & \\ 0 & 0 & \cdots & 1 & \cdots & 0 & 0 & 0 & \cdots & -1 \end{bmatrix} \tag{3.56}$$

This equation (3.55) essentially maps the reduced number of unknowns ($\mathbf{w}$) to the full boundary stress vector ($\mathbf{h}$). The matrix $\mathbf{P}$ is a mapping matrix that enforces the anti-periodic condition. It ensures that every node $\mathbf{\Psi}^{+}$ on one boundary has a corresponding opposite node $\mathbf{\Psi}^{-}$, and their contributions are properly accounted for. Each row corresponds to a single pair of opposite nodes. Each row has only two non-zero values. $+1$ at the location of the node on one boundary. And, -1 at the location of the corresponding node on the opposite boundary. As an example interpretation, suppose we have a simple 2D case with 4 boundary nodes. Nodes 1 and 3 are opposite pairs in the x-direction. Nodes 2 and 4 are opposite pairs in the y-direction. Then, $\mathbf{P}$ would look like

$$\mathbf{P} = \begin{bmatrix} 1 & 0 & -1 & 0 \\ 0 & 1 & 0 & -1 \end{bmatrix} \tag{3.57}$$

This means that the first equation enforces that the x - direction force on node 1 is the negative of node 3. The second equation enforces that the y - direction force on node 2 is

the negative of node 4. In overall, this expression (3.55) reduces the number of independent unknowns, making the system easier to solve. The matrix multiplication $\mathbf{P}^{\mathrm{T}}\mathbf{w}$ reconstructs the full boundary stress while ensuring the anti-periodicity condition is satisfied. By using this formulation, we can integrate the periodic boundary condition into the algebraic system efficiently.

By substituting Eq. (3.55) into Eq. (3.13) and using Eqs. (3.24) and (3.25), we obtain the solution of the RVE problem as as shown in Appendix B.1.4

$$\begin{bmatrix} \mathbf{K}_{II} & \mathbf{K}_{IB} & \mathbf{0} \\ \mathbf{K}_{IB}{}^{\mathrm{T}} & \mathbf{K}_{BB} & \mathbf{S}_B{}^{\mathrm{T}}\mathbf{P}^{\mathrm{T}} \\ \mathbf{0} & \mathbf{P}\mathbf{S}_B & \mathbf{0} \end{bmatrix} \begin{Bmatrix} \mathbf{a}_I \\ \mathbf{a}_B \\ \mathbf{w} \end{Bmatrix} = \begin{Bmatrix} \mathbf{0} \\ \mathbf{0} \\ \mathbf{P}\boldsymbol{\Theta}\mathbf{g} \end{Bmatrix} \tag{3.58}$$

Physically, Eq. (3.58) represents the finite element discretization of the Representative Volume Element (RVE) problem under periodic displacement boundary conditions. This equation ensures equilibrium, displacement compatibility, and periodicity within the system. The first row enforces equilibrium at the interior (bulk) nodes by ensuring that the net force at these nodes sums to zero. The second row governs equilibrium at the boundary nodes while incorporating periodic constraints through the Lagrange multipliers $\mathbf{w}$, which act as reaction forces maintaining periodicity. The third row imposes the periodicity constraint, ensuring that the displacements at opposite boundary nodes conform to the macroscopic deformation gradient $\mathbf{g}$. Collectively, these conditions guarantee that the RVE accurately represents the macroscopic material response under periodic loading conditions. Mathematically, Eq. (3.58) defines a coupled algebraic system that enforces static equilibrium through the stiffness matrices $\mathbf{K}_{II}, \mathbf{K}_{IB}, \mathbf{K}_{BB}$, which describe the force-displacement relationships of the interior and boundary nodes. Periodic boundary constraints are imposed using the matrix $\mathbf{P}$, which establishes the correspondence between displacements of periodic boundary node pairs. Additionally, periodicity is enforced through the Lagrange multipliers $\mathbf{w}$, introduced via the constraint term $\mathbf{S}_B^{\mathrm{T}}\mathbf{P}^{\mathrm{T}}$, ensuring that the system adheres to the required periodic conditions.

The last row in Eq. (3.58) can be interpreted as the imposition of the constraint in Eq. (3.53) and introduces the jump displacement constraint. For periodic boundary conditions in an RVE, the displacement jump across corresponding points on the periodic boundaries S^{+}_{RVE} and S^{-}_{RVE} is related to the macroscopic strain. This jump is expressed as Eq.

(3.53). This equation enforces periodic displacement constraints by ensuring that opposite boundary displacements correspond to macroscopic deformation. In a finite element setting, the displacement field is interpolated using shape functions and nodal displacements. For boundary nodes

$$\mathbf{u}(\mathbf{\Psi}) = \mathbf{A}\mathbf{a}_B \tag{3.59}$$

where, $\mathbf{A}$ is the shape function matrix. $\mathbf{a}_B$ is the vector of boundary nodal displacements. Since we are dealing with periodic boundaries, we partition $\mathbf{A}$ as

$$\mathbf{A}^{\mathrm{T}} = \begin{bmatrix} \mathbf{A}^{+\mathrm{T}} & \mathbf{A}^{-\mathrm{T}} \end{bmatrix} \tag{3.60}$$

where $\mathbf{A}^+$ and $\mathbf{A}^-$ are related to the nodes at the relevant half of the boundary at ${S_{RVE}}^+$ and ${S_{RVE}}^-$, respectively. We define $\mathbf{A}_{\text{half}} = \mathbf{A}^+ = \mathbf{A}^-$, simplifying the notation. Thus, the displacement jump can be rewritten as

$$\mathbf{u}(\mathbf{\Psi}^+) - \mathbf{u}(\mathbf{\Psi}^-) = \mathbf{A}_{\text{half}}(\mathbf{a}_B^+ - \mathbf{a}_B^-) \tag{3.61}$$

which expresses the displacement jump in terms of nodal displacements on the periodic boundaries. By Comparing the periodic boundary condition (3.53) with this expression (3.61), we get

$$\mathbf{A}_{\text{half}}(\mathbf{a}_B^+ - \mathbf{a}_B^-) = (\mathbf{\Psi}^+ - \mathbf{\Psi}^-)^{\mathrm{T}}\mathbf{g} \tag{3.62}$$

which shows how the displacement jump is directly related to the macroscopic deformation. Then, the periodicity matrix $\mathbf{P}$ is introduced to relate the full boundary nodal displacement vector $\mathbf{a}_B$ to the displacement difference across periodic boundaries as

$$\mathbf{P}\mathbf{a}_B = \mathbf{a}_B^+ - \mathbf{a}_B^-$$

Here, the matrix $\mathbf{P}$ is a selection and difference operator that extracts and subtracts corresponding nodal displacements from opposite periodic boundaries. It ensures that the periodic nodes are paired correctly, allowing the displacement jump to be computed au-

tomatically. Thus, we can rewrite the displacement jump equation (3.62) as

$$\mathbf{A}_{\text{half}}\mathbf{P}\mathbf{a}_B = (\mathbf{\Psi}^+ - \mathbf{\Psi}^-)^{\mathrm{T}}\mathbf{g} \tag{3.63}$$

This expresses the displacement jump in terms of the periodicity matrix $\mathbf{P}$, ensuring that periodic boundary conditions are satisfied. On the right-hand side of the equation (3.62), we observe that $(\mathbf{\Psi}^+ - \mathbf{\Psi}^-)^{\mathrm{T}}\mathbf{g}$ is a direct consequence of periodicity, meaning that the position difference between opposite nodes can also be expressed using $\mathbf{P}$ as

$$(\mathbf{\Psi}^+ - \mathbf{\Psi}^-)^{\mathrm{T}}\mathbf{g} = \mathbf{P}\mathbf{\Psi}^{\mathrm{T}}\mathbf{g} \tag{3.64}$$

Thus, substituting this (3.64) into our equation (3.63) gives

$$\mathbf{A}_{\text{half}}\mathbf{P}\mathbf{a}_B = \mathbf{P}\mathbf{\Psi}^{\mathrm{T}}\mathbf{g} \tag{3.65}$$

This equation shows how the displacement jump is governed by the macroscopic strain while maintaining periodicity through $\mathbf{P}$. In the integral formulation, we can express the previous as

$$\begin{aligned}
&\int_{S_{RVE}} \delta\boldsymbol{\lambda}\left(\mathbf{u} - \mathbf{\Psi}^{\mathrm{T}}\mathbf{g}\right)\mathrm{d}\Psi \\
&= \delta\mathbf{w}^{\mathrm{T}}\mathbf{P}\int_{S_{RVE}} \mathbf{G}^{\mathrm{T}}\left(\mathbf{A}\mathbf{a}_B - \mathbf{\Psi}^{\mathrm{T}}\mathbf{g}\right)\mathrm{d}\Psi \\
&= \delta\mathbf{h}^{\mathrm{T}}\left[\int_{S_{RVE}} \mathbf{G}^{\mathrm{T}}\left(\mathbf{A}\mathbf{a}_B^+ - \mathbf{\Psi}^{+\mathrm{T}}\mathbf{g}\right)\mathrm{d}\Psi + \int_{S_{RVE}} \mathbf{G}^{\mathrm{T}}\left(\mathbf{A}\mathbf{a}_B^- - \mathbf{\Psi}^{-\mathrm{T}}\mathbf{g}\right)\mathrm{d}\Psi\right] \\
&= \delta\mathbf{h}^{\mathrm{T}}\int_{S_{RVE}} \mathbf{G}^{\mathrm{T}}\underbrace{\left(\mathbf{A}_{\text{half}}\,\mathbf{P}\mathbf{a}_B - \mathbf{P}\mathbf{\Psi}^{\mathrm{T}}\mathbf{g}\right)}_{\text{Strong condition}}\mathrm{d}\Psi
\end{aligned} \tag{3.66}$$

Eq. (3.65) enforces the periodic displacement boundary conditions (strong condition) in terms of the finite element shape functions. If we apply the integral operator $\int_{S_{RVE}} \mathbf{G}^{\mathrm{T}}(\cdot)\,\mathrm{d}\Psi$

to both sides of this equation, we obtain

$$\int_{S_{RVE}} \mathbf{G}^{\mathrm{T}} \mathbf{A}_{\text{half}} \mathbf{P} \mathbf{a}_B \, \mathrm{d}\Psi = \int_{S_{RVE}} \mathbf{G}^{\mathrm{T}} \mathbf{P} \boldsymbol{\Psi}^{\mathrm{T}} \mathbf{g} \, \mathrm{d}\Psi \tag{3.67}$$

By recognizing that $\mathbf{S}_B$ and $\boldsymbol{\Theta}$ are defined as Eqs. (3.15) and (3.16) and assuming that the integral operator and $\mathbf{P}$ commute (i.e., periodicity is maintained under integration), we can rewrite the integrals as

$$\mathbf{P} \mathbf{S}_B \mathbf{a}_B = \mathbf{P} \boldsymbol{\Theta} \mathbf{g} \tag{3.68}$$

Thus, the periodic transformation remains valid at the integral level, confirming that the two expressions are equivalent as

$$\mathbf{A}_{\text{half}} \mathbf{P} \mathbf{a}_B = \mathbf{P} \boldsymbol{\Psi}^{\mathrm{T}} \mathbf{g} \quad \Leftrightarrow \quad \mathbf{P} \mathbf{S}_B \mathbf{a}_B = \mathbf{P} \boldsymbol{\Theta} \mathbf{g} \tag{3.69}$$

In overall, these two formulations are equivalent, since $\mathbf{S}_B$ and $\boldsymbol{\Theta}$ are derived by integrating the shape function matrix $\mathbf{A}$ and the position matrix $\boldsymbol{\Psi}^{\mathrm{T}}$ with $\mathbf{G}^{\mathrm{T}}$, respectively. This integral transformation preserves the periodic structure enforced by $\mathbf{P}$. Finally, we can express Eq. (3.53) as

$$\mathbf{u}\left(\boldsymbol{\Psi}_k^+\right) - \mathbf{u}\left(\boldsymbol{\Psi}_k^-\right) = \mathbf{A}_{\text{half}} \left(\mathbf{a}_B^+ - \mathbf{a}_B^-\right) = \left(\boldsymbol{\Psi}^+ - \boldsymbol{\Psi}^-\right)^{\mathrm{T}} \mathbf{g} = \mathbf{A}_{\text{half}} \mathbf{P} \mathbf{a}_B = \mathbf{P} \boldsymbol{\Psi}^{\mathrm{T}} \mathbf{g} \tag{3.70}$$

This equation expresses the periodic displacement constraint imposed on the RVE for computational homogenization. It enforces the continuity and periodicity of the displacement field across periodic boundaries, ensuring that the microscale problem is well-posed for extracting effective material properties. Physically, it expresses the displacement jump across opposite periodic boundaries of the RVE. The displacement difference between corresponding points $\boldsymbol{\Psi}_k^+$ and $\boldsymbol{\Psi}_k^-$ on opposite sides of the RVE must satisfy the periodicity condition. In overall, this equation mathematically enforces periodic boundary conditions in the RVE by linking microscopic boundary displacements to macroscopic strain fields using shape functions and the periodicity matrix.

3.3 Interpolation of displacement and Lagrange multiplier

The displacement field $\mathbf{u}$ is expressed in terms of two components: a continuous component and a discontinuous component. This is particularly useful in problems involving discontinuities such as cracks or interfaces within the material. The expression for the displacement field is given by

$$\mathbf{u} = \mathbf{N}\mathbf{d} + \mathbf{H}|_{\Gamma_{DI}} \mathbf{N}\boldsymbol{\beta} \tag{3.71}$$

Where, $\mathbf{N}$ is the matrix of the standard finite-element shape functions. And, $\mathbf{d}$ is the column vector of nodal displacement values. And, $\mathbf{H}|_{\Gamma_{DI}}$ is the vector of Heaviside functions evaluated at the discontinuity interface Γ_{DI}. And, $\boldsymbol{\beta}$ is the vector of enriched degrees of freedom.

In continuous component of Eq. (3.71), $\mathbf{N}\mathbf{d}$ represents the continuous part of the displacement field using standard finite-element interpolation. Here, $\mathbf{N}$ is the shape function matrix and $\mathbf{d}$ is the vector of nodal displacements. For a bilinear quadrilateral element, the shape function matrix $\mathbf{N}$ at the element level is defined as

$$\mathbf{N} = \begin{bmatrix} N_1 & 0 & N_2 & 0 & N_3 & 0 & N_4 & 0 \\ 0 & N_1 & 0 & N_2 & 0 & N_3 & 0 & N_4 \end{bmatrix} \tag{3.72}$$

This matrix represents the interpolation of the displacement field within a quadrilateral finite element using bilinear shape functions. A bilinear quadrilateral element has four nodes, each associated with a shape function N_i (for $i = 1, 2, 3, 4$). These shape functions are used to interpolate the displacement field within the element. The shape functions N_i are typically functions of the local coordinates (ξ, η) of the element. In terms of structure of the matrix $\mathbf{N}$, the matrix $\mathbf{N}$ is constructed to interpolate the displacement components in both the x- and y-directions. The matrix has two rows because we are considering displacements in two directions (x and y). Each row corresponds to one of the displacement components (u and v). In the first row (Interpolation of u - Component (Displacement in x-Direction)),

$$\begin{pmatrix} N_1 & 0 & N_2 & 0 & N_3 & 0 & N_4 & 0 \end{pmatrix}$$

Here, N_1 is the shape function for node 1 in the u-direction. 0 is the place holder for the v-direction at node 1. And, N_2 is the shape function for node 2 in the u-direction. 0 is the place holder for for the v-direction at node 2. And, N_3 is the shape function for node 3 in the u-direction. 0 is the place holder for the v-direction at node 3. And, N_4 is the shape function for node 4 in the u-direction. 0 is the place holder for the v-direction at node 4. In the second row (Interpolation of v - Component (Displacement in y-Direction)),

$$\begin{pmatrix} 0 & N_1 & 0 & N_2 & 0 & N_3 & 0 & N_4 \end{pmatrix}$$

Here, 0 is the place holder for the u-direction at node 1. N_1 is the shape function for node 1 in the v-direction. And, 0 is the place holder for the u-direction at node 2. N_2 is the shape function for node 2 in the v-direction. And, 0 is the place holder for the u-direction at node 3. N_3 is the shape function for node 3 in the v-direction. And, 0 is the place holder for the u-direction at node 4. N_4 is the shape function for node 4 in the v-direction.

In Eq. (3.72), the shape function matrix $\mathbf{N}$ is used to interpolate the displacement field within the element. When multiplied by the vector of nodal displacements $\mathbf{d}$, it provides the displacement at any point within the element. This interpolation is important in finite element analysis to obtain the continuous displacement field from discrete nodal values. By organizing the shape functions in this manner, the matrix $\mathbf{N}$ efficiently handles the interpolation for both displacement components (u and v) in a bilinear quadrilateral element, ensuring that the displacement field is accurately represented within the element.

In terms of nodal displacement vector $\mathbf{d}$ in Eq. (3.71), the vector $\mathbf{d}$ represents the displacements of the nodes in a finite element, specifically for a bilinear quadrilateral element. This vector is organized in a manner that includes both x- and y-direction displacements for each node. In terms of the structure of $\mathbf{d}$, the nodal displacement vector $\mathbf{d}$ is written as

$$\mathbf{d} = \left\langle \begin{array}{cccccccc} d_{11} & d_{12} & d_{21} & d_{22} & d_{31} & d_{32} & d_{41} & d_{42} \end{array} \right\rangle^{\mathrm{T}} \tag{3.73}$$

Here, d_{ij} represents the displacement at node i in the j-direction. And, i ranges from 1 to 4 (since there are four nodes in the bilinear quadrilateral element). j is either 1 or 2, representing the x- and y-direction displacements, respectively. In terms of components, d_{11} is the displacement in the x-direction at node 1. d_{12} is the displacement in the y-direction

at node 1. d_{21} is the displacement in the x-direction at node 2. d_{22} is the displacement in the y-direction at node 2. d_{31} is the displacement in the x-direction at node 3. d_{32} is the displacement in the y-direction at node 3. d_{41} is the displacement in the x-direction at node 4. d_{42} is the displacement in the y-direction at node 4. Furthermore, in Eq. (3.73), the vector $\mathbf{d}$ is organized by grouping the displacements of each node sequentially. First, the displacements for node 1 in both x- and y-directions are listed. Next, the displacements for node 2 in both x- and y-directions are listed. This pattern continues for nodes 3 and 4. Also, the notation $\langle \cdots \rangle^{\mathrm{T}}$ indicates that the values inside the brackets are transposed to form a column vector. Thus, $\mathbf{d}$ is a column vector with 8 entries (since there are 4 nodes, each with 2 displacement components). Moreover, the vector $\mathbf{d}$ is essential in finite element analysis as it represents the degrees of freedom for the displacement field within an element. When multiplied by the shape function matrix $\mathbf{N}$, it helps interpolate the displacement field inside the element. This interpolation allows the calculation of displacements, strains, and stresses at any point within the element based on the nodal values.

In discontinuous component of Eq. (3.71), $\mathbf{H}|_{\Gamma_{DI}}\,\mathbf{N}\boldsymbol{\beta}$ accounts for the discontinuous part of the displacement field across the interface Γ_{DI}. Here, Γ_{DI} represents a discontinuity interface within the finite element domain. This could be a crack, a material interface, or any other type of physical discontinuity where the displacement field is expected to have a jump or discontinuity. And, the Heaviside function $\mathbf{H}$ is a step function that is commonly used to model discontinuities. In the context of finite element analysis, the Heaviside function is used to capture the sudden change in displacement across the discontinuity interface. The notation $\mathbf{H}|_{\Gamma_{DI}}$ indicates that the Heaviside function is evaluated specifically at the discontinuity interface Γ_{DI}. This implies that the vector $\mathbf{H}$ is tailored to capture the behaviour of the displacement field right at the interface where the discontinuity occurs. In the context of the displacement interpolation with a jump, $\mathbf{H}|_{\Gamma_{DI}}$ plays a important role. It modifies the standard displacement interpolation to account for the discontinuity by introducing additional degrees of freedom. When multiplied by the vector of enriched degrees of freedom $\boldsymbol{\beta}$, it effectively introduces a term in the displacement field that represents the jump across Γ_{DI}. Furthermore, in discontinuous component of Eq. (3.71), in the context of finite element methods, especially when dealing with discontinuities like cracks or interfaces, standard degrees of freedom (displacements at nodes) are sometimes insufficient to accurately represent the displacement field near discontinuities. So, we use enriched degrees of freedom, which are additional parameters introduced to capture the complex behaviour of the dis-

placement field near discontinuities. Here, the vector $\boldsymbol{\beta}$ is used to collectively represent all the enriched degrees of freedom in the system. It extends the standard displacement degrees of freedom to include the effects of discontinuities. The vector $\boldsymbol{\beta}$ is given as

$$\boldsymbol{\beta} = \left\langle \begin{array}{cccccccc} \beta_{11} & \beta_{12} & \beta_{21} & \beta_{22} & \beta_{31} & \beta_{32} & \beta_{41} & \beta_{42} \end{array} \right\rangle^{\mathrm{T}} \tag{3.74}$$

Here, β_{ij} represents the enriched degree of freedom associated with node i in the j-th direction. This vector is arranged such that β_{11} and β_{12} correspond to the enriched degrees of freedom in the x- and y-directions for node 1. And, β_{21} and β_{22} correspond to the enriched degrees of freedom in the x- and y-directions for node 2. Similarly, β_{31}, β_{32}, β_{41}, and β_{42} correspond to nodes 3 and 4. Furthermore, each component β_{ij} can be thought of as an additional parameter that allows the finite element model to represent jumps or discontinuities in the displacement field at the corresponding node. These enriched degrees of freedom are particularly important in the surrounding areas of cracks or material interfaces where the displacement field may exhibit abrupt changes that standard degrees of freedom alone cannot capture.

In the context of finite element analysis, the displacement field $\mathbf{u}$ is expressed in terms of interpolation functions and nodal values. For complex problems involving discontinuities, such as cracks or material interfaces, the displacement field can be enriched with additional degrees of freedom to better capture the behaviour near these discontinuities. The general form for the displacement field $\mathbf{u}$ is given in Eq. (3.11) as $\mathbf{u} = \mathbf{A}\mathbf{a}$. Here, $\mathbf{u}$ represents the displacement field, $\mathbf{A}$ is a matrix containing the interpolation functions, and $\mathbf{a}$ is a vector of unknown parameters, which includes both the standard and enriched degrees of freedom. Now, the matrix $\mathbf{A}$ can be written for one element as

$$\mathbf{A} = \begin{bmatrix} \mathbf{N} & \mathbf{H}|_{\Gamma_{DI}}\,\mathbf{N} \end{bmatrix} \tag{3.75}$$

Here, this matrix $\mathbf{N}$ contains the standard finite element shape functions. For a bilinear quadrilateral element, $\mathbf{N}$ is structured to interpolate the displacement at the nodes of the element. This term $\mathbf{H}|_{\Gamma_{DI}}\,\mathbf{N}$ represents the enrichment of the displacement field. $\mathbf{H}|_{\Gamma_{DI}}$ is the vector of Heaviside functions defined at the discontinuity interface Γ_{DI}. The product $\mathbf{H}|_{\Gamma_{DI}}\,\mathbf{N}$ enriches the standard shape functions to account for the discontinuity. Now, the

vector $\mathbf{a}$ can be written for one element as

$$\mathbf{a}^{\mathrm{T}} = \left\langle \begin{array}{cc} \mathbf{d}^{\mathrm{T}} & \boldsymbol{\beta}^{\mathrm{T}} \end{array} \right\rangle \tag{3.76}$$

Here, $\mathbf{d}$ is the column vector of nodal displacement values, representing the standard degrees of freedom. For a bilinear quadrilateral element, $\mathbf{d}$ contains the displacements at the four nodes of the element in both x- and y-directions. This vector $\boldsymbol{\beta}$ contains the enriched degrees of freedom, which are additional parameters introduced to accurately represent the displacement field near discontinuities. Now, combining the standard and enriched components, the displacement field $\mathbf{u}$ for one element can be written as

$$\mathbf{u} = \mathbf{A}\mathbf{a} = \left[\begin{array}{cc} \mathbf{N} & \mathbf{H}|_{\Gamma_{DI}}\mathbf{N} \end{array} \right] \left[\begin{array}{c} \mathbf{d} \\ \boldsymbol{\beta} \end{array} \right] \tag{3.77}$$

This formulation allows the finite element model to capture both the continuous part of the displacement field and the discontinuities effectively. The matrix $\mathbf{A}$ incorporates both the standard shape functions and their enriched counterparts, while the vector $\mathbf{a}$ includes all the necessary degrees of freedom to describe the displacement field accurately. By incorporating both standard and enriched degrees of freedom, this approach provides a more comprehensive representation of the displacement field, especially in regions with discontinuities. This results in a more accurate and robust finite element analysis, capable of capturing complex behaviours that would otherwise be missed with standard shape functions alone.

In finite element analysis, boundary conditions play a important role in defining how the structure or material interacts with its environment. When dealing with problems involving discontinuities, such as cracks or interfaces between different materials, the handling of boundary conditions requires careful consideration. The constraints related to boundary conditions are applied to the standard nodal displacement values, denoted by $\mathbf{d}$. And, $\mathbf{d}$ represents the vector of displacements at the nodes of the finite element mesh. These displacements are the primary degrees of freedom in a standard finite element analysis without enrichment. The enriched degrees of freedom, denoted by $\boldsymbol{\beta}$, are introduced to capture the displacement discontinuities at interfaces within the material or structure. And, $\boldsymbol{\beta}$ contains additional parameters that enhance the standard finite element shape functions to accurately

represent discontinuities in the displacement field. The boundary conditions are applied only to the standard nodal displacements $\mathbf{d}$, not to the enriched degrees of freedom $\boldsymbol{\beta}$. This means that the specified displacements or forces at the boundaries of the finite element model are imposed on the standard nodal displacement values. And, the enriched degrees of freedom are free to adjust to capture the displacement discontinuities without being directly constrained by the boundary conditions. By this way, the enriched degrees of freedom are specifically designed to handle displacement discontinuities, such as jumps or cracks, within the material or structure. Constraining these enriched degrees of freedom could interfere with their ability to accurately represent the discontinuities. Therefore, they are left unconstrained to allow for a more accurate and flexible representation of the displacement field near discontinuities.

In finite element analysis, shape functions are used to interpolate the values of field variables, such as displacement, within an element. For a bilinear quadrilateral element, these shape functions are defined in terms of local coordinates. The element under consideration is a bilinear quadrilateral, which is a common type of element used in finite element analysis. And, the size of this element is 2×2 shown in Figure 3.2b, indicating that the element spans from -1 to 1 in both the ξ and ζ directions. These are the local coordinates used to define the shape functions. The shape functions N_1, N_2, N_3, N_4 are used to interpolate the values of field variables within the element. These functions depend on the local coordinates ξ and ζ. Furthermore, the local coordinates ξ and ζ range from -1 to 1. These coordinates are used to define the position within the parent element. In terms of shape functions, N_1 is the shape function associated with the node at $(\xi, \zeta) = (-1, -1)$. And, the formula for N_1 is

$$N_1 = \frac{(1-\xi)(1-\zeta)}{4} \tag{3.78}$$

This function is 1 at $(\xi, \zeta) = (-1, -1)$ and 0 at all other nodes of the element. Then, N_2 is the shape function associated with the node at $(\xi, \zeta) = (1, -1)$. The formula for N_2 is

$$N_2 = \frac{(1+\xi)(1-\zeta)}{4} \tag{3.79}$$

This function is 1 at $(\xi, \zeta) = (1, -1)$ and 0 at all other nodes of the element. Then, N_3 is the

shape function associated with the node at $(\xi, \zeta) = (1, 1)$. And, the formula for N_3 is

$$N_3 = \frac{(1+\xi)(1+\zeta)}{4} \tag{3.80}$$

This function is 1 at $(\xi, \zeta) = (1, 1)$ and 0 at all other nodes of the element. Then, N_4 is the shape function associated with the node at $(\xi, \zeta) = (-1, 1)$. And, the formula for N_4 is

$$N_4 = \frac{(1-\xi)(1+\zeta)}{4} \tag{3.81}$$

This function is 1 at $(\xi, \zeta) = (-1, 1)$ and 0 at all other nodes of the element. These shape functions are used to interpolate the displacements or other field variables across the element by weighting the contributions from each node based on their respective shape functions. Each shape function is designed to be 1 at its corresponding node and 0 at all other nodes, ensuring accurate interpolation within the element.

In finite element analysis within the RVE, local coordinates (z_1, z_2) are used for each element to simplify interpolation and integration processes. These local coordinates range from -1 to 1, making it straightforward to define shape functions and perform numerical integration. The RVE itself is situated in a global coordinate system $\mathbf{y} \in \bar{V}_{RVE}$, where $\bar{V}_{RVE}$ represents the closure of the RVE domain. The closure $\bar{V}_{RVE}$ includes all points within the RVE domain and its boundary. This notation is important for defining integrals and boundary conditions over the entire RVE, ensuring that both interior and boundary effects are considered. And, $\mathbf{y}$ represents the global coordinates in the RVE coordinate system. This dual coordinate system allows for precise calculations at the element level using local coordinates while accurately positioning these elements within the entire RVE using global coordinates. Figure 3.1 would typically illustrate this relationship, showing how local coordinates within each finite element map to the global coordinates of the RVE, ensuring that local computations integrate seamlessly into the global analysis.

The displacement jump at the discontinuity interface Γ_{DI} can be written as

$$[[\mathbf{u}]] = \mathbf{N}|_{\Gamma_{DI}} \boldsymbol{\beta} \tag{3.82}$$

In standard finite element analysis (FEM), the displacement field $\mathbf{u}$ is assumed to be continuous within an element. However, in the XFEM, discontinuities such as cracks or material interfaces are introduced. A displacement jump $[[\mathbf{u}]]$ occurs at these discontinuities, representing the difference in displacement across the interface. Mathematically, the displacement jump is expressed as

$$[[\mathbf{u}]] = \mathbf{u}^{+} - \mathbf{u}^{-} \tag{3.83}$$

where $\mathbf{u}^{+}$ is the displacement on one side of the interface. $\mathbf{u}^{-}$ is the displacement on the other side. The term $[[\mathbf{u}]]$ captures the discontinuous nature of the displacement across the interface. The finite element shape function matrix $\mathbf{N}$ is used to interpolate displacements within an element as we discussed before in Eq. (3.72). The displacement field is interpolated using $\mathbf{N}$, so the nodal displacement contributions to the displacement jump must also be represented using the same shape function matrix. Since the discontinuity exists only along the interface Γ_{DI}, we take the shape function matrix evaluated at the discontinuity interface, which is denoted as $\mathbf{N}|_{\Gamma_{DI}}$. In XFEM, additional enrichment functions are introduced to model discontinuities without requiring mesh refinement. A Heaviside function $H(x)$ is used as an enrichment function to represent a displacement jump. The enriched displacement component is controlled by the enriched degrees of freedom, represented by the vector $\boldsymbol{\beta}$ as Eq. (3.74). These enriched degrees of freedom allow the displacement field to be discontinuous across Γ_{DI}, which is necessary for modeling cracks and material interfaces. If the enrichment function was not included, the displacement field would remain continuous, making it impossible to model cracks or material discontinuities. By introducing enriched degrees of freedom $\boldsymbol{\beta}$, the displacement field can now be discontinuous, allowing the finite element formulation to capture material separation effectively. This formulation is fundamental in XFEM for handling problems such as fracture mechanics, where cracks propagate independently of the mesh. In overall, this equation (3.82) describes how the discontinuous displacement field is interpolated using enriched degrees of freedom at the interface. In general, the stress field within a heterogeneous continuum can be expressed in terms of the nodal displacements. The displacement field consists of both continuous and discontinuous components, as formulated in Eq. (3.71). The strain field $\boldsymbol{\varepsilon}$, defined as the gradient of the displacement field $\mathbf{u}$, is computed using the matrix $\mathbf{B}$, which contains the

derivatives of the shape functions. Consequently, the strain field is given by

$$\boldsymbol{\varepsilon} = \mathbf{B}\mathbf{d} + \mathbf{H}|_{\Gamma_{DI}}\,\mathbf{B}\boldsymbol{\beta} \tag{3.84}$$

The stress field $\boldsymbol{\sigma}$ is related to the strain field $\boldsymbol{\varepsilon}$ through the material property matrix $\mathbf{D}$, as expressed in Eq. (**??**). Substituting the strain field expression into the stress-strain relationship yields

$$\boldsymbol{\sigma} = \mathbf{D}\left(\mathbf{B}\mathbf{d} + \mathbf{H}|_{\Gamma_{DI}}\,\mathbf{B}\boldsymbol{\beta}\right) \tag{3.85}$$

This formulation provides the stress field in terms of the nodal displacements while accounting for both continuous and discontinuous contributions. Eq. (3.85) represents the stress field in a material containing discontinuities, such as cracks or interfaces between different materials. The stress field $\boldsymbol{\sigma}$ in two dimensions is expressed as

$$\boldsymbol{\sigma} = \begin{bmatrix} \sigma_{11} \\ \sigma_{22} \\ \sigma_{12} \end{bmatrix} \tag{3.86}$$

where $\boldsymbol{\sigma}$ is the stress field vector, consisting of the normal stresses (σ_{11} and σ_{22}) and the shear stress (σ_{12}) at a given point in the material. The material property matrix $\mathbf{D}$, previously defined as the stiffness matrix, establishes the relationship between strain and stress through the constitutive equation. This matrix depends on material properties such as Young's modulus and Poisson's ratio. The strain field associated with standard nodal displacements is represented by $\mathbf{B}\mathbf{d}$, where $\mathbf{B}$ is the strain-displacement matrix, which transforms nodal displacements into strain components, and $\mathbf{d}$ is the vector of nodal displacements, representing the finite element nodal displacements. This term accounts for the continuous deformation of the material, excluding any discontinuities. The strain contribution from the displacement jump is given by $\mathbf{H}|_{\Gamma_{DI}}\,\mathbf{B}\boldsymbol{\beta}$. Here, $\mathbf{H}|_{\Gamma_{DI}}$ represents the Heaviside function, which introduces a discontinuity in the displacement field across the interface Γ_{DI}. The term $\mathbf{B}\boldsymbol{\beta}$ corresponds to the strain field associated with the enriched degrees of freedom $\boldsymbol{\beta}$, which are introduced to model the displacement jump. This term accounts for the additional strain resulting from discontinuities, such as cracks or material interfaces. Furthermore, Eq. (3.85)

combines two distinct contributions to define the total stress field in the material. The first component, $\mathbf{Bd}$, represents the stress field due to the smooth, continuous deformation of the material, as captured by standard nodal displacements. The second component, $\mathbf{H}|_{\Gamma_{DI}}\mathbf{B}\boldsymbol{\beta}$, accounts for the additional stress contribution arising from discontinuities, such as cracks or interfaces, through the enriched degrees of freedom and the Heaviside function. By incorporating both continuous and discontinuous deformation effects, this formulation provides a comprehensive representation of the stress distribution in a heterogeneous material, enhancing the accuracy of the model in capturing complex mechanical behavior.

In cohesive zone modeling, the traction vector $\mathbf{t}$ at the discontinuity interface is related to the displacement jump through the interface stiffness matrix $\mathbf{T}$. This relationship is expressed as

$$\mathbf{t} = \mathbf{T}[\![\mathbf{u}]\!] \tag{3.87}$$

where $\mathbf{T}$ serves as the proportionality constant that quantifies the interface's resistance to separation. This formulation indicates that the traction vector $\mathbf{t}$ is directly proportional to the displacement jump $[\![\mathbf{u}]\!]$. To ensure the traction force is localized precisely at the discontinuity, the Dirac delta function $\boldsymbol{\delta}$ is introduced. The Dirac delta function is a mathematical function that is zero everywhere except at a specific location (in this case, the discontinuity interface $\boldsymbol{\delta}|_{\Gamma_{DI}}$). At this location, the function exhibits an infinite magnitude, ensuring that its integral over an infinitesimally small region equals unity. This property allows the function to confine the traction force exclusively to the discontinuity, such as a crack or material interface, without influencing other regions. Incorporating the Dirac delta function, the traction equation is modified as

$$\mathbf{t} = \mathbf{T}\boldsymbol{\delta}|_{\Gamma_{DI}}[\![\mathbf{u}]\!] \tag{3.88}$$

Finally, substituting the expression for the displacement jump $[\![\mathbf{u}]\!]$ into the traction equation yields the final expression for the traction vector at the discontinuity interface

$$\mathbf{t} = \mathbf{T}\boldsymbol{\delta}|_{\Gamma_{DI}}\mathbf{N}\boldsymbol{\beta} \tag{3.89}$$

Here, the traction vector $\mathbf{t}$ represents the forces per unit area acting at the discontinuity

interface Γ_{DI}. This traction vector accounts for the stresses that are transmitted across the interface, such as the normal and tangential forces at a crack or material boundary. And, the Dirac's delta function $\boldsymbol{\delta}$ is used to localize the traction forces precisely at the discontinuity interface Γ_{DI}. This function vanishes everywhere except at the interface, ensuring that the traction forces are only applied at the discontinuity. And, the matrix $\mathbf{T}$ imposes the interface stiffness. It is a 2x2 diagonal matrix that represents the cohesive resistance against the crack opening in both the normal and tangential directions. The components of $\mathbf{T}$ are assumed to be identical, indicating that the resistance to normal and tangential separations is the same and uncoupled. This formulation ensures that the cohesive forces acting across the discontinuity are properly accounted for, reflecting the material's resistance to separation and sliding at the interface (discontinuities).

In Eq. (3.89), the matrix $\mathbf{T}$ is introduced to impose the interface stiffness. This matrix quantifies the resistance of the interface (such as a crack or material boundary) to deformation. In this context, deformation refers to either the opening or sliding along the interface. The matrix $\mathbf{T}$ is a 2×2 diagonal matrix with identical components, meaning that it has non-zero values only on its diagonal, and these values are equal. The cohesive resistance described by $\mathbf{T}$ represents the material interface's ability to resist both separation in the normal direction and sliding in the tangential direction. Since the diagonal components are identical, the material exhibits the same resistance to normal and tangential deformations. Additionally, the directions are assumed to be uncoupled, implying that the resistance to opening (normal direction) does not influence the resistance to sliding (tangential direction) and vice versa. Mathematically, this uncoupling is represented by the diagonal structure of $\mathbf{T}$. The interface stiffness matrix $\mathbf{T}$ is defined as

$$\mathbf{T} = k\mathbf{I} \tag{3.90}$$

where k is the interface stiffness coefficient. This coefficient quantifies the stiffness or resistance of the interface to deformation. A higher value of k indicates greater resistance to deformation, meaning the interface behaves like a strong bond, effectively preventing separation. Conversely, a smaller value of k signifies a weaker interface, which may allow significant displacement discontinuities. The matrix $\mathbf{I}$ represents the 2×2 identity matrix,

which has ones on the diagonal and zeros elsewhere

$$\mathbf{I} = \begin{bmatrix} 1 & 0 \\ 0 & 1 \end{bmatrix} \tag{3.91}$$

By multiplying the stiffness coefficient k with the identity matrix $\mathbf{I}$, we obtain

$$\mathbf{T} = k \begin{bmatrix} 1 & 0 \\ 0 & 1 \end{bmatrix} = \begin{bmatrix} k & 0 \\ 0 & k \end{bmatrix} \tag{3.92}$$

This formulation clearly demonstrates that both the normal and tangential directions possess the same stiffness k, thereby making $\mathbf{T}$ a diagonal matrix with k as its diagonal elements.

Eq. (3.89) defines the traction vector $\mathbf{t}$ at the discontinuity interface. It is essential to understand that $\mathbf{t}$ is conjugate to the displacement jump at the interface, meaning that it represents the forces necessary to resist or balance this displacement jump. The traction vector $\mathbf{t}$ quantifies the forces per unit area acting at the interface. In a two-dimensional context, $\mathbf{t}$ is a vector with two components, each corresponding to the forces required to resist displacement jumps in orthogonal directions. The first component, t_n, is perpendicular to the interface (normal direction) and resists the opening or closing of the crack or interface. The second component, t_t, is parallel to the interface and opposes sliding along the interface. These two components are crucial for accurately characterizing the mechanical behavior at the interface, as they collectively define the complete state of traction (force per unit area) necessary to prevent displacement discontinuities. The Lagrange multiplier field $\boldsymbol{\lambda}$ is introduced to enforce constraints in the finite element method. The interpolation of $\boldsymbol{\lambda}$ is given by Eq. (3.12), where the matrix $\mathbf{G}$ is utilized to interpolate the Lagrange multiplier field $\boldsymbol{\lambda}$, thereby enforcing constraints at the interface. The matrix $\mathbf{G}$ is selected based on linear functions and, for a single element, is expressed as

$$\mathbf{G} = \begin{bmatrix} L_1 & 0 & L_2 & 0 \\ 0 & L_1 & 0 & L_2 \end{bmatrix} \tag{3.93}$$

Here, $\mathbf{G}$ is a 2×4 matrix, where each row corresponds to a spatial direction (e.g., the x and

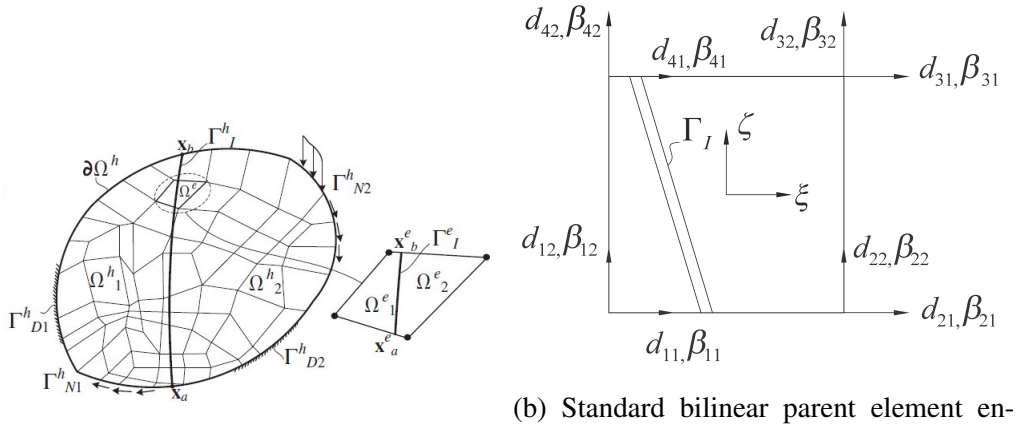

(a) Edge of the Element

(b) Standard bilinear parent element enriched to introduce discontinuity

Figure 3.2: Extended Finite Element Modelling

y directions in a two-dimensional setting). The terms L_1 and L_2 represent the linear shape functions associated with the boundary nodes of the element. These functions interpolate the values of the Lagrange multipliers at the boundary nodes. The first row of $\mathbf{G}$ corresponds to the x-direction, containing L_1 and L_2 in positions associated with the x-components of the Lagrange multipliers. Similarly, the second row corresponds to the y-direction, containing L_1 and L_2 in positions associated with the y-components. This structure ensures consistency in interpolation across both spatial directions. Physically, the Lagrange multiplier field $\boldsymbol{\lambda}$ is interpolated using linear shape functions, implying that within the boundary of the element, $\boldsymbol{\lambda}$ varies linearly from one node to the next. Furthermore, the matrix $\mathbf{G}$ governs how the nodal values of the Lagrange multipliers, contained in $\mathbf{h}$, are distributed along the element boundary.

For a one-dimensional edge, the linear shape functions L_1 and L_2 in Eq. (3.93) are defined as

$$\begin{aligned} L_1 &= \frac{0.5l - z_b}{l}, \\ L_2 &= \frac{0.5l + z_b}{l} \end{aligned} \tag{3.94}$$

These shape functions are used to interpolate the value of the Lagrange multiplier field for one element. The functions L_1 and L_2 vary linearly along the edge of the element, ensuring that the value at the midpoint is a weighted average of the values at the nodes. The variable z_b, as shown in Figure 3.3, represents the local coordinate along the edge of the element. It ranges from $-0.5l$ to $0.5l$, where l denotes the length of the edge. In the case of a quadrilateral element, l corresponds to the length of one of its sides. Specifically, l can be

expressed as $2a$ or $2b$, where a and b represent the half-lengths of the element along the two orthogonal directions (e.g., x and y), as illustrated in Figure 3.2b. Considering the function L_1:

- When $z_b = -0.5l$ (at one end of the edge), $L_1 = 1$.
- When $z_b = 0.5l$ (at the other end of the edge), $L_1 = 0$.
- L_1 decreases linearly from 1 to 0 as z_b moves from $-0.5l$ to $0.5l$.

Similarly, for L_2:

- When $z_b = -0.5l$, $L_2 = 0$.
- When $z_b = 0.5l$, $L_2 = 1$.
- L_2 increases linearly from 0 to 1 as z_b moves from $-0.5l$ to $0.5l$.

Physically, the linear shape functions L_1 and L_2 are used to interpolate the Lagrange multiplier field within an element. This interpolation ensures that at the midpoint of the edge ($z_b = 0$), the interpolated value is the average of the nodal values. The interpolation is linear, meaning that the value changes uniformly from one end of the edge to the other. Additionally, the Lagrange multipliers at the nodes control the constraints at the element level, with their influence being distributed linearly along the edge.

For any boundary node i of an element, the vector $\mathbf{h}_i$ in Eq. (3.12) can be expressed as

$$\mathbf{h}_i = \begin{bmatrix} \mathbf{h_i} \\ \mathbf{h_{i+1}} \end{bmatrix}, \tag{3.95}$$

where $\mathbf{h_i}$ and $\mathbf{h_{i+1}}$ are defined as

$$\mathbf{h_i} = \begin{bmatrix} h_{i,1} \\ h_{i,2} \end{bmatrix}, \quad \mathbf{h_{i+1}} = \begin{bmatrix} h_{i+1,1} \\ h_{i+1,2} \end{bmatrix} \tag{3.96}$$

The vector $\mathbf{h}_i$ represents unknown quantities (e.g., displacement constraints, forces, or Lagrange multipliers) at boundary node i and its adjacent node $i+1$, which are used to interpolate the Lagrange multiplier field. $\mathbf{h_i}$ is a sub-vector of $\mathbf{h}_i$ containing the unknowns

associated with node i. In Eq. (3.96), $h_{i,1}$ is the first component (e.g., the x - direction value of the unknown field, such as displacement, force, or Lagrange multiplier at node i). $h_{i+1,2}$ is the second component (e.g., y - direction value of the unknown at node $i+1$). In overall, these quantities are interpolated along the boundary to compute the Lagrange multiplier field, ensuring smooth enforcement of constraints. For any node i, the Lagrange multiplier field $\boldsymbol{\lambda}_i$ in Eq. (3.12) can be expressed as

$$\boldsymbol{\lambda}_i = \begin{bmatrix} \lambda_{i,1} \\ \lambda_{i,2} \end{bmatrix} \tag{3.97}$$

Eq. (3.97) represents the Lagrange multiplier field at node i in a two-dimensional problem. Physically, this field corresponds to interface forces (or tractions) that act to enforce constraints at the boundary of an element. The components $\lambda_{i,1}$ and $\lambda_{i,2}$ represent the traction (force per unit length or unit area) acting in the x and y directions, respectively. This traction is a reaction force applied at the interface to enforce constraints. By using interpolation, $\boldsymbol{\lambda}_i$ is obtained as Eq. (3.12)

$$\boldsymbol{\lambda}_i = \mathbf{G}\mathbf{h}_i, \tag{3.98}$$

where the interpolation matrix $\mathbf{G}$ is given by Eq. (3.93). Then, by substituting $\mathbf{h}_i$ into the equation for $\boldsymbol{\lambda}_i$, we get

$$\begin{bmatrix} \lambda_{i,1} \\ \lambda_{i,2} \end{bmatrix} = \begin{bmatrix} L_1 & 0 & L_2 & 0 \\ 0 & L_1 & 0 & L_2 \end{bmatrix} \begin{bmatrix} h_{i,1} \\ h_{i,2} \\ h_{i+1,1} \\ h_{i+1,2} \end{bmatrix} \tag{3.99}$$

Computing the matrix-vector product, we obtain

$$\boldsymbol{\lambda}_i = \begin{bmatrix} L_1 h_{i,1} + L_2 h_{i+1,1} \\ L_1 h_{i,2} + L_2 h_{i+1,2} \end{bmatrix} \tag{3.100}$$

This equation expresses the Lagrange multiplier field $\boldsymbol{\lambda}_i$ at node i as an interpolated combination of the unknowns at two adjacent boundary nodes (i and $i+1$). The first component

($\lambda_{i,1} = L_1 h_{i,1} + L_2 h_{i+1,1}$) represents the x - direction component of the Lagrange multiplier field at node i. It is interpolated using shape functions L_1 and L_2, which weight the contributions from the unknowns at nodes i and $i + 1$. Physically, it can represent a constraint force, traction, or reaction force in the x - direction. The second component ($\lambda_{i,2} = L_1 h_{i,2} + L_2 h_{i+1,2}$) represents the y - direction component of the Lagrange multiplier field at node i. It is similarly interpolated using the shape functions L_1 and L_2. Physically, like $\lambda_{i,1}$, this can represent a constraint force, traction, or reaction force, but in the y - direction. In overall, the Lagrange multiplier $\boldsymbol{\lambda}_i$ enforces constraints at the interface or boundary (e.g., displacement continuity or traction conditions). The shape functions L_1 and L_2 determine how the values from neighboring nodes contribute to the Lagrange multiplier at node i. The resulting vector $\boldsymbol{\lambda}_i$ describes forces (or constraints) acting in both x and y directions at the boundary node.

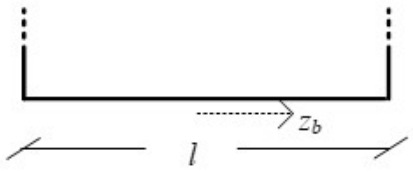

Figure 3.3: Edge of the Element

3.4 Stabilization of the XFEM

In the context of the (XFEM), the displacement jump function at the interface, as given in Eq. (3.82), exhibits a piecewise quadratic nature. This means that the function describing the discontinuity in displacement across the interface is not simply linear or constant but instead follows a quadratic form within each element. A piecewise quadratic function is a function that is quadratic within individual sub-domains (elements) but may exhibit discontinuities at the boundaries between these sub-domains. In XFEM, the displacement field is enriched to capture discontinuities and sharp gradients effectively, leading to the presence of quadratic terms in the displacement jump formulation. This function (3.82) contains quadratic bubbles. These quadratic bubble functions are commonly used in finite element formulations to enhance approximation properties, particularly for higher-order elements. However, in the standard XFEM approach, the presence of these bubble terms can lead to excessive oscillations in the computed traction field, especially under a stiff interface assumption, when the material contrast across the interface is significant e.g., Erkmen and Dias-da Costa [12]. Such oscillations arise because the quadratic bubble terms introduce artificial fluctuations in the traction along the interface, which are not physically realistic and can degrade the numerical stability and accuracy of the solution. This motivates the need for stabilization techniques, such as the decomposition of the displacement jump.

To mitigate these oscillations, the displacement jump function given in Eq. (3.82) is decomposed into two separate components

$$\left[\left[\mathbf{u}^h\right]\right] = \mathbf{N}|_{\Gamma_{DI}}\,\boldsymbol{\beta} = \overline{\mathbf{N}}_{\mathbf{c}}\big|_{\Gamma_l}\,\boldsymbol{\beta} + \overline{\boldsymbol{\Theta}}\,\boldsymbol{\beta} \tag{3.101}$$

The first component is an element-wise constant component represented by $\overline{\mathbf{N}}_{\mathbf{c}}\big|_{\Gamma_l}\boldsymbol{\beta}$. This part ensures that the discontinuity is captured without introducing excessive variations in the traction field. It provides a more stable representation of the discontinuity across the interface by preventing high-frequency oscillations. The second component is a quadratic bubble component represented by $\overline{\boldsymbol{\Theta}}\boldsymbol{\beta}$. This term accounts for higher-order variations within the element, which naturally arise in enriched XFEM formulations. However, this term can contribute to artificial oscillations in the traction field if left unchecked. By explicitly separating

these two components, the stabilization approach enables better numerical conditioning and suppresses oscillations while still maintaining the ability of XFEM to accurately represent discontinuities. This decomposition ultimately leads to improved convergence and solution accuracy, particularly in problems involving stiff material interfaces.

The matrix $\overline{\mathbf{N}}_{\mathbf{c}}\big|_{\Gamma_I}$ in Eq. (3.101) represents the shape functions associated with the discontinuity interface in an element-wise constant manner. It plays an important role in defining the displacement jump function while ensuring that the stabilization mechanism is properly incorporated into the XFEM formulation. This shape function matrix is given by

$$\overline{\mathbf{N}}_{\mathrm{c}}\big|_{\Gamma_I} = \begin{bmatrix} \bar{N}_{\Gamma 1} & 0 & \bar{N}_{\Gamma 2} & 0 & \bar{N}_{\Gamma 3} & 0 & \bar{N}_{\Gamma 4} & 0 \\ 0 & \bar{N}_{\Gamma 1} & 0 & \bar{N}_{\Gamma 2} & 0 & \bar{N}_{\Gamma 3} & 0 & \bar{N}_{\Gamma 4} \end{bmatrix} \tag{3.102}$$

This matrix structure highlights two key aspects: the separation of displacement components and the use of node-based shape functions. The first row corresponds to the shape functions affecting the horizontal displacement (u_x), while the second row corresponds to those influencing the vertical displacement (u_y). Additionally, each column pair represents a nodal shape function ($\bar{N}_{\Gamma 1}, \bar{N}_{\Gamma 2}, \bar{N}_{\Gamma 3}, \bar{N}_{\Gamma 4}$) at the interface, ensuring that displacement discontinuities are consistently represented in both coordinate directions. The shape functions $\bar{N}_{\Gamma i}$ are derived from the standard bilinear shape functions used in quadrilateral elements. Their expressions incorporate the parent element coordinates (ξ, ζ) and nodal locations (ξ_a, ζ_a, ξ_b, ζ_b), which define the position of the discontinuity within the element.

$$\begin{aligned}
\bar{N}_{\Gamma 1} &= \frac{1}{8}(1-\xi_a)(1-\zeta_a) + \frac{1}{8}(1-\xi_b)(1-\zeta_b) - \frac{1}{24}(\xi_a-\xi_b)(\zeta_a-\zeta_b), \\
\bar{N}_{\Gamma 2} &= \frac{1}{8}(1+\xi_a)(1-\zeta_a) + \frac{1}{8}(1+\xi_b)(1-\zeta_b) + \frac{1}{24}(\xi_a-\xi_b)(\zeta_a-\zeta_b), \\
\bar{N}_{\Gamma 3} &= \frac{1}{8}(1+\xi_a)(1+\zeta_a) + \frac{1}{8}(1+\xi_b)(1+\zeta_b) - \frac{1}{24}(\xi_a-\xi_b)(\zeta_a-\zeta_b), \\
\bar{N}_{\Gamma 4} &= \frac{1}{8}(1-\xi_a)(1+\zeta_a) + \frac{1}{8}(1-\xi_b)(1+\zeta_b) + \frac{1}{24}(\xi_a-\xi_b)(\zeta_a-\zeta_b)
\end{aligned} \tag{3.103}$$

Each shape function is constructed using standard bilinear interpolation functions, incorporating symmetry adjustments to account for discontinuities. Furthermore, the functions are defined based on the two nodal positions (ξ_a, ζ_a) and (ξ_b, ζ_b), which represent the coordinates of the interface points within the parent element. In overall, the shape function

components play an important role in defining how the displacement jump is distributed along the interface. Their element-wise constant structure helps stabilize the XFEM formulation by preventing excessive oscillations caused by quadratic bubble terms. Additionally, this formulation ensures that the displacement jump is accurately represented across the element boundary, which is essential for capturing discontinuities in heterogeneous materials. Consequently, this decomposition of shape functions provides a numerically stable and physically accurate representation of the displacement discontinuity along the interface in XFEM.

The matrix $\overline{\boldsymbol{\Theta}}$ in Eq. (3.101) represents the quadratic bubble component in the decomposition of the displacement discontinuity. This component plays a key role in capturing the higher-order variations of the discontinuity jump while preventing nonphysical oscillations. The matrix $\overline{\boldsymbol{\Theta}}$ is given as

$$\overline{\boldsymbol{\Theta}} = \begin{bmatrix} \bar{\Theta} & 0 & \bar{\Theta} & 0 & \bar{\Theta} & 0 & \bar{\Theta} & 0 \\ 0 & \bar{\Theta} & 0 & \bar{\Theta} & 0 & \bar{\Theta} & 0 & \bar{\Theta} \end{bmatrix} \tag{3.104}$$

The structure is similar to $\overline{\mathbf{N}}_{\mathbf{c}}\big|_{\Gamma_I}$, indicating that $\bar{\Theta}$ contributes to both horizontal (x-direction) and vertical (y-direction) displacement jumps. Each column corresponds to a nodal contribution, ensuring consistent shape representation across the interface. The repeated presence of $\bar{\Theta}$ across all terms highlights its uniform effect on all interface nodes. The function $\bar{\Theta}$ is given by

$$\bar{\Theta} = \frac{1}{16}\left(\xi_a - \xi_b\right)\left(\zeta_a - \zeta_b\right)\left(1 - s\right)^2 - \frac{1}{24}\left(\xi_a - \xi_b\right)\left(\zeta_a - \zeta_b\right) \tag{3.105}$$

where, ξ and ζ are the local coordinates in the parent element. s is a normalized coordinate along the discontinuity interface, constrained within $-1 \leq s \leq 1$. This function Eq. (3.105) defines a quadratic bubble shape function that ensures proper behavior along the interface. The $(1-s)^2$ term guarantees that $\bar{\Theta}$ is minimal at the interface endpoints ($s = \pm 1$), making it most significant at the center. Additionally, its dependence on the element's nodal positions $(\xi_a, \xi_b, \zeta_a, \zeta_b)$ allows it to adapt dynamically to the local element geometry and discontinuity placement. The quadratic bubble component $\overline{\boldsymbol{\Theta}}$ plays an important role in refining the representation of displacement discontinuities in XFEM. By enhancing the piece-wise quadratic nature of the displacement jump, it improves the accuracy of interface modeling. Additionally, incorporating this component helps stabilize the formulation by reducing non-physical

numerical oscillations that may arise from sharp discontinuities. Its quadratic dependence on s further enhances local approximation, enabling a more precise representation of curved or non-uniform displacement jumps, particularly in heterogeneous materials. In overall, $\overline{\boldsymbol{\Theta}}$ serves as an essential higher-order correction term that complements the constant part of the displacement jump, leading to a more stable and accurate numerical formulation in the (XFEM).

In the finite element formulation, the discontinuity interface is embedded within a parent element, and the positions of the interface edges within this element must be carefully defined. To achieve this, the local coordinates (ξ, ζ) are used to describe the interface edges in the reference (parent) element. The coordinate vector components at the two edges of the element are represented by (ξ_a, ζ_a) and (ξ_b, ζ_b), which denote the local coordinates of the first and second edges of the discontinuity within the parent element, respectively see Figure 3.2a. These local coordinates correspond to the physical coordinates $\mathbf{x}_a^e$ and $\mathbf{x}_b^e$ in the global coordinate system. While local coordinates (ξ, ζ) are used within the reference element to facilitate interpolation and shape function definitions, physical coordinates $\mathbf{x}^e$ describe the actual spatial location of the interface in the problem domain. The relationship between these coordinate systems is established through element shape functions, which map local coordinates to the global coordinate system. By using these local coordinate definitions, the formulation ensures a clear and consistent representation of the interface within each element, which is fundamental for accurate numerical integration and shape function evaluations in XFEM.

To enhance the stability of the numerical formulation and reduce oscillations in the discontinuous displacement field, we can modify the decomposition of the displacement jump by introducing an additional term as discussed in detail in Erkmen and Dias-da Costa [12]. Specifically, instead of using the original decomposition

$$\overline{\mathbf{N}}_{\mathbf{c}}\big|_{\Gamma_l}\boldsymbol{\beta} + \overline{\boldsymbol{\Theta}}\,\boldsymbol{\beta}$$

we replace it with

$$\overline{\mathbf{N}}_{\mathbf{c}}\big|_{\Gamma_l}\boldsymbol{\beta} + \chi\,\hat{\boldsymbol{\Theta}}\,\boldsymbol{\beta} \tag{3.106}$$

Here, $\hat{\boldsymbol{\Theta}}$ is a modified version of $\overline{\boldsymbol{\Theta}}$, and the parameter χ is a scalar multiplier that allows for

tuning the contribution of the quadratic bubble term. The validity and numerical stability of this modified decomposition rely on satisfying the orthogonality condition

$$\int_{\Gamma_I} \overline{\mathbf{N}}_{\mathbf{c}}^{\mathrm{T}}\Big|_{\Gamma_I} \mathbf{T}\,\hat{\boldsymbol{\Theta}}\,\mathrm{d}\Gamma = 0 \tag{3.107}$$

This condition ensures that the additional component $\hat{\boldsymbol{\Theta}}$ does not introduce spurious numerical artifacts into the solution. Specifically, the term $\mathbf{T}\hat{\boldsymbol{\Theta}}$ represents the modified shape function component projected onto the interface, and the integral over the interface must vanish. This guarantees that the new term does not interfere with the primary interpolation of the displacement field, preserving the stability and accuracy of the formulation. It should be noted that the scalar parameter χ plays an important role in the formulation while maintaining compliance with the orthogonality condition. Its magnitude does not affect the validity of this condition, meaning that any non-zero χ remains acceptable as long as $\hat{\boldsymbol{\Theta}}$ is properly constructed. However, χ can influence numerical stability and convergence, making it a potential tuning parameter in practical implementations. In computational applications, χ is often adjusted to optimize numerical performance, particularly for controlling oscillations in the displacement field. In overall, this modification (3.106) provides a more stable numerical formulation by ensuring that the displacement jump decomposition remains consistent with the orthogonality condition. By appropriately selecting $\hat{\boldsymbol{\Theta}}$ and ensuring the integral condition holds, we can improve solution accuracy and mitigate oscillations in enriched finite element formulations such as XFEM.

The parameter χ plays a critical role in stabilization by mitigating numerical instabilities associated with displacement discontinuities at the interface. Its effect can be understood through an analogy to a fictitious spring system, where χ introduces an artificial stiffness that resists excessive fluctuations, much like a physical spring dampens sudden movements. Without adequate stabilization, a small χ can lead to ill-conditioning, resulting in oscillatory or non-physical displacement jumps, whereas a sufficiently large χ effectively suppresses these instabilities, ensuring numerical stability. This approach aligns with established stabilization techniques in numerical methods, such as those discussed in Ventura and Tesei [54], where stabilization parameters like χ help maintain a good system by balancing enrichment functions in the XFEM framework. The optimal choice of χ is important for balancing numerical stability and solution accuracy. A very small χ may fail to suppress oscilla-

tions, leading to unstable results, while an excessively large χ can cause over-stiffening, potentially compromising accuracy. Therefore, a moderate χ must be selected to effectively dampen oscillations while preserving the precise representation of discontinuities in the solution. In overall, by treating χ as a fictitious spring stiffness, we can control numerical oscillations while maintaining stability. A properly chosen χ prevents ill-conditioning and ensures that the displacement jump is captured accurately in the extended finite element method (XFEM) framework.

The matrix $\hat{\boldsymbol{\Theta}}$ in Eq. (3.106) is carefully chosen to satisfy the orthogonality condition (3.107) while incorporating stabilization effects in the numerical framework. This choice is based on Legendre polynomials, which are commonly used in numerical methods for their orthogonality properties. The matrix $\hat{\boldsymbol{\Theta}}$ is formulated as

$$\hat{\boldsymbol{\Theta}} = \begin{bmatrix} -\widehat{\Theta}_1 - \widehat{\Theta}_2 & 0 & \widehat{\Theta}_2 - \widehat{\Theta}_3 & 0 & \widehat{\Theta}_3 + \widehat{\Theta}_4 & 0 & -\widehat{\Theta}_4 + \widehat{\Theta}_1 & 0 \\ 0 & -\widehat{\Theta}_1 - \widehat{\Theta}_2 & 0 & \widehat{\Theta}_2 - \widehat{\Theta}_3 & 0 & \widehat{\Theta}_3 + \widehat{\Theta}_4 & 0 & -\widehat{\Theta}_4 + \widehat{\Theta}_1 \end{bmatrix} \tag{3.108}$$

This formulation ensures that the stabilization terms align with the displacement jump decomposition while preserving the required orthogonality conditions. The components $\widehat{\Theta}_i$ in Eq. (3.108) are constructed using Legendre polynomials, which provide an optimal basis for approximating functions over an interval while ensuring minimal oscillations. These are expressed as follows

$$\widehat{\Theta}_1 = \sqrt{\frac{5}{2}}\left(\frac{3}{2}s^2 - \frac{1}{2}\right) \tag{3.109}$$

$$\widehat{\Theta}_2 = \sqrt{\frac{7}{2}}\left(\frac{5}{2}s^3 - \frac{3}{2}s\right) \tag{3.110}$$

$$\widehat{\Theta}_3 = \sqrt{\frac{9}{2}}\left(\frac{35}{8}s^4 - \frac{15}{4}s^2 + \frac{3}{8}\right) \tag{3.111}$$

$$\widehat{\Theta}_4 = \sqrt{\frac{11}{2}}\left(\frac{63}{8}s^5 - \frac{35}{4}s^3 + \frac{15}{8}s\right) \tag{3.112}$$

These components progressively capture higher-order variations in the discontinuity field. The first-order term $\widehat{\Theta}_1$, based on the second-degree Legendre polynomial $P_2(s)$, captures

quadratic variations along the interface. The second-order term $\widehat{\Theta}_2$, derived from the third-degree polynomial $P_3(s)$, accounts for cubic variations in the displacement discontinuity. The third-order term $\widehat{\Theta}_3$, built from the fourth-degree polynomial $P_4(s)$, introduces a quartic correction to the shape functions. Finally, the fourth-order term $\widehat{\Theta}_4$, based on the fifth-degree polynomial $P_5(s)$, provides higher-order refinement, enabling a more precise approximation of discontinuities. This hierarchical structure ensures improved accuracy while maintaining numerical stability. The use of Legendre polynomials in constructing $\hat{\mathbf{\Theta}}$ is significant due to their mathematical properties and numerical advantages. Their orthogonality property ensures that $\hat{\mathbf{\Theta}}$ satisfies the required orthogonality condition for stabilization, contributing to numerical robustness. Additionally, Legendre polynomials serve as optimal basis functions, minimizing oscillatory artifacts in numerical approximations and enhancing solution accuracy. Their efficient representation allows higher-order terms, such as $\widehat{\Theta}_3$ and $\widehat{\Theta}_4$, to effectively capture complex displacement discontinuities, making them ideal for enriched finite element formulations like XFEM. In overall, the choice of $\hat{\mathbf{\Theta}}$ using Legendre polynomial-based components in Eq. (3.108) provides a systematic stabilization approach in the XFEM framework. By ensuring orthogonality, it effectively suppresses spurious oscillations while preserving the accuracy of discontinuity representation along the interface.

3.5 Closing Remarks

The computational homogenization framework using the (XFEM) offers a robust numerical approach for analyzing heterogeneous materials. By leveraging vector-matrix notations and adopting boundary conditions tailored to specific macroscopic behaviors, the methodology enables precise modeling of Representative Volume Elements (RVEs). The derivation and implementation of boundary conditions, such as uniform displacement gradients, uniform traction, and periodic displacements, ensure flexibility in addressing various material behaviors under different loading scenarios. The mathematical precision of the formulation, as demonstrated by the algebraic representation of the RVE problem and the explicit partitioning of displacement and stress fields, guarantees consistency and accuracy. Moreover, the integration of the Lagrange multiplier field and approximated displacement functions enhances the method's computational efficiency, making it suitable for large-scale simulations.

The ability to impose constraints through tailored boundary conditions provides a significant advantage, as it allows for the seamless simulation of microstructural effects on macroscopic properties. The implementation of periodic boundary conditions and the enforcement of anti-periodicity for stress and displacement fluctuations further emphasize the framework's versatility in capturing realistic material responses. The schematic representation of boundary and interior nodes illustrates the detailed handling of boundary constraints, ensuring a systematic approach to homogenization. This comprehensive methodology establishes XFEM-based computational homogenization as a powerful tool for advancing material design and analysis, bridging the gap between microscopic heterogeneities and macroscopic material performance.

The stabilization of the (XFEM) is important in addressing the excessive traction oscillations that arise due to quadratic bubble terms in the displacement jump function. By decomposing the discontinuity jump into an element-wise constant and a quadratic bubble component, a more stable representation of the interface behavior is achieved. The modified formulation employs interface shape functions and additional terms to refine the displacement approximation, ensuring greater numerical stability under stiff interface conditions. The use of orthogonality conditions and the introduction of a scalar parameter χ further enhance this stabilization, effectively mitigating oscillatory behavior without compromising the accuracy of the solution. This approach demonstrates the capability of XFEM to handle complex interfaces with precision and reliability.

A significant contribution of this stabilization technique is its computational efficiency and adaptability. The parameter χ, set as a small value for simplicity, effectively functions as a fictitious spring, providing sufficient suppression of ill-conditioning. Furthermore, the selection of matrix components, such as $\hat{\mathbf{\Theta}}$, in terms of Legendre polynomials ensures that the orthogonality conditions are satisfied, thus preserving the method's robustness. This framework not only stabilizes XFEM under challenging conditions but also paves the way for its broader application in simulations involving heterogeneous materials. The methodology's sound theoretical foundation and practical effectiveness underscore its value as a tool for advanced finite element analyses.

Chapter 4

Case Studies

4.1 Introduction

The validation of the XFEM-based computational homogenization procedure is essential to assess its accuracy and reliability in predicting the effective material properties of heterogeneous media. In this chapter, two validation cases are presented, comparing the results obtained using the developed XFEM-based approach with those from established homogenization techniques, including the standard Finite Element-based Homogenization (HOM02D) in Guedes and Kikuchi [18] and the Voronoi Cell Finite Element Method (VCFEM) in Ghosh et al. [17]. The first validation case (4.2.1) considers representative volume elements (RVEs) with single and randomly dispersed circular inclusions, where the homogenized elastic modulus in the horizontal direction is examined for different volume fractions. The second validation case (4.2.2) investigates RVEs with short and long rectangular inclusions, comparing the computed homogenized material tensor components against alternative numerical and analytical methods from the literature. These comparisons provide a comprehensive assessment of the XFEM-based homogenization approach, demonstrating its capability to capture the mechanical behavior of complex microstructures with high accuracy.

Through detailed numerical experiments, the effectiveness of the XFEM-based homogenization technique is evaluated by systematically analyzing different microstructural con-

figurations and boundary conditions. The perfect bond assumption between inclusions and the matrix is incorporated using an interfacial stiffness parameter, ensuring that the homogenized properties remain unaffected beyond a specific threshold value. Furthermore, periodic boundary conditions are imposed to maintain consistency with classical homogenization frameworks. The study reveals that the XFEM-based approach yields results that closely match those obtained from VCFEM, HOM02D, and other reference solutions, with minor deviations attributed to the different modeling assumptions. The validation cases confirm that the proposed XFEM-based methodology is a robust and accurate tool for computational homogenization, providing reliable predictions of the effective material properties for a wide range of microstructural geometries and inclusion distributions.

The stabilization of the (XFEM) presents a fundamental challenge, particularly in mitigating oscillations that arise due to the presence of enriched degrees of freedom at material interfaces. One widely adopted approach to address this issue is the Stabilized XFEM (S-XFEM), where a stabilization parameter, χ, is introduced to control numerical instabilities. The appropriate selection of χ is important, as it directly influences the stiffness of the fictitious spring introduced to counteract spurious oscillations. While some studies suggest setting $\chi = 1$ as a universal choice, this approach may not be suitable for all cases, particularly in complex geometries or material distributions where the system may become either under or over-constrained. Thus, a more refined methodology is required to determine an optimal χ value that balances stability and accuracy across a range of applications. This section (4.3) introduces a systematic criterion for selecting χ, ensuring that stabilization is achieved without excessively constraining the system, thereby enhancing the robustness of S-XFEM for diverse material and interface configurations.

To validate the proposed criterion, a comparative analysis (4.4) is conducted against an existing methodology in Erkmen and Dias-da Costa [11] that determines χ based on the condition number of the system stiffness matrix. The study employs parametric analyses using Representative Volume Elements (RVEs) with varying inclusion distributions, material properties, and mesh refinements. The developed MATLAB-based computational framework iteratively evaluates χ by analyzing its effect on normal and tangential tractions at material interfaces, selecting an optimal value based on a predefined convergence criterion. This approach not only refines the stabilization strategy but also offers insights into whether a universal χ can be identified for different cases. The results demonstrate that the proposed criterion provides a more systematic and reliable selection of χ compared to con-

ventional approaches, ensuring improved numerical stability while preserving the accuracy of the stress field in S-XFEM.

4.2 Validation of the XFEM-based Homogenization

4.2.1 Validation Case 1

For validation purposes, we compare the results based on the developed XFEM based Computational Homogenization procedure with those based on the standard Finite Element based Homogenization referred by the name (HOM02D) in Guedes and Kikuchi [18] and the Voronoi Cell Finite Element Method (VCFEM) in Ghosh et al. [17]. All RVE sizes are taken as $100\,\text{mm} \times 100\,\text{mm}$ as shown in Figure 4.1. The bond between the inclusions and the matrix is considered stiff. Stiff bond was imposed in the XFEM-based modelling by assigning $k = 10^6\,\text{N/mm}^3$ in Eq. (3.90). This value is determined such that for any larger value the homogenized properties are not affected. We have used periodic boundary conditions.

The microstructure consists of boron-aluminum material whose properties are given in Table 4.1. Plane stress conditions are assumed for the homogenization. Four different volume fractions (30%, 40%, 50% and 60%) are considered. In the first group of cases, the base cell consists of a centrally located single circular inclusion, the diameter of which is varied to cause different volume fractions as shown in Figure 4.1, where 20×20 element mesh was used. In the second group of composites, a random dispersion of circular inclusions of different volume fractions constitute the microstructure. The corresponding XFEM meshes for different volume fractions are shown in Figure 4.2. It can be seen that in this case 50×50 element mesh was used to be able to accommodate all the inclusions without causing any contact.

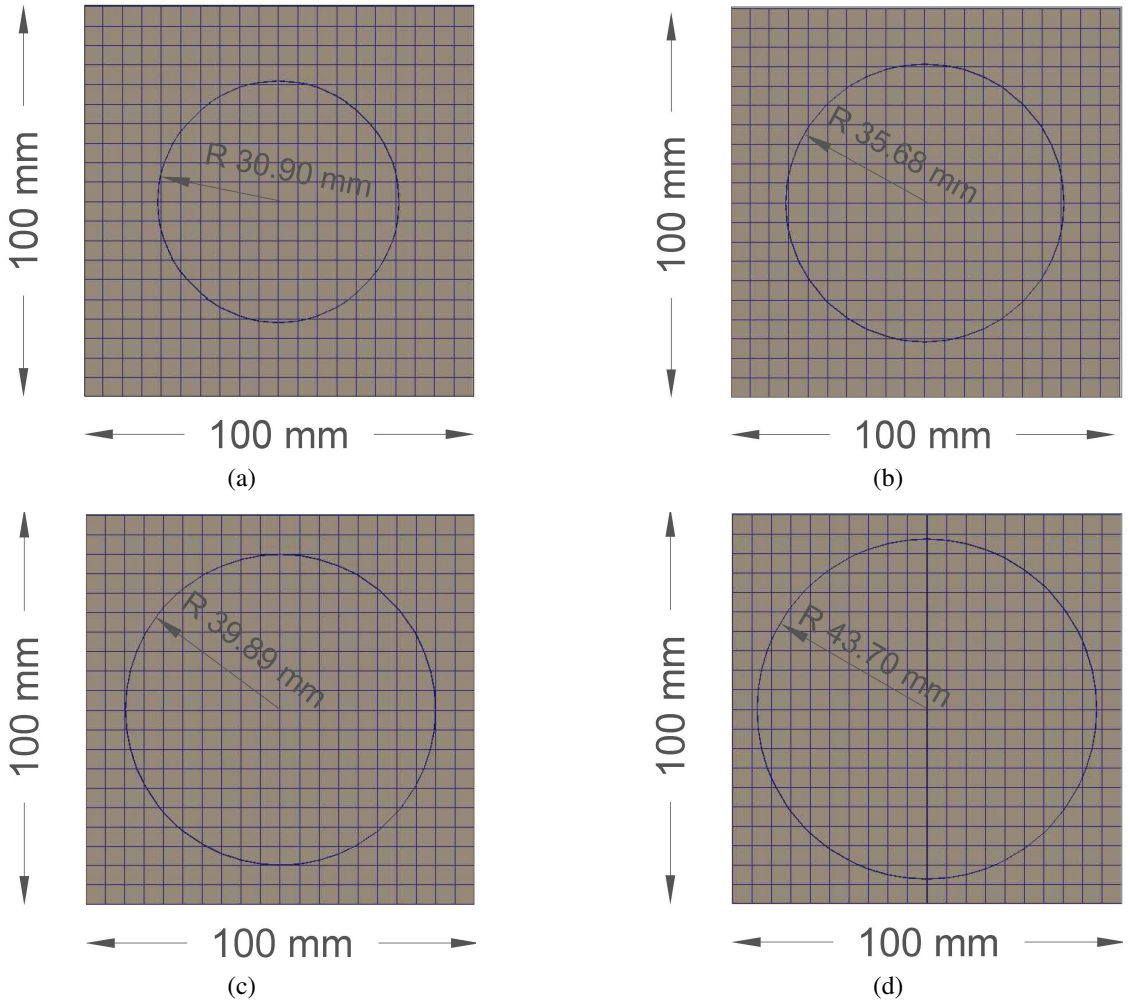

Figure 4.1: RVE with a single circular inclusion: (a) , (b) , (c) and (d) XFEM mesh for 30% , 40% , 50% and 60% volume fractions

Table 4.1: Properties of the RVE components in Figures 4.1 and 4.2

Parameter	**Value**
Young's modulus of the aluminum matrix	72.0×10^3 MPa
Poisson's ratio of the aluminum matrix	0.3333
Young's modulus of the inclusions	400.0×10^3 MPa
Poisson's ratio of the inclusions	0.300

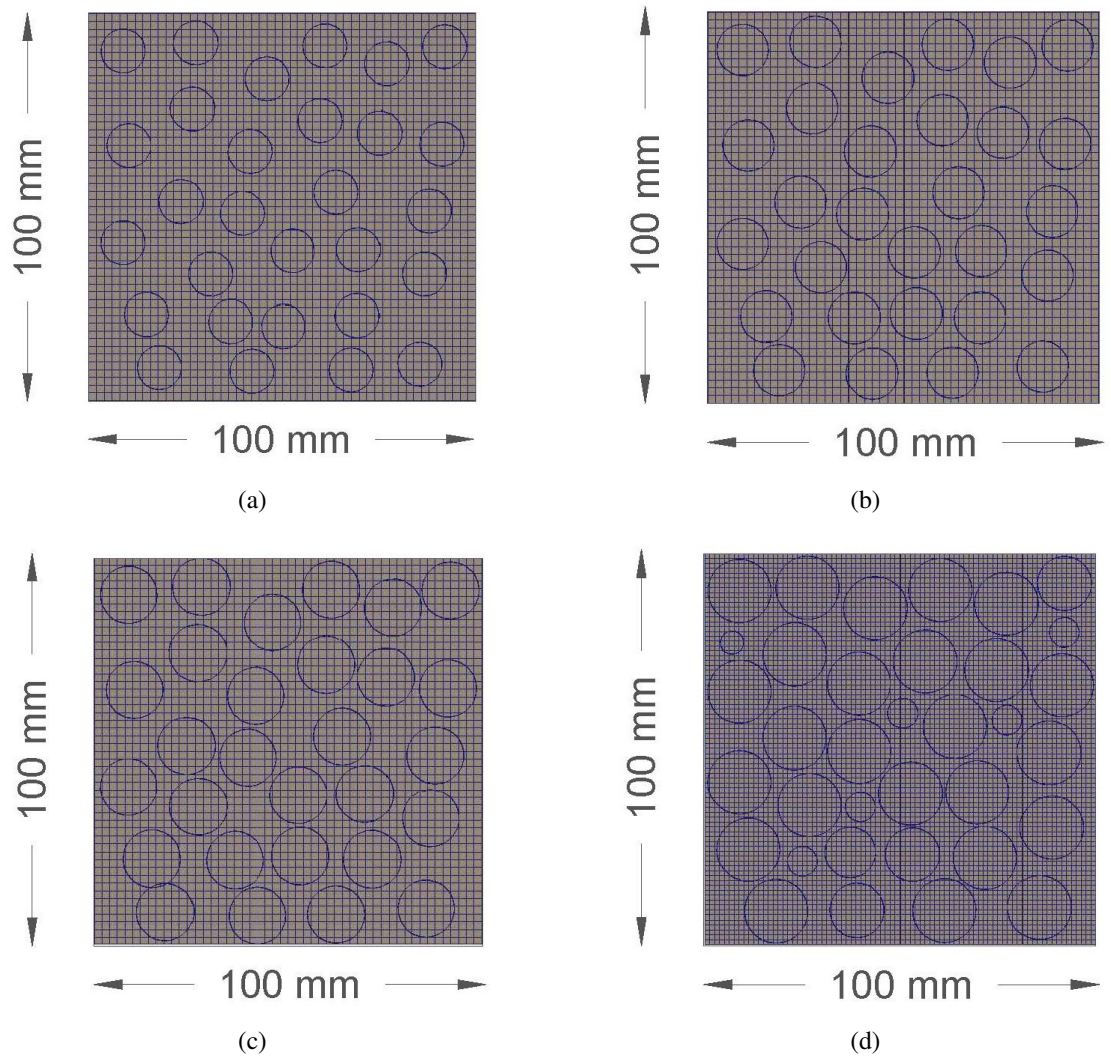

Figure 4.2: RVE with random distribution of circular inclusions (a) , (b) , (c) and (d) XFEM mesh for 30% , 40% , 50% and 60% volume fractions

For both RVE models shown in Figures 4.1 and 4.2, comparisons of the Young's modulus in the horizontal direction, i.e. (E1) against those based on VCFEM and HOM02D in Ghosh et al. [17] and Guedes and Kikuchi [18] are presented in Figure 4.3. It is interesting to note that Values of the homogenized Elastic Modulus (E1) for the randomly dispersed microstructure are slightly lower than those calculated based on single inclusion.

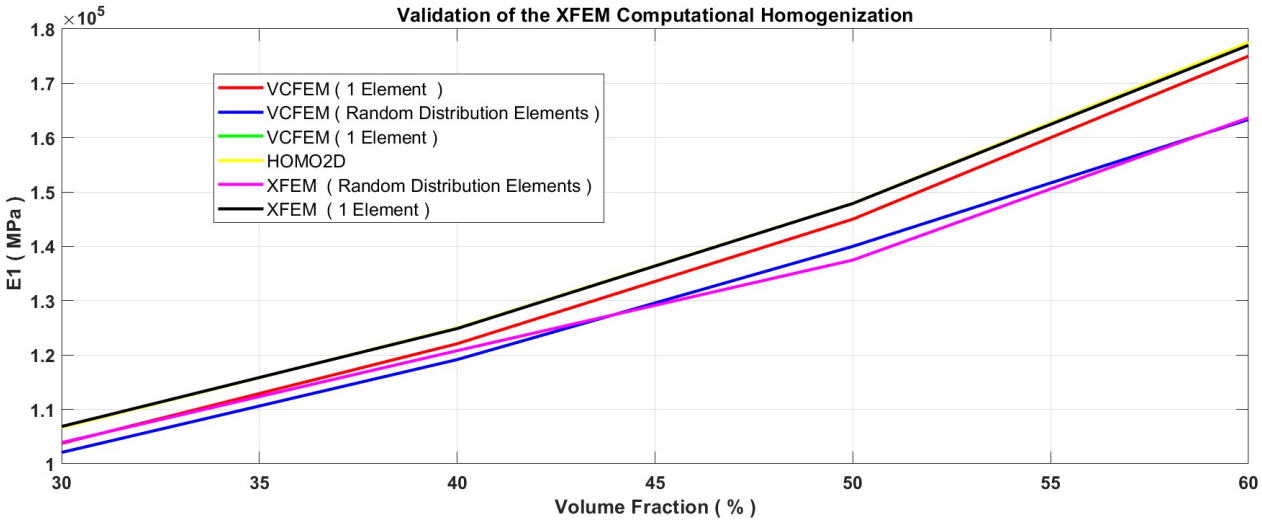

Figure 4.3: Homogenized Elastic Modulus considering different volume fractions.

4.2.2 Validation Case 2

Two representative volume elements, consisting of short and long inclusions with rectangular cross-sections are considered for homogenization and the results are compared with those based on alternative solutions provided in literature. The material properties of the constituents are given in Table 4.2.

Table 4.2: Properties of the RVE components in Figure 4.4

Parameter	**Value**
Young's modulus of the aluminum matrix	72.0×10^3 MPa
Poisson's ratio of the aluminum matrix	0.33
Young's modulus of the inclusions	400.0×10^3 MPa
Poisson's ratio of the inclusions	0.20

As shown in Figure 4.4a, for the short inclusions case, the volume fraction of inclusions is 0.375. On the other hand, from Figure 4.4b long inclusion case, it can be verified that the volume fraction is 0.5. In both cases 20×20 element mesh and periodic boundary conditions were used. Table 4.3 provides the components of the homogenized material

tensor $\hat{D}_{ijkl}$ given in Eq. (2.40) for the short inclusions case in Figure 4.4. Comparisons can be made between the XFEM-based results and those based on VCFEM and HOM02D, as well as the global-local FEM analysis in Fish and Wagiman [15] and the self consistent analytical method developed in Hashin and Wendt [20]. One can verify the excellent agreement between the homogenized material properties computed based on the developed XFEM against alternative predictions. From table 4.3, the differences between (XFEM and VCFEM) can be calculated as [D1111 (3.41%), D2222 (3.52%), D1212 (0.60%), D1122 (3.92%)].

Table 4.3: Comparison of homogenized material properties for short fibre model

	VCFEM	**HOMO2D**	**Fish and Wagiman (1992)**	**Self-Consistent**	**XFEM Computational Homogenization**
D_{1111} (MPa)	118807	122400	122457	132491	122854
D_{2222} (MPa)	139762	151200	151351	205753	144684
D_{1212} (MPa)	42440	42100	42112	51384	42692.8
D_{1122} (MPa)	38052	36230	36191	36191	36561.1

Table 4.4 shows the homogenized components of the homogenized material tensor $\hat{D}_{ijkl}$ for the long inclusion case shown in Figure 4.4b. The agreement between XFEM and VCFEM in particular, is excellent. From Table 4.4 the differences between (XFEM and VCFEM) for the long inclusions case can be calculated as [D1111 (5.82%), D2222 (8.90%), D1212 (4.1%), D1122 (0.95%)].

Table 4.4: Comparison of homogenized material properties for long fibre model

	VCFEM	**HOMO2D**	**Fish and Wagiman (1992)**	**Self-Consistent**	**XFEM Computational Homogenization**
D_{1111} (MPa)	136137	136100	136147	165548	144060
D_{2222} (MPa)	245810	245800	245810	247575	223974
D_{1212} (MPa)	46849.8	46850	46850	64887	48739.1
D_{1122} (MPa)	36076	36080	36076	42048	36418.1

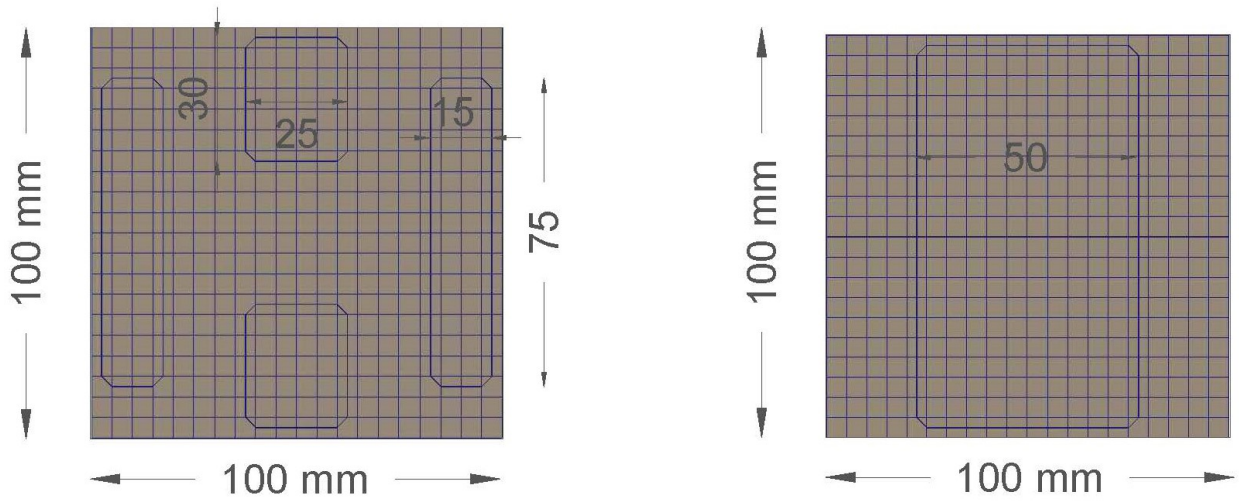

(a) Short inclusions

(b) Long inclusion

Figure 4.4: Microstructure with rectangular heterogeneities mesh for XFEM

4.3 Criteria for Optimal Selection of the Stabilization Parameter Chi in S-XFEM

In the context of stabilizing the (XFEM), the parameter χ plays an important role in controlling oscillations that arise due to quadratic bubble terms at the interface. While setting $\chi = 1$ has been shown to alleviate such issues in certain cases like Section 5.3.3, the selection of an appropriate value for χ is not always straightforward. The magnitude of χ directly influences the stiffness of the fictitious spring introduced to counteract these oscillations, and an improper value may lead to either insufficient stabilization or excessive constraint on the system. The need for a more refined approach to selecting χ arises because the optimal value may vary depending on the specific material properties, geometry, and interface conditions in different applications. Relying on a universal value like $\chi = 1$ may not provide sufficient stabilization in all scenarios, especially in complex cases where ill-conditioning is more pronounced. Therefore, it is important to develop new criteria that can guide the choice of χ for each particular case, ensuring optimal stabilization without over-constraining the system.

In Section 4.4, our new criterion will be compared with the methodology proposed by

Erkmen and Dias-da Costa [11] for calculating the penalty factor in XFEM. In their approach, they focus on the critical task of calculating the required penalty factor. This approach ultimately leads to an equation for the penalty factor χ^2, which, while not exact, provides an approximate range for use in subsequent case studies. Although the penalty factor χ^2 is based on approximations rather than exact derivation, it offers a practical range for effective stabilization.

In this section, we will not only introduce this criteria, but also attempt to answer the broader question: can we suggest a common χ for various situations? By addressing this, we aim to offer a systematic approach to determining the most suitable value of χ based on the specific characteristics of each problem, ensuring consistent performance and enhanced stability across a wide range of XFEM applications.

A new program has been developed to conduct extensive parametric studies for various cases, with the primary objective of determining a suitable chi value as shown in Figure 4.5. The program initiates with specified RVE Problem with appropriate boundary conditions such as uniform gradient, uniform traction, or periodic boundary conditions. Then, inducing a specific deformation pattern on the RVE boundaries. The program commences with pre-selected parameters such as the initial chi value, the maximum chi value, the step increment for each iteration, and the maximum allowable percentage difference between the stresses calculated by XFEM and S-XFEM. The analysis commences with the application of XFEM. Subsequently, the program proceeds with S-XFEM analysis, beginning with the initial chi value and iteratively increasing this value by the specified step increment. The iterative process continues until either the maximum chi value or the specified maximum percentage difference between XFEM and S-XFEM stress results is reached. Through this iterative approach, the program generates multiple chi values, all of which satisfy the pre-selected stress difference criteria. It is important to note that for each deformation pattern (x, y, or xy), the program compares the stresses in the corresponding direction. For example, when analyzing strain $\mathbf{g} = \left\langle \begin{array}{ccc} 1 & 0 & 0 \end{array} \right\rangle^{\mathrm{T}}$ in the x-direction, the difference between stresses in the x-direction from both methods is computed. The same procedure applies for the y and xy directions. The program then determines the optimal chi value by calculating the percentage change between the maximum normal tractions for each iteration of chi. It then selects the chi value for which the percentage change is less than 0.01. The same process is applied to the tangential tractions, resulting in two chi values. The larger of the two is considered the

optimal value, as it ensures the required percentage change of less than 0.01 is achieved in both normal and tangential tractions. For cases involving multiple inclusions, this process is repeated for each inclusion. For cases with multiple inclusions, the program repeats this process for each inclusion and identifies the most frequently occurring chi value as the optimal solution for the entire problem. The selection criteria employed by the program ensure that the optimal chi value effectively minimizes oscillations in normal and tangential tractions between the matrix and inclusions while maintaining a minimal difference in stress between XFEM and S-XFEM. It is important to emphasize that this approach is purely mathematical, focusing on optimization without any physical context.

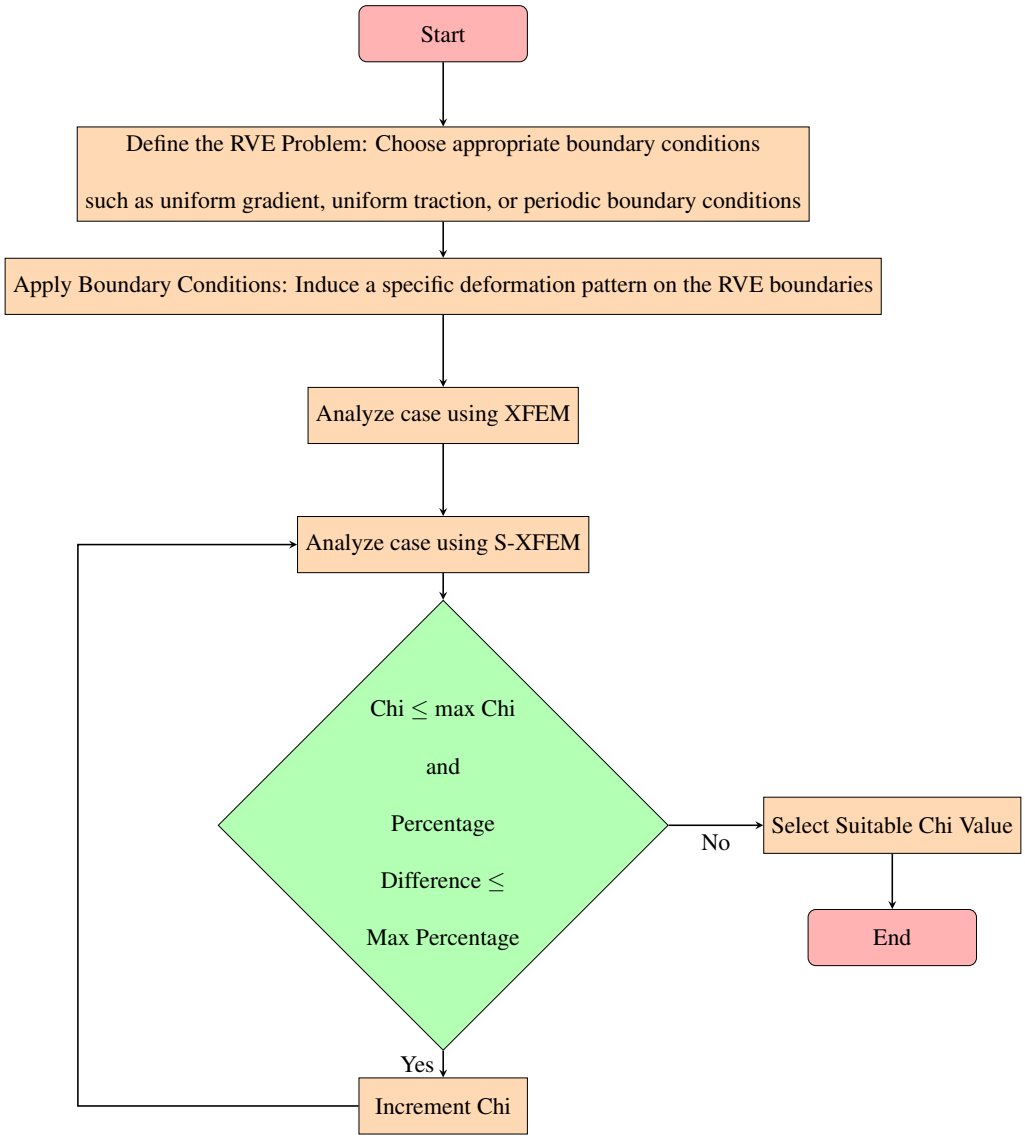

Figure 4.5: The Flowchart for Optimal Selection of the Parameter χ

4.4 Validation of Optimal Chi Selection Criteria in S-XFEM

For validation, we compare the results obtained using the developed criteria for optimal chi selection with those based on the approach proposed by Erkmen and Dias-da Costa [11]. Two Representative Volume Elements (RVEs) are used in this comparison with size set to 100 mm $\times$ 100 mm. The first RVE contains a single circular inclusion at its center, while the second consists of randomly distributed circular inclusions. In both RVEs, the volume fraction of the inclusion is 0.196. The analysis employs 30 $\times$ 30 and 50 $\times$ 50 element meshes with a 4 $\times$ 4 Gauss-Legendre quadrature rule for both uncracked and cracked bulk elements, along with 10 integration points along the cracks. This mesh configuration results in four RVE cases as shown in Figure 4.6. The interface stiffness coefficient is set as $k = 10^{20}\,\mathrm{N/mm^3}$ for all cases. The material properties of the RVE components are provided in Table 4.5. Additionally, the RVEs are analyzed under the assumption of a uniform displacement gradient, which serves as the boundary condition for all validation cases in this section.

Table 4.5: Material Properties of RVE Components.

Parameter	**Value**
Young's Modulus of Matrix	3.0×10^3 MPa
Poisson's Ratio of Matrix	0.20
Young's Modulus of Inclusions	70.0×10^3 MPa
Poisson's Ratio of Inclusions	0.20

In the following discussion, we refer to our criterion as approach 1, while the methodology proposed by Erkmen and Dias-da Costa [11] is referred as approach 2. Based on the results of both approaches see Table 4.6, approach 1 provides a single χ value for each strain type (displacement gradient g) across all cases, whereas approach 2 yields two distinct χ values (χ_1 and χ_2) for each case. In the case of a single inclusion see Figures 4.6a and 4.6b, approach 1 provides a χ value that falls within the range of the two separate χ values from approach 2 and is sufficient to reduce the oscillations at the interface. Higher χ val-

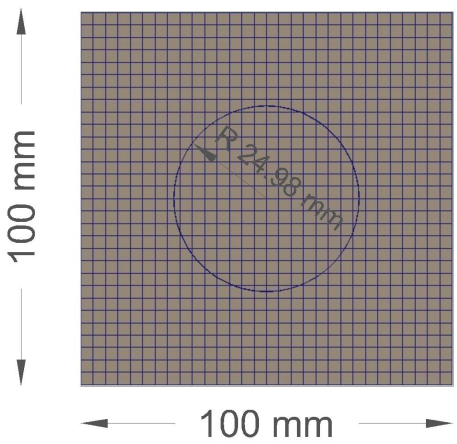

(a) Mesh A - 30x30 Grid with Single Inclusion

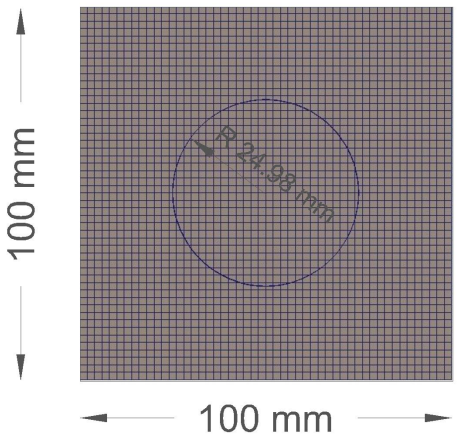

(b) Mesh B - 50x50 Grid with Single Inclusion

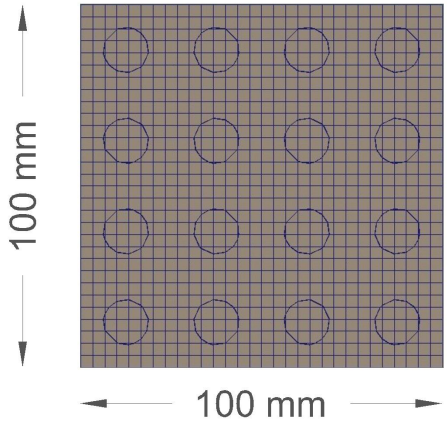

(c) Mesh C - 30x30 Grid with 16 Inclusions

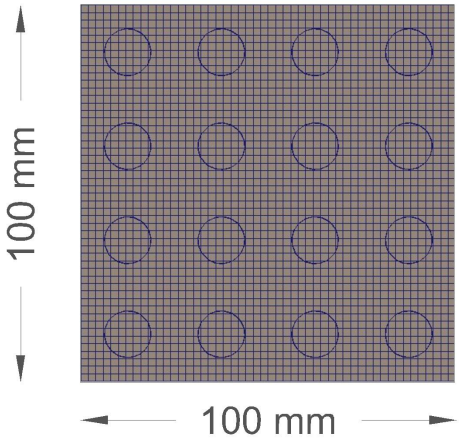

(d) Mesh D - 50x50 Grid with 16 Inclusions

Figure 4.6: RVEs used in the analyses

ues, though effective in preventing oscillations, can over-dampen the tractions, leading to inaccurate results. For multiple inclusions see Figures 4.6c and 4.6d, approach 1 continues to provide a χ value within the range of the two values from approach 2. However, when the mesh size increases, as seen in Figure 4.6d, approach 1 produces a higher χ value that falls outside the range of approach 2. Overall, the difference between the values obtained from the two approaches is minimal, as we are dealing with small χ values in this context.

Table 4.6: Comparison of χ Values for Different Strain Types Across Two Computational Approaches

Displacement Gradient g	**Mesh A**			**Mesh B**		
	Approach 1	**Approach 2**		**Approach 1**	**Approach 2**	
	χ	χ_1	χ_2	χ	χ_1	χ_2
$\mathbf{g} = \langle 1 \quad 0 \quad 0 \rangle^{\mathrm{T}}$	0.5	0.87	0.38	0.6	0.66	0.24
$\mathbf{g} = \langle 0 \quad 1 \quad 0 \rangle^{\mathrm{T}}$	0.5	0.87	0.38	0.6	0.66	0.24
$\mathbf{g} = \langle 0 \quad 0 \quad 1 \rangle^{\mathrm{T}}$	0.5	0.87	0.38	0.6	0.66	0.24
Displacement Gradient g	**Mesh C**			**Mesh D**		
	Approach 1	**Approach 2**		**Approach 1**	**Approach 2**	
	χ	χ_1	χ_2	χ	χ_1	χ_2
$\mathbf{g} = \langle 1 \quad 0 \quad 0 \rangle^{\mathrm{T}}$	0.6	0.8	0.48	0.8	0.61	0.25
$\mathbf{g} = \langle 0 \quad 1 \quad 0 \rangle^{\mathrm{T}}$	0.6	0.8	0.48	0.8	0.61	0.25
$\mathbf{g} = \langle 0 \quad 0 \quad 1 \rangle^{\mathrm{T}}$	0.4	0.8	0.48	0.9	0.61	0.25

4.5 Closing Remarks

The validation of the developed XFEM-based computational homogenization framework demonstrates its accuracy and effectiveness in predicting the homogenized properties of heterogeneous materials. Comparisons with established methods, including the standard finite element-based homogenization (HOM02D) in Guedes and Kikuchi [18] and the Voronoi Cell Finite Element Method (VCFEM) in Ghosh et al. [17], reveal a strong agreement, reinforcing the reliability of the proposed approach. The study systematically evaluates two

microstructural configurations: a single circular inclusion and a random dispersion of inclusions, with varying volume fractions. The results indicate that the homogenized Young's modulus in the horizontal direction (E1) for randomly dispersed inclusions is slightly lower than that for single inclusion cases, highlighting the influence of microstructural heterogeneity. Furthermore, for rectangular inclusions, the XFEM predictions align well with alternative numerical and analytical solutions, including global-local FEM analysis in Fish and Wagiman [15] and the self-consistent method in Hashin and Wendt [20], with only minor discrepancies. The differences between XFEM and VCFEM remain within an acceptable range for both short and long inclusion cases, demonstrating the robustness of the XFEM framework in capturing the effective material response. Overall, the findings confirm that the developed XFEM-based homogenization methodology provides an accurate and computationally efficient tool for modeling heterogeneous materials, making it a viable alternative to conventional homogenization techniques.

The selection of the stabilization parameter χ in S-XFEM is important for mitigating oscillations while maintaining numerical accuracy. This study (4.3) introduced a systematic criterion for determining the optimal χ value through an iterative MATLAB-based parametric approach, ensuring minimal deviation between XFEM and S-XFEM stress results. Compared to the methodology proposed by Erkmen and Dias-da Costa [11], which provides an approximate range for χ based on the condition number of the stiffness matrix, the proposed approach offers a single, optimized χ value tailored to each strain type across different cases. The validation using RVEs with single and multiple inclusions demonstrated that the proposed criterion effectively balances stabilization and accuracy by selecting the largest χ value that satisfies both normal and tangential traction constraints. Unlike the predefined ranges of χ obtained from existing methods, the new approach systematically identifies an optimal value that prevents excessive damping while ensuring stability. This refinement enhances the robustness of S-XFEM in handling complex interface conditions, offering a more reliable and generalizable stabilization strategy across diverse applications.

Chapter 5

Parametric Studies

5.1 Introduction

In the field of computational mechanics, parametric studies play an important role in evaluating the sensitivity of numerical models to key parameters that influence their accuracy and reliability. One of the fundamental aspects of such studies is the investigation of mesh dependency, which assesses how the discretization of a representative volume element (RVE) affects the computed elastic properties. The accuracy of stress distributions and homogenized material responses is significantly influenced by the chosen mesh size, necessitating a balance between computational efficiency and precision. Additionally, the interface bond properties between inclusions and the matrix have a profound impact on the overall mechanical behavior of composite materials. The transition from an imperfect bond to a perfect bond, controlled by the interface stiffness coefficient, alters stress distributions and homogenized elastic properties, particularly when different boundary conditions are applied. Understanding these effects is essential for ensuring the validity of computational homogenization techniques, such as those based on the (XFEM), in modeling the mechanical behavior of heterogeneous materials.

Beyond mesh dependency and interface bonding, the modeling of embedded fibers as inclusions introduces additional complexities in finite element analyses. Traditional finite element method (FEM) models often assume a perfect bond between fibers and the surround-

ing matrix, potentially oversimplifying the mechanical interactions within fiber-reinforced composites. By employing the XFEM-based homogenization approach, this study evaluates the impact of bond stiffness variation on the computed material properties and compares the results with conventional FEM models. Moreover, the stabilization of XFEM for stiff interface bonds is explored to address numerical challenges that arise when dealing with high interface stiffness values. These parametric studies provide valuable insights into the applicability and limitations of XFEM in capturing the mechanical behavior of composite materials with embedded inclusions or fibers. The findings contribute to the ongoing development of advanced numerical techniques that enhance the predictive capabilities of computational models for engineering applications.

In computational mechanics, the accurate selection of the parameter χ is important for achieving reliable results in numerical simulations involving the (XFEM) and its stabilized variant (S-XFEM). This study (5.4) systematically determines the optimal χ value by evaluating four representative cases that reflect diverse microstructural configurations: a centrally positioned circular inclusion, a centrally located rectangular inclusion, randomly distributed rectangular inclusions with varying orientations, and randomly distributed circular inclusions. Each case is analyzed within a 100 mm $\times$ 100 mm representative volume element (RVE) under periodic boundary conditions. The initial χ value is set to 0.10, with increments of 0.10 up to a maximum of 1.00, ensuring that the percentage difference between XFEM and S-XFEM stress calculations does not exceed 5.00%. To capture a broad spectrum of material behavior, four studies are conducted, varying the modulus of elasticity of the matrix and inclusions to represent scenarios with large, small, or negligible differences in stiffness. Additionally, the influence of interfacial bonding conditions is examined by considering both stiff and imperfect bonds, with interface stiffness coefficients set at $k = 10^6\,\mathrm{N/mm^3}$ and $k = 10^2\,\mathrm{N/mm^3}$, respectively. The findings provide a comprehensive framework for selecting the optimal χ value under different microstructural and material conditions, contributing to the accurate modeling of heterogeneous materials using XFEM-based approaches.

5.2 Effect of mesh size

A group of parametric studies are conducted by varying the mesh size, interface stiffness coefficient and boundary conditions. To illustrate the effect of mesh size, we refer to the first RVE model introduced in Figure 4.1a which is the case of 30% volume ratio with only one inclusion placed at the central of the RVE. The calculated elastic properties are based on one imposed strain configuration. We imposed the horizontal axial strain i.e. $\mathbf{g} = \left\langle \begin{array}{ccc} 1 & 0 & 0 \end{array} \right\rangle^{\mathrm{T}}$ and presented the mesh of the RVE models against the computed homogenized properties in Table 5.1, where the average stresses are also compared against maximum stresses. It can be verified from Table 5.1 that the 20×20 element mesh, that was used previously, is generating results within 5% when compared against the 30×30 element mesh.

Table 5.1: The effect of mesh size in strain at x-direction

Mesh Size (No. of Elements)	**Average Stresses (MPa)**			**Maximum Stresses (MPa)**		
	σ_{11}	σ_{22}	σ_{12}	σ_{11}	σ_{22}	σ_{12}
10×10	118254	35790	-7.062×10^{-6}	163000	48200	27400
15×15	117684	35911.5	-1.210×10^{-6}	162000	51900	35400
20×20	117850	35988.7	7.773×10^{-7}	161000	51500	30400
25×25	117804	35959.1	9.290×10^{-7}	161000	52900	30100
30×30	118121	36020.6	-1.564×10^{-7}	162000	48500	29400

5.3 Illustrating the interface bond effect

5.3.1 Alternative RVE boundary conditions

The sensitivity of the homogenized elastic properties to the type of boundary conditions is determined while the interface stiffness coefficient is varied. Figures 5.1 and 5.2 show the

average stresses while transitioning from imperfect bond towards stiff bond as the interface stiffness is increased. We used the first RVE model introduced in Figure 4.1a which is the case of 30% volume ratio with only one inclusion placed at the central of the RVE. All three types of boundary conditions are tested: periodic, displacement and traction boundary conditions. Figure 5.1 shows the average axial stress in the horizontal direction due to unit strain also in the horizontal direction i.e. $\mathrm{g} = \left\langle \begin{array}{ccc} 1 & 0 & 0 \end{array} \right\rangle^{\mathrm{T}}$. Figure 5.2 shows the average shear stress due to unit shear strain, i.e. $\mathrm{g} = \left\langle \begin{array}{ccc} 0 & 0 & 1 \end{array} \right\rangle^{\mathrm{T}}$. It can be seen from both Figures 5.1 and 5.2 that interface stiffness change has very significant influence on the average stress while difference in the results due to change in the assumed RVE boundary condition are within 5% at any interface stiffness level.

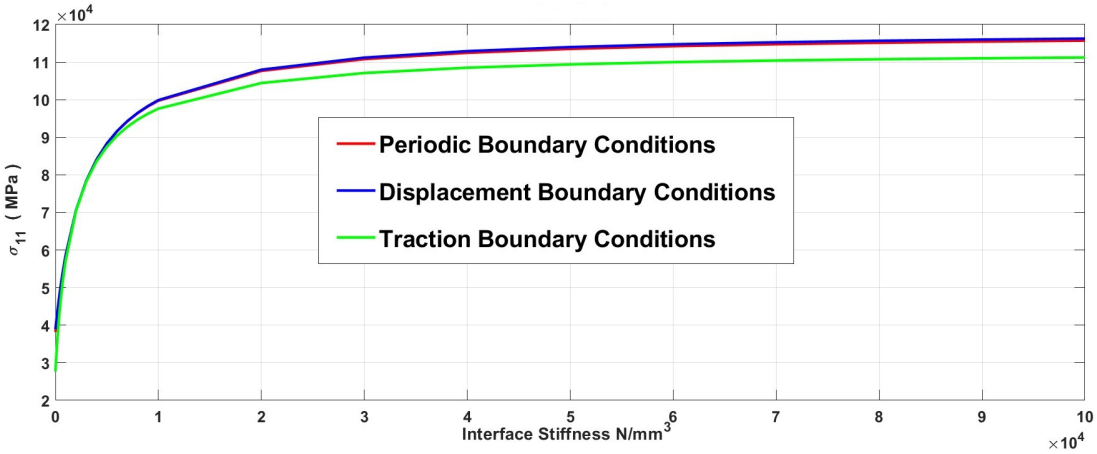

Figure 5.1: Average stress $\hat{\sigma}^1_{11}$ due to $\mathrm{g} = \left\langle \begin{array}{ccc} 1 & 0 & 0 \end{array} \right\rangle^{\mathrm{T}}$

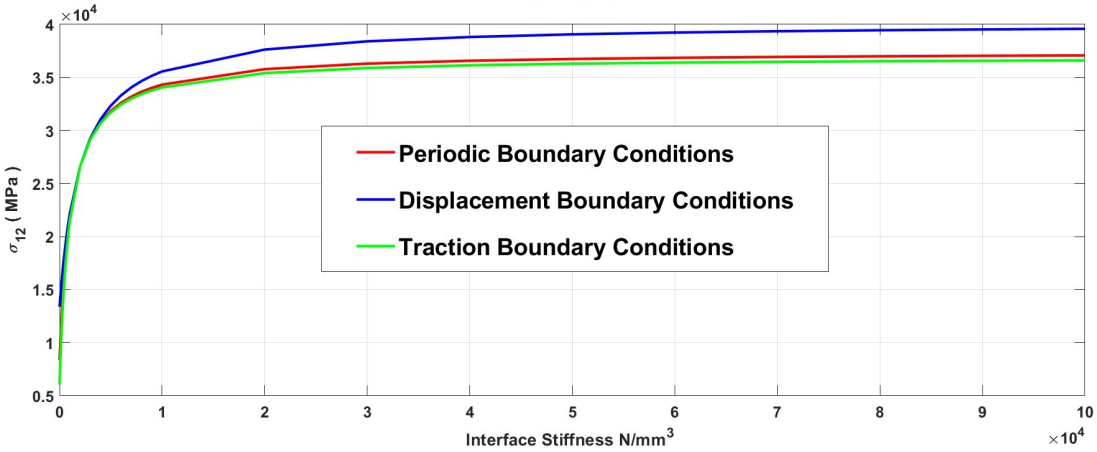

Figure 5.2: Average stress $\hat{\sigma}^3_{12}$ due to $\mathrm{g} = \left\langle \begin{array}{ccc} 0 & 0 & 1 \end{array} \right\rangle^{\mathrm{T}}$

Figure 5.3 provides a comparison of the stress distributions within the RVE between the cases of imperfect bond when $k = 1\,\mathrm{N/mm^3}$ and stiff bond, i.e. $k = 10 \times 10^4\,\mathrm{N/mm^3}$. By comparing the maximum stress values in Figure 5.3 against the average stress in Figure 5.1, it can be seen that as the stiffness between inclusions and matrix decreases the ratio between maximum stresses and average stresses increases. On the other hand, the maximum σ_{11} stress value for the stiff bond case is significantly higher than that of the imperfect bond case when they are both subjected to $\mathrm{g} = \left\langle \begin{array}{ccc} 1 & 0 & 0 \end{array} \right\rangle^{\mathrm{T}}$ as the overall stiffness of the RVE is significantly affected by the interface bond between the components.

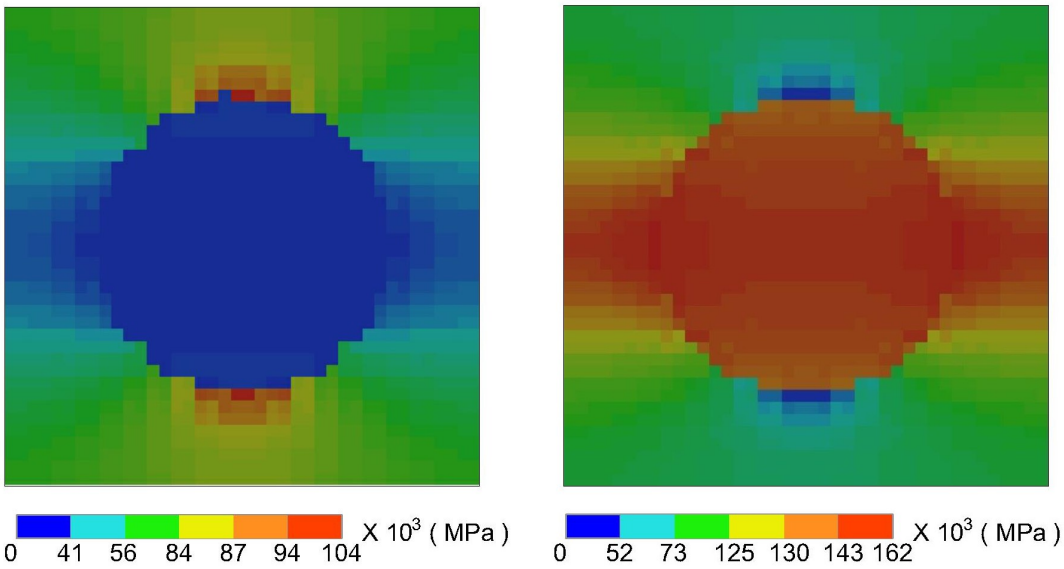

(a) Imperfect Bond (b) Stiff Bond

Figure 5.3: The local stress distribution σ_{11} due to $\mathrm{g} = \left\langle \begin{array}{ccc} 1 & 0 & 0 \end{array} \right\rangle^{\mathrm{T}}$

5.3.2 Modelling of fibres as inclusions via the XFEM

In many practical applications fibres are embedded into a raisin matrix to stiffen and strengthen the material. In finite element modelling of the RVE, 1D truss/bar type elements have been used previously e.g. Qian et al. [47]. However, it is crucial to take such the imperfect bond between the fibre and the matrix into account. For that purpose, we apply the developed XFEM based homogenization approach to a fibre embedded composite problem and compare against the FEM based approach. The material properties of the RVE content is as given in Table 5.2. We again use an RVE size of 100×100 mm^2 and 20×20

element mesh was used in both cases. As shown in Figure 5.4, the same mesh was used for both the XFEM and FEM based modelling. In the XFEM based modelling approach we have gradually reduced the bond stiffness, while adopting periodic boundary conditions only. The predictions of the average stress under unit strain in the horizontal direction i.e. $\mathrm{g} = \left\langle \begin{array}{ccc} 1 & 0 & 0 \end{array} \right\rangle^{\mathrm{T}}$ are presented in Tables 5.3 and 5.4.

Table 5.2: Material properties for matrix, inclusions and fibres

Parameter	**Value**
Young's modulus of the matrix	20.0×10^3 MPa
Poisson's ratio of the matrix	0.20
Young's modulus of the inclusions	60.0×10^3 MPa
Poisson's ratio of the inclusions	0.20
Young's modulus of the fibers	60.0×10^3 MPa
Area of fibers	45° fibers: 8 mm^2, horizontal and vertical fibers: 5 mm^2

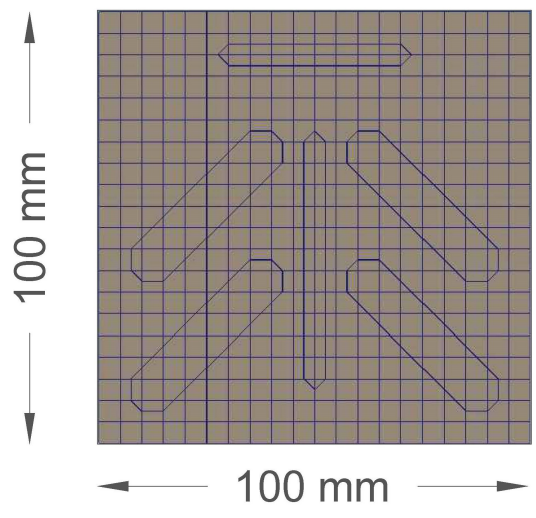

(a) The RVE model for inclusion

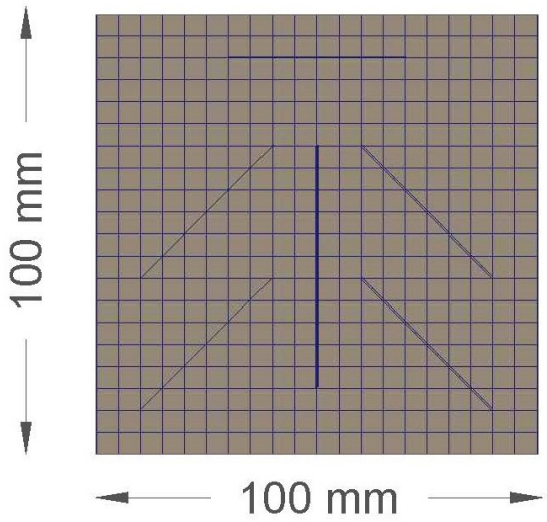

(b) The RVE model for fibres

Figure 5.4: RVE Models

Table 5.3: Results for RVE model of inclusions

Interface Stiffness k (N/mm^3)	**Young's Modulus** E_1 (MPa)	**Poisson's Ratio**	**Average Stresses** (MPa)		
			σ_{11}	σ_{22}	σ_{12}
100000	25160.20169	0.208223449	26300.5	5476.38	-0.330764
50000	24790.9238	0.206087	25890.5	5335.7	-0.642009
10000	22806.87464	0.192809636	23687.5	4567.17	-2.31657
5000	21301.53193	0.182432503	22034.9	4019.88	-4.44804
1000	16444.95744	0.152016831	16834	2559.05	-22.7246

Table 5.4: Results for RVE model of fibres

Young's Modulus E_1 (MPa)	**Poisson's Ratio**	**Average Stresses** (MPa)		
		σ_{11}	σ_{22}	σ_{12}
20085.7026	0.206184736	20977.5	4325.24	-4.11777×10^{-13}

It should be noted that in the FEM modelling the bond can only be assumed perfect between the fibres and the matrix. Despite the perfect bond assumption in FEM modelling, the average stress values presented in Table 5.4 are smaller than those of the perfect bond XFEM model given in the first row of Table 5.3. This difference can be attributed to the fact that even though the axial stiffness properties of the fibres are identical, in the XFEM modelling fibres also contribute to the overall stiffness with their lateral as well as shear stiffness properties. For example, the vertical fibre in the FEM model see Figure 5.4b has almost no influence on the calculated values under the imposed unit strain in horizontal direction. On the other hand, in the XFEM-based model shown in Figure 5.4a, the vertical member has a finite thickness and introduces a phase change which increases the stiffness in all directions in the region where it is embedded.

5.3.3 Stabilization of the XFEM for stiff interface bond

Based on the modification to the XFEM that we have introduced in section 3.4, in the current section we aim to illustrate the applicability and the outcomes of the developed methodology by performing parametric studies on two of the previously introduces cases. First, we refer back to the case introduced in Figure 4.1a whose material properties have already been introduced in Table 4.1. We assume stiff bond, for which the interface stiffness is taken as $k = 10^6\ \mathrm{N/mm^3}$ and for the imperfect bond the interface stiffness is taken as $k = 10^3\ \mathrm{N/mm^3}$. We impose unit strain in the horizontal direction i.e. $\mathrm{g} = \left\langle \begin{array}{ccc} 1 & 0 & 0 \end{array} \right\rangle^{\mathrm{T}}$. Table 5.5 provides a comparison of the homogenized elastic properties and average stresses, from which it can be verified that average values are slightly affected when either XFEM or the stabilized XFEM formulation (S-XFEM) is used. However, as discussed before the interface stiffness change has significant influence on the homogenized values.

Table 5.5: Equivalent elastic properties and Average stresses for RVE Figure 4.1a

Type (XFEM or S-XFEM)	**Case 1**				
	Young's Modulus E_1 (MPa)	**Poisson's Ratio**	**Average Stresses** (MPa)		
			σ_{11}	σ_{22}	σ_{12}
XFEM Stiff Bond	106859.62	0.31	117850.00	35988.70	0.00
XFEM Imperfect Bond	55237.87	0.24	58523.50	13866.70	0.00
S-XFEM Stiff Bond	110033.64	0.30	120750.00	35972.30	0.00
S-XFEM Imperfect Bond	55826.23	0.24	59143.40	14006.70	-0.72

On the other hand, Figure 5.5 shows the interface tractions around the inclusion in both normal and tangential directions based on the standard XFEM and the stabilized XFEM. Figure 5.5a shows that when the interface bond is stiff, the standard XFEM formulation produces oscillatory results. By comparing Figures 5.5a and 5.5b, it can be verified that S-XFEM alleviates the oscillatory behaviour of the interface traction field. However, as shown in Figures 5.5c and 5.5d for when the interface bond stiffness is reduced the oscillations diminish and both XFEM and S-XFEM produce almost identical results. Thus, oscillatory

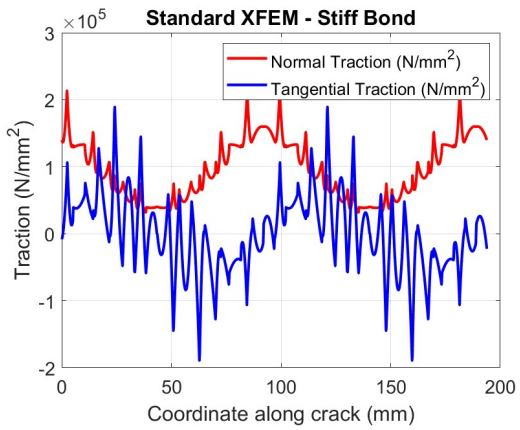

(a) XFEM - Stiff Bond

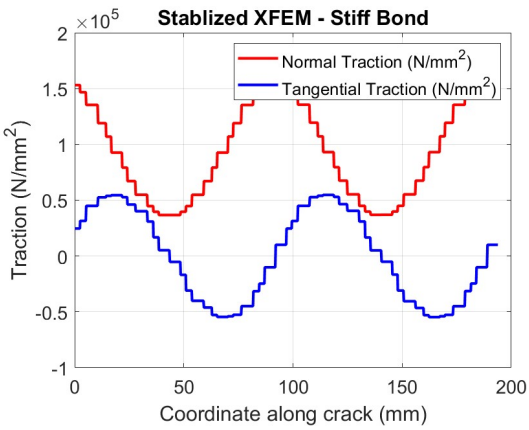

(b) SXFEM - Stiff Bond

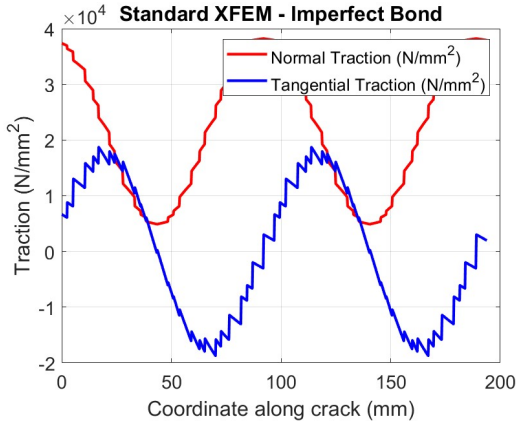

(c) XFEM - Imperfect Bond

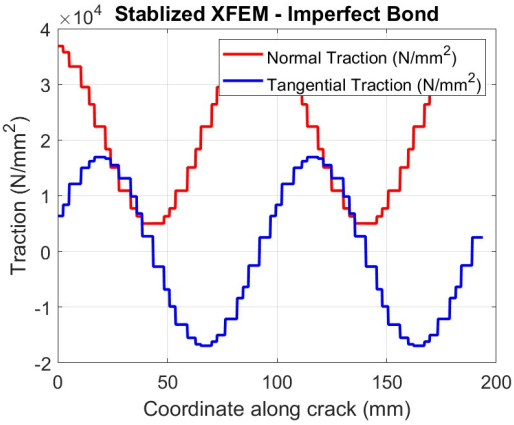

(d) SXFEM - Imperfect Bond

Figure 5.5: Interface Tractions - Stabilization - Case 1

tractions tend to occur when the interface stiffness is increased.

For the second case, we refer back to Figure 4.4b, whose material properties have been previously provided in Table 4.2. The homogenized properties for four different analysis options is presented in Table 5.6. Again for the stiff bond we use $k = 10^6\ \mathrm{N/mm^3}$ and for the imperfect bond we use $k = 10^3\ \mathrm{N/mm^3}$ for the interface stiffness. Table 5.6 provides a comparison of the homogenized elastic properties and average stress predictions between XFEM and S-XFEM under unit strain in the horizontal direction i.e. $\mathbf{g} = \left\langle \begin{array}{ccc} 1 & 0 & 0 \end{array} \right\rangle^{\mathrm{T}}$. Again, it can be verified that average values are slightly affected between XFEM and S-XFEM.

Table 5.6: Equivalent elastic properties and Average stresses for RVE Figure 4.4b

Type (XFEM or S-XFEM)	**Case 2**				
	Young's Modulus E_1 (MPa)	**Poisson's Ratio**	**Average Stresses** (MPa)		
			σ_{11}	σ_{22}	σ_{12}
XFEM Stiff Bond	134857.77	0.25	144060.00	36410.40	0.00
XFEM Imperfect Bond	40702.49	0.18	42055.70	7544.02	0.00
S-XFEM Stiff Bond	141607.85	0.25	151440.00	38588.00	0.00
S-XFEM Imperfect Bond	41964.78	0.18	43332.20	7697.64	0.00

On the other hand, Figure 5.6 shows the interface tractions around the inclusion in both normal and tangential directions. It is interesting to note that XFEM produces a significant jump in the stiff interface case only at the four corners where the interface is inclined. As explained in section 3.4, this is because those bubble components disappear when the interface is horizontal or vertical, i.e. $\xi_a = \xi_b$ or $\zeta_a = \zeta_b$. It can be verified from Figure 5.6b that S-XFEM suppresses the traction jumps at the corner in the case of the stiff interface, which otherwise is in excellent agreement with the standard XFEM results.

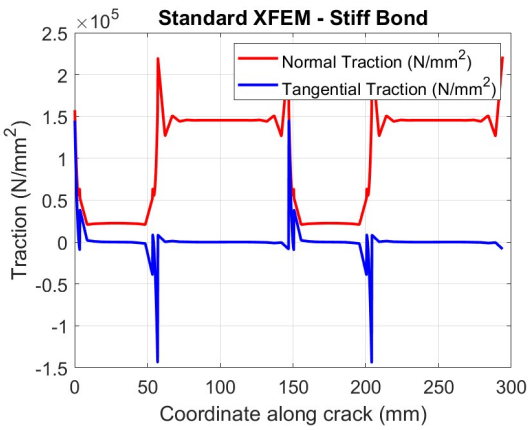

(a) XFEM - Stiff Bond

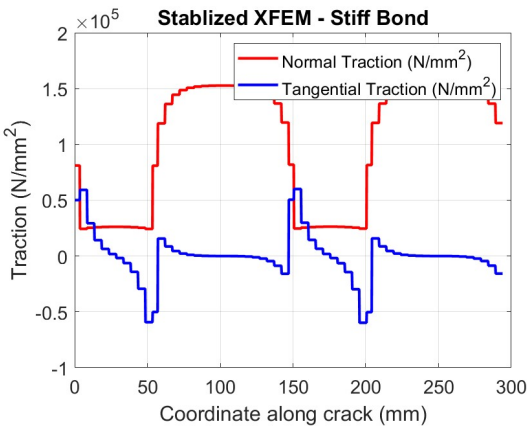

(b) SXFEM - Stiff Bond

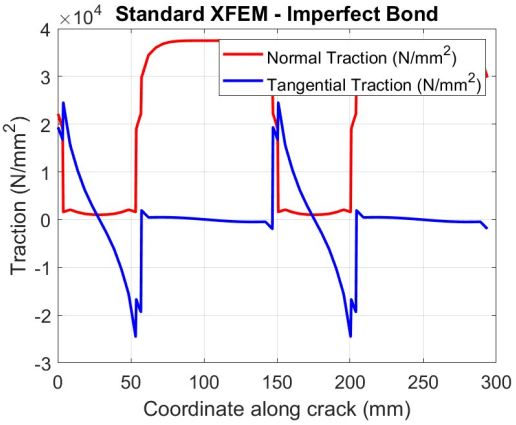

(c) XFEM - Imperfect Bond

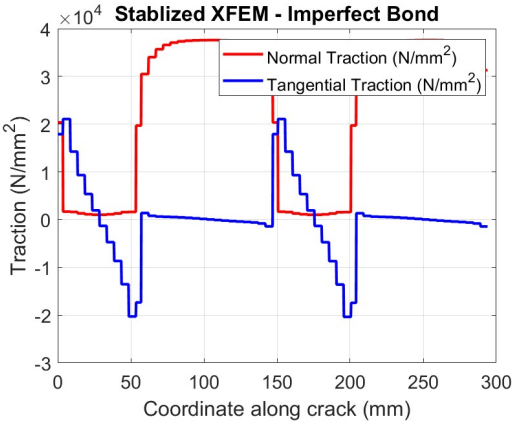

(d) SXFEM - Imperfect Bond

Figure 5.6: Interface Tractions - Stabilization - Case 2

5.4 Selection of the optimal Chi value

In this section, the criterion in Figure 4.5 will be applied to four distinct cases, each representing potential scenarios encountered in nature. Case 1 involves a single circular inclusion located at the center of the representative volume element (RVE) see Figure 4.1a. Case 2 considers a single rectangular inclusion positioned at the center of the RVE see Figure 4.4b. Case 3 examines randomly distributed rectangular inclusions with varying orientations see Figure 5.4a. Finally, Case 4 explores randomly distributed circular inclusions see Figure 4.2a. In all four cases, the size of the representative volume element (RVE) is set to 100 mm $\times$ 100 mm, with periodic boundary conditions applied throughout. The initial value χ is selected as 0.10. And, the increment is 0.10. And, the maximum value of χ is selected as

1.00. Also, the maximum allowable percentage difference between the stresses calculated by XFEM and S-XFEM is selected as 5.00. To ensure a comprehensive analysis, various material properties were tested to cover a wide range of possibilities. Additionally, the effect of stiff and imperfect bonds at the interface between the matrix and the inclusions was examined. The interface stiffness coefficient for stiff bond is set as $k = 10^6\,\mathrm{N/mm^3}$. And, the interface stiffness coefficient for imperfect bond is set as $k = 10^2\,\mathrm{N/mm^3}$. Regarding material properties, particularly the modulus of elasticity for both the matrix and inclusions, different values were employed. Small variations in the modulus of elasticity were used to simulate scenarios where the values for the matrix and inclusions were either similar or slightly different. In contrast, significantly different values were used to model cases where the modulus of elasticity for the matrix and inclusions varied substantially. And to achieve that, four studies will be conducted. Study 1 (see Table 5.7) will investigate cases with a large difference in the modulus of elasticity between the matrix and inclusion. Study 2 (see Table 5.8) will examine cases where the modulus of elasticity values for the matrix and inclusion are large but closely matched. Study 3 (see Table 5.9) will address scenarios with a small difference in the modulus of elasticity between the two. Finally, Study 4 (see Table 5.10) will analyse cases where the modulus of elasticity values for both the matrix and inclusion are small and closely matched.

Table 5.7: Material Properties of RVE Components in Study 1

Parameter	**Case 1**	**Case 2**	**Case 3**	**Case 4**
Young's Modulus of Matrix (MPa)	150.0×10^3	100.0×10^3	40.0×10^3	120.5×10^3
Poisson's Ratio of Matrix	0.20	0.33	0.20	0.33
Young's Modulus of Inclusions (MPa)	600.0×10^3	350.0×10^3	80.0×10^3	550.0×10^3
Poisson's Ratio of Inclusions	0.30	0.20	0.20	0.33

Table 5.8: Material Properties of RVE Components in Study 2

Parameter	**Case 1**	**Case 2**	**Case 3**	**Case 4**
Young's Modulus of Matrix (MPa)	600.0×10^3	400.0×10^3	250.0×10^3	500.0×10^3
Poisson's Ratio of Matrix	0.30	0.20	0.20	0.20
Young's Modulus of Inclusions (MPa)	500.0×10^3	400.0×10^3	240.0×10^3	550.0×10^3
Poisson's Ratio of Inclusions	0.30	0.20	0.20	0.20

Table 5.9: Material Properties of RVE Components in Study 3

Parameter	**Case 1**	**Case 2**	**Case 3**	**Case 4**
Young's Modulus of Matrix (MPa)	50.0×10^3	40.0×10^3	40.0×10^3	40.0×10^3
Poisson's Ratio of Matrix	0.20	0.33	0.20	0.20
Young's Modulus of Inclusions (MPa)	10.0×10^3	100.0×10^3	20.0×10^3	20.0×10^3
Poisson's Ratio of Inclusions	0.20	0.20	0.20	0.20

Table 5.10: Material Properties of RVE Components in Study 4

Parameter	**Case 1**	**Case 2**	**Case 3**	**Case 4**
Young's Modulus of Matrix (MPa)	50.0×10^3	50.0×10^3	20.0×10^3	22.0×10^3
Poisson's Ratio of Matrix	0.20	0.20	0.20	0.20
Young's Modulus of Inclusions (MPa)	50.0×10^3	50.0×10^3	20.0×10^3	20.0×10^3
Poisson's Ratio of Inclusions	0.20	0.20	0.20	0.20

Table 5.11: Optimal Chi Values for Various Deformation Patterns and Interface Stiffness Types in Study 1

Displacement Gradient g	Case 1				Case 2			
	Stiff Bond		Imperfect Bond		Stiff Bond		Imperfect Bond	
	Chi Value	Differences	Chi Value	Differences	Chi Value	Differences	Chi Value	Differences
$g = \left\langle 1 \quad 0 \quad 0 \right\rangle^T$	0.6	0.6942	0.1	-0.00094	0.4	2.9072	0.1	-0.0256
$g = \left\langle 0 \quad 1 \quad 0 \right\rangle^T$	0.7	0.6969	0.1	-0.00094	0.3	4.0298	0.1	-0.0048
$g = \left\langle 0 \quad 0 \quad 1 \right\rangle^T$	0.5	0.8947	0.1	-0.00235	0.4	4.9950	0.1	-0.0495
Displacement Gradient g	**Case 3**				**Case 4**			
	Stiff Bond		**Imperfect Bond**		**Stiff Bond**		**Imperfect Bond**	
	Chi Value	**Differences**	**Chi Value**	**Differences**	**Chi Value**	**Differences**	**Chi Value**	**Differences**
$g = \left\langle 1 \quad 0 \quad 0 \right\rangle^T$	1.0	1.7134	0.1	0.0247	0.1	4.9523	0.1	-0.1223
$g = \left\langle 0 \quad 1 \quad 0 \right\rangle^T$	1.0	1.5495	0.1	0.0210	0.1	5.3565	0.1	-0.0676
$g = \left\langle 0 \quad 0 \quad 1 \right\rangle^T$	1.0	0.9872	0.1	0.0451	0.1	4.8096	0.1	-0.1006

Table 5.12: Optimal Chi Values for Various Deformation Patterns and Interface Stiffness Types in Study 2

Displacement Gradient g	Case 1				Case 2			
	Stiff Bond		Imperfect Bond		Stiff Bond		Imperfect Bond	
	Chi Value	Differences	Chi Value	Differences	Chi Value	Differences	Chi Value	Differences
$g = \left\langle 1 \quad 0 \quad 0 \right\rangle^T$	0.2	0.0363	0.1	-0.0009	0.6	0.0266	0.1	-0.0102
$g = \left\langle 0 \quad 1 \quad 0 \right\rangle^T$	0.2	0.0366	0.1	-0.0009	0.6	0.0268	0.1	-0.0016
$g = \left\langle 0 \quad 0 \quad 1 \right\rangle^T$	0.1	0.0608	0.1	-0.0025	0.7	0.0271	0.1	-0.0570
Displacement Gradient g	**Case 3**				**Case 4**			
	Stiff Bond		**Imperfect Bond**		**Stiff Bond**		**Imperfect Bond**	
	Chi Value	**Differences**	**Chi Value**	**Differences**	**Chi Value**	**Differences**	**Chi Value**	**Differences**
$g = \left\langle 1 \quad 0 \quad 0 \right\rangle^T$	1.0	0.3870	0.1	0.0042	0.1	-0.0535	0.1	-0.0065
$g = \left\langle 0 \quad 1 \quad 0 \right\rangle^T$	1.0	0.3368	0.1	0.0035	0.1	-0.0335	0.1	-0.0052
$g = \left\langle 0 \quad 0 \quad 1 \right\rangle^T$	1.0	0.2973	0.1	0.0107	0.1	-0.0519	0.1	-0.0133

Table 5.13: Optimal Chi Values for Various Deformation Patterns and Interface Stiffness Types in Study 3

Displacement Gradient g	**Case 1**				**Case 2**			
	Stiff Bond		**Imperfect Bond**		**Stiff Bond**		**Imperfect Bond**	
	Chi Value	**Differences**	**Chi Value**	**Differences**	**Chi Value**	**Differences**	**Chi Value**	**Differences**
$g = \left\langle 1 \quad 0 \quad 0 \right\rangle^T$	0.7	0.6760	0.1	-0.0043	0.3	1.5985	0.1	-0.0373
$g = \left\langle 0 \quad 1 \quad 0 \right\rangle^T$	0.8	0.6763	0.1	-0.0043	0.2	1.7327	0.1	-0.0100
$g = \left\langle 0 \quad 0 \quad 1 \right\rangle^T$	0.5	0.9865	0.1	-0.0050	1.0	3.1211	0.1	-0.0549
Displacement Gradient g	**Case 3**				**Case 4**			
	Stiff Bond		**Imperfect Bond**		**Stiff Bond**		**Imperfect Bond**	
	Chi Value	**Differences**	**Chi Value**	**Differences**	**Chi Value**	**Differences**	**Chi Value**	**Differences**
$g = \left\langle 1 \quad 0 \quad 0 \right\rangle^T$	1.0	0.3025	0.1	0.0261	0.3	0.8849	0.1	-0.0689
$g = \left\langle 0 \quad 1 \quad 0 \right\rangle^T$	1.0	0.3374	0.1	0.0240	0.3	0.8064	0.1	-0.0677
$g = \left\langle 0 \quad 0 \quad 1 \right\rangle^T$	1.0	0.1987	0.1	0.0520	0.2	0.7506	0.1	-0.1240

Table 5.14: Optimal Chi Values for Various Deformation Patterns and Interface Stiffness Types in Study 4

Displacement Gradient g	**Case 1**				**Case 2**			
	Stiff Bond		**Imperfect Bond**		**Stiff Bond**		**Imperfect Bond**	
	Chi Value	Differences	Chi Value	Differences	Chi Value	Differences	Chi Value	Differences
$g = \left\langle 1 \quad 0 \quad 0 \right\rangle^T$	0.1	0.0075	0.1	-0.0071	0.1	-0.0050	0.1	-0.0336
$g = \left\langle 0 \quad 1 \quad 0 \right\rangle^T$	0.1	0.0075	0.1	-0.0071	0.1	-0.0050	0.1	-0.0073
$g = \left\langle 0 \quad 0 \quad 1 \right\rangle^T$	0.1	0.0101	0.1	-0.0165	0.1	-0.0029	0.1	-0.0478
Displacement Gradient g	**Case 3**				**Case 4**			
	Stiff Bond		**Imperfect Bond**		**Stiff Bond**		**Imperfect Bond**	
	Chi Value	Differences	Chi Value	Differences	Chi Value	Differences	Chi Value	Differences
$g = \left\langle 1 \quad 0 \quad 0 \right\rangle^T$	1.0	-0.0197	0.1	0.0424	0.1	0.0338	0.1	-0.1500
$g = \left\langle 0 \quad 1 \quad 0 \right\rangle^T$	1.0	-0.0250	0.1	0.0397	0.1	0.0468	0.1	-0.2927
$g = \left\langle 0 \quad 0 \quad 1 \right\rangle^T$	1.0	-0.0143	0.1	0.0733	0.1	0.0228	0.1	-0.2277

Based on the parametric studies conducted (see Tables 5.11, 5.12, 5.13 and 5.14), it is clear that a universal χ value cannot be applied across various situations. Each case requires a specific χ value to minimize oscillations in tractions and ensure that the differences between XFEM and S-XFEM results remain minimal. The appropriate χ value for each case is influenced by several factors, including boundary conditions, loading direction, material properties, mesh size, number of inclusions, shape and orientation of inclusions, their distribution, RVE size, and the number of integration points (for both uncracked and cracked elements, as well as along the cracks). Moreover, cases with multiple inclusions often require different χ values for each inclusion within the same scenario. In summary, the developed criteria provide a tailored χ value for each specific case, ensuring accurate results.

5.5 Closing Remarks

The parametric studies conducted in these sections (5.2 and 5.3) provide important insights into the influence of mesh size, interface bond conditions, and modeling approaches on the homogenized elastic properties of composite materials. The analysis of mesh refinement demonstrates that a 20×20 element mesh produces results within 5.00% accuracy compared to a finer 30×30 mesh, indicating computational efficiency without significant loss of accuracy. The investigation of interface bond effects reveals that as the interface stiffness increases, the average stress values approach those of a perfect bond, with variations in boundary conditions yielding differences within a 5.00% margin. Moreover, the comparison between XFEM and FEM modeling approaches highlights the significance of incorporating imperfect bond conditions, as XFEM allows for a more accurate representation of interfacial effects. The findings indicate that the stiffness contribution of fibers is more realistically captured in XFEM due to its ability to account for lateral and shear stiffness, whereas FEM assumes a perfect bond, leading to discrepancies in stress predictions. Furthermore, the study illustrates that as the interface bond weakens, the ratio between maximum and average stresses increases, emphasizing the role of interfacial properties in overall mechanical behavior. These results underscore the importance of carefully selecting mesh resolution, boundary conditions, and modeling techniques when simulating composite materials, ensuring accurate representation of their mechanical response.

The parametric investigation conducted in this section (5.4) systematically analyzed the selection of the optimal χ value across four distinct cases representing various inclusion geometries and distributions within a representative volume element (RVE). The study encompassed four different material property configurations, ranging from scenarios with a significant disparity in the modulus of elasticity between the matrix and inclusions to cases where the properties were closely matched. The results demonstrated that the optimal χ value is influenced by multiple factors, including the type of inclusion, the material contrast, and the nature of the interface stiffness (stiff or imperfect bond). Additionally, the results reveal that imperfect interface bonds generally necessitate lower χ values compared to stiff bonds to maintain the allowable percentage difference between XFEM and S-XFEM stress calculations. The interplay between the deformation pattern and the inclusion configuration further affects the optimal selection of χ, with variations observed across different displacement gradients. These insights contribute to the broader understanding of parameter selection in extended finite element modeling, ensuring both computational efficiency and accuracy in modeling heterogeneous materials.

Chapter 6

Conclusion

The study of computational homogenization, as presented in chapter 2, provides a systematic approach for deriving effective macroscopic properties of heterogeneous materials while accounting for their microscopic behaviours. Through the adoption of fundamental principles, such as the equilibrium equations and constitutive relations, the framework allows for the representation of complex material behaviour with reduced computational complexity.

This chapter 2 began with the definition of field equations and the weak form, emphasizing the relationship between stress, strain, and displacement fields within heterogeneous media. By utilizing the constitutive relationship in index notation, we introduced the stress tensor and material modulus matrix, capturing the isotropic properties of the material. The Galerkin weak form formulation of the equilibrium equations demonstrated how governing laws can be enforced weakly, thus allowing for numerical treatment using finite element methods.

An important component of computational homogenization is the concept of scale separation, where the macroscopic and microscopic scales are decoupled. By introducing a scaling parameter , which governs the ratio of microscopic to macroscopic dimensions, the asymptotic expansion of displacement and stress fields was formulated. This enabled the decomposition of the displacement field into a macroscopic part, which governs the global response, and higher-order microscopic contributions, which reflect the oscillatory effects of material heterogeneity. Through this formulation, the homogenized material properties

were obtained as the effective response when , a condition representing infinitesimally small micro-structures.

The derivation of the homogenized equilibrium equations revealed that the macroscopic displacement field is independent of the fast coordinate , while the stress tensor comprises contributions from both macroscopic and microscopic scales. By introducing a two-scale approach, the analysis extended to a periodic cell representative of the micro-structure, where localized oscillations are averaged to produce global homogenized properties. The resulting variational setting provided a rigorous mathematical foundation for the homogenization process, ensuring compatibility between microscopic fluctuations and macroscopic gradients.

By integrating the equilibrium conditions over the unit cell and incorporating virtual displacement fluctuations, the microscopic stress-strain relationship was established. This relationship enabled the computation of the effective material properties, which subsequently replaced the heterogeneous domain with an equivalent homogeneous material for macroscopic analysis. Such homogenized models significantly reduce computational costs while maintaining accuracy in predicting global behaviour.

Overall, computational homogenization offers a powerful tool for analyzing complex heterogeneous materials, where direct numerical simulations of the entire structure would be complicated. The ability to separate scales and derive effective properties not only simplifies the problem but also provides valuable insights into material behaviour across multiple length scales. The methods discussed in this chapter form the foundation for multi-scale modelling, enabling engineers and scientists to design and analyze advanced materials with tailored properties.

Future extensions of this work could involve higher-order homogenization methods, which account for non-local effects and capture finer details of micro-structural behaviour. Additionally, incorporating time-dependent effects, such as plasticity, into the homogenization framework would further enhance its applicability to real-world materials and structures. By continuing to refine these methods, computational homogenization will remain at the forefront of multi-scale modelling, enabling the efficient analysis and design of next-generation materials and systems.

The chapter 3 has provided a detailed exploration of the methodologies and mathematical formulations necessary for implementing boundary conditions in (RVE) simulations. The use of (XFEM) has proven to be a robust framework for addressing the complexities

associated with heterogeneous materials, particularly in accommodating discontinuities and intricate boundary constraints. By leveraging vector-matrix notations and discretized forms, the chapter has elucidated the essential components of computational homogenization, enabling the effective resolution of microstructural mechanics problems.

The detailed exposition on RVE boundary conditions including uniform displacement gradient, uniform traction, and periodic displacement underscores the versatility of the proposed framework. The uniform displacement gradient condition simplifies the boundary interactions by assuming no micro-fluctuations, while the uniform traction condition addresses the challenges of maintaining stress uniformity across boundaries. The periodic displacement condition, with its emphasis on anti-periodicity and reduced degrees of freedom, demonstrates an elegant mechanism for handling periodic boundary interactions in heterogeneous media. Each condition is supported by comprehensive mathematical derivations, offering a clear roadmap for implementation.

Furthermore, the inclusion of illustrative schematics and mesh representations enhances the understanding of the physical and numerical concepts presented. The detailed partitioning of matrices and vectors into boundary and internal nodes, coupled with the explicit treatment of boundary constraints, ensures that the formulations remain grounded in practical applicability. These representations bridge the gap between theoretical formulations and real-world computational challenges.

The chapter 3 also emphasizes the role of interpolation functions and their interpolatory properties in simplifying the computational complexity of the RVE problem. By carefully constructing these functions, the boundary conditions are seamlessly integrated into the global problem, ensuring numerical stability and accuracy. This aspect is particularly critical when dealing with fine-scale fluctuations and their periodic counterparts, as shown in the periodic displacement condition.

The mathematical rigor and methodological depth of this chapter 3 contribute significantly to the field of computational mechanics. By addressing both theoretical foundations and practical implementation strategies, the chapter equips researchers and practitioners with the tools necessary to tackle complex homogenization problems in heterogeneous materials. The systematic approach adopted here lays a strong foundation for future research and development in computational homogenization, particularly in advancing XFEM-based methodologies.

The stabilization approach for the XFEM presented in section 3.4 effectively addresses

the excessive traction oscillations caused by the quadratic bubble terms in the displacement jump representation. By decomposing the discontinuity jump into an element-wise constant and a quadratic bubble component, the method enables the formulation of a stabilized framework. The introduction of the scalar parameter χ and its incorporation into the stabilization matrix $\hat{\Theta}$ further demonstrate the robustness of this approach. The orthogonality condition ensures that the stabilization effect is achieved without compromising the physical accuracy of the XFEM solutions. Moreover, the use of Legendre polynomials to define the stabilization matrix highlights the mathematical rigor and flexibility of the proposed methodology. The careful design of this stabilization technique ensures numerical stability while maintaining computational efficiency, which is important for practical applications. The insights gained from this stabilization framework not only enhance the reliability of the XFEM for stiff interface problems but also provide a foundation for further advancements in the development of robust numerical methods for discontinuous problems.

In conclusion, this chapter 3 has demonstrated the efficacy of computational homogenization with XFEM in capturing the nuanced behavior of heterogeneous materials. The formulations and methodologies presented here not only provide a robust framework for current applications but also pave the way for innovative extensions, such as multi-scale modeling and the integration of machine learning techniques for enhanced computational efficiency. As computational power continues to advance, the approaches outlined in this chapter are poised to play a pivotal role in solving increasingly complex material design and analysis problems. Also, this chapter has developed a robust stabilization methodology to address traction oscillations in the (XFEM) caused by the quadratic bubble terms within the displacement jump formulation.

The validation of the XFEM-based computational homogenization framework demonstrates its accuracy in predicting the homogenized material properties of composite microstructures. Comparisons with established methods in literature review, including HOMO2D, VCFEM, global-local FEM, and self-consistent analytical models, reveal excellent agreement, with minor deviations within an acceptable range. The results indicate that the XFEM approach effectively captures the influence of inclusion distribution and volume fraction on the effective material properties. Notably, randomly dispersed microstructures exhibit slightly lower homogenized elastic moduli compared to single-inclusion models, highlighting the role of microstructural configuration. Furthermore, the computed homogenized stiffness components for both short and long inclusion cases align well with alternative nu-

merical and analytical predictions, reinforcing the robustness of the XFEM-based method for multiscale material modeling.

The selection of the stabilization parameter χ in S-XFEM is important for mitigating oscillations at the interface while maintaining computational accuracy. A new criterion was developed to determine the optimal χ value systematically, ensuring minimal stress deviation between XFEM and S-XFEM while avoiding over-constraining the system. The proposed methodology, validated against an existing penalty factor approach, demonstrated its effectiveness across various representative volume elements, including cases with single and multiple inclusions. Comparative analyses showed that the proposed approach provided a single χ value that consistently reduced oscillations without excessive damping, unlike the existing method, which yielded multiple χ values for different strain types. The validation results confirmed the robustness of the proposed criterion in stabilizing numerical solutions across different problem configurations. Consequently, this work offers a systematic and computationally efficient approach for selecting χ, enhancing the stability and accuracy of S-XFEM in modeling complex material interfaces.

The parametric studies conducted in this work demonstrate the influence of mesh size, interface bond conditions, and boundary conditions on the homogenized elastic properties of representative volume elements (RVEs). It is observed that a 20×20 element mesh provides results within 5.00% accuracy compared to a 30×30 mesh, ensuring computational efficiency without significant loss of precision. The interface bond effect is shown to be a critical factor, where increasing interface stiffness significantly influences stress distributions, with perfect bonds leading to higher maximum stresses compared to imperfect bonds. Additionally, the choice of boundary conditions has a relatively minor effect, with variations remaining within 5.00% across different conditions. The XFEM-based approach effectively captures imperfect bonding effects, demonstrating its advantages over conventional FEM, particularly in modeling embedded fibers where lateral and shear stiffness contributions impact overall behavior. Additionally, the stabilization methodology introduced for stiff interface bonds is validated through parametric analyses, confirming its effectiveness in ensuring numerical stability and accuracy in highly stiff interface conditions. These findings provide valuable insights into the modeling of composite materials, highlighting the importance of appropriate numerical techniques in capturing the mechanical behavior of complex microstructures.

In this study, the selection of the optimal χ value was investigated across four distinct

cases representing different inclusion geometries and distributions within a representative volume element (RVE). The analysis considered variations in material properties, including the modulus of elasticity of the matrix and inclusions, as well as the influence of interface stiffness under both stiff and imperfect bonding conditions. Across four studies, different contrasts in elastic properties were examined, ranging from large discrepancies to closely matched values, to comprehensively assess the impact of material heterogeneity. The results demonstrated that the optimal χ value varies depending on the inclusion geometry, material contrast, and deformation mode, with stiff and imperfect bonding conditions yielding distinct trends. These findings provide critical insights into the appropriate selection of χ to enhance the accuracy and efficiency of S-XFEM in modeling heterogeneous materials.

Bibliography

[1] Konstantinos Agathos, Stéphane PA Bordas, and Eleni Chatzi. Improving the conditioning of xfem/gfem for fracture mechanics problems through enrichment quasi-orthogonalization. *Computer Methods in Applied Mechanics and Engineering*, 346: 1051–1073, 2019.

[2] A Ahmed and LJ Sluys. Anomalous behavior of bilinear quadrilateral finite elements for modeling cohesive cracks with xfem/gfem. *International journal for numerical methods in engineering*, 94(5):454–472, 2013.

[3] Éric Béchet, Nicolas Moës, and Barbara Wohlmuth. A stable lagrange multiplier space for stiff interface conditions within the extended finite element method. *International Journal for Numerical Methods in Engineering*, 78(8):931–954, 2009.

[4] Ted Belytschko and Tom Black. Elastic crack growth in finite elements with minimal remeshing. *International journal for numerical methods in engineering*, 45(5):601–620, 1999.

[5] Ted Belytschko, Nicolas Moës, Shuji Usui, and Chandu Parimi. Arbitrary discontinuities in finite elements. *International Journal for Numerical Methods in Engineering*, 50(4):993–1013, 2001.

[6] Ted Belytschko, Wing Kam Liu, Brian Moran, and Khalil Elkhodary. *Nonlinear finite elements for continua and structures*. John wiley & sons, 2014.

[7] DC Borges, WMG Quaresma, GR Fernandes, and JJC Pituba. Evaluation of a proposed model for concrete at mesoscopic scale. *Revista IBRACON de Estruturas e Materiais*, 10:1087–1112, 2017.

[8] E Bosco, VG Kouznetsova, and MGD3340087 Geers. Multi-scale computational homogenization–localization for propagating discontinuities using x-fem. *International Journal for Numerical Methods in Engineering*, 102(3-4):496–527, 2015.

[9] René de Borst, Joris JC Remmers, and Alan Needleman. Mesh-independent discrete numerical representations of cohesive-zone models. *Engineering fracture mechanics*, 73(2):160–177, 2006.

[10] E Erkmen, S Malek, and C Ayranci. An xfem-based computational homogenization framework for thermal conductivity evaluation of composites with imperfectly bonded inclusions. *Engineering Research Express*, 2(4):045030, 2020.

[11] Emre Erkmen and Daniel Dias-da Costa. Alleviation of the oscillatory tractions in the extended finite element method. In *Canadian Society of Civil Engineering Annual Conference*, pages 715–731. Springer, 2022.

[12] Recep Emre Erkmen and Daniel Dias-da Costa. Stabilization of the extended finite element method for stiff embedded interfaces and inclusions. *International Journal for Numerical Methods in Engineering*, 122(24):7378–7408, 2021.

[13] John Douglas Eshelby. The determination of the elastic field of an ellipsoidal inclusion, and related problems. *Proceedings of the royal society of London. Series A. Mathematical and physical sciences*, 241(1226):376–396, 1957.

[14] Gabriela R Fernandes, Maria Júlia Marques Silva, Jordana F Vieira, and José JC Pituba. A 2d rve formulation by the boundary element method considering phase debonding. *Engineering Analysis with Boundary Elements*, 104:259–276, 2019.

[15] Jacob Fish and Amir Wagiman. Multiscale finite element method for a periodic and nonperiodic heterogeneous medium. *ASME Applied Mechanics Division-publications-AMD*, 157:95–95, 1993.

[16] Erez Gal, E Suday, and Haim Waisman. Homogenization of materials having inclusions surrounded by layers modeled by the extended finite element method. *International Journal for Multiscale Computational Engineering*, 11(3), 2013.

[17] Somnath Ghosh, Kyunghoon Lee, and Suresh Moorthy. Multiple scale analysis of heterogeneous elastic structures using homogenization theory and voronoi cell finite element method. *International journal of solids and structures*, 32(1):27–62, 1995.

[18] JoséMiranda Guedes and Noboru Kikuchi. Preprocessing and postprocessing for materials based on the homogenization method with adaptive finite element methods. *Computer methods in applied mechanics and engineering*, 83(2):143–198, 1990.

[19] Zvi Hashin and Shmuel Shtrikman. A variational approach to the theory of the elastic behaviour of multiphase materials. *Journal of the Mechanics and Physics of Solids*, 11(2):127–140, 1963.

[20] Zvi Hashin and FW Wendt. Theory of composite materials. *Mechanics of composite materials*, pages 201–242, 1970.

[21] Rodney Hill. A self-consistent mechanics of composite materials. *Journal of the Mechanics and Physics of Solids*, 13(4):213–222, 1965.

[22] Badri Hiriyur, Haim Waisman, and George Deodatis. Uncertainty quantification in homogenization of heterogeneous microstructures modeled by xfem. *International Journal for Numerical Methods in Engineering*, 88(3):257–278, 2011.

[23] Mark H Holmes. *Introduction to perturbation methods*, volume 20. Springer Science & Business Media, 2012.

[24] H Ji and JE Dolbow. On strategies for enforcing interfacial constraints and evaluating jump conditions with the extended finite element method. *International Journal for Numerical Methods in Engineering*, 61(14):2508–2535, 2004.

[25] Toufik Kanit, Samuel Forest, Isabelle Galliet, Valérie Mounoury, and Dominique Jeulin. Determination of the size of the representative volume element for random composites: statistical and numerical approach. *International Journal of solids and structures*, 40(13-14):3647–3679, 2003.

[26] Varvara Kouznetsova, WAM Brekelmans, and FPT1005 Baaijens. An approach to micro-macro modeling of heterogeneous materials. *Computational mechanics*, 27(1): 37–48, 2001.

[27] Fredrik Larsson, Kenneth Runesson, Sepehr Saroukhani, and Reza Vafadari. Computational homogenization based on a weak format of micro-periodicity for rve-problems. *Computer Methods in Applied Mechanics and Engineering*, 200(1-4):11–26, 2011.

[28] Amir Latifaghili, Milad Bybordiani, Recep Emre Erkmen, and Daniel Dias-da Costa. An extended finite element method with polygonal enrichment shape functions for crack propagation and stiff interface problems. *International Journal for Numerical Methods in Engineering*, 123(6):1432–1455, 2022.

[29] Sheng Liang, Menghui Liao, Chongzhi Tu, and Rong Luo. Fabricating and determining representative volume elements of two-dimensional random aggregate numerical model for asphalt concrete without damage. *Construction and Building Materials*, 357:129339, 2022.

[30] Charles T Lynch. *CRC Handbook of Materials Science: Material Composites and Refractory Materials*, volume 2. CRC press, 2020.

[31] Siming Ma, Xuezheng Zhang, Tijun Chen, and Xiaoming Wang. Microstructure-based numerical simulation of the mechanical properties and fracture of a ti-al3ti core-shell structured particulate reinforced a356 composite. *Materials & Design*, 191:108685, 2020.

[32] Jens M Melenk and Ivo Babuška. The partition of unity finite element method: basic theory and applications. *Computer methods in applied mechanics and engineering*, 139(1-4):289–314, 1996.

[33] Alexander Menk and Stéphane PA Bordas. A robust preconditioning technique for the extended finite element method. *International Journal for Numerical Methods in Engineering*, 85(13):1609–1632, 2011.

[34] Julia Mergheim, Ellen Kuhl, and Paul Steinmann. A finite element method for the computational modelling of cohesive cracks. *International Journal for Numerical Methods in Engineering*, 63(2):276–289, 2005.

[35] Jean-Claude Michel, Hervé Moulinec, and Pierre Suquet. Effective properties of composite materials with periodic microstructure: a computational approach. *Computer methods in applied mechanics and engineering*, 172(1-4):109–143, 1999.

[36] Christian Miehe and Andreas Koch. Computational micro-to-macro transitions of discretized microstructures undergoing small strains. *Archive of Applied Mechanics*, 72:300–317, 2002.

[37] Nicolas Moës and Ted Belytschko. Extended finite element method for cohesive crack growth. *Engineering fracture mechanics*, 69(7):813–833, 2002.

[38] Nicolas Moës, John Dolbow, and Ted Belytschko. A finite element method for crack growth without remeshing. *International journal for numerical methods in engineering*, 46(1):131–150, 1999.

[39] Nicolas Moës, Eric Béchet, and Matthieu Tourbier. Imposing dirichlet boundary conditions in the extended finite element method. *International Journal for Numerical Methods in Engineering*, 67(12):1641–1669, 2006.

[40] Hervé Moulinec and Pierre Suquet. A numerical method for computing the overall response of nonlinear composites with complex microstructure. *Computer methods in applied mechanics and engineering*, 157(1-2):69–94, 1998.

[41] Thuc Nhu Nguyen, R Emre Erkmen, Leandro FM Sanchez, and Jianchun Li. Stiffness degradation of concrete due to alkali-silica reaction: A computational homogenization approach. *ACI Materials Journal*, 2020.

[42] Vinh Phu Nguyen, Oriol Lloberas-Valls, Martijn Stroeven, and Lambertus Johannes Sluys. On the existence of representative volumes for softening quasi-brittle materials–a failure zone averaging scheme. *Computer Methods in Applied Mechanics and Engineering*, 199(45-48):3028–3038, 2010.

[43] E Norouzi, B Li, and RE Erkmen. Computational homogenization to identify elastic properties of soil-rock mixtures at normal and freezing temperatures. In *ARMA US Rock Mechanics/Geomechanics Symposium*, pages ARMA–2021. ARMA, 2021.

[44] Emad Norouzi, Biao Li, and R Emre Erkmen. Modelling equivalent elastic properties of imperfectly bonded soil-rock mixtures using an xfem-based computational homogenization. *Computers and Geotechnics*, 144:104638, 2022.

[45] RU Patil, BK Mishra, and Indra Vir Singh. A new multiscale xfem for the elastic properties evaluation of heterogeneous materials. *International Journal of Mechanical Sciences*, 122:277–287, 2017.

[46] José J de C Pituba, Gabriela R Fernandes, and Eduardo A de Souza Neto. Modeling of cohesive fracture and plasticity processes in composite microstructures. *Journal of Engineering Mechanics*, 142(10):04016069, 2016.

[47] C Qian, LT Harper, TA Turner, S Li, and NA Warrior. Establishing size effects in discontinuous fibre composites using 2d finite element analysis. *Computational materials science*, 64:106–111, 2012.

[48] Joris JC Remmers, R de Borst, and Alan Needleman. A cohesive segments method for the simulation of crack growth. *Computational mechanics*, 31:69–77, 2003.

[49] Angelo Simone. Partition of unity-based discontinuous elements for interface phenomena: computational issues. *Communications in Numerical Methods in Engineering*, 20(6):465–478, 2004.

[50] M Stroeven, H Askes, and LJ1060 Sluys. Numerical determination of representative volumes for granular materials. *Computer methods in applied mechanics and engineering*, 193(30-32):3221–3238, 2004.

[51] Natarajan Sukumar, David L Chopp, Nicolas Moës, and Ted Belytschko. Modeling holes and inclusions by level sets in the extended finite-element method. *Computer methods in applied mechanics and engineering*, 190(46-47):6183–6200, 2001.

[52] Erik Svenning, Martin Fagerström, and Fredrik Larsson. On computational homogenization of microscale crack propagation. *International Journal for Numerical Methods in Engineering*, 108(1):76–90, 2016.

[53] S Turteltaub. Inelastic analysis of structures, milan jirásek and zdeněk p. bažant, john wiley & sons, 2002, isbn 0-471-98716-6, 758 pages. *Structural and Multidisciplinary Optimization*, 24(1):87–88, 2002.

[54] Giulio Ventura and Claudia Tesei. Stabilized x-fem for heaviside and nonlinear enrichments. *Advances in Discretization Methods: Discontinuities, Virtual Elements, Fictitious Domain Methods*, pages 209–228, 2016.

[55] Garth N Wells and LJ1013 Sluys. A new method for modelling cohesive cracks using finite elements. *International Journal for numerical methods in engineering*, 50(12): 2667–2682, 2001.

[56] Peter Wriggers and SO Moftah. Mesoscale models for concrete: Homogenisation and damage behaviour. *Finite elements in analysis and design*, 42(7):623–636, 2006.

[57] Chunsheng Zhou, Kefei Li, and Xiaoyun Pang. Effect of crack density and connectivity on the permeability of microcracked solids. *Mechanics of Materials*, 43(12): 969–978, 2011.

Appendix A

Mathematical Derivations - Computational Homogenization

A.1 Derivations - Field equations and the weak form

A.1.1 Galerkin equilibrium - Eq. (2.9)

We start with the equilibrium equation in the domain Ω Eq. (2.6). Then, we multiply the equilibrium equation by δu_i and integrate over the domain Ω

$$\int_\Omega \delta u_i \frac{\partial \sigma_{ij}}{\partial x_j} \, \mathrm{d}\Omega - \int_\Omega \delta u_i p_i \, \mathrm{d}\Omega = 0 \tag{A.1}$$

We now focus on the first integral

$$\int_\Omega \delta u_i \frac{\partial \sigma_{ij}}{\partial x_j} \, \mathrm{d}\Omega$$

To transform this term, we use the divergence theorem which states

$$\int_{\Omega} \frac{\partial v_j}{\partial x_j} \, \mathrm{d}\Omega = \int_{\Gamma} v_j n_j \, \mathrm{d}\Gamma \tag{A.2}$$

where v_j is a vector field, n_j is the outward unit normal to the boundary Γ, and Γ is the boundary of Ω. We apply this theorem to the first integral by choosing $v_j = \delta u_i \sigma_{ij}$. Thus,

$$\int_{\Omega} \frac{\partial (\delta u_i \sigma_{ij})}{\partial x_j} \, \mathrm{d}\Omega = \int_{\Gamma} \delta u_i \sigma_{ij} n_j \, \mathrm{d}\Gamma \tag{A.3}$$

Then, by using the product rule for differentiation, we have

$$\frac{\partial (\delta u_i \sigma_{ij})}{\partial x_j} = \delta u_i \frac{\partial \sigma_{ij}}{\partial x_j} + \sigma_{ij} \frac{\partial \delta u_i}{\partial x_j} \tag{A.4}$$

Then, substituting this back into the integral, we get

$$\int_{\Omega} \delta u_i \frac{\partial \sigma_{ij}}{\partial x_j} \, \mathrm{d}\Omega = \int_{\Omega} \left(\frac{\partial (\delta u_i \sigma_{ij})}{\partial x_j} - \sigma_{ij} \frac{\partial \delta u_i}{\partial x_j} \right) \, \mathrm{d}\Omega \tag{A.5}$$

Then, by separating the integrals, we get

$$\int_{\Omega} \delta u_i \frac{\partial \sigma_{ij}}{\partial x_j} \, \mathrm{d}\Omega = \int_{\Omega} \frac{\partial (\delta u_i \sigma_{ij})}{\partial x_j} \, \mathrm{d}\Omega - \int_{\Omega} \sigma_{ij} \frac{\partial \delta u_i}{\partial x_j} \, \mathrm{d}\Omega \tag{A.6}$$

Then, by applying the divergence theorem to the first term on the right-hand side, we get

$$\int_{\Omega} \frac{\partial (\delta u_i \sigma_{ij})}{\partial x_j} \, \mathrm{d}\Omega = \int_{\Gamma} \delta u_i \sigma_{ij} n_j \, \mathrm{d}\Gamma \tag{A.7}$$

where Γ is the boundary of Ω and n_j is the outward normal to Γ. Then, we have

$$\int_{\Omega} \delta u_i \frac{\partial \sigma_{ij}}{\partial x_j} \, \mathrm{d}\Omega = \int_{\Gamma} \delta u_i \sigma_{ij} n_j \, \mathrm{d}\Gamma - \int_{\Omega} \sigma_{ij} \frac{\partial \delta u_i}{\partial x_j} \, \mathrm{d}\Omega \tag{A.8}$$

This boundary Γ consists of two parts: Γ_D (Dirichlet boundary) and Γ_N (Neumann boundary). Therefore

$$\int_{\Gamma} \delta u_i \sigma_{ij} n_j \, \mathrm{d}\Gamma = \int_{\Gamma_D} \delta u_i \sigma_{ij} n_j \, \mathrm{d}\Gamma_D + \int_{\Gamma_N} \delta u_i \sigma_{ij} n_j \, \mathrm{d}\Gamma_N \tag{A.9}$$

Since the admissible displacement field u_i is prescribed on the boundary Γ_D according to Eq. (2.7), the variation δu_i must vanish on this boundary, where $\delta u_i = 0$ on the Dirichlet boundary Γ_D. This ensures that any virtual displacement (variation) considered in the weak form does not alter the fixed boundary conditions. Then, the first term vanishes

$$\int_{\Gamma_D} \delta u_i \sigma_{ij} n_j \, \mathrm{d}\Gamma_D = 0 \tag{A.10}$$

Then, we have

$$\int_{\Gamma} \delta u_i \sigma_{ij} n_j \, \mathrm{d}\Gamma = \int_{\Gamma_N} \delta u_i \sigma_{ij} n_j \, \mathrm{d}\Gamma_N \tag{A.11}$$

Then, by combining these results, we obtain

$$\int_{\Omega} \delta u_i \frac{\partial \sigma_{ij}}{\partial x_j} \, \mathrm{d}\Omega = \int_{\Gamma_N} \delta u_i \sigma_{ij} n_j \, \mathrm{d}\Gamma_N - \int_{\Omega} \sigma_{ij} \frac{\partial \delta u_i}{\partial x_j} \, \mathrm{d}\Omega \tag{A.12}$$

Then, substituting this term $\frac{\partial \sigma_{ij}}{\partial x_j}$ by p_i according to Eq. (2.6) and organize the equation, then we have

$$\int_{\Gamma_N} \delta u_i \sigma_{ij} n_j \, \mathrm{d}\Gamma_N - \int_{\Omega} \sigma_{ij} \frac{\partial \delta u_i}{\partial x_j} \, \mathrm{d}\Omega - \int_{\Omega} \delta u_i p_i \, \mathrm{d}\Omega = 0 \tag{A.13}$$

Then, applying the Neumann boundary condition ($\sigma_{ji} n_i = -s_j$) on Γ_N, which is the same as ($\sigma_{ij} n_j = -s_i$) due to the symmetry of ($\sigma_{ij} = \sigma_{ji}$). So, the weak form of the equilibrium equation with the given boundary conditions

$$-\int_{\Omega} \frac{\partial (\delta u_i)}{\partial x_j} \sigma_{ij} \, \mathrm{d}\Omega - \int_{\Gamma_N} \delta u_i s_i \, \mathrm{d}\Gamma - \int_{\Omega} \delta u_i p_i \, \mathrm{d}\Omega = 0 \tag{A.14}$$

The term $-\frac{\partial \delta u_i}{\partial x_j}$ can be rewritten as $-\delta \frac{\partial u_i}{\partial x_j}$ because the variation δ applies to the entire derivative expression. So, the final Galerkin weak form is given as

$$\int_\Omega \delta \frac{\partial u_i}{\partial x_j} \sigma_{ij} \, \mathrm{d}\Omega + \int_\Omega \delta u_i p_i \, \mathrm{d}\Omega + \int_{\Gamma_N} \delta u_i s_i \, \mathrm{d}\Gamma = 0 \tag{A.15}$$

which corresponds to Eq. (2.9) in Section 2.2.

A.2 Derivations - Separation of Scales and First Order Homogenization

A.2.1 Cauchy homogenization - Eqs. (2.17), (2.18) and (2.19)

By substituting Eq. (2.11) into Eq. (2.2) and using the derivative transform in Eq. (2.13), we get the following operations, the displacement expansion is given by Eq. (2.11) as

$$u_i(x_i, y_i) = \bar{u}_i(x_i, y_i) + \eta \bar{\bar{u}}_i(x_i, y_i) + \eta^2 \bar{\bar{\bar{u}}}_i(x_i, y_i) + \dots$$

Then, substituting the displacement expansion into the stress-strain relation Eq. (2.2)

$$\sigma_{ij} = D_{ijkl} \frac{\partial}{\partial x_l} \left(\bar{u}_k + \eta \bar{\bar{u}}_k + \eta^2 \bar{\bar{\bar{u}}}_k + \dots \right) \tag{A.16}$$

Then, expanding the derivatives

$$\sigma_{ij} = D_{ijkl} \left(\frac{\partial \bar{u}_k}{\partial x_l} + \eta \frac{\partial \bar{\bar{u}}_k}{\partial x_l} + \eta^2 \frac{\partial \bar{\bar{\bar{u}}}_k}{\partial x_l} + \dots \right) \tag{A.17}$$

The partial differential operator transformation in Eq. (2.13) is given as

$$\frac{\partial}{\partial x_i} \rightarrow \frac{\partial}{\partial x_i} + \frac{1}{\eta} \frac{\partial}{\partial y_i}$$

Then, applying this transformation to the partial derivative term in the stress-strain relation

$$\frac{\partial}{\partial x_l} \rightarrow \frac{\partial}{\partial x_l} + \frac{1}{\eta}\frac{\partial}{\partial y_l} \tag{A.18}$$

Then, substituting this transformation into the expanded expression

$$\sigma_{ij} = D_{ijkl}\left(\frac{\partial \bar{u}_k}{\partial x_l} + \frac{1}{\eta}\frac{\partial \bar{u}_k}{\partial y_l} + \eta\frac{\partial \bar{\bar{u}}_k}{\partial x_l} + \frac{1}{\eta}\eta\frac{\partial \bar{\bar{u}}_k}{\partial y_l} + \dots\right) \tag{A.19}$$

Now, the final expansion including terms up to η^5 order is given as

$$\begin{aligned}\sigma_{ij} = D_{ijkl}\Bigg(&\frac{\partial \bar{u}_k}{\partial x_l} + \frac{1}{\eta}\frac{\partial \bar{u}_k}{\partial y_l} + \eta\frac{\partial \bar{\bar{u}}_k}{\partial x_l} + \frac{1}{\eta}\eta\frac{\partial \bar{\bar{u}}_k}{\partial y_l} \\ &+ \eta^2\frac{\partial \bar{\bar{\bar{u}}}_k}{\partial x_l} + \frac{1}{\eta}\eta^2\frac{\partial \bar{\bar{\bar{u}}}_k}{\partial y_l} + \eta^3\frac{\partial \bar{\bar{\bar{\bar{u}}}}_k}{\partial x_l} + \frac{1}{\eta}\eta^3\frac{\partial \bar{\bar{\bar{\bar{u}}}}_k}{\partial y_l} \\ &+ \eta^4\frac{\partial \bar{\bar{\bar{\bar{\bar{u}}}}}_k}{\partial x_l} + \frac{1}{\eta}\eta^4\frac{\partial \bar{\bar{\bar{\bar{\bar{u}}}}}_k}{\partial y_l} + \eta^5\frac{\partial \bar{\bar{\bar{\bar{\bar{\bar{u}}}}}}_k}{\partial x_l} + \frac{1}{\eta}\eta^5\frac{\partial \bar{\bar{\bar{\bar{\bar{\bar{u}}}}}}_k}{\partial y_l} + \dots\Bigg)\end{aligned} \tag{A.20}$$

Then, we identify terms corresponding to different orders of η and extract the coefficients of each order of η to form new equations. For leading order (η^-1) terms, we have $\frac{1}{\eta}\frac{\partial \bar{u}_k}{\partial y_l}$. The zero power ($\eta^0$) terms, we have $\frac{\partial \bar{u}_k}{\partial x_l}$, $\frac{\partial \bar{\bar{u}}_k}{\partial y_l}$. First order ($\eta^1$) terms, we have $\frac{\partial \bar{\bar{u}}_k}{\partial x_l}$, $\frac{\partial \bar{\bar{\bar{u}}}_k}{\partial y_l}$. The new equations that observed after making the previous operations are the following

$$\check{\sigma}_{ij} = D_{ijkl}\frac{\partial \bar{u}_k}{\partial y_l} \tag{A.21}$$

$$\tilde{\sigma}_{ij} = D_{ijkl}\left(\frac{\partial \bar{u}_k}{\partial x_l} + \frac{\partial \bar{\bar{u}}_k}{\partial y_l}\right) = \bar{\sigma}_{ij} + \bar{\bar{\sigma}}_{ij} \tag{A.22}$$

$$\tilde{\bar{\sigma}}_{ij} = D_{ijkl}\left(\frac{\partial \bar{\bar{u}}_k}{\partial x_l} + \frac{\partial \bar{\bar{\bar{u}}}_k}{\partial y_l}\right) \tag{A.23}$$

which correspond to Eqs. (2.17), (2.18) and (2.19) in Section 2.3.

A.2.2 Homogenization equilibrium - Eqs. (2.25) and (2.26)

The stress tensor $\tilde{\sigma}_{ij}$ is give by Eq. (2.18) as

$$\tilde{\sigma}_{ij} = D_{ijkl}\left(\frac{\partial \bar{u}_k}{\partial x_l} + \frac{\partial \bar{\bar{u}}_k}{\partial y_l}\right) = \bar{\sigma}_{ij} + \bar{\bar{\sigma}}_{ij}$$

where, $\bar{\sigma}_{ij} = D_{ijkl}\frac{\partial \bar{u}_k}{\partial x_l}$ and $\bar{\bar{\sigma}}_{ij} = D_{ijkl}\frac{\partial \bar{\bar{u}}_k}{\partial y_l}$. And, the equilibrium equation is given by

$$\frac{\partial \sigma_{ij}}{\partial x_j} + \frac{1}{\eta}\frac{\partial \sigma_{ij}}{\partial y_j} = p_i \tag{A.24}$$

Then, substituting $\tilde{\sigma}_{ij}$ into σ_{ij}, given that

$$\sigma_{ij} = \tilde{\sigma}_{ij} = D_{ijkl}\left(\frac{\partial \bar{u}_k}{\partial x_l} + \frac{\partial \bar{\bar{u}}_k}{\partial y_l}\right) \tag{A.25}$$

Then, substituting the previous expression into the equilibrium equation

$$\frac{\partial}{\partial x_j}\left(D_{ijkl}\left(\frac{\partial \bar{u}_k}{\partial x_l} + \frac{\partial \bar{\bar{u}}_k}{\partial y_l}\right)\right) + \frac{1}{\eta}\frac{\partial}{\partial y_j}\left(D_{ijkl}\left(\frac{\partial \bar{u}_k}{\partial x_l} + \frac{\partial \bar{\bar{u}}_k}{\partial y_l}\right)\right) = p_i \tag{A.26}$$

Then, distributing the partial derivatives

$$D_{ijkl}\left(\frac{\partial^2 \bar{u}_k}{\partial x_j \partial x_l} + \frac{\partial^2 \bar{\bar{u}}_k}{\partial x_j \partial y_l}\right) + \frac{1}{\eta}D_{ijkl}\left(\frac{\partial^2 \bar{u}_k}{\partial y_j \partial x_l} + \frac{\partial^2 \bar{\bar{u}}_k}{\partial y_j \partial y_l}\right) = p_i \tag{A.27}$$

Then, governing terms according to their order, i.e., $O(1)$ and $O(1/\eta)$. Terms of order $(1/\eta)$ are

$$D_{ijkl}\left(\frac{\partial^2 \bar{u}_k}{\partial y_j \partial x_l} + \frac{\partial^2 \bar{\bar{u}}_k}{\partial y_j \partial y_l}\right) \tag{A.28}$$

As η approaches zero, this term can become unbounded. So, in order for the overall stress σ_{ij} to remain bounded and satisfy the periodicity assumption, this part must be zero

$$\frac{\partial}{\partial y_j}\left(D_{ijkl}\left(\frac{\partial \bar{u}_k}{\partial x_l}+\frac{\partial \bar{\bar{u}}_k}{\partial y_l}\right)\right)=0 \tag{A.29}$$

Then, this results in the following equation

$$\frac{\partial \sigma_{ij}}{\partial y_j}=0 \quad \text{in} \quad \mathrm{Y} \tag{A.30}$$

which corresponds to Eq. (2.25) in Section 2.3. The Eq. (A.30) indicates that the stress distribution must be periodic and balanced within the unit cell Y. Also, this ensures the internal consistency and periodicity of the microscopic stress distribution. Terms of order (1) are

$$D_{ijkl}\left(\frac{\partial^2 \bar{u}_k}{\partial x_j \partial x_l}+\frac{\partial^2 \bar{\bar{u}}_k}{\partial x_j \partial y_l}\right)=p_i \tag{A.31}$$

Since $\bar{u}_i$ is independent of y_i, it does not contribute to derivatives with respect to y_i. However, $\bar{\bar{u}}_k$ explicitly depends on y_l because it accounts for the microstructural variations. Therefore, $\frac{\partial \bar{\bar{u}}_k}{\partial y_l} \neq 0$ in general. Under the assumption of scale separation and periodicity in the microstructural unit cell, the contribution from $\frac{\partial^2 \bar{\bar{u}}_k}{\partial x_j \partial y_l}$ (mixed derivatives with respect to macro and micro coordinates) can be considered negligible, as the variation with respect to x_j is dominant on the macroscopic scale. Then, we simplify the equation to

$$D_{ijkl}\frac{\partial^2 \bar{u}_k}{\partial x_j \partial x_l}=p_i \tag{A.32}$$

Then, this results in the following equation

$$\frac{\partial \sigma_{ij}}{\partial x_j}=p_i \quad \text{in} \quad \Omega \tag{A.33}$$

which corresponds to Eq. (2.26) in Section 2.3.

A.3 Derivations - Variational Setting for Homogenization

A.3.1 Homogenization Galerkin - Eq. (2.27)

We start with the equilibrium equation in the domain Ω in Eq. (2.26) as

$$\frac{\partial \sigma_{ij}}{\partial x_j} - p_i = 0 \quad \text{in} \quad \Omega$$

Then, we multiply the equilibrium equation by $\delta \bar{u}_i$ and integrate over the domain Ω

$$\int_\Omega \delta \bar{u}_i \frac{\partial \sigma_{ij}}{\partial x_j} \, \mathrm{d}\Omega - \int_\Omega \delta \bar{u}_i p_i \, \mathrm{d}\Omega = 0 \tag{A.34}$$

We now focus on the first integral

$$\int_\Omega \delta \bar{u}_i \frac{\partial \sigma_{ij}}{\partial x_j} \, \mathrm{d}\Omega$$

To transform this term, we use the divergence theorem which states

$$\int_\Omega \frac{\partial v_j}{\partial x_j} \, \mathrm{d}\Omega = \int_\Gamma v_j n_j \, \mathrm{d}\Gamma \tag{A.35}$$

where v_j is a vector field, n_j is the outward unit normal to the boundary Γ, and Γ is the boundary of Ω. We apply this theorem to the first integral by choosing $v_j = \delta \bar{u}_i \sigma_{ij}$. Thus,

$$\int_\Omega \frac{\partial (\delta \bar{u}_i \sigma_{ij})}{\partial x_j} \, \mathrm{d}\Omega = \int_\Gamma \delta \bar{u}_i \sigma_{ij} n_j \, \mathrm{d}\Gamma \tag{A.36}$$

Then, by using the product rule for differentiation, we have

$$\frac{\partial (\delta \bar{u}_i \sigma_{ij})}{\partial x_j} = \delta \bar{u}_i \frac{\partial \sigma_{ij}}{\partial x_j} + \sigma_{ij} \frac{\partial \delta \bar{u}_i}{\partial x_j} \tag{A.37}$$

Then, substituting this back into the integral, we get

$$\int_{\Omega} \delta\bar{u}_i \frac{\partial \sigma_{ij}}{\partial x_j} \, \mathrm{d}\Omega = \int_{\Omega} \left(\frac{\partial (\delta\bar{u}_i \sigma_{ij})}{\partial x_j} - \sigma_{ij} \frac{\partial \delta\bar{u}_i}{\partial x_j} \right) \mathrm{d}\Omega \tag{A.38}$$

Then, by separating the integrals, we get

$$\int_{\Omega} \delta\bar{u}_i \frac{\partial \sigma_{ij}}{\partial x_j} \, \mathrm{d}\Omega = \int_{\Omega} \frac{\partial (\delta\bar{u}_i \sigma_{ij})}{\partial x_j} \, \mathrm{d}\Omega - \int_{\Omega} \sigma_{ij} \frac{\partial \delta\bar{u}_i}{\partial x_j} \, \mathrm{d}\Omega \tag{A.39}$$

Then, by applying the divergence theorem to the first term on the right-hand side, we get

$$\int_{\Omega} \frac{\partial (\delta\bar{u}_i \sigma_{ij})}{\partial x_j} \, \mathrm{d}\Omega = \int_{\Gamma} \delta\bar{u}_i \sigma_{ij} n_j \, \mathrm{d}\Gamma \tag{A.40}$$

where Γ is the boundary of Ω and n_j is the outward normal to Γ. Then, we have

$$\int_{\Omega} \delta\bar{u}_i \frac{\partial \sigma_{ij}}{\partial x_j} \, \mathrm{d}\Omega = \int_{\Gamma} \delta\bar{u}_i \sigma_{ij} n_j \, \mathrm{d}\Gamma - \int_{\Omega} \sigma_{ij} \frac{\partial \delta\bar{u}_i}{\partial x_j} \, \mathrm{d}\Omega \tag{A.41}$$

This boundary Γ consists of two parts: Γ_D (Dirichlet boundary) and Γ_N (Neumann boundary). Therefore

$$\int_{\Gamma} \delta\bar{u}_i \sigma_{ij} n_j \, \mathrm{d}\Gamma = \int_{\Gamma_D} \delta\bar{u}_i \sigma_{ij} n_j \, \mathrm{d}\Gamma_D + \int_{\Gamma_N} \delta\bar{u}_i \sigma_{ij} n_j \, \mathrm{d}\Gamma_N \tag{A.42}$$

Since the admissible displacement field u_i is prescribed on the boundary Γ_D according to Eq. (2.7), the variation $\delta\bar{u}_i$ must vanish on this boundary, where $\delta\bar{u}_i = 0$ on the Dirichlet boundary Γ_D. This ensures that any virtual displacement (variation) considered in the weak form does not alter the fixed boundary conditions. Then, the first term vanishes

$$\int_{\Gamma_D} \delta\bar{u}_i \sigma_{ij} n_j \, \mathrm{d}\Gamma_D = 0 \tag{A.43}$$

Then, we have

$$\int_{\Gamma} \delta\bar{u}_i \sigma_{ij} n_j \, \mathrm{d}\Gamma = \int_{\Gamma_N} \delta\bar{u}_i \sigma_{ij} n_j \, \mathrm{d}\Gamma_N \tag{A.44}$$

Then, by combining these results, we obtain

$$\int_{\Omega} \delta\bar{u}_i \frac{\partial \sigma_{ij}}{\partial x_j} \, \mathrm{d}\Omega = \int_{\Gamma_N} \delta\bar{u}_i \sigma_{ij} n_j \, \mathrm{d}\Gamma_N - \int_{\Omega} \sigma_{ij} \frac{\partial \delta\bar{u}_i}{\partial x_j} \, \mathrm{d}\Omega \tag{A.45}$$

Then, substituting this term $\frac{\partial \sigma_{ij}}{\partial x_j}$ by p_i according to Eq. (2.26) and organize the equation, then we have

$$\int_{\Gamma_N} \delta\bar{u}_i \sigma_{ij} n_j \, \mathrm{d}\Gamma_N - \int_{\Omega} \sigma_{ij} \frac{\partial \delta\bar{u}_i}{\partial x_j} \, \mathrm{d}\Omega - \int_{\Omega} \delta\bar{u}_i p_i \, \mathrm{d}\Omega = 0 \tag{A.46}$$

Then, applying the Neumann boundary condition ($\sigma_{ji} n_i = -s_j$) on Γ_N, which is the same as ($\sigma_{ij} n_j = -s_i$) due to the symmetry of ($\sigma_{ij} = \sigma_{ji}$). So, the weak form of the equilibrium equation with the given boundary conditions is

$$-\int_{\Omega} \frac{\partial (\delta\bar{u}_i)}{\partial x_j} \sigma_{ij} \, \mathrm{d}\Omega - \int_{\Gamma_N} \delta\bar{u}_i s_i \, \mathrm{d}\Gamma - \int_{\Omega} \delta\bar{u}_i p_i \, \mathrm{d}\Omega = 0 \tag{A.47}$$

The term $-\frac{\partial \delta\bar{u}_i}{\partial x_j}$ can be rewritten as $-\delta\frac{\partial \bar{u}_i}{\partial x_j}$ because the variation δ applies to the entire derivative expression. So, the weak form of the equilibrium equation is given as

$$\int_{\Omega} \delta \frac{\partial \bar{u}_i}{\partial x_j} \sigma_{ij} \, \mathrm{d}\Omega + \int_{\Omega} \delta\bar{u}_i p_i \, \mathrm{d}\Omega + \int_{\Gamma_N} \delta\bar{u}_i s_i \, \mathrm{d}\Gamma = 0 \tag{A.48}$$

We now consider the homogenization scenario, where the stress tensor σ_{ij} is equivalent to the effective stress tensor $\hat{\sigma}_{ij}$, which is obtained by averaging the stress tensor over a single unit cell. Consequently, the weak form of the equilibrium equation for the homogenized problem at the global scale is expressed as follows

$$\int_{\Omega} \delta \frac{\partial \bar{u}_i}{\partial x_j} \hat{\sigma}_{ij} \, \mathrm{d}\Omega + \int_{\Omega} \delta\bar{u}_i p_i \, \mathrm{d}\Omega + \int_{\Gamma_N} \delta\bar{u}_i s_i \, \mathrm{d}\Gamma = 0 \tag{A.49}$$

which corresponds to Eq. (2.27) in Section 2.4.

A.3.2 Homogenization boundary - Eq. (2.30)

We begin with the equilibrium equation (2.25) in the periodic cell Y, which is defined as

$$\frac{\partial \sigma_{ij}}{\partial y_j} = 0 \quad \text{in} \quad \mathrm{Y}$$

To derive the weak form, we multiply this equation by the virtual displacement fluctuations $\delta\bar{\bar{u}}_i$ and integrate over the domain Y

$$\int_Y \delta\bar{\bar{u}}_i \frac{\partial \sigma_{ij}}{\partial y_j} \,\mathrm{dY} = 0 \tag{A.50}$$

This integral contains a derivative of σ_{ij}. Our objective is to transfer this derivative into $\delta\bar{\bar{u}}_i$ and apply the divergence theorem, which states

$$\int_Y \frac{\partial v_j}{\partial y_j} \,\mathrm{dY} = \int_\Psi v_j n_j \,\mathrm{d}\Psi, \tag{A.51}$$

where v_j is a vector field, n_j is the j-th component of the unit normal vector to the boundary Ψ, and $\Psi = \partial\mathrm{Y}$ represents the boundary of the cell. Next, applying the product rule for differentiation

$$\frac{\partial(\delta\bar{\bar{u}}_i \sigma_{ij})}{\partial y_j} = \delta\bar{\bar{u}}_i \frac{\partial \sigma_{ij}}{\partial y_j} + \sigma_{ij} \frac{\partial \delta\bar{\bar{u}}_i}{\partial y_j}, \tag{A.52}$$

we rearrange the expression to isolate the original term

$$\delta\bar{\bar{u}}_i \frac{\partial \sigma_{ij}}{\partial y_j} = \frac{\partial(\delta\bar{\bar{u}}_i \sigma_{ij})}{\partial y_j} - \sigma_{ij} \frac{\partial \delta\bar{\bar{u}}_i}{\partial y_j} \tag{A.53}$$

Substituting this back into the integral, we obtain

$$\int_Y \delta\bar{\bar{u}}_i \frac{\partial \sigma_{ij}}{\partial y_j} \,\mathrm{dY} = \int_Y \left(\frac{\partial(\delta\bar{\bar{u}}_i \sigma_{ij})}{\partial y_j} - \sigma_{ij} \frac{\partial \delta\bar{\bar{u}}_i}{\partial y_j} \right) \mathrm{dY} \tag{A.54}$$

By separating the integrals, we get

$$\int_Y \delta\bar{\bar{u}}_i \frac{\partial \sigma_{ij}}{\partial y_j}\,\mathrm{dY} = \int_Y \frac{\partial(\delta\bar{\bar{u}}_i \sigma_{ij})}{\partial y_j}\,\mathrm{dY} - \int_Y \sigma_{ij} \frac{\partial \delta\bar{\bar{u}}_i}{\partial y_j}\,\mathrm{dY} \tag{A.55}$$

Now, applying the divergence theorem to the first term on the right-hand side, we choose $v_j = \delta\bar{\bar{u}}_i \sigma_{ij}$, yielding

$$\int_Y \frac{\partial(\delta\bar{\bar{u}}_i \sigma_{ij})}{\partial y_j}\,\mathrm{dY} = \int_\Psi \delta\bar{\bar{u}}_i \sigma_{ij} n_j\,\mathrm{d\Psi} \tag{A.56}$$

Thus, the equation becomes

$$\int_Y \delta\bar{\bar{u}}_i \frac{\partial \sigma_{ij}}{\partial y_j}\,\mathrm{dY} = \int_\Psi \delta\bar{\bar{u}}_i \sigma_{ij} n_j\,\mathrm{d\Psi} - \int_Y \sigma_{ij} \frac{\partial \delta\bar{\bar{u}}_i}{\partial y_j}\,\mathrm{dY} \tag{A.57}$$

Based on the equilibrium condition in Eq. (2.25), we find that

$$\int_Y \delta\bar{\bar{u}}_i \frac{\partial \sigma_{ij}}{\partial y_j}\,\mathrm{dY} = 0$$

Thus, the equation becomes

$$\int_\Psi \delta\bar{\bar{u}}_i \sigma_{ij} n_j\,\mathrm{d\Psi} - \int_Y \sigma_{ij} \frac{\partial \delta\bar{\bar{u}}_i}{\partial y_j}\,\mathrm{dY} = 0 \tag{A.58}$$

Then, by rearranging the equation, we get

$$\int_Y \frac{\partial \delta\bar{\bar{u}}_i}{\partial y_j} \sigma_{ij}\,\mathrm{dY} - \int_\Psi \delta\bar{\bar{u}}_i \sigma_{ij} n_j\,\mathrm{d\Psi} = 0$$

The term $\frac{\partial \delta\bar{\bar{u}}_i}{\partial y_j}$ can be rewritten as $\delta\frac{\partial \bar{\bar{u}}_i}{\partial y_j}$ because the variation δ applies to the entire derivative expression. Then, the final weak form of equilibrium within the periodic cell Y becomes

$$\int_Y \delta\frac{\partial \bar{\bar{u}}_i}{\partial y_j} \sigma_{ij}\,\mathrm{dY} - \int_\Psi \delta\bar{\bar{u}}_i \sigma_{ij} n_j\,\mathrm{d\Psi} = 0 \tag{A.59}$$

which corresponds to Eq. (2.30) in Section 2.4.

A.4 Derivations - RVE boundary value problem

A.4.1 Macroscopic strain - Eq. (2.37)

By substituting the simplified displacement field Eq. (2.35) into this integral (2.36) , we get

$$\int_{S_{RVE}} u_i n_j \, \mathrm{d}\Psi = \int_{S_{RVE}} (\psi_j g_{ij} + u_i') \, n_j \, \mathrm{d}\Psi \tag{A.60}$$

The integral on the right-hand side can be decomposed into two parts as

$$\int_{S_{RVE}} u_i n_j \, \mathrm{d}\Psi = \int_{S_{RVE}} \psi_j g_{ij} n_j \, \mathrm{d}\Psi + \int_{S_{RVE}} u_i' n_j \, \mathrm{d}\Psi \tag{A.61}$$

Then, to simplify the first integral on the right-hand side, we use the divergence theorem, which (also known as Gauss's theorem) relates the flow (or flux) of a vector field through a closed surface to the divergence of the vector field inside the surface. Mathematically, for a vector field $\mathbf{F}$, it is stated as

$$\int_S \mathbf{F} \cdot \mathbf{n} \, \mathrm{dS} = \int_V \nabla \cdot \mathbf{F} \, \mathrm{dV} \tag{A.62}$$

Here, V represents a spatial volume, while S denotes its boundary surface. The unit normal vector $\mathbf{n}$ points outward from S. The term $\nabla \cdot \mathbf{F}$ refers to the divergence of the vector field $\mathbf{F}$. In this case, we define $\mathbf{F} = (\psi_j g_{ij})$, where ψ_j is a coordinate and g_{ij} is a constant gradient tensor component. Applying the divergence theorem, we transform a surface integral into an equivalent volume integral. To do so, we first compute the divergence of $\mathbf{F}$ by taking the partial derivative with respect to the spatial coordinate y_j as

$$\nabla \cdot \mathbf{F} = \frac{\partial}{\partial y_j} (\psi_j g_{ij}) \tag{A.63}$$

Since g_{ij} is constant over the RVE (as it represents a uniform gradient), it can be factored out as

$$\frac{\partial(\psi_j g_{ij})}{\partial y_j} = g_{ij}\frac{\partial \psi_j}{\partial y_j} \tag{A.64}$$

Then, the volume integral over the RVE becomes

$$\int_{V_{RVE}} \frac{\partial(\psi_j g_{ij})}{\partial y_j}\,\mathrm{dY} = \int_{V_{RVE}} g_{ij}\frac{\partial \psi_j}{\partial y_j}\,\mathrm{dY} \tag{A.65}$$

According to the divergence theorem, this volume integral is equivalent to the surface integral as

$$\int_{S_{RVE}} \psi_j g_{ij} n_j\,\mathrm{d\Psi} = \int_{V_{RVE}} g_{ij}\frac{\partial \psi_j}{\partial y_j}\,\mathrm{dY} \tag{A.66}$$

Here, n_j represents the components of the unit normal vector $\mathbf{n}$ on the surface S_{RVE} (boundary of the RVE), and ψ_j is the position vector component on the surface. Since g_{ij} is constant over the volume, we can take it outside of the integral as

$$\int_{S_{RVE}} \psi_j g_{ij} n_j\,\mathrm{d\Psi} = g_{ij}\int_{V_{RVE}} \frac{\partial \psi_j}{\partial y_j}\,\mathrm{dY} \tag{A.67}$$

Here, this is because ψ_j is just a spatial coordinate, and its derivative with respect to itself is always 1. So, we have

$$\frac{\partial \psi_j}{\partial y_j} = 1 \tag{A.68}$$

Thus, the final expression for the volume integral becomes

$$g_{ij}\int_{V_{RVE}} \frac{\partial \psi_j}{\partial y_j}\,\mathrm{dY} = g_{ij}\int_{V_{RVE}} \mathrm{dY} \tag{A.69}$$

Then, we combine the surface and volume integrals as the following

$$\int_{S_{RVE}} u_i n_j\,\mathrm{d\Psi} = \int_{S_{RVE}} \psi_j g_{ij} n_j\,\mathrm{d\Psi} + \int_{S_{RVE}} u_i' n_j\,\mathrm{d\Psi},$$

$$\int_{S_{RVE}} \psi_j g_{ij} n_j \, \mathrm{d}\Psi = g_{ij} \int_{V_{RVE}} \mathrm{dY},$$

$$\int_{S_{RVE}} u_i n_j \, \mathrm{d}\Psi = g_{ij} \int_{V_{RVE}} \mathrm{dY} + \int_{S_{RVE}} u'_i n_j \, \mathrm{d}\Psi \tag{A.70}$$

Then, we need to consider both $u_i n_j$ and $u_j n_i$ contributions for several reasons. In continuum mechanics, particularly in linear elasticity, both the strain and stress tensors are symmetric. This symmetry ensures that deformations in the i and j directions are treated equivalently. When evaluating deformation energy or work, it is essential to account for all interactions between displacement components and normal vectors. To accurately describe material deformation, the average deformation gradient over the RVE boundary is considered. This gradient is represented as the symmetrized form of the displacement field gradient, naturally incorporating both $u_i n_j$ and $u_j n_i$. Including both terms ensures a complete and consistent formulation, fully capturing the influence of the displacement field at the boundary. Omitting either term would disregard part of the boundary contributions, leading to an incomplete or inaccurate characterization of the material's response. Therefore, we have

$$\int_{S_{RVE}} (u_i n_j + u_j n_i) \, \mathrm{d}\Psi = \left(g_{ij} \int_{V_{RVE}} \mathrm{dY} + \int_{S_{RVE}} u'_i n_j \, \mathrm{d}\Psi + g_{ji} \int_{V_{RVE}} \mathrm{dY} + \int_{S_{RVE}} u'_j n_i \, \mathrm{d}\Psi \right) \tag{A.71}$$

By considering that the integral of the micro-fluctuations vanishes over the RVE boundary, we get

$$\int_{S_{RVE}} u'_i n_j \, \mathrm{d}\Psi = 0 \quad and \quad \int_{S_{RVE}} u'_j n_i \, \mathrm{d}\Psi = 0 \tag{A.72}$$

which simplifies our equation to

$$\int_{S_{RVE}} (u_i n_j + u_j n_i) \, \mathrm{d}\Psi = (g_{ij} + g_{ji}) \int_{V_{RVE}} \mathrm{dY} \tag{A.73}$$

Since g_{ij} and g_{ji} are symmetrical, we have

$$g_{ij} + g_{ji} = 2 g_{ij} \tag{A.74}$$

Therefore, we have

$$\frac{1}{2}\int_{S_{RVE}} (u_i n_j + u_j n_i)\, \mathrm{d}\Psi = g_{ij} \int_{V_{RVE}} \mathrm{dY} \tag{A.75}$$

which corresponds to Eq. (2.37) in Section 2.5.

A.4.2 Homogenized relation - Eq. (2.38)

By taking the variation of the potential energy of the Representative Volume Element (RVE) problem, the local weak form of equilibrium is obtained. To enforce the required constraint, Lagrange multipliers λ_i are introduced, ensuring that the microscopic displacement u_i at the RVE boundary remains consistent with the macroscopic displacement gradient g_{ij}. The total displacement u_i at any point on the RVE boundary can be decomposed, as previously discussed in Eq. (2.31). Where $\bar{u}_i(\bar{y}_i)$ represents the macroscopic displacement, $(\psi_j - \bar{y}_j)g_{ij}$ accounts for the displacement induced by the macroscopic displacement gradient, and u_i' denotes the micro-fluctuations. For simplicity and without loss of generality, we assume $\bar{u}_i(\bar{y}_i) = 0$, set $\bar{y}_i = 0$, and neglect the micro-fluctuations. Consequently, the displacement expression simplifies to $u_i = \psi_j g_{ij}$. The constraint to be enforced using the Lagrange multipliers is thus given by

$$u_i - \psi_j g_{ij} = 0 \quad \text{on} \quad S_{RVE} \tag{A.76}$$

Within the framework of the weak form formulation, the primary contributing terms can be expressed as the following integral expressions: the volume integral term as

$$\int_{V_{RVE}} \delta \frac{\partial \bar{\bar{u}}_i}{\partial y_j} \sigma_{ij}\, \mathrm{d}Y, \tag{A.77}$$

the boundary integral term enforcing traction

$$\int_{S_{RVE}} \delta \bar{\bar{u}}_i \lambda_i\, \mathrm{d}\Psi, \tag{A.78}$$

and the constraint term involving the displacement gradient

$$\int_{S_{RVE}} \delta\lambda_i(u_i - \psi_j g_{ij})\,\mathrm{d}\Psi \tag{A.79}$$

By combining these terms, the weak form of the local equilibrium within the RVE is obtained as

$$\int_{V_{RVE}} \delta\frac{\partial\bar{\bar{u}}_i}{\partial y_j}\sigma_{ij}\mathrm{d}\Upsilon + \int_{S_{RVE}} \delta\bar{\bar{u}}_i\lambda_i\mathrm{d}\Psi + \int_{S_{RVE}} \delta\lambda_i\left(u_i - \psi_j g_{ij}\right)\mathrm{d}\Psi = 0 \tag{A.80}$$

which corresponds to Eq. (2.38) in Section 2.5.

Appendix B

Mathematical Derivations - Computational Homogenization With XFEM

B.1 Derivations - Implementation of the RVE Boundary Conditions

B.1.1 Lagrangian matrix - Eq. (3.13)

To reach the final algebraic form of the RVE problem, we need to substitute the interpolated forms of the displacement field (3.11) and the Lagrange multiplier field (3.12) into the weak form of the RVE problem Eq. (2.38) which is defined in terms of tensor index. The first integral term of Eq. (2.38) is

$$\int_{V_{RVE}} \delta \left(\frac{\partial \bar{\bar{u}}_i}{\partial y_j} \right) \sigma_{ij} \, \mathrm{dY} \tag{B.1}$$

where, $\bar{\bar{u}}_i$ is the microscopic displacement field inside the RVE. σ_{ij} is the stress tensor. δ denotes the variation (virtual displacement principle). y_j are the spatial coordinates. We aim to express this in terms of matrix notation. Before doing that, we need to show the difference between Between $\bar{\bar{u}}_i$ and u_i in Eq. (2.38). $\bar{\bar{u}}_i$ represents the microscopic displacement

field within the RVE. And, u_i refers to the actual displacement of boundary points on S_{RVE}, which includes contributions from both microscopic fluctuations and macroscopic deformation. More specifically, $\bar{\bar{u}}_i$ describes the displacement field inside the RVE, meaning that it captures the local deformations within the material. u_i represents the displacement field on the boundary of the RVE. This distinction is important because, in homogenization methods, we express $\bar{\bar{u}}_i$ using shape functions or interpolation functions, while u_i must satisfy compatibility conditions on the RVE boundary. Now, we can say that

$$\bar{\bar{\mathbf{u}}} = \mathbf{A}\mathbf{a} \tag{B.2}$$

This substitution is valid because $\mathbf{A}$ represents the shape functions (or interpolation functions) used to approximate the microscopic displacement field. And, $\mathbf{a}$ represents the unknown degrees of freedom of the displacement field. Thus, whenever $\bar{\bar{u}}_i$ appears in the weak form equation, we can replace it with $\mathbf{A}\mathbf{a}$ to obtain the discrete system of equations. By taking the gradient of Eq. (B.2), we get

$$\frac{\partial \bar{\bar{\mathbf{u}}}}{\partial \mathbf{y}} = \frac{\partial \mathbf{A}}{\partial \mathbf{y}}\,\mathbf{a} \tag{B.3}$$

Thus, the variation of the displacement gradient is

$$\delta\left(\frac{\partial \bar{\bar{\mathbf{u}}}}{\partial \mathbf{y}}\right) = \frac{\partial \mathbf{A}}{\partial \mathbf{y}}\,\delta\mathbf{a} \tag{B.4}$$

Now, substituting this into the integral (B.1), we get

$$\int_{V_{RVE}} \delta\left(\frac{\partial \mathbf{A}}{\partial \mathbf{y}}\mathbf{a}\right)^{\mathrm{T}} \boldsymbol{\sigma}\,\mathrm{dY} \tag{B.5}$$

The reason for introducing the transpose when moving from tensor notation to Voigt notation is related to how matrix and tensor operations are represented in different notational

systems. In tensor notation, the stress-strain relationship follows

$$\sigma_{ij} = D_{ijkl}\,\varepsilon_{kl} \tag{B.6}$$

where σ_{ij} is the Cauchy stress tensor. D_{ijkl} is the fourth-order stiffness tensor. ε_{kl} is the strain tensor. In Voigt notation, second-order tensors (like stress and strain) are written as column vectors for computational convenience as

$$\boldsymbol{\sigma} = \begin{bmatrix} \sigma_{11} \\ \sigma_{22} \\ \sigma_{33} \\ \sigma_{12} \\ \sigma_{23} \\ \sigma_{31} \end{bmatrix}, \quad \boldsymbol{\varepsilon} = \begin{bmatrix} \varepsilon_{11} \\ \varepsilon_{22} \\ \varepsilon_{33} \\ 2\varepsilon_{12} \\ 2\varepsilon_{23} \\ 2\varepsilon_{31} \end{bmatrix}$$

This allows us to express the constitutive relation in matrix form as $\boldsymbol{\sigma} = \mathbf{D}\boldsymbol{\varepsilon}$, where $\mathbf{D}$ is the stiffness matrix. Now, let's return to why the Transpose? The integral we're considering is (B.1), where $\frac{\partial \bar{\bar{u}}_i}{\partial y_j}$ is the displacement gradient. The virtual variation δ applies to the displacement gradient. Expanding in Voigt notation, we express the strain-displacement relation as

$$\boldsymbol{\varepsilon} = \frac{\partial \mathbf{A}}{\partial \mathbf{y}}\,\mathbf{a} \tag{B.7}$$

where $\frac{\partial \mathbf{A}}{\partial \mathbf{y}}$ is the strain-displacement matrix. And, $\mathbf{a}$ is the vector of nodal displacements. Thus, the virtual strain is

$$\delta\boldsymbol{\varepsilon} = \frac{\partial \mathbf{A}}{\partial \mathbf{y}}\,\delta\mathbf{a} \tag{B.8}$$

Then, by rewriting this integral $\int_{V_{RVE}} \delta\left(\frac{\partial \bar{\bar{u}}_i}{\partial y_j}\right)\sigma_{ij}\,\mathrm{dY}$ in Voigt notation

$$\delta\boldsymbol{\varepsilon}\,\boldsymbol{\sigma}^{\mathrm{T}} \tag{B.9}$$

Substituting $\delta\boldsymbol{\varepsilon} = \frac{\partial \mathbf{A}}{\partial \mathbf{y}}\,\delta\mathbf{a}$, we get

$$\frac{\partial \mathbf{A}}{\partial \mathbf{y}}\,\mathbf{a}\,\boldsymbol{\sigma}^{\mathrm{T}} \tag{B.10}$$

However, in integral expressions, the conventional form for energy consistency is

$$\int_{V_{RVE}} \delta\boldsymbol{\varepsilon}^{\mathrm{T}}\boldsymbol{\sigma}\,\mathrm{dY} \tag{B.11}$$

Since

$$\delta\boldsymbol{\varepsilon}^{\mathrm{T}} = \delta\left(\frac{\partial\mathbf{A}}{\partial\mathbf{y}}\mathbf{a}\right)^{\mathrm{T}} \tag{B.12}$$

Thus, in order for the integral to maintain proper multiplication order in Voigt notation, the transpose appears as

$$\int_{V_{RVE}} \delta\left(\frac{\partial\mathbf{A}}{\partial\mathbf{y}}\mathbf{a}\right)^{\mathrm{T}}\boldsymbol{\sigma}\,\mathrm{dY} \tag{B.13}$$

Then, by using the linear elastic constitutive relation

$$\boldsymbol{\sigma} = \mathbf{D}\frac{\partial\mathbf{A}}{\partial\mathbf{y}}\mathbf{a} \tag{B.14}$$

where $\mathbf{D}$ is the material stiffness matrix. And, $\frac{\partial\mathbf{A}}{\partial\mathbf{y}}$ is the strain-displacement matrix. Then by substituting this into the integral, we get

$$\int_{V_{RVE}} \delta\left(\frac{\partial\mathbf{A}}{\partial\mathbf{y}}\mathbf{a}\right)^{\mathrm{T}}\mathbf{D}\frac{\partial\mathbf{A}}{\partial\mathbf{y}}\,\mathbf{a}\,\mathrm{dY} \tag{B.15}$$

Since $\delta\mathbf{a}$ is a virtual displacement, we factor it out

$$\delta\mathbf{a}^{\mathrm{T}}\int_{V_{RVE}} \left(\frac{\partial\mathbf{A}}{\partial\mathbf{y}}\right)^{\mathrm{T}}\mathbf{D}\frac{\partial\mathbf{A}}{\partial\mathbf{y}}\,\mathrm{dY}\,\mathbf{a} \tag{B.16}$$

Recognizing that the stiffness matrix $\mathbf{K}$ of the RVE is defined as

$$\mathbf{K} = \int_{V_{RVE}} \left(\frac{\partial\mathbf{A}}{\partial\mathbf{y}}\right)^{\mathrm{T}}\mathbf{D}\frac{\partial\mathbf{A}}{\partial\mathbf{y}}\,\mathrm{dY} \tag{B.17}$$

which simplifies to

$$\delta \mathbf{a}^{\mathrm{T}} \mathbf{K} \mathbf{a} \tag{B.18}$$

Now, let's move to the second integral from Eq. (2.38) which is

$$\int_{S_{RVE}} \delta \bar{\bar{u}}_i \lambda_i \, \mathrm{d}\Psi \tag{B.19}$$

where $\delta \bar{\bar{u}}_i$ is the virtual displacement variation. λ_i is the Lagrange multiplier field (which represents traction forces on the boundary). S_{RVE} is the boundary surface of the RVE where these tractions act. By taking the variation of Eq. (B.2), we get

$$\delta \bar{\bar{\mathbf{u}}} = \mathbf{A} \delta \mathbf{a} \tag{B.20}$$

Since $\delta \bar{\bar{u}}_i$ represents the virtual displacement in tensor notation, we replace it with its corresponding matrix representation as

$$\delta \bar{\bar{u}}_i = \mathbf{A} \delta \mathbf{a} \tag{B.21}$$

Thus, the integral becomes

$$\int_{S_{RVE}} \delta \bar{\bar{u}}_i \lambda_i \, \mathrm{d}\Psi = \int_{S_{RVE}} (\mathbf{A} \delta \mathbf{a})^{\mathrm{T}} \boldsymbol{\lambda} \, \mathrm{d}\Psi \tag{B.22}$$

Again, in order for the integral to maintain proper multiplication in Voigt notation, we take the transpose in the previous integral. Since $\boldsymbol{\lambda}$ is a vector, taking the transpose of $\mathbf{A}\delta\mathbf{a}$ gives

$$\delta \mathbf{a}^{\mathrm{T}} \mathbf{A}^{\mathrm{T}} \boldsymbol{\lambda} \tag{B.23}$$

We approximate the Lagrange multiplier field in Eq. (3.12), where $\mathbf{G}$ is the interpolation function for the Lagrange multiplier field. And, $\mathbf{h}$ is the vector of unknown Lagrange mul-

tipliers. Then, by substituting this into the integral (B.22), we get

$$\delta \mathbf{a}^{\mathrm{T}} \int_{S_{RVE}} \mathbf{A}^{\mathrm{T}} \mathbf{G} \mathbf{h} \, \mathrm{d}\Psi \tag{B.24}$$

We now define the matrix $\mathbf{S}$ as

$$\mathbf{S} = \int_{S_{RVE}} \mathbf{G}^{\mathrm{T}} \mathbf{A} \, \mathrm{d}\Psi \tag{B.25}$$

By applying the transpose identity $(\mathbf{G}^{\mathrm{T}}\mathbf{A})^{\mathrm{T}} = \mathbf{A}^{\mathrm{T}}\mathbf{G}$, then our integral simplifies to

$$\delta \mathbf{a}^{\mathrm{T}} \mathbf{S}^{\mathrm{T}} \mathbf{h} \tag{B.26}$$

From Eq. (2.38), the third integral is

$$\int_{S_{RVE}} \delta \lambda_i \left(u_i - \psi_j g_{ij} \right) \mathrm{d}\Psi \tag{B.27}$$

where $\delta\lambda_i$ is the virtual variation of the Lagrange multiplier field. u_i is the displacement field. $\psi_j g_{ij}$ represents the prescribed macroscopic displacement field. S_{RVE} is the boundary surface of the RVE. Then, from Eq. (3.11), we approximate the displacement boundary field as

$$\mathbf{u} = \mathbf{A}\mathbf{a} \tag{B.28}$$

Then, by substituting Eq. (B.28) into the integral (B.27), we get

$$\int_{S_{RVE}} \delta \boldsymbol{\lambda} \left(\mathbf{A}\mathbf{a} - \boldsymbol{\Psi}^{\mathrm{T}} \mathbf{g} \right) \mathrm{d}\Psi \tag{B.29}$$

where $\boldsymbol{\Psi}$ is global coordinate matrix associated with all k nodes on the surface of the discretized microstructure as in Miehe and Koch [36]. And, it's defined as

$$\boldsymbol{\Psi} = \begin{bmatrix} \boldsymbol{\Psi}_1 & \boldsymbol{\Psi}_2 & \cdots & \boldsymbol{\Psi}_k \end{bmatrix} \tag{B.30}$$

And, $\mathbf{\Psi}$ is a matrix that depends on the coordinates of the nodal point k in the reference configuration, for example

$$\mathbf{\Psi}_k = \frac{1}{2}\begin{bmatrix} 2y_1 & 0 \\ 0 & 2y_2 \\ y_2 & y_1 \end{bmatrix}_k \tag{B.31}$$

In 2D Voigt notation, the displacement gradient tensor g_{ij} is represented as a 3-component vector (which is symmetric) as the following

$$\mathbf{g} = \begin{pmatrix} g_{11} \\ g_{22} \\ 2g_{12} \end{pmatrix}$$

Again, in order for the integral to maintain proper multiplication in Voigt notation, we take the transpose in $\mathbf{\Psi}$ when multiplied by g.

In tensor notation, the third integral of Eq. (2.38) originally used index summation (dot product), which is naturally scalar. However, when converting to Voigt notation (matrix form), we switch to standard column-vector representation. $\boldsymbol{\lambda}$ is a column vector. And, the expression $(\mathbf{Aa} - \mathbf{\Psi}^{\mathrm{T}}\mathbf{g})$ is also a column vector. For the integral to remain scalar, the variation $\delta\boldsymbol{\lambda}$ must be written as a row vector before multiplying the column vector $(\mathbf{Aa} - \mathbf{\Psi}^{\mathrm{T}}\mathbf{g})$. This is achieved by taking the transpose as

$$\delta\boldsymbol{\lambda}^{\mathrm{T}}\left(\mathbf{Aa} - \mathbf{\Psi}^{\mathrm{T}}\mathbf{g}\right) \tag{B.32}$$

Then, by taking the variation of the Lagrange multiplier field in Eq. (3.12)

$$\delta\boldsymbol{\lambda}^{\mathrm{T}} = \mathbf{G}^{\mathrm{T}}\delta\mathbf{h}^{\mathrm{T}} \tag{B.33}$$

Substituting this into the integral (B.32), we get

$$\int_{S_{RVE}} \delta\mathbf{h}^{\mathrm{T}}\mathbf{G}^{\mathrm{T}}(\mathbf{Aa} - \mathbf{\Psi}^{\mathrm{T}}\mathbf{g})\,\mathrm{d}\Psi \tag{B.34}$$

Then, by expanding the terms

$$\delta\mathbf{h}^{\mathrm{T}} \int_{S_{RVE}} \mathbf{G}^{\mathrm{T}}\mathbf{A}\,\mathrm{d}\Psi\,\mathbf{a} - \delta\mathbf{h}^{\mathrm{T}} \int_{S_{RVE}} \mathbf{G}^{\mathrm{T}}\boldsymbol{\Psi}^{\mathrm{T}}\,\mathrm{d}\Psi\,\mathbf{g} \tag{B.35}$$

From Eq. (B.25), We define the matrix $\mathbf{S}$. Similarly, we define the matrix $\boldsymbol{\Theta}$ as

$$\boldsymbol{\Theta} = \int_{S_{RVE}} \mathbf{G}^{\mathrm{T}}\boldsymbol{\Psi}^{\mathrm{T}}\,\mathrm{d}\Psi \tag{B.36}$$

Using these definitions, our integral simplifies to

$$\delta\mathbf{h}^{\mathrm{T}}\mathbf{S}\mathbf{a} - \delta\mathbf{h}^{\mathrm{T}}\boldsymbol{\Theta}\mathbf{g} \tag{B.37}$$

Now, collecting all terms

$$\delta\mathbf{a}^{\mathrm{T}}\mathbf{K}\mathbf{a} + \delta\mathbf{a}^{\mathrm{T}}\mathbf{S}^{\mathrm{T}}\mathbf{h} + \delta\mathbf{h}^{\mathrm{T}}\mathbf{S}\mathbf{a} - \delta\mathbf{h}^{\mathrm{T}}\boldsymbol{\Theta}\mathbf{g} = 0 \tag{B.38}$$

where $\mathbf{K}$ is the stiffness matrix. $\mathbf{S}$ represents the coupling between displacements and Lagrange multipliers. $\boldsymbol{\Theta}$ relates the Lagrange multipliers to the macroscopic displacement constraints. $\mathbf{a}$ is the vector of unknown displacement degrees of freedom. $\mathbf{h}$ is the vector of Lagrange multipliers. $\mathbf{g}$ represents the prescribed macroscopic displacement field. Since this equation must hold for arbitrary virtual variations $\delta\mathbf{a}$ and $\delta\mathbf{h}$, we can separate the terms that multiply each of these variations. In terms multiplying $\delta\mathbf{a}^{\mathrm{T}}$, we have

$$\delta\mathbf{a}^{\mathrm{T}}(\mathbf{K}\mathbf{a} + \mathbf{S}^{\mathrm{T}}\mathbf{h}) = 0 \tag{B.39}$$

This must hold for all $\delta\mathbf{a}$, so we conclude

$$\mathbf{K}\mathbf{a} + \mathbf{S}^{\mathrm{T}}\mathbf{h} = 0 \tag{B.40}$$

In terms multiplying $\delta\mathbf{h}^{\mathrm{T}}$, we have

$$\delta\mathbf{h}^{\mathrm{T}}(\mathbf{S}\mathbf{a} - \boldsymbol{\Theta}\mathbf{g}) = 0 \tag{B.41}$$

Since this must hold for all $\delta\mathbf{h}$, we conclude

$$\mathbf{S}\mathbf{a} - \boldsymbol{\Theta}\mathbf{g} = 0 \tag{B.42}$$

$$\mathbf{S}\mathbf{a} = \boldsymbol{\Theta}\mathbf{g} \tag{B.43}$$

We now can write these two equations as a single matrix system

$$\begin{bmatrix} \mathbf{K} & \mathbf{S}^{\mathrm{T}} \\ \mathbf{S} & 0 \end{bmatrix} \begin{Bmatrix} \mathbf{a} \\ \mathbf{h} \end{Bmatrix} = \begin{Bmatrix} \mathbf{0} \\ \boldsymbol{\Theta}\mathbf{g} \end{Bmatrix} \tag{B.44}$$

which corresponds to Eq. (3.13) in Section 3.2.

B.1.2 Uniform displacement gradient - Eq. (3.36)

We now derive the algebraic form of the RVE problem under uniform displacement gradient boundary conditions. This is achieved by substituting Eq. (3.35), Eq. (3.24), and Eq. (3.25) into Eq. (3.13). The resulting algebraic formulation of the RVE problem is given by Eq. (3.13) as

$$\begin{bmatrix} \mathbf{K} & \mathbf{S}^{\mathrm{T}} \\ \mathbf{S} & 0 \end{bmatrix} \begin{Bmatrix} \mathbf{a} \\ \mathbf{h} \end{Bmatrix} = \begin{Bmatrix} \mathbf{0} \\ \boldsymbol{\Theta}\mathbf{g} \end{Bmatrix}$$

From Eq. (3.24) and Eq. (3.25), we know that

$$\mathbf{K} = \begin{bmatrix} \mathbf{K}_{II} & \mathbf{K}_{IB} \\ \mathbf{K}_{IB}^{\mathrm{T}} & \mathbf{K}_{BB} \end{bmatrix}$$

$$\mathbf{S} = \begin{bmatrix} \mathbf{S}_I & \mathbf{S}_B \end{bmatrix}$$

Similarly, we partition the displacement vector $\mathbf{a}$ in Eq. (3.23) as

$$\mathbf{a} = \begin{Bmatrix} \mathbf{a}_I \\ \mathbf{a}_B \end{Bmatrix}$$

Substituting these into Eq. (3.13) gives

$$\begin{bmatrix} \begin{bmatrix} \mathbf{K}_{II} & \mathbf{K}_{IB} \\ \mathbf{K}_{IB}^{\mathrm{T}} & \mathbf{K}_{BB} \end{bmatrix} & \begin{bmatrix} \mathbf{S}_I^{\mathrm{T}} \\ \mathbf{S}_B^{\mathrm{T}} \end{bmatrix} \\ \begin{bmatrix} \mathbf{S}_I & \mathbf{S}_B \end{bmatrix} & 0 \end{bmatrix} \begin{Bmatrix} \mathbf{a}_I \\ \mathbf{a}_B \\ \mathbf{h} \end{Bmatrix} = \begin{Bmatrix} \mathbf{0} \\ \boldsymbol{\Theta}\mathbf{g} \end{Bmatrix} \tag{B.45}$$

The expression of $\mathbf{S}^{\mathrm{T}}$ in Eq. (B.45) follows from the row-wise partitioning of $\mathbf{S}$. Specifically, $\mathbf{S}$ is structured as Eq. (3.25) , where $\mathbf{S}_I$ corresponds to internal nodes and $\mathbf{S}_B$ to boundary nodes. Taking the transpose of $\mathbf{S}$ interchanges its rows and columns, transforming it into a column-partitioned matrix

$$\mathbf{S}^{\mathrm{T}} = \begin{bmatrix} \mathbf{S}_I^{\mathrm{T}} \\ \mathbf{S}_B^{\mathrm{T}} \end{bmatrix} \tag{B.46}$$

This structure is particularly relevant in the Lagrangian equation in matrix form Eq. (3.13), where $\mathbf{S}^{\mathrm{T}}$ must conform to the partitioning of $\mathbf{a}$ into $\mathbf{a}_I$ and $\mathbf{a}_B$. By adopting this form, the multiplication $\mathbf{S}^{\mathrm{T}}\mathbf{h}$ results in a vector of the same dimension as $\mathbf{a}$, ensuring compatibility within the matrix equation. Consequently, transposing $\mathbf{S}$ requires the individual transposition of each block component, yielding $\mathbf{S}_I^{\mathrm{T}}$ and $\mathbf{S}_B^{\mathrm{T}}$. Overall, we express $\mathbf{S}^{\mathrm{T}}$ in Eq. (B.45) as given in Eq. (B.46) because $\mathbf{S}$ is originally partitioned row-wise, and its transpose naturally converts it into a column-partitioned form. This transformation ensures proper alignment for matrix multiplication with $\mathbf{a}$, preserving the structural integrity of the equation.

let's return back to Eq. (B.45). By expanding the matrix-vector product, we obtain two separate equations. The first is equation for nodal displacement equilibrium

$$\begin{bmatrix} \mathbf{K}_{II} & \mathbf{K}_{IB} \\ \mathbf{K}_{IB}^{\mathrm{T}} & \mathbf{K}_{BB} \end{bmatrix} \begin{Bmatrix} \mathbf{a}_I \\ \mathbf{a}_B \end{Bmatrix} + \begin{bmatrix} \mathbf{S}_I^{\mathrm{T}} \\ \mathbf{S}_B^{\mathrm{T}} \end{bmatrix} \mathbf{h} = \begin{Bmatrix} \mathbf{0} \\ \mathbf{0} \end{Bmatrix} \tag{B.47}$$

Breaking this into two separate equations for internal and boundary nodes

$$\mathbf{K}_{II}\mathbf{a}_I + \mathbf{K}_{IB}\mathbf{a}_B + \mathbf{S}_I^{\mathrm{T}}\mathbf{h} = \mathbf{0} \tag{B.48}$$

$$\mathbf{K}_{IB}^{\mathrm{T}}\mathbf{a}_I + \mathbf{K}_{BB}\mathbf{a}_B + \mathbf{S}_B^{\mathrm{T}}\mathbf{h} = \mathbf{0} \tag{B.49}$$

The second is equation for Lagrange multipliers

$$\begin{bmatrix} \mathbf{S}_I & \mathbf{S}_B \end{bmatrix} \begin{Bmatrix} \mathbf{a}_I \\ \mathbf{a}_B \end{Bmatrix} + 0 \cdot \mathbf{h} = \mathbf{\Theta}\mathbf{g} \tag{B.50}$$

$$\mathbf{S}_I\mathbf{a}_I + \mathbf{S}_B\mathbf{a}_B = \mathbf{\Theta}\mathbf{g} \tag{B.51}$$

Then, we substitute Eq. (3.35) into the previous equations (B.48) and (B.51). Thus, the nodal displacement equilibrium equation (internal nodes) (B.48) becomes

$$\mathbf{K}_{II}\mathbf{a}_I + \mathbf{K}_{IB}\mathbf{\Psi}^{\mathrm{T}}\mathbf{g} + \mathbf{S}_I^{\mathrm{T}}\mathbf{h} = \mathbf{0} \tag{B.52}$$

Rearranging

$$\mathbf{K}_{II}\mathbf{a}_I + \mathbf{S}_I^{\mathrm{T}}\mathbf{h} = -\mathbf{K}_{IB}\mathbf{\Psi}^{\mathrm{T}}\mathbf{g} \tag{B.53}$$

Similarly, the Lagrange multiplier equation (B.51) becomes

$$\mathbf{S}_I\mathbf{a}_I + \mathbf{S}_B\mathbf{\Psi}^{\mathrm{T}}\mathbf{g} = \mathbf{\Theta}\mathbf{g} \tag{B.54}$$

Rearranging

$$\mathbf{S}_I\mathbf{a}_I = \left(\mathbf{\Theta} - \mathbf{S}_B\mathbf{\Psi}^{\mathrm{T}}\right)\mathbf{g} \tag{B.55}$$

Eq. (B.49) represents the equilibrium condition for the boundary degrees of freedom. It comes from the system of equations derived from the finite element discretization of the RVE problem, where $\mathbf{K}_{IB}^{\mathrm{T}}$ represents the interaction between internal (I) and boundary (B) nodes. $\mathbf{K}_{BB}$ corresponds to the stiffness contributions associated with the boundary nodes. $\mathbf{S}_B^{\mathrm{T}}\mathbf{h}$ captures the contribution of the Lagrange multipliers. This equation ensures force

equilibrium at the boundary nodes. One key aspect of the RVE problem is that boundary nodes are not treated as independent unknowns. Instead, they are expressed in terms of macroscopic displacement fluctuations. This is achieved using a homogenization constraint as given in Eq. (3.35). By substituting $\mathbf{a}_B = \boldsymbol{\Psi}^{\mathrm{T}}\mathbf{g}$ into the equilibrium equation, we eliminate $\mathbf{a}_B$ as an independent variable. Now, substituting $\mathbf{a}_B = \boldsymbol{\Psi}^{\mathrm{T}}\mathbf{g}$ into Eq. (B.49) yields

$$\mathbf{K}_{IB}^{\mathrm{T}}\mathbf{a}_I + \mathbf{K}_{BB}\boldsymbol{\Psi}^{\mathrm{T}}\mathbf{g} + \mathbf{S}_B^{\mathrm{T}}\mathbf{h} = \mathbf{0} \tag{B.56}$$

Since this equation does not introduce new independent unknowns (it only relates known quantities), it does not contribute additional information needed to solve for $\mathbf{a}_I$ and $\mathbf{h}$. Thus, it can be omitted from the final system without loss of generality. In overall, Eq. (B.56) was neglected because boundary displacements are not independent variables but are expressed in terms of the macroscopic deformation through $\mathbf{a}_B = \boldsymbol{\Psi}^{\mathrm{T}}\mathbf{g}$. Substituting this relation into the boundary equation does not introduce additional unknowns but instead expresses a known relationship, which does not contribute new solvable equations. The key unknowns in the final system are $\mathbf{a}_I$ (internal displacements) and $\mathbf{h}$ (Lagrange multipliers), which are already fully determined by the reduced system. Thus, we do not need to include this equation (B.56) in the final system, as all necessary constraints and equilibrium conditions are already enforced by the remaining equations.

Rewriting these equations (B.53) and (B.55) in a matrix form yields

$$\begin{bmatrix} \mathbf{K}_{II} & \mathbf{S}_I^{\mathrm{T}} \\ \mathbf{S}_I & 0 \end{bmatrix} \begin{Bmatrix} \mathbf{a}_I \\ \mathbf{h} \end{Bmatrix} = \begin{Bmatrix} -\mathbf{K}_{IB}\boldsymbol{\Psi}^{\mathrm{T}}\mathbf{g} \\ \left(\boldsymbol{\Theta} - \mathbf{S}_B\boldsymbol{\Psi}^{\mathrm{T}}\right)\mathbf{g} \end{Bmatrix} \tag{B.57}$$

which corresponds to Eq. (3.36) in Subsection 3.2.1.

B.1.3 Uniform traction - Eq. (3.46)

We now derive the algebraic form of the RVE problem under uniform traction boundary conditions. This is achieved by substituting Eq. (3.43) into Eq. (3.13) and using Eqs. (3.24) and (3.25). The resulting algebraic formulation of the RVE problem after substituting all

the partitioned matrices is given by Eq. (B.45) as

$$\begin{bmatrix} \begin{bmatrix} \mathbf{K}_{II} & \mathbf{K}_{IB} \\ \mathbf{K}_{IB}^{\mathrm{T}} & \mathbf{K}_{BB} \end{bmatrix} & \begin{bmatrix} \mathbf{S}_I^{\mathrm{T}} \\ \mathbf{S}_B^{\mathrm{T}} \end{bmatrix} \\ \begin{bmatrix} \mathbf{S}_I & \mathbf{S}_B \end{bmatrix} & 0 \end{bmatrix} \begin{Bmatrix} \mathbf{a}_I \\ \mathbf{a}_B \\ \mathbf{h} \end{Bmatrix} = \begin{Bmatrix} \mathbf{0} \\ \boldsymbol{\Theta}\mathbf{g} \end{Bmatrix}$$

By expanding the given block matrix equation explicitly and multiplying the block matrix with the vector in the first row, we obtain

$$\begin{bmatrix} \mathbf{K}_{II} & \mathbf{K}_{IB} \\ \mathbf{K}_{IB}^{\mathrm{T}} & \mathbf{K}_{BB} \end{bmatrix} \begin{Bmatrix} \mathbf{a}_I \\ \mathbf{a}_B \end{Bmatrix} + \begin{bmatrix} \mathbf{S}_I^{\mathrm{T}} \\ \mathbf{S}_B^{\mathrm{T}} \end{bmatrix} \mathbf{h} = \begin{Bmatrix} \mathbf{0} \\ \mathbf{0} \end{Bmatrix} \tag{B.58}$$

This expands into two equations

$$\begin{cases} \mathbf{K}_{II}\mathbf{a}_I + \mathbf{K}_{IB}\mathbf{a}_B + \mathbf{S}_I^{\mathrm{T}}\mathbf{h} = \mathbf{0} \\ \mathbf{K}_{IB}^{\mathrm{T}}\mathbf{a}_I + \mathbf{K}_{BB}\mathbf{a}_B + \mathbf{S}_B^{\mathrm{T}}\mathbf{h} = \mathbf{0} \end{cases} \tag{B.59}$$

By multiplying the block matrix with the vector in the second row, we obtain

$$\begin{bmatrix} \mathbf{S}_I & \mathbf{S}_B \end{bmatrix} \begin{Bmatrix} \mathbf{a}_I \\ \mathbf{a}_B \end{Bmatrix} + 0 \cdot \mathbf{h} = \boldsymbol{\Theta}\mathbf{g} \tag{B.60}$$

Which simplifies to

$$\mathbf{S}_I\mathbf{a}_I + \mathbf{S}_B\mathbf{a}_B = \boldsymbol{\Theta}\mathbf{g} \tag{B.61}$$

Thus, the final expanded system becomes

$$\begin{cases} \mathbf{K}_{II}\mathbf{a}_I + \mathbf{K}_{IB}\mathbf{a}_B + \mathbf{S}_I^{\mathrm{T}}\mathbf{h} = \mathbf{0} \\ \mathbf{K}_{IB}^{\mathrm{T}}\mathbf{a}_I + \mathbf{K}_{BB}\mathbf{a}_B + \mathbf{S}_B^{\mathrm{T}}\mathbf{h} = \mathbf{0} \\ \mathbf{S}_I\mathbf{a}_I + \mathbf{S}_B\mathbf{a}_B = \boldsymbol{\Theta}\mathbf{g} \end{cases} \tag{B.62}$$

This fully expanded form presents a system of equations coupling the variables $\mathbf{a}_I, \mathbf{a}_B$, and $\mathbf{h}$. Due to $\mathbf{S}_I$, which is defined through the boundary integral and vanishes at internal nodes, the final expanded system becomes

$$\begin{cases} \mathbf{K}_{II}\mathbf{a}_I + \mathbf{K}_{IB}\mathbf{a}_B = \mathbf{0} \\ \mathbf{K}_{IB}^{\mathrm{T}}\mathbf{a}_I + \mathbf{K}_{BB}\mathbf{a}_B + \mathbf{S}_B^{\mathrm{T}}\mathbf{h} = \mathbf{0} \\ \mathbf{S}_B\mathbf{a}_B = \boldsymbol{\Theta}\mathbf{g} \end{cases} \tag{B.63}$$

By substituting Eq. (3.43), the final expanded system becomes

$$\mathbf{K}_{II}\mathbf{a}_I + \mathbf{K}_{IB}\mathbf{a}_B = \mathbf{0} \tag{B.64}$$

$$\mathbf{K}_{IB}^{\mathrm{T}}\mathbf{a}_I + \mathbf{K}_{BB}\mathbf{a}_B + \mathbf{S}_B^{\mathrm{T}}\mathbf{H}^{\mathrm{T}}\mathbf{r} = \mathbf{0} \tag{B.65}$$

$$\mathbf{S}_B\mathbf{a}_B = \boldsymbol{\Theta}\mathbf{g} \tag{B.66}$$

By multiplying both sides of Eq. (B.66) by H, we get

$$\mathbf{H}\mathbf{S}_B\mathbf{a}_B = \mathbf{H}\boldsymbol{\Theta}\mathbf{g} \tag{B.67}$$

Eq. (B.66) defines the relationship between the boundary displacements $\mathbf{a}_B$ and the macroscopic traction-related term $\boldsymbol{\Theta}\mathbf{g}$, where $\mathbf{S}_B$ is the matrix responsible for enforcing the boundary conditions. The right-hand side, $\boldsymbol{\Theta}\mathbf{g}$, represents the imposed macroscopic strain. In Eq. (3.43), the matrix $\mathbf{H}$ is introduced to ensure uniform boundary stress by interpolating the boundary constraints using $\mathbf{r}$, a vector containing two unknowns, r_1 and r_2. The key motivation for multiplying Eq. (B.66) by $\mathbf{H}$ is to reformulate the boundary displacement equation in a manner that is compatible with the uniform traction condition. The matrix $\mathbf{H}$ has a specific structure that couples boundary nodes that are images of each other, ensuring that boundary conditions are imposed in a way that enforces uniform traction. This transformation eliminates unnecessary degrees of freedom, reducing the number of independent equations while properly imposing the constraint. Overall, multiplying Eq. (B.66) by $\mathbf{H}$ restructures the equation so that the uniform traction condition is naturally enforced. This

approach ensures that boundary displacements are not prescribed explicitly but are instead linked through $\mathbf{H}$ in a way that maintains stress uniformity. Additionally, it reduces the number of independent unknowns, making the system more efficient while still satisfying the necessary boundary conditions. By rewriting these equations (B.64), (B.65) and (B.67) in a matrix form yields

$$\begin{bmatrix} \mathbf{K}_{II} & \mathbf{K}_{IB} & \mathbf{0} \\ \mathbf{K}_{IB}{}^{\mathrm{T}} & \mathbf{K}_{BB} & \mathbf{S}_B{}^{\mathrm{T}}\mathbf{H}^{\mathrm{T}} \\ \mathbf{0} & \mathbf{H}\mathbf{S}_B & \mathbf{0} \end{bmatrix} \begin{Bmatrix} \mathbf{a}_I \\ \mathbf{a}_B \\ \mathbf{r} \end{Bmatrix} = \begin{Bmatrix} \mathbf{0} \\ \mathbf{0} \\ \mathbf{H}\boldsymbol{\Theta}\mathbf{g} \end{Bmatrix} \tag{B.68}$$

which corresponds to Eq. (3.46) in Subsection 3.2.2.

B.1.4 Periodic displacement - Eq. (3.58)

We now derive the algebraic form of the RVE problem under uniform traction boundary conditions. This is achieved by substituting Eq. (3.55) into Eq. (3.13) and using Eqs. (3.24) and (3.25). The resulting algebraic formulation of the RVE problem after substituting all the partitioned matrices is given by Eq. (B.45) as

$$\begin{bmatrix} \begin{bmatrix} \mathbf{K}_{II} & \mathbf{K}_{IB} \\ \mathbf{K}_{IB}^{\mathrm{T}} & \mathbf{K}_{BB} \end{bmatrix} & \begin{bmatrix} \mathbf{S}_I^{\mathrm{T}} \\ \mathbf{S}_B^{\mathrm{T}} \end{bmatrix} \\ \begin{bmatrix} \mathbf{S}_I & \mathbf{S}_B \end{bmatrix} & 0 \end{bmatrix} \begin{Bmatrix} \mathbf{a}_I \\ \mathbf{a}_B \\ \mathbf{h} \end{Bmatrix} = \begin{Bmatrix} \mathbf{0} \\ \boldsymbol{\Theta}\mathbf{g} \end{Bmatrix}$$

By expanding the given block matrix equation explicitly and multiplying the block matrix with the vector in the first row, we obtain

$$\begin{bmatrix} \mathbf{K}_{II} & \mathbf{K}_{IB} \\ \mathbf{K}_{IB}^{\mathrm{T}} & \mathbf{K}_{BB} \end{bmatrix} \begin{Bmatrix} \mathbf{a}_I \\ \mathbf{a}_B \end{Bmatrix} + \begin{bmatrix} \mathbf{S}_I^{\mathrm{T}} \\ \mathbf{S}_B^{\mathrm{T}} \end{bmatrix} \mathbf{h} = \begin{Bmatrix} \mathbf{0} \\ \mathbf{0} \end{Bmatrix}$$

This expands into two equations

$$\begin{cases} \mathbf{K}_{II}\mathbf{a}_I + \mathbf{K}_{IB}\mathbf{a}_B + \mathbf{S}_I^{\mathrm{T}}\mathbf{h} = \mathbf{0} \\ \mathbf{K}_{IB}^{\mathrm{T}}\mathbf{a}_I + \mathbf{K}_{BB}\mathbf{a}_B + \mathbf{S}_B^{\mathrm{T}}\mathbf{h} = \mathbf{0} \end{cases}$$

By multiplying the block matrix with the vector in the second row, we obtain

$$\begin{bmatrix} \mathbf{S}_I & \mathbf{S}_B \end{bmatrix} \begin{Bmatrix} \mathbf{a}_I \\ \mathbf{a}_B \end{Bmatrix} + 0 \cdot \mathbf{h} = \boldsymbol{\Theta}\mathbf{g}$$

Which simplifies to

$$\mathbf{S}_I\mathbf{a}_I + \mathbf{S}_B\mathbf{a}_B = \boldsymbol{\Theta}\mathbf{g}$$

Thus, the final expanded system becomes

$$\begin{cases} \mathbf{K}_{II}\mathbf{a}_I + \mathbf{K}_{IB}\mathbf{a}_B + \mathbf{S}_I^{\mathrm{T}}\mathbf{h} = \mathbf{0} \\ \mathbf{K}_{IB}^{\mathrm{T}}\mathbf{a}_I + \mathbf{K}_{BB}\mathbf{a}_B + \mathbf{S}_B^{\mathrm{T}}\mathbf{h} = \mathbf{0} \\ \mathbf{S}_I\mathbf{a}_I + \mathbf{S}_B\mathbf{a}_B = \boldsymbol{\Theta}\mathbf{g} \end{cases}$$

This fully expanded form presents a system of equations coupling the variables $\mathbf{a}_I, \mathbf{a}_B$, and $\mathbf{h}$. Due to $\mathbf{S}_I$, which is defined through the boundary integral and vanishes at internal nodes, the final expanded system becomes

$$\begin{cases} \mathbf{K}_{II}\mathbf{a}_I + \mathbf{K}_{IB}\mathbf{a}_B = \mathbf{0} \\ \mathbf{K}_{IB}^{\mathrm{T}}\mathbf{a}_I + \mathbf{K}_{BB}\mathbf{a}_B + \mathbf{S}_B^{\mathrm{T}}\mathbf{h} = \mathbf{0} \\ \mathbf{S}_B\mathbf{a}_B = \boldsymbol{\Theta}\mathbf{g} \end{cases}$$

By substituting Eq. (3.55), the final expanded system becomes

$$\mathbf{K}_{II}\mathbf{a}_I + \mathbf{K}_{IB}\mathbf{a}_B = \mathbf{0} \tag{B.69}$$

$$\mathbf{K}_{IB}^{\mathrm{T}}\mathbf{a}_I + \mathbf{K}_{BB}\mathbf{a}_B + \mathbf{S}_B^{\mathrm{T}}\mathbf{H}^{\mathrm{T}}\mathbf{w} = \mathbf{0} \tag{B.70}$$

$$\mathbf{S}_B\mathbf{a}_B = \boldsymbol{\Theta}\mathbf{g} \tag{B.71}$$

By multiplying both sides of Eq. (B.71) by $\mathbf{P}$, we get

$$\mathbf{P}\mathbf{S}_B\mathbf{a}_B = \mathbf{P}\boldsymbol{\Theta}\mathbf{g} \tag{B.72}$$

Eq. (B.71) enforces that the boundary nodal displacements are constrained by the macroscopic displacement gradient. $\mathbf{S}_B$ is the matrix responsible for enforcing the boundary conditions. It relates nodal displacements to boundary constraints. $\mathbf{a}_B$ represents the displacements at the boundary nodes. This term $\boldsymbol{\Theta}\mathbf{g}$ represents the macroscopic displacement gradient imposed on the RVE boundary due to the applied macroscopic strain. The matrix $\boldsymbol{\Theta}$ ensures that the macroscopic strain $\mathbf{g}$ is consistently applied. The main reason for multiplying both sides by $\mathbf{P}$ is to reduce the number of degrees of freedom while ensuring that periodicity constraints are properly enforced. This comes from the periodic boundary condition assumption Eq. (3.53). $\mathbf{P}$ a matrix that enforces periodicity by reducing the number of independent boundary nodes. Periodic boundary conditions state that displacements at periodic boundary pairs must be linked. That means for every node at $\boldsymbol{\Psi}^+$, there exists a corresponding node at $\boldsymbol{\Psi}^-$ such that their relative displacement follows a specific pattern dictated by the macroscopic deformation $\mathbf{g}$. By multiplying by $\mathbf{P}$, we remove redundant degrees of freedom and ensure that only independent boundary conditions are retained. Mathematically, the matrix $\mathbf{P}$ has a structure where each row has two non-zero entries: $+1$ for a node on one boundary and -1 for its corresponding periodic image. When we multiply $\mathbf{P}$ by $\mathbf{S}_B\mathbf{a}_B$, we enforce the periodic displacement condition by eliminating redundant boundary constraints. Thus, after applying $\mathbf{P}$, the equation enforces the periodicity constraint by eliminating redundant degrees of freedom. In overall, this transformation is important for obtaining a solvable system that correctly incorporates periodic boundary conditions while maintaining mathematical consistency. By rewriting these equations (B.69), (B.70) and

(B.72) in a matrix form yields

$$\begin{bmatrix} \mathbf{K}_{II} & \mathbf{K}_{IB} & \mathbf{0} \\ \mathbf{K}_{IB}{}^{\mathrm{T}} & \mathbf{K}_{BB} & \mathbf{S}_B{}^{\mathrm{T}}\mathbf{P}^{\mathrm{T}} \\ \mathbf{0} & \mathbf{P}\mathbf{S}_B & \mathbf{0} \end{bmatrix} \begin{Bmatrix} \mathbf{a}_I \\ \mathbf{a}_B \\ \mathbf{w} \end{Bmatrix} = \begin{Bmatrix} \mathbf{0} \\ \mathbf{0} \\ \mathbf{P}\boldsymbol{\Theta}\mathbf{g} \end{Bmatrix} \tag{B.73}$$

which corresponds to Eq. (3.58) in Subsection 3.2.2.